Cranfield University

Andrew Pickwell

Design and Development of Micro-electromechanical Acoustic Emission Sensors

School of Applied Sciences

PhD

Academic Year: 2011 - 2012

Supervisor: Prof. Robert Dorey
and Prof. David Mba

January 2012

Cranfield University

School of Applied Science

PhD

Academic Year: 2011 - 2012

Andrew Pickwell

Design and Development of Micro-electromechanical Acoustic Emission Sensors

Supervised by: Prof. Robert Dorey
and Prof. David Mba

January 2012

To my parents, Michael and Janet Pickwell; my sister, Annette Monument; my family; and my friends whose support and encouragement have made this thesis possible.

Acknowledgements

I would like to acknowledge the support and guidance provided by my supervisors, Prof. Robert Dorey and Prof. David Mba, which has been invaluable throughout the course of this research. My thanks go to Dr. Christopher Shaw, Mr Andrew Stallard and Mr Matthew Taunt whose technical expertise and advice has been essential in carrying out the experimental phase of this work.

Thanks also go to friends and colleagues in the Microsystems and Nanotechnology Centre including Mr Matt Hockley, Dr. Paul Jones, Dr. Glenn Leighton, Mr Matt Stock and Mr Mark Tillman whose advice and moral support has been highly valued. The moral support provided by my family and friends has also been greatly appreciated.

Finally I would like to acknowledge the financial support provided by the EPSRC and Cranfield University.

Abstract

Non-Destructive Testing (NDT) is a vital technique in modern engineering, enabling the monitoring of the structural health of a component and therefore enabling the prediction of component failure. Once the structural health of a component is known, timely maintenance can be carried out to prevent component failure which may have resulted in costly downtime or injury. One NDT technique which has been of increasing interest over recent years is Acoustic Emission (AE) monitoring. AE monitoring technology has been successfully combined with preventative maintenance, saving millions of pounds worldwide.

There are issues with current AE monitoring technology which limit the effectiveness of AE monitoring in NDT applications. Current technology is costly to implement. This cost prohibits continuous monitoring which is more effective at assessing the health of the structural component in real time. Currently AE is limited to scheduled testing which may fail to detect flaws before component failure occurs. The high cost of AE testing equipment also means that AE sensors must be removed after testing and so may not be placed in locations with limited access, potentially limiting the effectiveness of the AE monitoring. Micro-Electromechanical Systems (MEMS) AE devices provide solutions to these issues. Low cost MEMS AE devices may be placed permanently on a structure, enabling continuous monitoring of areas with limited access. In this work several MEMS AE devices have been developed.

A lead zirconate titanate (PZT) film 17.6μm thick has been embedded into a Kovar test plate used to represent a structural element. Simulated AE has been generated by Hsu-Neilson pencil break tests and the signal detected by the thick film device has been benchmarked against a commercially available AE sensor of a traditional design.

The embedded thick film was shown to effectively detect the simulated AE and characterisation of the material through the use of dispersion curves was possible. It was found that reducing the number of material interface layers that the AE wave must pass through, between the structural element being monitored and the active element of the AE sensor, significantly increased the percentage of energy transferred.

As such, processes enabling the release of PZT thick films (1μm-100μm) from substrates, which provide support for the films during manufacture, were developed. Titanium and copper foils were employed as sacrificial substrates which were to be completely removed. Issues with the support of the thick film on titanium foil resulted in the destruction of the film during the removal of the substrate. The copper foil substrate was successfully removed, however, issues with the co-processing of copper and PZT resulted in a conductive PZT film unsuitable for use as a MEMS AE sensor. The use of sodium silicate as a non-metallic release layer was subsequently investigated. Drying and calcining processes were developed to produce a film with a surface morphology suitable for co-processing with PZT. It was found that the drying and calcining processes which resulted in a suitable surface morphology for PZT co-processing also reduced solubility, limiting the use of sodium silicate as a substrate release layer.

The successful deposition of thick film PZT onto titanium foil was an interesting avenue of investigation. Thick film PZT on a titanium foil substrate was developed and employed as a MEMS AE sensor to be mounted on a structural element. Benchmarking tests were carried out on a steel test plate, comparing the MEMS AE device to a commercially available AE Sensor. The thick film on titanium foil was found to perform well, successfully detecting artificially generated AE and characterising the dimensions of the test plate through the use of dispersion curves and AE wave reflections. The thick film devices on titanium foil were also tested on a dynamic system. A signal to noise ratio lower than one resulted in the thick film on titanium foil sensors being unable to detect AE in the dynamic system.

Benchmarking was also carried out on a PZT/polymer AE sensor

which has been developed in this work to provide a solution to the low temperature deposition of embedded MEMS AE sensors. Limiting deposition temperatures was important in enabling the embedding of MEMS AE devices on polymer structural elements without causing damage to the structure. The PZT/polymer AE sensor effectively detected AE generated in a steel test plate but the characterisation of the test plate was not possible due to distortion of the AE signal and a low signal to noise ratio.

Future work was discussed with the aim of solving some of the issues encountered during the development of the MEMS AE sensors. Avenues for future investigation were identified including wireless MEMS devices and the use of MEMS AE devices in AE arrays allowing for the location of flaws within the structural element being monitored.

Nomenclature

ϵ_r	Relative permittivity
A_i	Asymmetric Lamb wave component
AE	Acoustic Emission
AFC	Active Fibre Composite
CSD	Chemical Solution Deposition
CVD	Chemical Vapour Deposition
d_{31}	31 piezoelectric coefficient
d_{33}	33 piezoelectric coefficient
DRIE	Deep Reactive Ion Etching
EHDA	Electro-Hydrodynamic Atomization
EM	Electro-Magnetic
FBG	Fibre Bragg Grating
FFT	Fast Fourier Transform
FT	Fourier Transform
IPA	Isopropanol
KNN	Potassium sodium niobate
KOH	Potassium hydroxide

MBE	Molecular Beam Epitaxy
MEMS	Micro-Electromechanical System
MPB	Morphotrophic Phase Boundary
NDT	Non-Destructive Testing
PAC	Physical Acoustics Corporation
PLD	Pulsed Laser Deposition
pO_2	Partial pressure of oxygen
PVDF	Poly-vinylidene fluoride
PZT	Lead zirconate titanate
RIE	Reactive Ion Etching
S_i	Symmetric Lamb wave component
TMAH	Tetra-methyl ammonium hydroxide
US	Ultra-Sonic
UV	Ultra-Violet
WFT	Windowed Fourier Transform
WT	Wavelet Transform

Contents

List of Figures

List of Tables

Chapter 1

Introduction

1.1 Acoustic Emissions Monitoring

The use of condition monitoring to prevent component or structural failure, or unplanned machine downtime is a multi-billion pound industry worldwide. Non-Destructive Testing (NDT) is an important aspect of condition monitoring as it allows monitoring to take place without damage to the component under observation and in some cases whilst the component is in operation. NDT is utilised in many different industrial sectors including civil [7, 8, 9], aerospace [10] and nuclear [11, 12]. There are several NDT techniques which can be utilised in condition monitoring. One widely employed NDT technique is Acoustic Emission (AE) monitoring.

Acoustic Emission (AE) monitoring has long been used as an indicator of structural integrity. One of the first known applications of AE testing was the monitoring of pottery during firing [13]. This type of audible AE monitoring has been used in one form or another for several thousand years with examples being found in metallurgy during the twinning of pure tin and the martensite transformation of steel [8, 14]. Audible AE monitoring also found use as a pre-failure warning in mines when creaking timber would precede collapse [14].

AE techniques for monitoring crack progression in laboratory conditions were initially investigated scientifically in 1934 by Kishinouye [15]. Kishinouye monitored cracking in wood to simulate the fracture of the earth's crust during earthquakes [16]. Other early tests were carried out on inaudible AE during the 1930's-40's

and various electromechanical monitoring systems were developed including electronic amplification of the received acoustic signal.

The 1950's saw the beginning of the first real research effort into AE in the western world with the publication of Joseph Kaiser's dissertation [8, 16, 17]. Kaiser carried out testing on metal tensile specimens and recorded the AE emissions related to the magnitude of the tensile stress to which the specimens were exposed. Kaiser's work was also the first documentation of the Kaiser effect. The Kaiser effect is useful in AE monitoring of structural elements as it can be used to ascertain the loading which the element is exposed to under normal operating conditions by exposing the element to an increasing load until AE signals are detected.

Kaiser's work led to the publication of 'Acoustic Emission' by B.H. Schofield in 1961. This is the first known use of the term Acoustic Emission [8]. In the 1960's working groups were formed to encourage ongoing research in the field of AE The focus of these working groups in the 60's was often that of dislocations as the cause of AE. It was at this point that AE became an accepted NDT technique [17].

AE monitoring has found use in a myriad of applications since becoming an accepted NDT technique. One of the first major applications in which AE found use was the monitoring of concrete under structural loading [8, 18]. As the use of AE monitoring in industry became more widespread the viability of using continuous AE monitoring was limited by economic considerations [16]. Research into the mechanics of AE, including characterization of emission sources and wave propagation, increased in intensity [18] to facilitate a change in the way which AE monitoring was carried out.

Modern AE monitoring is a vital technique in monitoring the changes in structural or component health over time. AE monitoring is traditionally used as part of a scheduled maintenance programme. When a structural component is placed under load, stress concentrations form around micro-cracks or dislocations in the material. When the load is increased these cracks can propagate through the material, increasing in size and reducing the macro-scale properties of the material. As these cracks propagate sound is produced. This sound, or AE, travels through the material and can be detected by an acoustic sensor. The

energy of these signals are related to the crack size and when combined with the frequency of AE events can be used to assess the structural health of the material.

As the structural integrity is reduced by the increase in crack size and frequency in the material, the risk of structural failure increases. Structural failure is undesirable for many reasons including unplanned machine downtime caused by unexpected failure, damage to related components such as rotating shaft damage during bearing failure and the risk to the health of people affected by the failing component. For example between 1990 and 2007 there were 1104 deaths in the US alone from commuter aircraft crashes, many of which were the result of previously undetected structural damage [19]. The minimization of these risks is vital in modern engineering and AE is essential in the drive to predict and prevent failures before they occur.

The application of AE is currently limited by several factors. Contemporary AE monitoring systems are bulky and expensive, costing thousands of pounds and requiring skilled technicians to implement for even a short period of time. It is impractical to permanently affix AE sensor to all but the most valuable of assets. This limits the application of structural health monitoring on structural components which are inaccessible or where there are constraints on space and weight; such as those found in the aerospace and nuclear industries.

Micro-ElectroMechanical System (MEMS) can provide solutions to these issues. MEMS processing techniques allow for the production of low cost thick film AE sensors which are over two orders of magnitude thinner than the smallest of traditional AE sensors. Low cost devices are advantageous as they can be permanently attached to the component which requires monitoring with relatively little capital investment. This means that sensors can be applied during component construction in enclosed spaces without significantly increasing the production cost, enabling monitoring at scheduled time intervals or continuously over the life of the component.

1.2 Research Aims and Objectives

This work aims to utilise MEMS manufacturing techniques to produce thick film AE sensors which are capable of being employed in structurally integrated applications, either through direct integration or through the release of the device from the substrate material on which it was manufactured.

The objectives of this work are outlined below:

- Proof of concept testing.
- Develop and benchmark structurally integrated thick film AE sensors.
- Investigate sacrificial substrates and substrate release layers.
- Develop MEMS devices for use in AE sensing applications.

1.3 Thesis Structure

In Chapter 2 of this work a literature review was conducted, focusing on AE signal characteristics and AE technology. Materials involved in the manufacture of piezoelectric AE devices and the manufacturing techniques utilised were reviewed. Manufacturing techniques employed in this work were identified in Chapter 3. Thick film AE sensors were manufactured by thick film processing techniques. An initial device was manufactured and tested as a proof of concept in Chapter 4.

In Chapter 5 a thick film AE device was embedded directly onto the structural element which required monitoring and the sensor performance was then benchmarked against a conventional, commercially available AE sensor. Signal analysis was carried out to fully characterise the performance of the structurally integrated device. Features of the signal related to the physical properties of the structural element through which the AE is transmitted were identified.

Work was carried out in Chapter 6 to identify methods by which the the lead zirconate titanate (PZT) films, deposited for use in AE sensing applications, may be released from the substrate upon which they are deposited. Both sacrificial substrates and substrate release layers were investigated. Copper and titanium,

which were removed by chemical etching, were investigated as metallic sacrificial substrates. Sodium silicate was investigated as a release layer which may be removed, using water as an etchant. Future work to improve the method by which PZT films are released was identified.

PZT films were deposited on metallic foil substrates including Kovar and titanium in Chapter 7. The PZT deposited on titanium was developed into a device for AE monitoring. The AE device on titanium foil was then benchmarked against a commercially available sensor in static and dynamic testing situations to ascertain the effectiveness of the thick film at detecting AE.

A polymer/PZT system was developed for use in the structural integration of MEMS AE sensors with manufacturing temperatures below 150°C in Chapter 8. The PZT/polymer film properties were investigated, compared to theoretical properties, and refined. An improved polymer/PZT film was deposited on an aluminium foil substrate and then benchmarked against commercially available AE sensors.

A summary of the work was conducted (Chapter 9) and future work in the development of MEMS AE devices was discussed (Chapter 10). The future work identified avenues for further development of the work carried out. Conclusions were drawn from the work and presented in Chapter 11. Published work related to this thesis was presented in appendix B

Chapter 2

Literature Review

2.1 Acoustic Emissions

Modern AE monitoring technology has changed very little since the 1960's and is now an integral part of NDT. AE monitoring has been combined with preventative maintenance to great effect, it can provide early warning of structural or machine failure and saves companies millions of pounds by preventing avoidable unplanned machine downtime. Modern AE monitoring is tasked with detection of AE from many sources including changes in crack geometry, corrosion, dislocation movement, twinning and material phase change [20]. Another important application for AE in modern NDT is the monitoring of fibre breakage and delamination in composite materials utilised in many applications such as aircraft wing structures [20].

AE monitoring is not only tasked with monitoring overall structural health but also with identifying the location of the structural flaws [20]. Machines or structural elements are monitored at specific intervals and a record of the overall component 'health' is stored. Changes in this record over time can identify problems which can be overcome before a failure occurs. Due to the advanced warning afforded by AE monitoring, maintenance can be carried out during pre-planned downtime and avoiding costly disruption.

To enable the effective implementation of AE monitoring an understanding of the characteristics of the generation and transmission of AE is important, both through the structure being monitored and across the interface between the trans-

mission media and the sensor employed for AE monitoring. An understanding of the properties of state of the art sensors used in the detection of AE and the signal processing carried out to characterise AE is also vital to the effective implementation of AE monitoring and to the development of low cost, disposable AE sensors which widen the range of applications for which AE monitoring is applicable.

2.1.1 Acoustic Emissions Monitoring Technology

Modern AE monitoring systems are complex and require an understanding of several key components to function effectively. These components include the structural element being monitored, the coupling between the element and the sensor, the sensor (A, figure 2.1), the pre-amplification (B, figure 2.1) and the data collection and analysis equipment (C, figure 2.1).

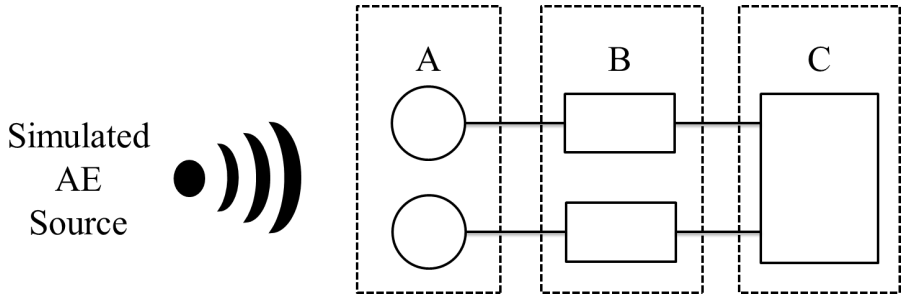

Figure 2.1: A schematic of an AE detection system used to detect simulated and real world AE; showing a simulated AE signal, two sensors (A), pre-amplifiers (B) and a data acquisition system (C) [1].

The structural element under scrutiny is the first important component. An understanding of the way in which AE waves travel through the component is vital to the execution of AE monitoring. Complex surface geometry and heterogeneous material properties may affect the transmission of the AE waves through the media by both attenuating and absorbing the AE wave energy. An understanding of these phenomenon is important to ensure that the sensors are affixed to the structure in the best possible locations and that the distance between the sensors is not too great.

2.1.2 Acoustic Wave Properties

Whilst it has been found that AE can be generated by many sources, as noted above, detection of AE would be useless without an understanding the fashion in which AE travels through the transmission material. The energy from AE is transmitted through the material medium in the form of a wave. The type of energy wave transmitting the energy is related to the geometry of the transmission medium and on the properties of the AE source.

There are two main types of AE: transient and continuous. In the field of NDT by AE monitoring the vast majority of signals produced by AE sources are transient. These emissions are bursts of energy caused by individual events. An example of this type of emission can be seen in the propagation of cracks through a material. When excessive stress is placed on a material at the macro-scale a crack will develop, this results in a stress concentration. The stress concentration results in the crack propagating in discrete steps through the material as stress at the point of the concentration increases. Each discrete change of the crack dimensions produces a burst of energy which travels through the material in the form of a transient acoustic wave. Continuous waveforms occur in AE when the time between transient events is less than the time taken for each event to reduce in amplitude below a set threshold level. When this occurs the transient events overlap, forming one continuous waveform.

Transient waves exhibit several properties of interest, regardless of the mode in which the wave propagates. Properties of interest include [13, 21]:

- Maximum amplitude.
- Ringdown count.
- Rise time.
- Event duration.
- Amplitude distribution slope.
- Event energy.

Properties which can be identified directly from the time domain signal of a detected AE waveform can be seen in figure 2.2 [22]. Time domain analysis of these properties can be carried out to characterise the source of the AE and the overall structural health of the component. Characterisation of the important

time domain properties is carried out in section 2.1.4.1.

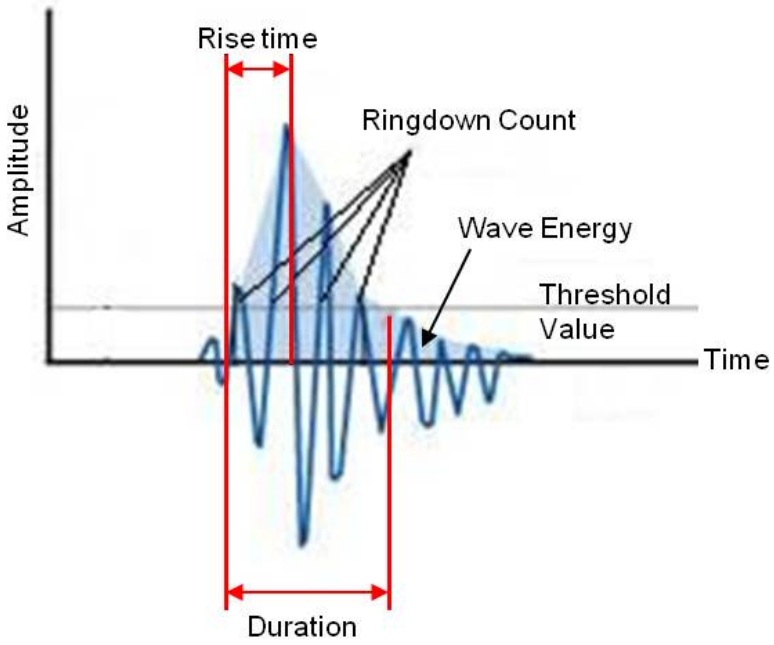

Figure 2.2: A time domain AE plot identifying parameters of the AE signal important in the characterisation of structural damage.

2.1.2.1 Types of Acoustic Waves

Another important area of understanding which is vital to the successful implementation of AE monitoring is the physical process by which the AE propagates through the transmission medium. There are various different acoustic wave propagation modes including longitudinal, shear, creep, Love, Rayleigh and Lamb waves. While the way in which the AE transmits through the medium depends largely on the geometry of the transmission medium, all of the propagation methods involve the transmission of energy by the vibration of the atoms that comprise the transmission medium. Graphical representations of the transmission methods can be seen in figure 2.3.

Longitudinal Waves

Longitudinal wave transmission (figure 2.3a) involves the vibration of particles

along the direction of wave propagation in a bulk material. The wave transmission mode involves alternating rarefaction and compression of particles within the medium. This is the transmission mode by which sound propagates through a semi-infinite bulk medium and waves of this type exhibit a characteristic velocity related to material density and elastic properties [2].

Shear Waves

A shear or transverse wave (figure 2.3b) is a bulk wave propagation mode and exhibits a characteristic velocity related to the elastic properties and the density of the transmission medium [2]. In shear waves the particle vibration is perpendicular to the direction of wave propagation. Electromagnetic waves exhibit this type of propagation mode.

Creep Waves

Creep waves (figure 2.3c) occur when longitudinal waves interact with the interface between the bulk medium and the surrounding environment at an angle. The longitudinal wave energy is partially reflected back into the material and partially refracted along the bulk medium/environment interface. The refracted longitudinal wave energy is called a creep or head wave and exhibits similar properties to the longitudinal wave from which it is derived.

Love Waves

Love waves are shear waves which occur at the interface between the transmission medium and the surrounding environment. Love waves have all the characteristics of shear waves on the surface of the medium but the wave amplitude reduces dramatically at a depth of a few wavelengths. Love waves have been extensively investigated as it is this propagation mode by which seismic waves are transmitted through the Earth's crust during earthquakes.

Rayleigh Waves

Like Love waves, Rayleigh waves are found at the surface of a semi-infinite bulk medium. Rayleigh waves area also known as surface waves (figure 2.3d) and are a result of the interaction of the surface of the transmission medium with both transverse and longitudinal waves. Rayleigh waves exhibit a characteristic velocity generally slower than either contributing mode [2]. Due to this combination of longitudinal and transverse particle motion with the medium surface, the particle vibration in this type of wave propagation takes the form of an elliptical movement which is perpendicular to the surface of the transmission medium. Waves in the ocean propagate in this fashion.

Lamb Waves

Lamb waves (figure 2.3e) require special attention in NDT and more specifically in the field of AE monitoring and have been the focus of extensive study [23, 24, 25, 26, 27]. Like Rayleigh waves, Lamb waves are guided by the surface of the transmission medium. Lamb waves occur away from the AE source [28] when the transmission medium thickness is of a similar dimension to the wavelength of the AE and when the planar dimensions are much greater than the thickness [19]. As the transmission medium has a thickness of similar dimensions to the wavelength both the top and the bottom surfaces interact with the waveform. Lamb waves are the most common wave propagation mode in modern engineering structures which make extensive use of metal or polymer plate materials which exhibit the dimensional properties for Lamb waves to occur.

The complex mathematical description of Lamb waves has been carried out by several researchers since the first description by Lamb in 1917 [19]. Lamb waves were found to be a superposition of both longitudinal and transverse waves with infinite wave modes comprising of both symmetric and asymmetric components [19]. The symmetric (right, figure 2.3e) and asymmetric (left, figure 2.3e) components of plate waves will be referred to as S_i and A_i, where 'i' is the wave mode and with an order between zero and infinity. Particle vibration in S_i waveforms, whilst usually smaller in magnitude than in the A_i waveform, exhibits a large component of motion parallel to the plane of the wave propagation direction. The A_i waveform exhibits a large component of motion perpendicular to

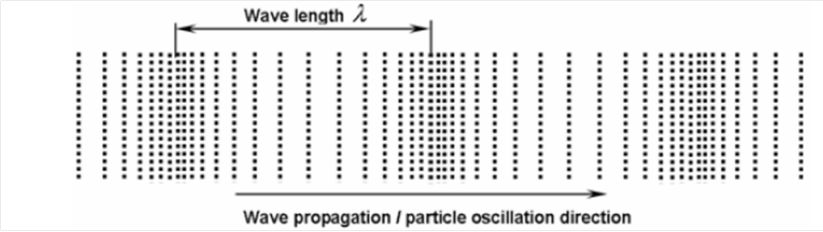

(a) Longitudinal Wave

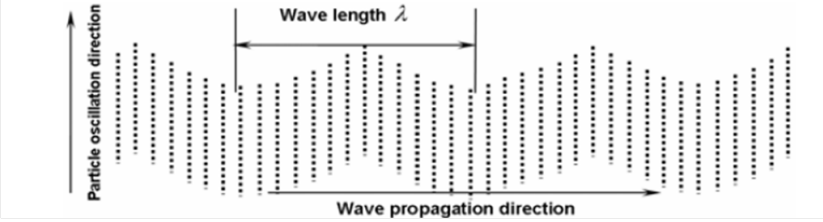

(b) Shear Wave

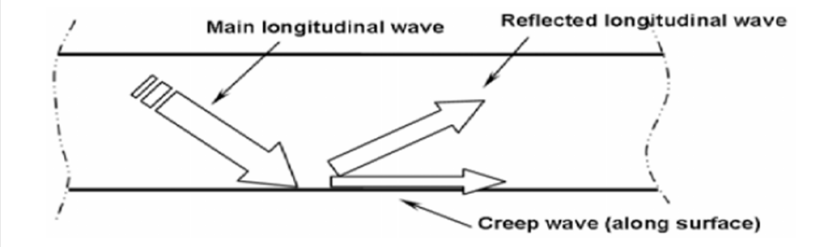

(c) Creep Wave

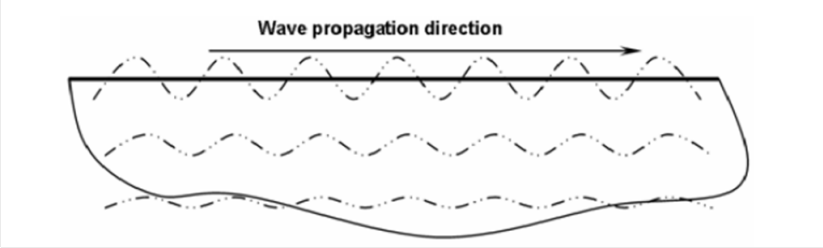

(d) Rayleigh Wave

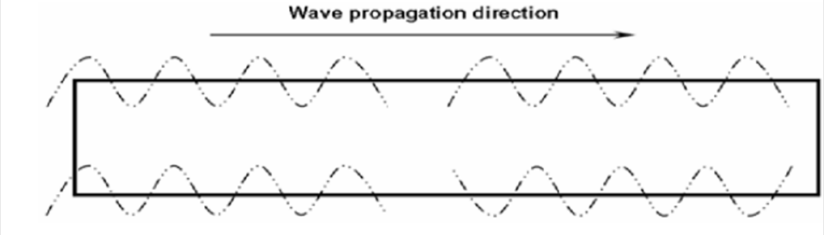

(e) Lamb Waves, asymmetric (left) and symmetric (right)

Figure 2.3: AE transmission waveforms [2]

the plane of the direction of wave propagation.

Each frequency component of the overall wave form propagates through the transmission medium with a different velocity related to the component frequency and the material properties of the transmission medium this is called the wave phase velocity [29] [28]. The velocity of the wave phase is defined as the product of the wavelength and the frequency of the wave [19]. There is also a group wave velocity which is the velocity with which the overall waveform propagates through the transmission medium. The velocity of the wave group is defined in equation 2.1.

$$C_g = \frac{d\omega}{d\left(\frac{\omega}{C_p}\right)} \tag{2.1}$$

Where C_g is the wave group velocity, C_p is the wave phase velocity and ω is the central frequency of the wave multiplied by 2π [19].

Phase and group velocities can be employed, along with plate thickness to calculate and plot the velocity of S_i and A_i wave modes against frequency. These plots are known as dispersion curves and are useful for AE applications as detailed in section 2.1.4.1 [30].

Dispersion curves and known wave velocities aid in the use of arrays to identify the source of an AE emission. Traditionally source identification has been carried out using the time at which the AE signal amplitude first crosses the threshold level. This is made more difficult to identify by the variation in wave velocity and therefore arrival time due to dispersion [28]. Understanding dispersion and utilizing wavelet frequency analysis (section 2.1.4.1) can enable the use of arrival time of a single waveform component to be identified. As the velocity of single waveform components will not vary relative to each other, using the arrival time of an individual component leads to much improved arrival time identification and therefore much more accurate location of the AE source. In practice resonant sensors are employed to improve source location as the sensitivity of these sensors to a narrow frequency band provides a degree of consistency in arrival time regardless of the dispersion of the wave energy.

2.1.2.2 Signal Attenuation

Attenuation is the loss of energy in a wave travelling through a medium between the source and the detecting sensor. Attenuation has several causes but invariably results in the signal received at the detecting sensor having lower amplitude than the signal at the source of the AE [31]. Geometric spreading, internal friction, energy dissipation into adjacent media and the spreading of frequency components [2] are all methods by which an AE signal may be attenuated. The signal amplitude may also be reduced as the AE wave travels between different transmission media, including the AE sensor designed for detecting the wave. This attenuation is caused by a mismatch of acoustic impedance between different transmission media.

Geometric Spreading

Attenuation due to the energy spreading effects of distance in a free-field, ideal system are described by equation 2.2. This equation shows that doubling the distance between sensor locations results in a reduction of received signal power by 6dB; the signal power is proportional to the inverse square of the distance from source [2]. The reduction in signal power is related to the area of the wave front increasing as the distance between the AE source and wave front increases, effectively spreading the finite energy over a wider area. This effect is dominant close to the source of the AE and dominates signal attenuation caused by other attenuation effects [2].

$$SPL_2 = SPL_1 - 20log\left(\frac{R_2}{R_1}\right) \tag{2.2}$$

Where "SPL_1" is the Sound Power Level at distance "R_1" from point of sound origin and "SPL_2" is the Sound Power Level at distance "R_2" from point of sound origin.

Internal Friction

The level of signal attenuation is greater in non-ideal, real world structures due to material inclusions, grain boundaries and variation in material density which alter the acoustic impedance within the material. This type of signal attenuation is caused by viscous friction within the material converting wave energy to heat. This effect is more dominant at larger distances from the source of the AE than geometric spreading [2]. As AE signals are weak at origin the effects of attenuation must be counteracted by the inclusion of a pre-amplifier in the system [20]. There is also some signal distortion which is caused by attenuation due to viscous friction in the material [31]. The distortion, including a change in waveform rise time, is not affected by signal amplification. In high friction materials these effects must be taken into account when analysing AE signals.

Energy Dissipation to the Surroundings

Signal strength can also be lost to the surrounding environment depending on the wave propagation mode. Waves in which particle vibration is parallel to the surface of the transmission medium interfacing with a surrounding material, such as an interface between a plate and a surrounding fluid, lose very little energy to the surrounding material. This is due to the difficulty of transmitting in-plane vibration across a boundary layer [19]. Wave propagation modes in which the particle vibration direction is perpendicular to the interface between the surface of the plate and the surrounding environment will transmit considerably more energy to the surrounding environment [19]. This is of importance in AE monitoring as S_i and A_i Lamb waves exhibit particle vibration directions parallel and perpendicular to the surface of the plate respectively as described in section 2.1.2.1. Therefore signal loss to the surrounding environment is of concern where A_i waves are being observed; this results in S_i waves propagating over greater distances that A_i waves [19].

Spreading of Frequency Components and Directionality

As described in section 2.1.2.1 each frequency component of a waveform exhibits a different characteristic velocity related to the frequency of the component

and the material properties of the transmission medium. This gives rise to a phenomenon known a phase spreading. As time from emission increases the wave spreads out due to the effect of some frequency components travelling faster than others [2]. While no energy is lost to the surrounding environment due to this effect, the spreading of the wave energy over a larger area results in the received maximum amplitude reducing as distance from the source increases [19]. The extent to which the peak amplitude is reduced depends on both the dispersion gradient and the bandwidth of the waveform [2].

Another important factor to consider is the directionality of the AE source, AE caused by crack progression may not have an equal sound power in all directions. Reflection and loss where the wave interacts with the boundary layer between the transmission media and the surrounding environment will also reduce signal energy. As such it is clear that the locations for sensor placement must be carefully considered to optimise the efficiency of the monitoring equipment.

Acoustic Impedance Mismatch

Acoustic impedance, measured in Rayls, is an important factor in the transmission of acoustic energy when material interfaces are involved. Acoustic impedance is therefore an essential parameter to understand in AE monitoring as it has a strong influence on the transmission of acoustic energy over the interface between the transmission medium, the coupling layer and the sensor. The acoustic impedance of a material is the product of the velocity of the AE and the density of the material [20]. Therefore the acoustic impedance also varies with the frequency dependant velocity of the AE.

The greater the acoustic mismatch, the greater the fraction of acoustic energy reflected from the interface and therefore the smaller the fraction of transmitted energy. The relationship between the acoustic impedance values of two materials at an interface and the transmitted energy across that interface is shown by equation 2.3 [20]. From this equation it is clear that the acoustic impedance mismatch between the sensor and the element under observation must be minimised to maximise the energy transmitted across the interface.

$$T = 1 - \left(\frac{Z_1 - Z_2}{Z_1 + Z_2} \right)^2 \tag{2.3}$$

Where "T" is the fraction of AE transmitted across material interface, "Z_1" and "Z_2" are the acoustic impedance of materials 1 and 2 respectively.

If the sensor is directly pressed onto the element under observation then a thin air layer will be present between the sensor and the element under observation. Air has a very different acoustic impedance to both structural materials, 5 orders of magnitude lower than the metals and polymers, and ceramics from which the sensor active element, wear plate and structural element under observation are made. This air layer can result in much of the acoustic energy from an AE wave being reflected back into the transmission medium, not transmitted into the sensor material. This effect is minimised by the use of coupling layers.

2.1.2.3 Coupling Layers

A coupling layer is required between the structural element under observation and the AE sensor. The coupling materials employed exhibit an acoustic impedance closer to that of the sensor and structural material than air. This limits the AE signal attenuation caused by the acoustic impedance differential between the structure, the inter-facial layer and the sensor. The effects of acoustic impedance mismatch between these elements can be described by equation 2.3. Differences in the acoustic impedance can also cause the AE waveform to become distorted [32]. It is therefore important to ensure that all air bubbles are removed from the coupling layer. Calibration can be carried out to assess and compensate for the effects of the coupling layer on the transmitted energy [33] as discussed in section 2.1.3.3.

The coupling material utilised is determined by the structural element and the type of sensor in use. For long term applications with robust materials and sensors an adhesive such as super-glue can be used. For applications in which the structural element or the sensor is fragile then grease is used. Where grease is employed as a coupling agent it is important that a small compressive force is

used to ensure a good contact between the sensor and the structural element.

2.1.3 Sensors

AE sensors are vital in the conversion of the mechanical vibrations, due to AE events, into an electrical signal which can be monitored by computer. Without an effective sensor the other components of an AE detection system are rendered ineffective. As such it is clear that the sensor design is key and there are several solutions to detecting AE signals. Most AE sensors are of a resonant type [20]; many different device types have also been researched for use in AE monitoring, including several commercially available AE sensors. These devices are discussed in detail in sections 2.1.3.1 and 2.1.3.2.

2.1.3.1 Commercial Sensors

Piezoelectric Sensors

Most modern commercial sensors are designed around a single, bulk piezoelectric element sandwiched between two circular electrodes, one of which is in contact with the sensor exterior casing to provide electrical isolation. A wear plate is used to protect the piezoelectric element from damage. A backing material is used to limit reflections from the interface between top of the piezoelectric element and the casing [34]. A typical single element piezoelectric commercial sensor cutaway showing the device internal features can be seen in figure 2.4.

PZT is the piezoelectric material which has found widest use in AE sensor manufacture. Bulk PZT, is the material most commonly used for the AE sensor element - bulk materials are defined as being greater than 100μm in thickness. PZT is used because, as discussed in section 2.3.1, it exhibits properties which are suited to detecting AE inputs whilst still being low cost compared to a single crystal element. The dimensions - width and depth - and the speed of sound within the sensor element dictate the resonant frequencies of the device as shown in equation 2.4.

Piezoelectric elements resonate at a wavelength that is twice the thickness of

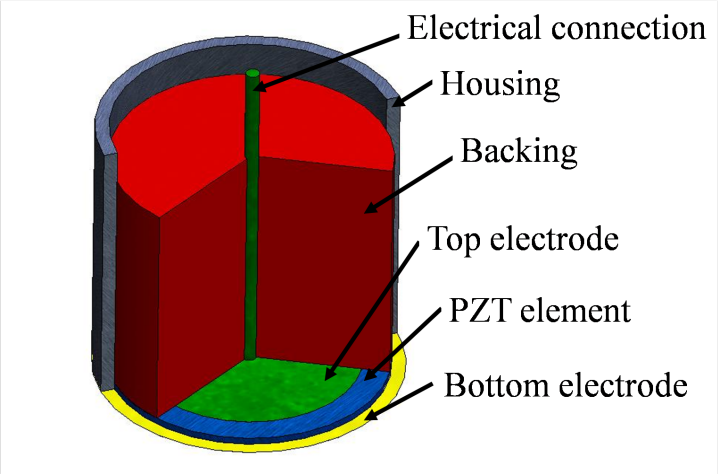

Figure 2.4: Cutaway of a single element piezoelectric AE sensor

the element. AE testing is usually carried out at between 100kHz and 1MHz [35]. The speed of sound in PZT is known to be 4350m/s [36], from this it can be calculated using equation 2.4 that the corresponding wavelength is 4.35mm and 43.50mm. As such piezoelectric elements between 2.175mm and 21.750mm thick resonate in the thickness mode in AE applications.

Single element sensors with dimensions resulting in a resonant response in the frequency band employed for AE monitoring are considered to be resonant sensors. Most operate within a narrow frequency range, this narrow resonant frequency window is highly sensitive and enables the detection of low amplitude AE events [8]. Single element sensors can be used as wide band devices, this lowers the sensitivity to the waveforms due to high damping [8]. For wide band sensors it is important for the resonant frequency of the sensor element to fall outside of this operational frequency band [37] to give a consistent response regardless of the frequency of the waveforms detected; if the AE signal excites the sensor resonance then the response to an input signal will be of a disproportionately high amplitude.

Another important factor which is related to the physical dimensions of the active piezoelectric element is the electrical impedance of the device. The resonant response to an input signal correlates with an electrical impedance peak. The frequency at which this peak occurs is dependent of the electromechanical properties of the piezoelectric element.

$$F = \frac{c}{\lambda} \tag{2.4}$$

Where "F" is the frequency, "c" is the speed of sound in the piezoelectric element and "λ" is the thickness of piezoelectric element.

Sensor designs vary depending on the applications for which they are intended, although most have only a single piezoelectric element operating in the 31 piezoelectric coefficient (d_{31}) direction to detect the S_i Lamb waveform [20]. The sensor electrodes are designed to be circular as the sensitivity of different shaped electrodes, such as square, are strongly affected by the direction from which the AE signal arrives [19].

The electrode should also have a diameter approximately half the wavelength of the Lamb wave under observation. This is rarely possible because as the frequency of AE decreases, the desired electrode diameter increases. As the detection of AE takes place over a wide frequency range, the matching of electrodes to all of the frequencies in that range is not possible. Phase spreading of the AE is also an issue as the extent to which phase spreading occurs depends on both the material properties and the distance of the sensor from the source of the AE. As phase spreading increases the desired electrode diameter also increases. As such AE sensors more often measure the average displacement over the sensor area [19].

Commercial bulk sensors are attached to the surface of the component being monitored. Sensors mounted on the surface in such a way become vulnerable to external noise, increasing the uncertainty over the properties of measured signals. It is therefore desirable to have the option of structurally integrating AE monitoring devices to reduce these effects [19]. Structural integration of AE sensing equipment in systems such as glass fibre lay-ups may have adverse effects on the structural properties of the material, effectively building in an inclusion. The effects of structural integration on material properties are currently poorly understood [19].

Differential sensors have been designed which consist of a piezoelectric disc cut into two semi-circular elements. One element is positively poled, the other negatively poled and electrical connections are made to both [38]. AE input sig-

nals generate a response from both elements, one response is positive and the other negative. The responses are then electronically subtracted during pre-amplification. The AE signals are oppositely poled, whereas the noise signals introduced in the cables, carrying both the positive and negative signals, are positive. As a result the combined signals, following electronic subtraction, double the amplitude of the AE signal. Any signals caused by electronic interference in the cable between the sensor and the pre-amp are also subtracted and therefore cancel to zero. This results in a larger signal amplitude and a smaller noise amplitude and, therefore, a more favourable signal to noise ratio as shown in figure 2.5. The advantages of differential sensors are a compromise with added manufacturing complexity, which results in a higher unit cost and thus limits the use of differential sensors to applications where a higher signal to noise ratio is necessary.

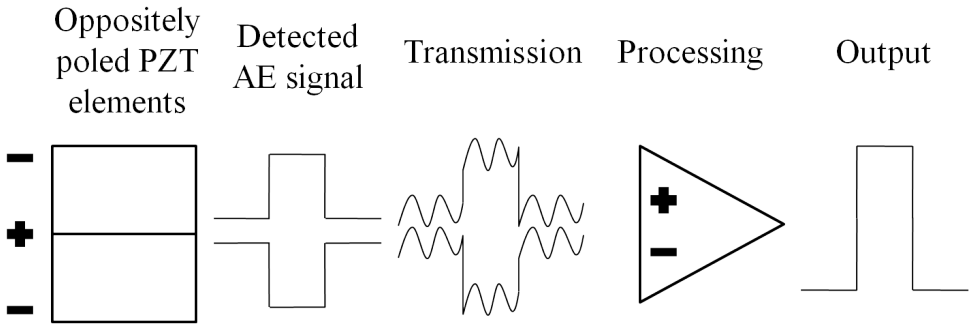

Figure 2.5: Schematic showing how the subtraction of dual signals, from oppositely poled piezoelectric elements sharing one common ground electrode in the centre, can double the amplitude of oppositely polarised AE signals whilst reducing electronic noise imposed on the signal during signal transmission.

In addition to PZT sensors, devices have been designed with the piezoelectric materials exhibiting high Curie temperature so that polarization is not lost in high temperature monitoring applications. Monitoring with these devices can be carried out over large temperature ranges, between -200°C and 540°C [39] in some cases. Sensors are also available for underwater applications. Sensors designed to operate underwater not only have to be fully waterproof at high water pressures but also require an in-built charge pre-amplifier to boost the output signal.

Laser Interferometry

Contact-less sensors are available commercially in the form of laser interfer-

ometry devices. Laser interferometry is used to measure the absolute position of the surface of the material under observation. Any variation to the position of the surface, caused by vibration or by an AE can be detected [40]. Interferometry has the benefit of being able to provide quantitatively comparable results in so far as there are no variations in coupling or sensor calibration. However, there are still variations in the material properties which can cause inconsistent attenuation in seemingly identical components. Laser interferometry is a high cost technique which utilises bulky equipment and may not be suitable for many applications [19]. Despite these drawbacks interferometry may still be used in sensor calibration as described in section 2.1.3.3.

Fibre-Optic Sensors

Fibre-optic sensors operate in one of three modes; interferometry, light intensity variation and Fibre Bragg Grating (FBG). The interferometry method operates much as laser interferometry described above. Light intensity is effective for relatively large changes in displacement but lacks the sensitivity required for effective Lamb wave detection. FBG is a useful technique in AE detection.

FBGs can be manufactured by different methods depending on the application. For applications in which uniform grating separations are required, such as AE detection, high intensity Ultra-Violet (UV) light is used to pattern the UV sensitive fibre core. Two beams of high intensity UV light are introduced directly to the photosensitive core of the fibre-optic for a limited period of time. The two beams of UV light cause a regular interference pattern on the photosensitive core, changing the material properties. The change in material properties is affected by the exposure period.

In operation light is directed down the fibre optic and passes over the FBG which reflects a certain wavelength of light, whilst allowing all other wavelengths through. The wavelength of light reflected is a product of twice the mean effective refractive index of the fibre core and the grating period [19]. This results in the light in the fibre optic after passing through the FBG being of a known wavelength.

The vibration of a Lamb wave propagating through the fibre causes a variation

in both the mean effective refractive index and the grating period. Therefore a shift in the spectrum of light reflected from the fibre-optic indicates an AE [19]. For this technique to be effective the FBG sensor must be seven times shorter [19] than the Lamb wave wavelength. This technique is effective at detecting Lamb waves and the fibre-optic components of the sensors can be integrated into glass-fibre composites providing for structurally integrated sensing.

There are several problems with the use of FBG for AE detection. The problem of interference from external light sources must be limited in order for signal detection to be possible. One of the major drawbacks of FBG is that the sensitivity of the FBG to waveforms with a direction of travel which is not along the axis of the fibre is reduced [19]. Therefore wave components which run at any angle other than the axis of the sensor will result in a lower amplitude response, limiting the potential for quantitative comparison of AE signals. This problem can be reduced by utilising an array of FBG sensors in different axial orientations.

Another problem is encountered due to the rapid change in sensor dimensions and therefore reflected light wavelength caused by Lamb waves. For these changes to be adequately observed a spectrometer with a fast refresh rate, up to 10MHz is required. This equipment adds significant cost to the overall detection set-up. Cost is also added due to the expense incurred by the manufacture of the sensing fibre-optics. These fibre-optics are fragile and when broken are almost impossible to fix without replacing the whole component [19].

2.1.3.2 Sensors Under Development

A large body of research has been carried out into the development of new sensor technology. Commercial sensors can, among other issues, be prohibitively expensive for use in sensor arrays [20] so new technology is needed to enable continuous monitoring by sensor arrays. Different materials and designs have been considered including polymer and thin film PZT MEMS sensors as a means of integrating devices and reducing device cost. A lead free alternative to commercial devices is also being investigated due to environmental concerns over the use of lead [41]. To become commercially viable all of these solutions must exhibit either comparable sensitivity to commercial solutions or offer other advantages which commercial devices cannot. To ensure the correct solution for AE detection is

employed it is essential to understand the positives and negatives of each sensor type. As such the different types of sensors under development and potential applications in which they may be employed are discussed in this section.

Lead-Free Sensors

Lead-free sensors have been developed which are similar in design to commercial AE devices. The bulk PZT element has been replaced by a bulk potassium sodium niobate (KNN) element. When tested, some lead free sensors have been found to exhibit a greater response than a smaller commercial bulk PZT sensor to a simulated AE signal. This higher response is explained by Lam *et al.* as a result of a larger sensing area and a lower electrical impedance [42]. KNN is discussed along with other lead free materials in section 2.2.2.

Lead-free sensors are preferable to PZT sensors as there are environmental concerns associated with the use of lead. Lead used in AE sensing applications is currently exempt from EU environmental regulations. Once a suitable lead-free replacement material is identified which exhibits properties comparable to that of PZT, PZT will lose exemption from the EU regulations.

Thin Film Sensors

Work was carried out in the early 1990's on the integration of thin film PZT AE devices, along with pre-amplification and signal processing hardware, onto a silicon chip. This integrated sensor and pre-amplifier was then permanently fixed to an aircraft structural component to provide an early warning against component failure [43]. In 1999 work was carried out which suggested that thin-film PZT, manufactured using a low temperature method, was a very promising material for use in MEMS AE applications. These works show that there are valid applications for thin film PZT AE sensors but that thin film sensors are considerably less sensitive than bulk AE sensors. This is due to the properties of thin film materials being an order of magnitude lower than those of bulk materials.

For the thin film PZT to operate effectively as an AE sensor a high quality deposition is required [43]. Low temperature (700°C to 800°C) processing is also

essential to enable integration with a silicon substrate [44]. Sol-gel spin coating has been found to provide such a film. Films deposited by spin coating sol-gel may only be deposited over a small surface area, typically 150mm diameter, and the properties of the film vary slightly across the film diameter. The limited dimensions of the substrate is disadvantageous as this prohibits the deposition of large numbers of devices or continuous production. Sol-gel spin coating must also be carried out on select substrates to ensure the deposited film epitaxial and thus has the maximum possible properties. This prohibits the direct deposition of the film onto the structural element.

Following the testing of the thin film AE sensor it was found that as the film thickness increased so the AE detection sensitivity also increased. This finding indicates that thick film AE sensing technology is an interesting field for further study [43] as thick films provide a compromise between the properties of bulk materials and the benefits of thin film materials.

Poly-Vinylidene Fluoride

Thin film PZT is not the only MEMS AE sensing technology to have been integrated into silicon substrate systems. Polymer devices have been investigated including poly-vinylidene fluoride (PVDF). PVDF has the advantage that the acoustic impedance is ∼3.92MRayls, this is low compared to that of piezoelectric ceramics such as the commercially available PZT 5A which has a acoustic impedance of ∼31.6MRayls. PVDF also exhibits a higher sensitivity (g_{33}) to incoming signals than PZT 5A, ∼339x10^{-3}Vm/N compared to ∼24.8x10^{-3}Vm/N [45]. This lower acoustic impedance results in a greater transfer of AE energy into the sensing element in monitoring applications on low acoustic impedance materials, such as polymers. Combined with the higher sensitivity this produces a greater response to an incoming AE signal.

PVDF AE sensors show great potential for integration with structural materials and have been integrated into glass fibre reinforced laminate structures. It was found that the integration of the PVDF sensors did not adversely influence the mechanical properties of the laminate but further study is needed to assess the risk of stress concentrations in dynamic loading situations due to the inclusion of the PVDF sensors potentially weakening the material. The integrated

PVDF AE sensors were shown to effectively detect AE due to static loading and to effectively identify the mechanism resulting in the AE [46]. These sensors have significant advantages over traditional bulk AE sensors. The PVDF sensors offer a reduction in weight and space consumption over traditional AE systems while maintaining effective AE detection capability.

A corrugated, multi-layer PVDF element electrically connected in parallel can also be used for the detection of AE within the 100kHz to 1MHz range usually employed for AE monitoring [45]. This operational bandwidth makes this type of PVDF AE device more appropriate for the characterisation of the source of the AE, however, the overall sensitivity to AE signals is reduced when compared to the resonant PVDF sensor which may be integrated into the structural material. As such the sensor design is dependent on the application in which the resultant sensor is employed.

A piezoelectric poly-vinylidene fluoride-trifluoroethylene (PVDF-TrFE) coated micro-machined silicon membrane AE sensor [47] has good sensing characteristics about the resonant frequency of the film but exhibits poor detection qualities away from the film resonance. The film can be tailored to detect signals of different frequencies by altering the physical properties of the system, such as membrane diameter and film thickness. These characteristics make PVDF-TrFE sensors of this type ideal for use in the detection of AE signals but limited in the identification and characterisation of the root cause of the AE as only a narrow frequency band may be effectively detected.

It is clear that PVDF is a flexible material in the design and development of AE sensing devices. The integration of PVDF into composite laminate structures offers superior AE sensing potential than that attained through the use of bulk AE devices. PVDF devices may also be employed in the detection of AE on the surface of a non-polymeric structural element, however, in this case the use of thin film devices affixed to the element surface may be more advantageous. This is due to the thin film device exhibiting superior properties while the PVDF device no longer has the advantage of exhibiting a low acoustic impedance by being more closely matched to the substrate material.

Piezoelectric Paint

A further development in integrated AE sensors is the use of piezoelectric paint. Piezoelectric paint is a composite of a piezoelectric material, commonly PZT, in a polymer matrix and has been extensively investigated for use in AE sensing applications [20]. This type of sensor has advantages over ceramic sensing elements in applications where polymers are being monitored because, like PVDF sensors, it has acoustic impedance properties close to those of the polymer structural element. Another advantage of PZT paint devices is the strong coupling between the active element and the material under observation. This is due to the paint being bonded onto the material surface during the drying process. This reduces any variation between devices due to variation in coupling.

In piezoelectric paints the piezoelectric particles are randomly dispersed throughout the polymer matrix in a 0-3 system. PZT paint has been developed with 33 piezoelectric coefficient (d_{33}) values up to 28pC/N, this compares to thick film PZT values of $\sim$100pC/N and bulk values of +600pC/N. The d_{33} of the piezoelectric paint is high enough to be of use in AE applications and a piezoelectric paint surface crack detection system has already been demonstrated [20]. Experimental work by Li and Zhang [20] has shown that PZT paint devices can be comparable to commercial sensors and are valid for use in AE sensor applications.

Piezoelectric paint has been developed with PZT concentrations of up to 53% by volume in epoxy [20]. PZT concentrations higher than this become difficult to handle during manufacturing [48]. The paint needs to be fully mixed by a high shear process and a Ultra-Sonic (US) bath before being deposited. Deposition needs to be carried out soon after mixing as the PZT settles out of solution quickly [48]. This settling may result in a non-homogeneous film along with difficulty at the deposition stage due to nozzle clogging.

There are several deposition methods, of which spray coating is a favoured method [48]. Films can be deposited in situ by spray coating. Once the film has been dried, silver paint electrodes [48] can be applied and then a halogen lamp used to heat the paint film while a field is applied to pole the film. The poling of piezoelectric paint films of these types requires high voltages (up to 600V) and extended time periods (1h) [20]. This technique has produced films with good piezoelectric properties including a d_{33} of 33pC/N. Spray coated films of up to

200μm have been deposited [48].

Low temperature deposition of piezoelectric elements is of great interest for use in AE sensing applications. Low temperature deposition enables the integration of AE sensors with a wide range of structural materials and therefore the direct transmission of AE from the structural element to the sensor active element. Piezoelectric paints enable this low temperature deposition and are relatively low cost when compared to current AE technology as the material consumption and wastage is significantly lower than bulk processing techniques. As such, the use of piezoelectric paint for AE applications is a solution which requires further development.

Piezoelectric paints are a microscopically complex mixture of piezoelectric particles in non-piezoelectric matrix, the properties of such materials is necessarily complex [49]. A method for estimating the macroscopic piezoelectric properties of the composite paint is desired. The effective permittivity of composite paint films can be mathematically modelled by several equations which are chosen depending on the geometry and orientation of the particles in the matrix and the volume percentage of PZT [49].

The Maxwell Garnett and the Bruggeman symmetric equations, 2.5 and 2.6, are both widely used for calculating the effective permittivity of materials where the difference in relative permittivity between the piezoelectric inclusions and the matrix material is small [50, 51]. The Maxwell Garnett and the Bruggeman symmetric equations both assume that the inclusions are symmetrically distributed throughout the matrix [50].

The Bruggeman symmetric equation is more effective when the volume fraction of the inclusion is above the percolation threshold, meaning that the equation only produces an effective estimate of effective permittivity when the symmetrically distributed inclusions are in contact with each other, i.e. not completely insulated by the matrix [50]. It has been found that the Maxwell Garnett equation is the better estimation with small volumes of inclusions and the Bruggeman symmetric equation is a better estimation at larger inclusion volumes [50].

$$\epsilon_{eff} = \epsilon_e + \epsilon_e \left(\frac{\frac{f}{3} \sum_{j=x,y,z} \left(\frac{\epsilon_i - \epsilon_e}{\epsilon_e + N_j(\epsilon_i - \epsilon_e)} \right)}{1 - \frac{f}{3} \sum_{j=x,y,z} \left(\frac{N_j(\epsilon_i - \epsilon_e)}{\epsilon_e + N_j(\epsilon_i - \epsilon_e)} \right)} \right) \tag{2.5}$$

$$\epsilon_{eff} = \epsilon_e + \frac{f}{3}(\epsilon_i - \epsilon_e) \sum_{j=x,y,z} \frac{\epsilon_{eff}}{\epsilon_{eff} + N_j(\epsilon_e - \epsilon_{eff})} \tag{2.6}$$

Where ϵ_{eff} is the effective permittivity of the macro-scale composite and ϵ_e and ϵ_i are the relative permittivity of the matrix and inclusion materials, respectively. f is the volume fraction of inclusions and N_j is the depolarization factor of the inclusion which varies with inclusion geometry for spheroids having dimensions in the x,y and z directions of a_x, a_y and a_z respectively, as defined by equations 2.7 and 2.8 for prolate ($a_z > a_x = a_y$) and oblate ($a_z < a_x = a_y$) spheroids [50].

$$N_z = \frac{1 - e^2}{2e^3} \left(ln \frac{1 + e}{1 - e} - 2e \right) \tag{2.7}$$

$$N_x = N_y = \frac{1}{2}(1 - N_z)$$

$$\texttt{Where } e = \sqrt{1 - \frac{a_x^2}{a_z^2}}$$

$$N_z = \frac{1 + e^2}{e^3}(e - tan^{-1}e) \tag{2.8}$$

$$N_x = N_y = \frac{1}{2}(1 - N_z)$$

$$\texttt{Where } e = \sqrt{\frac{a_x^2}{a_z^2} - 1}$$

In a PZT paint system, the distribution of inclusions is only symmetric when mixing has been completely effective. As the mixing of the PZT paint is rarely this effective, equations to describe a non-symmetric distribution of inclusions within a matrix are also required. There are equations which can be used to model effective permittivity in non-symmetric distribution including the Bruggeman non-symmetric (equation 2.9), Sen-Scala-Cohen (equation 2.10), Looyenga (equation 2.11) and Lichtenecker (equation 2.12). It should be noted that the Bruggeman non-symmetric equation results from an iterative use of the Maxwell Garnett and the Bruggeman symmetric equations [50]. Jylha-Sihvola [50] have developed an equation which combines the accuracy of the Bruggeman non-symmetric at low inclusion volume fractions with the accuracy of the Sen-Scala-Cohen equation at high inclusion volume fractions.

$$\frac{\epsilon_i - \epsilon_{eff}}{\epsilon_i - \epsilon_e} = (1-f)\left(\frac{\epsilon_{eff}}{\epsilon_e}\right)^{\frac{1}{3}} \tag{2.9}$$

$$\frac{\epsilon_{eff} - \epsilon_e}{\epsilon_i - \epsilon_e} = f\left(\frac{\epsilon_{eff}}{\epsilon_i}\right)^{\frac{1}{3}} \tag{2.10}$$

$$\epsilon_{eff}^{\frac{1}{3}} = (1-f)\epsilon_e^{\frac{1}{3}} + f\epsilon_i^{\frac{1}{3}} \tag{2.11}$$

$$log\left(\epsilon_{eff}\right) = f \cdot log\left(\epsilon_i\right) + (1-f) log\left(\epsilon_e\right) \tag{2.12}$$

For low inclusion volume fractions (f<0.35) the Bruggeman non-symmetric equation has been found to offer good agreement with experimental data [52]. For a ratio of the relative permittivity of the inclusions over that of the matrix (R_ϵ) between 20 and 40 the Lichtenecker logarithmic equation has been found to be an appropriate approximation however at a R_ϵ below this level the Lichtenecker

equation significantly underestimates the effective permittivity of the composite. At a R_ϵ of 100 or above the Lichtenecker equation is a very effective approximation of the effective permittivity of the composite [53]. All models predict that elliptical inclusions produce a higher effective permittivity than spherical inclusions.

In PZT/polymer paint systems the limits of the ϵ_r are defined by the ϵ_r of the materials of which the system is composed, for example the ϵ_r of a PZT/PVAc system may exhibit an ϵ_r between 3.2 and 1300. Despite an ϵ_r between 3.2 and 1300 being the limits, these values for ϵ_r are only observed when the volume loading of PZT is either below 1% or above 99%. In non-symmetric loading situations, depending on the theoretical model employed, the theoretical ϵ_r tends to be below 200 when the volume loading of PZT is 0.5 or lower, this can be seen in figure 2.6.

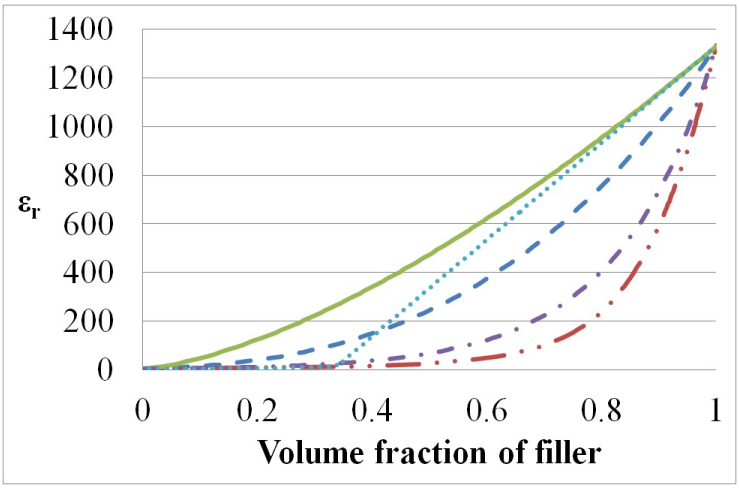

Figure 2.6: Plot showing a comparison between the Bruggeman non-symmetric (dashed, double dot), the Jylha-Sihvola (dotted line), the Lichtenecker (dashed, single dot), the Looyenga (dashed line) and the Sen-Scala-Cohen (solid line) approximations for variation in ϵ_r with volume loading of PZT for a system of PZT/PVAc with an ϵ_r variation between 3.2 and 1300.

Piezoelectric paints offer superior integration options than any other type of AE sensing device. The paints can be deposited directly onto the material which requires AE monitoring, which cuts out issues of attenuation across wear plates or substrate materials. It is also possible to deposit piezoelectric paints in areas which would be inaccessible to film or bulk sensor devices. Depending on the circumstances and the geometry of the structure which requires AE monitoring, the lower piezoelectric properties of piezoelectric paints when compared to film

or bulk AE sensors may be out-weighed by the benefits.

Active Fibre Composite Sensors

AFC devices also consist of piezoelectric inclusions in a composite matrix. Unlike the piezoelectric paint devices the inclusions are not randomly orientated particles but uniaxially arranged fibres. Conventional ceramic piezoelectric element devices are often actuated in the d_{31} direction which has a piezoelectric coefficient lower than that of the d_{33} direction which the AFC devices are activated in [34]. The main benefit of this arrangement is that AFC devices are particularly sensitive to S_i waveforms which is not achievable in traditional bulk and film sensors.

Whilst AFC devices can be as effective as commercial AE devices under certain circumstances, permanently mounted and parallel to the direction of travel of the incoming signal. AFCs which are temporarily bonded to the surface of the structural element lose 15dB of sensitivity compared with similarly mounted commercial devices. This loss of sensitivity increases to up to 40dB when the direction of emission travel is perpendicular to the AFC fibres [34]. These drawbacks mean that to achieve results that are comparable to bulk or film sensors the AFC must be carefully oriented on the surface of the structural element.

As the sources of AE are at unknown locations in structural materials under load, the efficient orientation of AFC devices on the material surface is usually not possible. This issue can be addressed by using a multiple lay-up of AFC fibres with orientations of 0°, 45°, 90° and 135° as shown in figure 2.7. This arrangement will improve the operational performance of AFC devices considerably by reducing the sensitivity loss due to the direction of AE travel. The integration of AFC in composite laminates such as carbon fibre or in polymer structures is of particular interest as an application for AFC sensors as closely matched acoustic impedance characteristics make these sensors more suitable for this application than bulk, film or other polymer sensors.

Capacitive Type Sensor

Capacitive type integrated AE arrays have been developed by Greve et al.

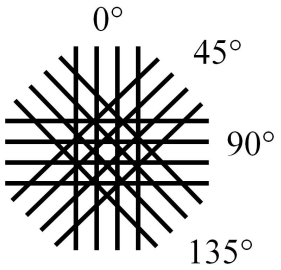

Figure 2.7: Schematic showing fibre orientation in a multi-layer AFC sensor.

[54]. Out-of-plane AE excitation causes a dimensional change in the sensor and therefore a variation in capacitance. The change in capacitance can be detected. In-plane capacitative AE devices have also been developed [54]. In this case in-plane AE excitation causes a shearing motion in the plane of finger electrodes. This shear motion causes the air gap between the electrodes to change and thus the capacitance to change measurably. A combination of in-plane and out-of-plane sensor units can be combined in an array to enable full signal detection.

This capacitive sensor design is an effective contact-less sensing solution, however, the system has added complexity when compared to other existing technologies which rely on physical contact with the structural element under observation. This complexity adds cost to the production of the system and results in the device production process lacking in repeatability. This lack of repeatability in production leads to variation in the sensor dimensions and therefore performance, making calibration of individual devices in the array essential.

Capacitive sensors can also only monitor either in plane or out of plane AE compared to contact sensors which measure both types of AE waves. This is a severe limitation of capacitive sensors which adds complexity to the characterisation of the AE source. These drawbacks limit the application of capacitive sensors to situations in which physical contact with the structural element is not possible.

2.1.3.3 Sensor Calibration

Regardless of the sensor type employed in AE detection, calibration is necessary to eliminate the effects of the sensor and coupling variation. This process is necessary to enable the use of sensor arrays and is essential for the use of sensors to identify physical characteristics of the AE source.

Currently there are no calibration methods that can be used in situ [55], this means that calibration of the absolute sensitivity of AE monitoring equipment is not possible for real world applications. Therefore the use of AE technology to quantitatively identify the damage which the component under observation has sustained is not currently viable. Various technologies have been investigated under laboratory conditions including the use of: Hsu-Neilson testing [56], US transducers [33], thermoelastic pulsed laser, elastic ball drop [33, 55], comparison using laser interferometry and reciprocal calibration [40].

The Hsu-Neilson test has long been the accepted method of carrying out in situ calibration. This method involves the repeated breaking of a pencil lead onto the surface of the material under observation. The AE detected from this pencil break can be compared across several sensors and can give an indication on the reproducibility of detection [56]. This type of testing does not enable a quantitative calibration of sensors in situ [55] due to the variation in energy released when the pencil lead breaks in combination with the variation in wave energy as it arrives at the various sensor positions. This variation in wave energy is caused by energy loss as the wave travels through a transmission medium with inconsistent material properties, varying geometry and distance from emission source as discussed in section 2.1.2.2 [57]. These issues are shared by other similar methods such as glass capillary fracture [55].

Sensors can be calibrated against each other or against a baseline device by comparing the response shown by the device to controlled excitation by an US transducer. This method of calibration suffers from the same sensitivity to variation in coupling as that which affects the AE sensor during normal operation. This issue can be overcome by the use of a pin shape transducer element in combination with a bulk element sensor. The transducer is used to generate a pulse of known energy; the more efficient the coupling of the transducer is, the less energy the backing sensor will detect. This set up can be used to identify the quality of the transducer coupling [33]. This makes the calibration of AE sensors, using the transducer as a simulated source, more accurate. Even with the coupling factor of the transducer taken into account, in situ calibration is still difficult in most cases due to the variations of wave propagation caused by the transmission medium geometry. There is also an issue with the transducer being a relative energy source, the transducer requires accurate calibration to be used

as an absolute energy source [55].

Elastic ball drop and thermoelastic pulsed laser techniques have been suggested as calibration techniques as the energy output of both is well understood and can be estimated with a good degree of accuracy. Both of these techniques eliminate the issues with coupling that reduce the effectiveness of US transducer calibration methods and so are favourable for validating quantitative analysis techniques. In the elastic ball drop method the potential energy of the ball is transferred into acoustic energy in the material, thus generating a simulated AE [33]. This technique is not appropriate for use in the calibration of sensors in real world situations as the height from which the ball is dropped, along with the angle at which the ball impacts the surface of the structural element, affect the magnitude of the generated energy. A variation of generated energy is undesirable in calibration tests.

Thermoelastic pulsed laser emission techniques involve the use of laser pulses directed onto the surface of the material under observation. The laser pulses induce elastic strain energy in the transmission medium and the variation in the strain energy results in the AE. The magnitude of the energy generated by the laser pulses is dependent on several material parameters including the elasticity modulus and thermal properties and several laser properties such as pulse duration, energy and irradiation area [55]. This technique is proven in laboratory conditions; however, use of this technique in a real world application is impractical especially in applications where access is limited [58] and equipment cost is an issue.

Another laser based calibration technique is laser interferometry [40]. Laser interferometry is used to take point measurements of the absolute displacement of the surface of the transmission medium. This displacement can then be compared to the voltage of individual piezoelectric AE sensors to be used as a calibration metric. In the case of an array of sensors the interferometer can be used to ensure all sensors are calibrated to the same standard. The issues with the use of interferometer in real world applications are the same as those for thermoelastic pulsed laser calibration. The use of a laser requires health and safety to be considered and the equipment is costly as well as being inappropriate for many applications [19].

Reciprocity is a method by which one AE device in an array is used to calibrate the other devices. One AE sensor is used as the calibration device to which all the other AE sensors in an array are compared. A voltage is used to drive the sensor causing the device to effectively act as a transducer which can generate a US signal in the transmission medium. The US signal is then used to calibrate the other AE sensors in the sensor array, with the voltage of US emission being compared to the received voltage. This process is then repeated with the other devices becoming the calibration standard in turn. This method ensures that all of the sensors are calibrated to the same standard. This method cannot be used to calibrate the sensor output to the absolute displacement of the surface of the transmission medium and as such has limitations in the calibration of devices for qualitative AE properties evaluation.

2.1.3.4 Pre-Amplification

Pre-amplification is important in AE monitoring applications. Pre-amplification boosts the signal from the sensor before the signal is transmitted to the data-logger. Boosting the signal amplitude is important as it increases the ratio of the signal amplitude to the amplitude of the electronic interference induced in the wire used to connect the pre-amplifier to the data-logger. The pre-amplifier is positioned as close to the sensor as possible to minimise electrical interference in the wire between the sensor and the pre-amplifier.

Many different pre-amplifiers are commercially available for both BNC and differential sensor inputs. A power input from the sensor as power is drawn from the data-logger output. Pre-amplifiers with variable amplification are available, common amplification values include 20dB, 40dB and 60dB. Most pre-amplifiers amplify the signal voltage; however, for applications in which long cable lengths are required, charge amplifiers are employed. Charge amplifiers do not exhibit the same sensitivity to attenuation of the signal as voltage amplifiers [59].

Plug-in high-pass, low-pass and band-pass filters are available commercially. These filters are used to remove noise from the signal at source. Pre-amplifiers have been designed which are resistant to various hazards, enabling their use in varied environments.

2.1.4 Data Collection and Analysis

Once the AE has been generated, has propagated throughout the transmission medium, been detected and converted to an electrical signal by the AE sensor the signal is then amplified and transmitted to a data-logger. The data logger stage is essential as it enables visualization of the signal. The waveform can then be manipulated into a form which can be analysed to provide information about the source of the AE by use of mathematical processing.

The pre-amplified signal is transmitted to the computer data-logger via either a co-axial cable or a wireless transmitter/receiver array. A computer with an appropriate installed Peripheral Component Interconnection (PCI) board is used to convert the raw data into a digital form. PCI boards are available with multiple inputs so that an array of several sensors can be monitored simultaneously. The data-logging software is configured to match the sensor and pre-amplifier used. Once configured for the hardware employed a pre-trigger level can be set at an amplitude just higher than that of the electrical and mechanical noise. This ensures that only relevant data is recorded. The recorded data can also be amplified using the data logger. Amplifying using the data logging software has the disadvantage that all of the signal is amplified including the noise.

An electrical impedance mismatch between the sensor, pre-amplifier and the data logging software can cause similar problems to the acoustic impedance mismatch between the structural element, the coupling media and the AE sensor. Loss of signal amplitude and an increase of noise can both arise from an electrical impedance mismatch. The electrical impedance of a component varies with the frequency of the signal it is transmitting.

The impedance of the pre-amplifier is variable with changing pre-amplification level and the data logger software is set up to match the pre-amplifier electrical impedance. In the case of the mismatch between the AE sensor and the pre-amplifier a different method is employed. As the impedance of the AE sensor is related to the physical properties of the active piezoelectric element the impedance of the sensor can only be varied by the addition of extra electrical components. These components would not compensate for the variable impedance of the pre-amplifier. As such a different solution is required.

2.1.4.1 Time-Frequency Analysis

Once the AE waveform has propagated through the transmission medium and been detected by the sensor, the sensor electrical output is pre-amplified and collected and various analysis methods must take place to assess the information that the waveform contains. Without this step the data collected would indicate little about the source of the AE and about the condition of the component from which the AE originated. Data analysis can be carried out in the time domain and in the frequency domain. The different domains can be used to extract differing information from the signal.

Time Domain

Detected AE signals are often presented in the time domain. This enables the identification of the important wave properties including the maximum amplitude, rise time, duration, ring down count and total event energy as discussed in section 2.1.2. Some of the important properties of a transient AE wave are identified in figure 2.8. Along with these, other properties of the signal can be identified including kurtosis, characteristic time moment, trend cycle component and time of flight [19].

The maximum, or peak, amplitude of an AE event is related to the event intensity and, in some materials, can be used to identify the cause of the AE. The maximum amplitude of the signal is also affected by sensor properties such as operational frequency bandwidth and damping coefficient, material damping properties and the set threshold level. The threshold level is set so that the AE monitoring system is triggered to start recording data when the signal amplitude crosses the threshold. The threshold level is set suitably high so that noise does not trigger the AE system to record. Often a log scale is employed to enhance the accuracy for both high and low amplitude signals [13].

Ringdown counts represent the number of times that the amplitude crosses the threshold level per individual emission event. A theoretical ideal AE can be modelled as a sinusoidal wave with an exponential decay and therefore an event with a high maximum amplitude will have a large number of ringdown counts. Ringdown counts can be used as an indication of various properties of the source

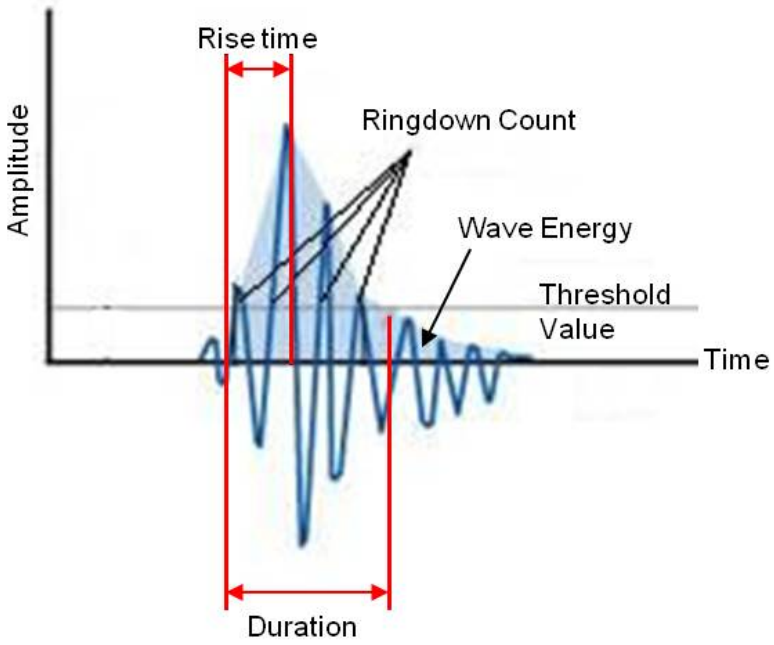

Figure 2.8: A time domain AE plot identifying parameters of the AE signal important in the characterisation of structural damage.

such as the stress intensity factor or the fatigue crack propagation rate. These relationships are shown in equations 2.13 and 2.14 respectively. The same factors affect the signal ringdown counts as affect the maximum amplitude of the signal. To enable effective AE monitoring these variables must be understood and controlled [13].

$$N \sim K^n \tag{2.13}$$

$$\frac{dN}{dc} \sim \frac{da}{dc} \tag{2.14}$$

Where "N" is the total number of counts, "K" is the stress intensity factor, "n" is a constant between 2 and 10, "a" is the crack size and "c" is the total number of cycles [21].

The maximum amplitude of the AE signal can be related to the cumulative number of events and the cumulative ringdown counts through the overall time the event takes to decay from maximum amplitude to below the amplitude of the

set threshold value and the amplitude distribution slope parameter, as shown in equation 2.15 [13]. The amplitude distribution slope parameter is the gradient of the log of the cumulative number of events which cross the threshold value against the log of the threshold value itself and can be mathematically described by equation 2.16 [60]. The amplitude distribution slope parameter may also be used to characterise AE events. Large amplitude distribution slope values indicate a larger proportion of AE events with small maximum amplitudes, whereas a small amplitude distribution slope value indicates a larger proportion of events with large maximum amplitudes [61].

$$N = \frac{Pf\tau}{b} \tag{2.15}$$

$$P = k(V_i)^{-b} \tag{2.16}$$

Where "N" is the cumulative number of AE counts; "P" is the cumulative number of events above "V_i", which is the threshold voltage; "f" is the resonant frequency of the sensor; τ is the event decay time, "k" is a constant and "b" is the amplitude distribution slope parameter.

AE events result in a release of energy into a transmission medium. As such the event energy of a detected AE waveform can be related to the energy of the AE source itself. The energy of an AE event can be measured directly from the raw AE signal by calculating the area under the waveform. Quantification of the AE waveform energy enables the characterization of the source including the identification of the mechanical energy of the event, the strain rate or even the deformation mechanism causing the AE. It is not possible to identify these parameters by ringdown counting without significant signal manipulation [13].

These properties can be used to qualitatively assess the extent of damage to a structure. Quantitative analysis of AE sources is currently difficult to implement as the properties of the AE depend largely on the material properties, the geometry of the transmission media and on other variables such as the sensor properties and the coupling between the sensor and the material under observation. This means that even on seemingly identical structures the magnitude of AE signals may not be comparable [33].

The Kaiser effect is another useful property of AE which is employed in identifying the health of a structure. The Kaiser effect states that a material will not exhibit AE until the loading to which the material is exposed exceeds the previous loading on that material (figure 2.9) [14]. At a certain loading, dictated by the mechanical properties and on the damage within the material, the Felicity effect takes over. Once the Felicity effect takes over and emissions are detected before the element is loaded to the previous maximum (figure 2.9), the ratio of load at which the AE resumes to the maximum load experienced by the element is known as the Felicity Ratio. The Felicity ratio varies with every loading cycle, low ratios are indicative of large dislocations within the material [62] therefore the Felicity ratio is a useful phenomenon in the field of AE testing.

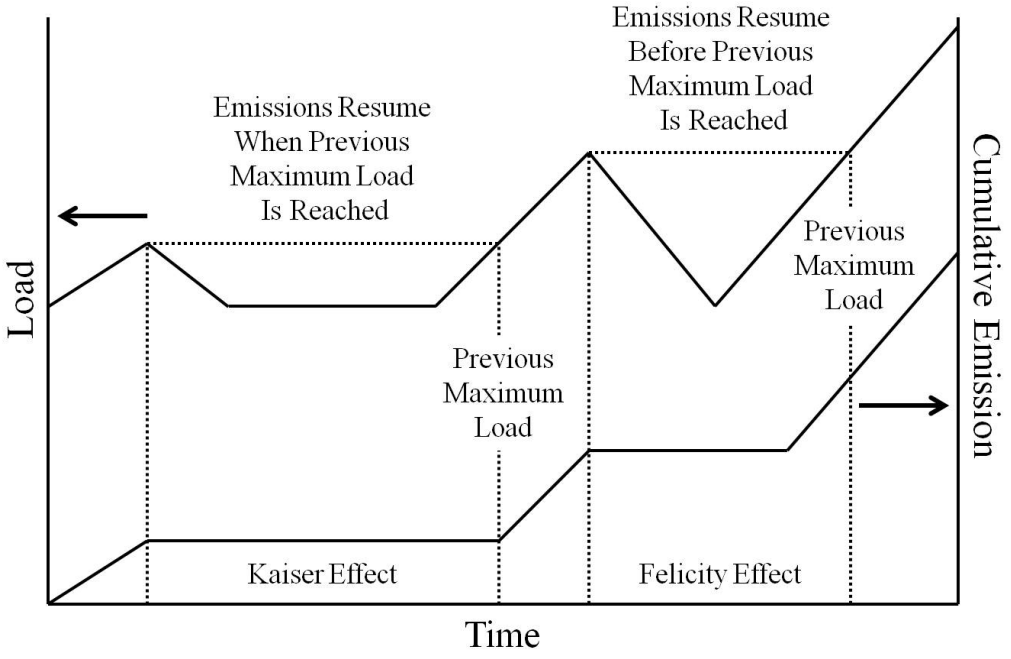

Figure 2.9: A schematic showing cumulative emission against load with the Kaiser and Felicity effects clearly marked.

These properties are consistent throughout the field of AE monitoring regardless of AE source, wave type, transmission media and sensing technology. These properties are employed in the basic function of AE; identifying the extent of damage in structural components.

There are many different methods employed in extracting the required wave properties in the time domain. The Hilbert transform is one widely used method and

has much in common with Fast Fourier Transform (FFT). This method can be used to identify the energy component of the wave with respect to time, enabling the identification of the time at which damage occurs during the AE event. This technique is limited in comparison to the frequency domain and wavelet transforms discussed later in this section as this technique is only applicable in certain simplified cases [19].

Another useful technique for identifying the structural integrity of a component is that of correlation. Correlation relies on a comparison to a benchmark state. A correlation coefficient is calculated in which unity represents a completely identical signal. Auto-correlation may be carried out to identify useful AE properties in the signal which have been masked by noise. The auto-correlation of the damaged component can then be divided by the auto-correlation of the benchmarked health of the component to give a ratio curve. The ratio curve provides a clear indicator of any differences between the two signals [19].

Frequency Domain

The frequency content of the detected AE waveform offers useful information about the source of the emission. In dynamic cases, such as those involving bearing damage for example, the frequency content can aid in identifying which component of the bearing is damaged. Each component in a roller bearing - the inner raceway, outer raceway, cage and bearing element - exhibits a different characteristic frequency. It is not possible to identify the frequency components in the time domain and so it is necessary to transform the signal to the frequency domain. Once the transform has been carried out peaks of high amplitude at the characteristic frequencies of the damaged components become apparent enabling effective diagnosis of the problem.

The use of Fourier Transform (FT) is a well understood method for transforming signals from the time domain f(t) to the frequency domain F(ω). The formula for applying a FT to an AE signal, f(t), and the inverse of the FT process are shown in equation 2.17 and 2.18 respectively [18]. For use in applications such as AE, where f(t) is short, a periodicity is assumed in the calculation of the FT. This essentially represents the non-stationary AE waveform as a continuous, stationary waveform for ease of calculation [18] [63].

$$F(\omega) = \int f(t).e^{(-i\omega t)}dt \tag{2.17}$$

$$f(t) = \left(\frac{\pi}{2}\right) \int F(\omega).e^{(i\omega t)}dt \tag{2.18}$$

FTs are effective but require a lot of computing power to carry out often making the time for computation impractical, particularly in AE application when the number of data points is large. A signal with N data points transformed by the Fourier transform requires $2N^2$ computations. The number of computations can be reduced by the use of a FFT which only requires $2N\ \log_2 N$ computations. FFT can be achieved by several mathematical methods, which are all well understood [19]. The improved FFT calculation speed is a compromise with accuracy, the use of FFT introduces a rounding error to the result. This rounding error is negligible in comparison to the absolute data values in AE applications and so FFT is a commonly used signal processing technique [18].

Digital filtering can be applied by the use of FFT to impose high-frequency, low-frequency and bandpass filtering [19]. Frequency filtering must be used with care as the removal of signal components which appear as noise may be masking AE signal components which would be lost in the filter. Filtering of frequencies outside of the range of interest for AE can be useful in increasing the signal to noise ratio. Once filtering of this kind has been carried out the FFT process can be reversed and the signal returned to the time domain as desired.

Wavelet Transforms

The Wavelet Transform (WT) is a signal processing method employed when the variation of the amplitude and frequency components of a signal with time are of interest [64]. These conditions occur regularly in AE applications and so WT have become an increasingly popular signal processing technique [19] since being introduced in 1996 [18]. WTs are used to calculate the frequency amplitude of a wave with respect to time and are essentially waveforms with a limited time period and an average amplitude of zero [18, 19].

The choice between continuous and discrete analysis is based on the required results from analysis. When the identification of wave energy change in time is required continuous waveform analysis is employed. Discrete analysis is more useful for the removal of noise and the extraction of AE properties.

The mathematical representation of a continuous wavelet transform is shown in equation 2.19, with the complex conjugate denoted by the overbar, along with the admissibility condition in equation 2.20 [63]. The admissibility condition is utilised to assess the suitability of the analysing wavelet, $\psi(t)$, for use in AE applications. The admissibility condition makes use of $\widehat{\psi}(\omega)$, the FT of $\psi(t)$. Any analysing wavelet can be utilised providing that the admissibility condition is met [63].

$$(w_\psi s)(b,a) = \frac{1}{\sqrt{a}} \int_{-\infty}^{\infty} f(t) \overline{\psi\left(\frac{t-b}{a}\right)} dt, \tag{2.19}$$

where a > 0

$$\infty > \int_{-\infty}^{\infty} \frac{|\widehat{\psi}\omega|^2}{|\omega|} d\omega \tag{2.20}$$

There are many analysing wavelets, for both continuous and discrete analysis, which meet the admissibility condition shown in equation 2.20. Choosing the correct analysing wavelet is vital, incorrect wavelet choice can reduce the accuracy of AE signal analysis [19]. An appropriate analysing wavelet is one which closely resembles the waveform to be analysed. This similarity is measured by the wavelet coefficient, a higher coefficient indicating greater similarity [19]. There are several WTs in common use including; Gaussian, Haar, Daubechies, Morlet, Mexican Hat and Meyer [19].

One WT of particular interest for AE analysis in this work is the Daubechies WT. Daubechies WT is based on the Haar WT and has a scaling function given by equation 2.21 [21] in which the coefficient "c_k" is defined by Daubechies [65]. This leads to the waveform being defined as shown in equation 2.22 [21]. For the Daubechies WT to be employed the sample length must be a power of two. The

frequency components of the sample are given by the wavelet levels, each level containing a number of coefficients equal to two to the power of the level [21]. The notation for Daubechies WT containing n coefficients is given as Dn. The shape of the WT is dramatically changed by the number of coefficients and so varying the coefficient can enable closer matching of the WT to the signal being analysed.

$$\phi_j(t) = \sum_{k=0}^{N-1} c_k \phi_{(j-1)}(2t-k) \tag{2.21}$$

$$\psi(t) = \sum_{k=0}^{N-1} (-1)^k c_k \phi(2t+k-N+1) \tag{2.22}$$

Once a suitable analysing wavelet has been used to calculate the frequency content with respect to time, the time period, or window, of the WT window is moved along the time axis until there is only a small overlap with the first time window calculation step. The calculation is repeated and the window moved and this process is repeated until all the waveform has been processed. This procedure results in the waveform spectrogram [18]. The window size of the WT has a strong influence on the resolution of the transform. A WT with a window of comparable size to the entire waveform will have very poor resolution, whereas a greater resolution can be attained by employing a smaller window at the expense of a greater number of required calculations [18, 19].

One technique which is largely analogous to WT is that of windowed FT (WFT). If a window is used with FT the FT can behave in a similar fashion to WT. A Windowed Fourier Transform (WFT), also known as a Gabor transform, can be used to estimate the frequency content of a waveform with respect to time. Gabor transforms use a Gaussian function as a window, w(t), and operate with a constant window length of the order of magnitude of the lowest frequency signal being processed [18, 28]. Like a WT the window is moved along the time axis by overlapping increments, τ until the whole time period of the signal, t, has been analysed. The equation describing the Gabor transform is shown below (equation 2.23). The Gabor transform, WFT, is windowed by the Gaussian function (equation 2.24), where σ is constant [18].

$$[WFT](\omega, t) = \int_{-\infty}^{\infty} f(t).w(t-\tau).exp(i\omega t)dt \tag{2.23}$$

$$w(t-\tau) = \frac{e^{[-((t-\tau)^2]}}{\sigma^2} \tag{2.24}$$

The resolution of the Gabor transform is the same as the window length [66]. If the frequency content of the waveform has a large bandwidth then there will be considerable uncertainty in the analysis of the higher frequency signal components. The window size of WFTs, unlike WTs, is not scaled with signal frequency [18]. This results in a loss of resolution introduces uncertainty in high frequency processing which is not present in WT. Despite this uncertainty Gabor transforms are still an effective tool in AE signal processing.

2.2 Materials: Piezoelectricity

Once an understanding of the source, transmission and properties of AE has been gained along with an understanding of how current state of the art AE monitoring technology and signal processing functions; it is important to understand the piezoelectric materials which enable AE monitoring. Only with a firm understanding of piezoelectric materials will it be possible to develop and improve AE monitoring technology.

2.2.1 Early History

When any material is subjected to an electric field the dimensions of the material experience a microscopic change. Piezoelectric materials are not only subject to this effect but also the converse; when a force is applied to a piezoelectric material, changing the material dimensions, an electrical charge is produced. The discovery of piezoelectricity by Jacques and Pierre Curie in 1880 following extensive work on the pyroelectric effect, initially went largely unappreciated. It wasn't until several years later that the full potential of piezoelectricity was realised [67].

Ferroelectricity was identified in 1920 in the study of Rochelle salt [68, 69]. Ferroelectric materials are a sub-group of pyroelectric materials, which in turn are a sub group of piezoelectric materials [70]. Ferroelectric materials exhibit spontaneously polarised domains [68] with multiple electrical orientation states. The orientation of the domains can be changed by the application of an electrical field [71, 72]. Above the Curie temperature the lattice structure is centre symmetric and therefore the material ceases to be ferroelectric. At temperatures below the material Curie point some Ferroelectric materials, such as PZT, may exhibit a perovskite structure an example of which can be seen in figure 2.10.

As a material cools from a temperature above the Curie temperature of the material individual crystals have a tendency to orient about their crystal axis. While the crystal orientations are fixed, the domains present in the material naturally fall into an orientation which minimises the elastic strain within the material [73]. As a result of the material domain orientation to the position of least stress, the offset negatively charged ion is also oriented to the position of least stress.

When a force is applied to the material, all of the ions within the material move. The relative movement of the negatively charged ion compared to the movement of the rest of the ions, results in a change in the natural electrical charge of the material. In ferroelectric materials which are un-poled the natural orientation of crystals to the position of least internal stress results in a domain orientations which, when a force is applied, result in a net charge of zero across the material at a macro-scale. Poling can be used to orient the domains and thus the offset negative ions so that a force applied to the material results in a net electrical charge in the macro scale material.

The orientation of domains means that when a force is applied to the material a net electrical charge is produced and can be measured. It has been found that the relative deflection of the negative ion is not the only contributing factor to the net electrical charge produced, domain wall motion has been found to contribute significantly to the net electrical charge. Work has been carried out to engineer the material structure in an attempt to improve these properties [74].

In 1921, a year after the discovery of ferroelectricity, the first useful piezoelectric device was manufactured. An electrical oscillator was manufactured using non-

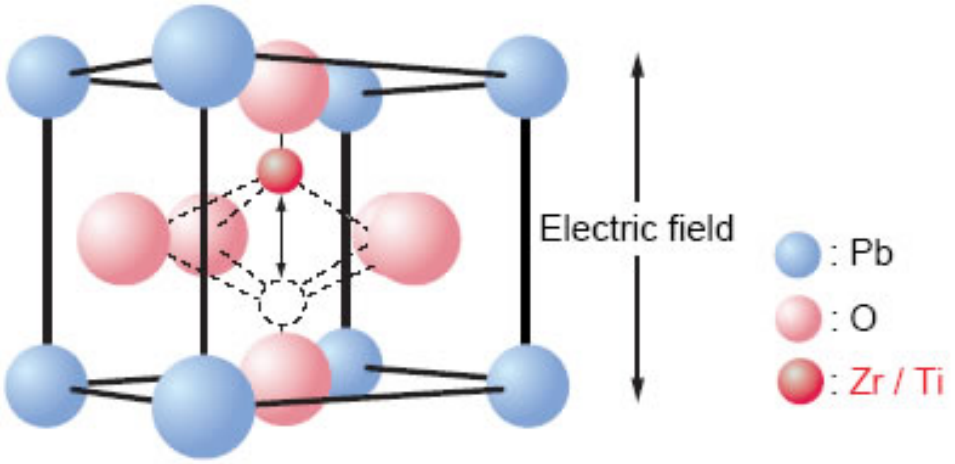

Figure 2.10: The perovskite crystal lattice structure of PZT, exhibiting an offset, negatively charged Zr/Ti ion [3]

ferroelectric single crystal quartz as a piezoelectric element. Even then piezoelectricity was not commercially viable. Single crystal quartz was costly, rare and difficult to work with. The first use of single crystal quartz for AE sensing applications was recorded in 1936 [75]. One issue with single crystal AE devices was the difficulty of achieving a reproducible crystal dimensions and properties, this issue limited the application of AE sensor arrays in detecting the AE source location without significant sensor calibration work. The single crystal element was also prohibitively expensive.

In the 1940's it was discovered that mixed-oxide ferroelectric materials, such as barium titanate ($BaTiO_3$), exhibited the piezoelectric effect when electrically poled [70]. By 1947 the first commercially available $BaTiO_3$ products were being manufactured. PZT ($Pb(Zr_x, Ti_{x-1})O_3$; $0 \leqslant x \leqslant 1$) was investigated in the 1950's and found to exhibit a stronger piezoelectric effect than $BaTiO_3$, becoming the modern material of choice.

2.2.2 Modern Materials

Since the early developments in piezoelectricity numerous piezoelectric materials have been developed for use in modern applications. An understanding of these materials is important as each material exhibits different advantages and disadvantages in the context of AE monitoring applications. PZT has become the most prevalent for sensing applications due to comparative stability across a

wide range of environmental conditions and relatively high piezoelectric properties along with a low production costs compared to single crystal materials [75]. Whilst PZT has found many applications, other materials have been researched and employed in various MEMS applications depending upon the required properties.

Aluminium nitride

AlN is a non-ferroelectric material which exhibits piezoelectricity due to the polar wurzite structure of the material [76]. For AlN properties to be maximised, the material must be in the [001] orientation with the polarization aligned. Even in a well aligned film the piezoelectric properties are still poor in relation to PZT. AlN exhibits a d_{33} of 3.4pC/N and a ϵ_r of 10.5, one and two orders of magnitude smaller than PZT films of similar dimensions respectively [77]. AlN films of over 5μm thickness [78] with good [001] orientations can be deposited by either RF sputtering [78] or DC magnetron sputtering [77] leading to deposition temperatures below 500°C. In some cases deposition of good quality films has been carried out at temperatures as low as 180°C [76].

Aluminium nitride (AlN) has found use in AE sensing technology due to a low permittivity and loss [76] while thicker AlN films have been employed as acoustic wave resonators [78]. The low values of these parameters lead to a higher amplitude output and therefore an improved signal to noise ratio [76] which is ideal for AE applications.

Despite having piezoelectric properties which are poor in comparison to PZT, AlN has advantages in addition to the low permittivity and loss a high Curie temperature [78] makes AlN a useful material in sensor applications [76]. Whilst low temperature processing, low permittivity and low loss make AlN a useful material for sensing applications the poor piezoelectric properties and the the difficulty involved in depositing a well oriented film over a large surface area limit the application of AlN. For these reasons AlN has not found widespread use in AE sensing applications.

Zinc Oxide

Zinc oxide (ZnO) is another well understood, non-ferroelectric material and has found many applications as a MEMS piezoelectric material; including sensors, transducers and surface acoustic wave devices [78, 79]. ZnO is often deposited by growing a thin film by a sputtering process [78, 79, 80]. The deposition of a good quality ZnO film is difficult to achieve [76] and relies heavily upon processing conditions and substrate properties [80]. Even a ZnO film of good quality exhibits considerably lower piezoelectric properties than a PZT [78].

The properties of ZnO make it a useful material for AE sensing applications. However, the difficulties in depositing ZnO over large areas, similar to issues found with the deposition of AlN, is not conducive to the integration of sensors with structural elements. Another issue with the deposition of ZnO onto various structural materials or substrates, which are compatible with integration, is the difficulty of growing an epitaxial film on substrate materials which have not been correctly prepared. This can be avoided in some cases by the use of barrier layers [80] but in most cases this is either impractical or adds excessive cost to the process, limiting possible usage in AE applications.

Poly-Vinylidene Fluoride

Piezoelectric polymers have found use in AE applications owing to favourable acoustic impedance properties (section 2.1.3.2) and flexibility [19]. One piezoelectric polymer which is favoured is PVDF [19]. PVDF is a ferroelectric co-polymer [76] with good piezoelectric properties [46]. The piezoelectric properties are poor in comparison to PZT which has a d_{33} an order of magnitude greater [81]. The d_{31} of PVDF has also been found to be considerably lower than that of PZT [81].

The disadvantages of the relatively poor piezoelectric properties are, in some cases, out-weighed by the advantages of the acoustic matching and the ability to structurally integrate PVDF with composite materials as discussed in section 2.1.3.2. These properties make PVDF an ideal solution for some AE sensing applications, such as the need to integrate AE sensors with composite structural elements. In these cases the low temperatures involved in the deposition and poling of the PVDF mean that the manufacture of an AE device is possible without

damaging the structural element requiring observation.

The deposition of PVDF for AE sensing applications has advantages over the use of AlN and ZnO in that PVDF can be deposited without the need for specialised equipment or close control of deposition conditions. PVDF may be deposited on a structural element in situ, leading to considerable flexibility in the applications for which PVDF may be considered.

Barium Titanate

Solid state $BaTiO_3$ production is a recognised technique [82]. Sol-gel $BaTiO_3$ has been found to produce films with good piezoelectric properties and significant advantages over traditional production methods [83, 82]. Sol-gel techniques lead to films with controllable particle size and composition, sol-gel $BaTiO_3$ films can be created using low cost deposition technique. The sol-gel process can also be used to produce a $BaTiO_3$ powder with a particle size of less than 1μm [82].

In recent years the use of barium titanate ($BaTiO_3$) in transducer applications has declined rapidly. $BaTiO_3$ has instead found use in high dielectric constant capacitors [70]. $BaTiO_3$ has a Curie temperature of 120°C which limits the applications for which the material is suitable [70] as AE sensors may be required to operate at elevated temperatures. The operation of AE sensors at temperatures approaching the Curie temperature of $BaTiO_3$ could result in the depolarisation of the device. $BaTiO_3$ also exhibits a considerably lower sintering temperature than PZT [70]. This is of benefit as a lower sintering temperature enables the integration of the material with a wider range of substrates.

$BaTiO_3$ exhibits a lower electromechanical coupling coefficient and a d_{33} half that of PZT, the d_{31} is also considerably lower than that of PZT [70]. These lower properties have lead to PZT becoming favoured over $BaTiO_3$ for current commercial AE sensing applications.

2.2.3 Lead Zirconate Titanate

PZT, as stated in section 2.2.2 above, has become the most prevalent piezoelectric material in sensor and actuator applications. This is due to the good piezoelectric properties and the large degree to which those properties can be customised by changing the chemical composition of the material. The good baseline properties of PZT stem from the crystal lattice structure of the material. There has been a continuing drive over several years to improve the properties of PZT [74]. This section will identify some of the key work that has been carried out into improving the material properties of PZT.

Research has shown that PZT exhibits two different ferroelectric phases below the materials Curie temperature (∼350°C [84]), rhombohedral and tetragonal, depending on the material composition. It can be seen that when the zirconate component is prevalent the PZT takes on a rhombohedral phase. Higher proportions of titanate cause the PZT crystal structure to be tetragonal [31]. The boundary between these two phases is known as the Morphotrophic Phase Boundary (MPB).

The MPB for PZT is found at a Zr/Ti ratio of 52/48 (figure 2.11) [31]. At this point there are the maximum number of ferroelectric domain orientation directions. This enables greater piezoelectric properties to be attained as there are a greater number of possible domain orientations [85]. The position of the MPB is also stable with respect to temperature, meaning that the phase change boundary between rhombohedral and tetragonal varies little as temperature changes. This is very important for commercial AE sensing applications [75].

Poling can be carried out to arrange domains into an orientation as close to that of the field as the crystal axis allows. Switching the polarization 180° has no effect on the strain within the material [73]. Poling of tetragonal PZT has an orienting effect on 90° whilst the poling of rhombohedral PZT orients the 71° and 109° domains. In PZT with compositions near the MPB both tetragonal and rhombohedral phases are present. Therefore in MPB materials the 71°, 90°, 109° and 180° domains are orientated by poling [73]. This leads to a greater degree of domain orientation and therefore increased piezoelectric properties.

An excess of lead is needed to ensure the production of the most effective com-

position during the PZT manufacturing process as lead is lost during the heating stages due to thermal volatility, especially at higher temperatures [86]. A shortage of lead can effect the stoichiometry of the film, degrading the properties.

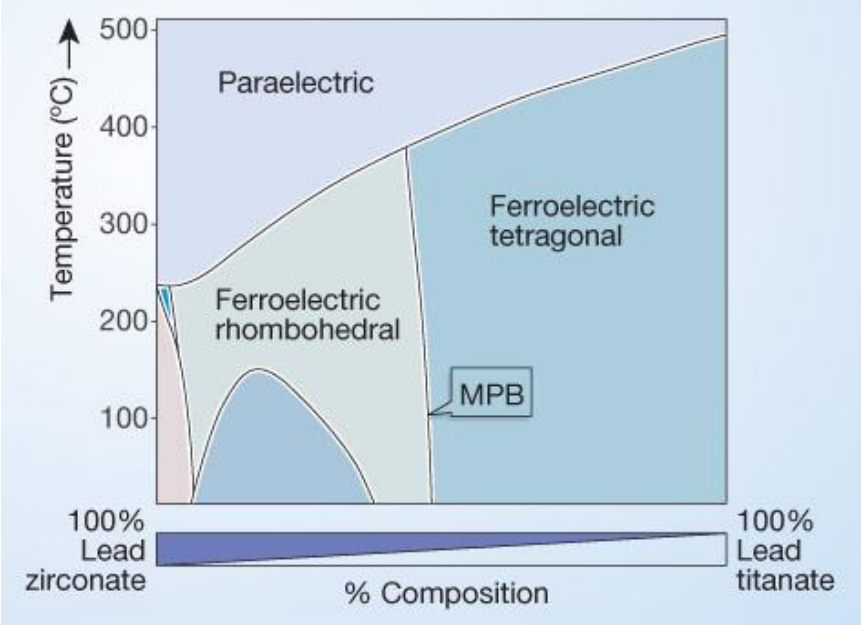

Figure 2.11: PZT phase diagram [4]

Various other methods can be employed to modify the material properties of PZT. One such method is the addition of dopants and various materials [87, 88, 89] to modify the PZT. For MEMS applications it is also important to understand and control how the PZT film interacts with substrate upon which it is deposited. The support of a substrate material is vital in the deposition of film material as the fragile film would otherwise be damaged or destroyed. The substrate which has found most use in MEMS PZT deposition is silicon. Silicon is employed as a substrate due to the stability of the material and the possibilities for integration with other electrical components integrated with the silicon substrate. Modification of PZT by the use of dopants and sintering aids may be used to improve the compatibility of the PZT with the substrate material.

There has been a strong drive towards lowering the processing temperature of PZT. PZT has traditionally been processed at temperatures in the region of 1200°C [90]. Lowering the processing temperature is important for several reasons. High temperature processing can result in loss of volatile components such as PbO to the atmosphere during processing, which reduces the electromechanical performance of the material [91, 89, 86]. This loss of PbO results in a need

for high temperature PZT processing to be carried out under an excess of lead or in a lead rich environment. At high temperatures lead can also diffuse into silicon, causing porosity and limiting the use of silicon as a substrate material [91]. Higher processing temperatures also limit the electrode materials that can be successfully employed [92, 93, 94, 95], copper for example melts at 1080°C [96].

One of the main methods for reducing sintering temperatures is the addition of liquid phase sintering aides to the PZT [91]. There have been many liquid phase sintering aides investigated but of particular interest for this work are Cu_2O/PbO [91, 96, 97, 89, 90]. Lanthanum has also been employed in lower quantities [$(Pb_{1-x}La_x)(Zr_yTi_{1-y})O_3$; $0.001 \leqslant x \leqslant 0.02$, $0 \leqslant y \leqslant 1$]. PZT doped with lanthanum at these levels has also shown significantly altered electrical properties when compared with un-doped PZT.

Liquid phase sintering aides become liquid during the sintering process. This enables greater freedom for grain rearrangement processes during sintering and results in increased film density and grain packing; therefore increased film properties. High volumes of sintering aides should be avoided as the electromechanical properties of the film may be adversely effected as the sintering aide becomes the dominant material [91].

Lanthanum modified PZT, lead lanthanum zirconate titanate (PLZT), has been the focus of a significant research effort [98, 70]. The electrical properties can be altered by changing the concentration of lanthanum and zirconium [99]. PLZT of composition [$(Pb_{1-x}La_x)(Zr_yTi_{1-y})O_3$; $0 < x \leqslant 0.2$, $0 \leqslant y \leqslant 1$] has been widely investigated. Using this method the properties can be adapted to suit the application for which the material is required. The use of strontium to dope PZLT has also been investigated and it has been found that both the d_{33} and the relative permittivity of the material are improved significantly by the doping process [87]. However, despite these tailored material properties, PLZT is not a material which has found widespread use in AE applications.

The versatility of PZT and the ability to combine the good material properties, including piezoelectric and electromechanical coupling coefficients [41], with several different manufacturing methods, as discussed in section 2.3 make PZT the material of choice in many applications. Some applications in which PZT offers advantages over other materials include: RF MEMS switches [100, 101];

actuators; micro-motors, pumps and valves; gyroscopes; ultrasonic and, crucially for this work, acoustic sensors [76].

2.2.3.1 Environmental Concerns

Despite over 40 years of research and development into the properties of PZT for use in many applications, including bulk and MEMS AE devices, alternatives are required. European Union environmental policy is driving for a limitation on the use of non-environmentally friendly materials such as lead [41]. PZT is currently subject to an exemption on anti-lead legislation but this is reliant on PZT having far superior properties when compared with lead-free piezoelectric materials such as zinc oxide [102], aluminium nitride [77], bismuth titanate or barium titanate [103]. Once a viable replacement for PZT has been identified, PZT will lose the EU exemption and the alternative will be employed.

Work is being carried out on KNN as a potential material as a like for like replacement for PZT but currently the material properties are not sufficient to replace PZT [41, 104]. Despite these poorer properties a KNN element has been demonstrated in AE sensing applications [42].

2.3 Materials: Current Technology

The properties of piezoelectric materials such as PZT are only of use if the material can be manufactured and shaped into active elements of specified, required size. Many technologies have been developed which are used for patterning PZT at varying scales from bulk elements (thickness$\geqslant$0.1mm) to thin film (thickness$\leqslant$1μm). This section of this work will discuss the processing techniques for these different scale ranges briefly and will focus on the thick film processing technologies employed in this work which result in films between 1μm and 100μm thick.

2.3.1 Bulk Materials Processing

Bulk active elements have many advantages over both thin and thick film elements. Bulk materials are materials with a thickness greater than 100μm and can be manufactured to have a slightly greater domain sizes than film materials. The increase in grain size improves material properties as there is a higher ratio of piezoelectric material to grain boundary in the material [73]. The higher volume to surface area ratio of the material also limits the loss of lead to the surrounding environment during higher temperature processes, this reduction in lead loss aides in improving the material properties as discussed in section 2.2.3 [86].

Another reason for the greater properties of bulk PZT when compared to thin or thick film PZT is that the film type PZT requires a supportive structure, or substrate, as a PZT film does not have sufficient mechanical strength to be left free standing. The use of a substrate as a supporting structure reduces the material properties of the film by causing stress due to a differential in thermal expansion rates and high film shrinkage caused by the removal of solvent and the film crystallization. The film is constrained to the substrate and so at large magnitudes of shrinkage the stress experienced by the PZT film can be great enough to cause serious cracking of the material [105].

The thickness of bulk PZT, whilst aiding in the reduction of stress in the material and improving the material electro-mechanical properties does have drawbacks. The thickness of the material limits the possibility of device integration. There is currently a drive for smaller devices which can be integrated along with other components onto one printed circuit board (PCB), this is impractical with bulk active elements. Bulk elements are also comprised of a greater amount of material, this leads to added expense and reduces the extent to which the device can be considered disposable. The larger size of bulk devices also causes manufacturing issues.

Bulk materials, by definition are larger in size than films and a top down manufacturing process is often employed. This type of processing starts with a billet of material which is then machined using a micro-mill or a powder blasting technique to the desired dimensions. This is a wasteful process as much of the billet is unwanted and subsequently discarded. The processing of MEMS components

from bulk also requires a high sintering temperature (1200°C) [106]. This higher temperature combined with the relatively high surface area to volume ratio makes controlling the stoichiometry of the material difficult but achievable with added cost [106].

Another disadvantage of the mechanical processing techniques employed in bulk material processing is that the size and complexity of component it is possible to manufacture is limited by the capability of the equipment used to manufacture the component. For example the size and accuracy of any feature created by use of micro-milling is limited by the size of the milling head and the accuracy with which that head can be controlled. The accuracy and possible feature size which mechanical machining technology can produce are related to the machining equipment cost. To produce accurate, small features can be extremely costly. These constraints mean that whilst the material properties of bulk PZT are better than those of films type PZT the difficulty in creating precision components, smaller than $\sim 50\mu$m, is a limiting factor.

Currently modern AE sensor technology makes use of bulk sensing elements, however, there is a drive towards miniaturization and low cost, disposable devices. Bulk technology is unable to fulfil these requirements, as such it is important to consider both thin and thick film technologies.

2.3.2 Thin Film Processing

Thin film processing techniques can provide a low cost alternative to bulk processing. Thin film processing techniques are employed to deposit films of piezoelectric material, such as PZT, in layers of a thickness of less than one micron onto a substrate material. Whilst thin film materials have properties which can vary widely from those of bulk materials the applications in which these films find use are similar; however, the miniaturization of devices developed by thin film processing greatly increases the scope for developing disposable AE devices which can be left in situ. There are various methods by which thin films can be deposited including Chemical Vapour Deposition (CVD), Molecular Beam Epitaxy (MBE), Pulsed Laser Deposition (PLD) and sol-gel [91]. These methods produce films which exhibit a textured surface and can be epitaxially orientated depending on the deposition process. Thin film deposited by these methods are 100% dense

[44], which leads to improved properties.

Chemical Vapour Deposition and Molecular Beam Epitaxy

CVD is a process which has been in development since the 1960s which involves vaporizing chemicals containing the required elements for the final product onto a heated substrate [107]. The processing parameters for this method depend largely on the materials used but a vapour pressure of 50mTorr or above is desirable at ambient temperatures. A pressure of 3.5mbar can be used when the substrate is heated to 525°C to deposit PZT. The precursor chemicals used for the manufacture of PZT are $Pb(thd)_2$, $Zr_2(OPr^i)_6(thd)_2$ and $Ti(OPr^i)_2(thd)_2$, where "thd" is 2,2,6,6,-tetramethyl-3,5-heptanedionate, a highly toxic chemical. This process results in a deposition rate of 2μm/h [108].

A technique closely related to CVD is that of MBE. In MBE the materials that are to be deposited are vaporised and passed over a heated substrate in a high vacuum. The materials then condense onto the substrate and react together to form the final film. The deposition rate for this method is much slower than that of the other methods described here. This method can be used to grow films which are several atomic layers thick but is not suitable for films of a thickness much greater than this. The method is more expensive than other similar methods as the very high vacuum level required for a good quality deposition is difficult to attain.

Pulsed Laser Deposition

PLD uses a laser directed at a pre-prepared ceramic target to create a plasma which is then directed at the substrate requiring coating. The properties of the deposited film depend largely upon the pressure in the chamber and the temperature and distance of the substrate [109]. In the initial stages of the film deposition defects form allowing a collision region to form. This collision region enables the condensation of particles on the surface of the substrate and, when the condensation rate reaches sufficient levels, the subsequent growth of the film.

The properties of both the substrate and the plasma influence the rate of deposi-

tion. Whilst the deposition rate of PLD is lower than that of CVD, the collision region enables a higher than normal rate of nuclei formation. This means that films formed by PLD exhibit a higher density than those deposited by CVD. One of the main disadvantages is that the plasma properties are difficult to control and therefore the properties of the resultant film can be unpredictable. Like other techniques discussed in this section, PLD can only be used to coat small areas of the substrate.

Chemical Solution Deposition

Chemical Solution Deposition (CSD) can be carried out via several routes including; dip coating, spin coating or metalloorganic deposition [70]. Spin coating is a technique which is of particular interest for this work. The work carried out on developing thin film sol-gel deposition technology was influential in the development of the composite sol-gel technique for the deposition of thick film materials, which is the main technique employed in this work.

Sol-gel has been utilised as a thin film production method since the 1970's and is well understood [70]. PZT sol is a colloidal suspension of lead, zirconium and titanium which can be formed by several routes [86, 110], one of which involves reacting lead acetate, zirconium propoxide and titanium iso-propoxide in a solvent which, in this work is 2-methoxyethanol [111]; other solvents including ethylene glycol [110] have also been employed.

Spin coating is employed to ensure the film is a homogeneous layer. The substrate must be cleaned to ensure film adherence, this may be achieved by using barrel etching to remove organic contaminates and an US bath in isopropanol (IPA) [111]. The acceleration to which the sol-gel is exposed is counteracted by the viscous drag in the sol-gel. The process of spin coating is initially controlled by viscous flow before the process of evaporation takes over [112].

$$t = x\left(\frac{e}{2(1-x)K}\right)^{\frac{1}{3}} \tag{2.25}$$

$$e = C\sqrt{\omega}$$

$$K = \frac{\rho\omega^2}{3\eta}$$

The final film thickness (t) can be estimated using equation 2.25 where "e" and "K" are the evaporation and flow constants, "x" is the solid content of the sol-gel, "ω" is the angular velocity of the substrate, ρ and η are the sol density and viscosity respectively and C is a constant depending on whether the air flow over the substrate is laminar or turbulent [112]. This equation shows that the film thickness for a material is related to the spin speed by the power of -1/2.

Once spin coating is complete the solvent is driven off in a drying stage at 200°C, the organic material removed by pyrolysation at 300°C - 400°C. Once pyrolysation is complete the process is repeated several times until the desired film thickness is attained. The film is then crystallised by sintering at temperatures of 600°C and above.

Thin films manufactured by sol-gel spin coating exhibit homogeneous properties which can be controlled by the film chemical composition. This technique is only practical for depositing thin films with a thickness below 1μm because a greater film thickness requires lengthy processing and a large number of spin coating depositions. The risk of cracking during heat treatment also increases with thickness due to the large amount of shrinkage caused by the removal of liquid from the system, combined with the film being constrained by the substrate materials inducing very high stresses into the thin film [91].

2.3.3 Thick Film Processing

While thin film processing is low cost and fulfils the requirement of miniaturised device manufacture, thin films lack the piezoelectric sensitivity to be an effective

substitute for bulk active elements in AE sensing applications. Thick film technology provides a compromise between the properties offered by bulk and thin film processing [91]. Thick film compromises between the greater electro-mechanical properties of bulk materials and the flexibility and miniaturization potential of thin film. Thick film has the potential for bottom up device manufacture in the same way as thin film, eliminating the wasteful top down mechanical processing techniques employed on bulk materials [92, 106].

Greater film thickness can produce a greater actuation force in the case of actuators, or for the production of greater amplitudes and the detection of lower amplitudes in the cases of US transducers and AE sensors respectively. Added film thickness can also be used to reduce the frequency range that both US transducers and AE devices can effectively operate over [44]. This film thickness is attainable using thick film processing as opposed to thin film techniques. Thin film processes are too time consuming, costly and generate large stresses in the final film [92, 44].

Film integration and bottom up manufacturing, along with greater film properties of PZT thick films compared to those attainable by PZT thin film processing, make the use of PZT thick films for AE sensing a desirable area of research. The deposition of thick films requires the deposition of powder suspended in a carrier fluid onto a substrate. The carrier fluid is then completely removed by drying, resulting in a layer of powder on the surface of the substrate. Common carrier fluids include water or solvents. Sintering aids and binders are added to the carrier fluid alongside the PZT powder. Films composed of a composite slurry utilise the solvents in PZT sol as a carrier fluid, this composite slurry approach is the method of PZT manufacture employed in this work.

2.3.3.1 Deposition Techniques

There are various deposition and patterning techniques used in the processing of thick film PZT with various qualities. The deposition of thick films can be achieved by several methods including composite spin coating, screen printing, tape casting, ink jet printing and various spray coating techniques. Each of these techniques deposits films with various characteristics. The appropriate technique must be chosen based on the requirements of individual situations. Where these

techniques involve the deposition of a composite slurry it is important to identify the desired powder loading in the composite to be deposited; low powder loadings can be deposited by an unmodified CSD process such as dip coating or dripping the material onto the substrate before drying, medium powder loadings require a modified CSD route such as spin coating, materials with high powder loadings should be deposited by tape casting or screen printing [106].

Composite Spin Coating

A widely used method of depositing a film with a thickness between 1μm and 50μm is CSD by spin coating as this technique offers many advantages including close control over the thickness and composition of the film along with the ability to deposit large film areas at low cost [106]. The CSD technique can be modified to produce greater film thickness by depositing a composite layer composed of slurry with sol infiltrations. Slurry is manufactured by the addition of powder of the same stoichiometry as the sol-gel [86]. This slurry is then thoroughly mixed by ball milling. Sintering aides can be added to the slurry and these operate in the same way as in bulk materials and bring the sintering temperature down to between 700°C to 800°C [90] depending on the deposition process.

Composite spin coating involves the deposition of PZT slurry onto an appropriately sized wafer which is then rotated at several thousand revolutions per minute [106]. The spinning process follows the same physical model as described in section 2.3.2 and removes the excess slurry leaving a thin layer on the surface of the substrate. This thin layer ($\sim$2μm) is then dried and pyrolysed to remove the solvent and the organic materials. Once the layer has been dried then the process can be repeated with another layer of slurry depending on the required thickness of the final film [105].

Once the desired number of layers of slurry have been deposited sol-gel infiltrations are carried out to increase the film density. The infiltrations are made by depositing diluted sol-gel of the same stoichiometry as that used to manufacture the slurry onto the surface of the film and repeating the spinning process. This process allows the sol to infiltrate into the pores of the slurry film whilst the forces induced by the spinning process ensure that there is an even distribution of sol and no excess on the surface of the film. The heating process is then repeated

to dry and pyrolyse the sol before the infiltration step is repeated.

The composite layers and sol-gel infiltrations are often represented by the notation C and S respectively. The notation for the composite spin coating process is [yC+zS] where "y" is the number of composite slurry layers, "z" is the number of infiltrations carried out on "y" composite slurry layers. [yC+zS] forms one composite film layer unit and this process can be repeated "x" times giving a final notation of x[yC+zS] [105].

The number of infiltrations carried out per one or two layers of composite slurry deposition are important. The film electro-mechanical properties, such as ϵ_r and $e_{31,f}$, improve as the number of infiltrations and therefore film density increases. This improvement of properties as the film porosity is reduced is due to the increased efficiency of stress transfer through the film [44]. Like thin film spin coating the thick film deposition exhibits homogeneous properties across large areas of the substrate wafer. However, unlike thin film technology thick films deposited by composite spin coating have heterogeneous properties throughout the film thickness.

Where a x[C+4S] system is employed with a 1.1 molar sol diluted 1:1 by volume with 2-methoxyethanol, the pores become saturated by the infiltrations and this causes excess sol to sit on the surface of the film. As the concentration of the sol used for the infiltration changes the number of infiltrations required to fully saturate the pores changes proportionately. This surface is then covered by another composite layer and the process is repeated. This repetition results in the formation of x-1 sol-rich interfacial layers throughout the film. These interfacial layers alter the electrical and etch properties of the material.

During the sintering process a large amount of liquid is removed from the film. More liquid is removed from the sol-rich layers than the rest of the film and this differential induces stress causing excessive cracking and the film properties reduce accordingly [105]. This effect is much reduced in x[2C+4S] systems as the sol to slurry ratio is halved meaning that there is not a sufficient volume of sol to saturate the pores in the composite slurry layer [105]. Ideally there should be enough sol to saturate the pores but not a sufficient sol volume to form a sol-rich interfacial layer. Considering this, a maximum of four infiltration steps are recommended per composite layer.

Thick film spin coating with sol-gel infiltrations produces a film with a significantly higher density than other thick film deposition techniques, as the sol-gel infiltrations are difficult to carry out without the spinning process to ensure an even and thin layer. The thick film system does exhibit a greater number of micro-cracks than in thin film systems, due to the large loss of liquid and stress induced in the film due to the constraints of the substrate combined with the difference in thermal expansion coefficients between the substrate and the film during the sintering process [91].

Screen Printing

The most common deposition technique is screen printing, in which a flexible patterned screen mesh made of steel or nylon [91] is suspended 0.5mm above the substrate requiring coating and coated in a paste like ink. The ink consists of PZT with sintering aides in an organic solvent carrier phase [113, 91]. A squeegee is then passed over the screen, forcing the ink through the pre-prepared pattern onto the substrate. This process can then be repeated to add thickness to the film. A typical process can produce a film thickness of between 10μm and 60μm [114]. A mesh density of 250 wires per inch has been demonstrated, this density gives a feature resolution of approximately 10μm [113]. This negates the need for post deposition processing to pattern the film.

Films deposited by screen printing lack resolution which is not prohibitive for the development of integrated AE sensors. One major limiting factor on the usefulness of screen printing in AE applications is the high porosity of the resultant films. This poor density limits the piezoelectric properties of the film. The density can be improved but requires a high sintering temperature, up to 1200°C [92, 105], relative to that employed in sol-gel processing. The temperatures required are often above those at which silicon can be employed as a substrate and lead migration becomes a serious issue unless a suitable barrier layer is employed [114]. This means that devices have to be manufactured separately and prohibits device integration [115] on silicon; there is a possibility of employing ceramics or high melting point metals as substrate materials.

Tape Casting

Tape casting is a deposition technique used to deposit a continuous film onto various substrate materials. The ceramic slurry is deposited onto the substrate in front of a doctor blade. The substrate is then dragged away from the blade, forcing the slurry under the blade into a thin layer. The thickness of the film can be controlled by the height of the blade above the substrate. The substrate and deposited film can be moved through a heater to sinter the slurry in-situ enabling continuous production.

Tape casting can be used to produce films with a thickness on the order of millimetres [105]. As this technique is essentially a continuous version of screen printing it suffers from the same issues with resolution and poor density. The issue of poor density prohibits the integration of tape cast PZT onto silicon due to the high temperatures required to ensure maximum densification [92, 105]. Once again, intelligent selection of substrate materials can negate this issue.

Ink Jet Printing

Ink jet printing is a mechanised deposition technique. The ink jet printer deposits a composite droplet with a very low powder loading compared to that used in spin coating, 0.083g of powder/ml of sol compared to 1.5g of powder/ml sol [106]. Printing is more often carried out as a pure sol-gel process. Ink jet printing can be used in either a continuous flow printing technique or individual drops can be deposited to give added control over deposition location [91].

Despite the added control over the placement of droplets due to the mechanisation of the process, the actual resolution of ink jet printing is in the order of tens of microns, commercial printer exhibits a resolution of $\sim 20\mu$m [91]. This resolution can be improved by the reduction of droplet size. To reach a droplet size capable of giving adequate resolution for MEMS applications without post-processing, the removal of PZT powder from the system is necessary. This is because the droplet size required to result in a resolution on the order of 100nm-200nm is of a size similar to that of a single PZT particle [106]. A 0.2μm resolution is acceptable for AE sensing applications as the feature size is on the order of hundreds of microns.

Modelling has been carried out to determine the physics of ink jet printing and to enable greater flexibility in depositing patterned films [116]. This work was experimentally validated and showed that a continuous track of material could be printed with careful control of the printing parameters; such as drop size, frequency and angle. This does not improve the resolution of ink jet printing but is none the less a useful technique in MEMS processing, particularly for low resolution applications such, such as AE device manufacture.

A direct writing technique, similar to that of inkjet printing, using a micro-pen has also been demonstrated as has a technique combining UV sensitive chemicals with PZT. The PZT is then deposited and selectively exposed to UV radiation, the unwanted material can then be removed in a development stage [91].

Spray Coating and Electro-Hydrodynamic Atomisation

Spray coating is a low tech deposition technique, similar to that used in spray painting. The PZT slurry is ejected from a nozzle under pressure and deposited onto a substrate surface. This technique produces poor film homogeneity due to the presence of large agglomerations of particles in the spray.

Electro-Hydrodynamic Atomization (EHDA) is a spray coating technique which uses a DC voltage applied between a charged suspension with a powder loading lower than 1% and a bottom electrode [91]. EHDA is a technique which was developed for use with liquids and adapted for use with colloidal suspensions. EHDA uses a combination of Electrophoretic Deposition (EPD) and spray coating effects to disperse a spray into drops [92]. There are several possible spray geometries produced by EHDA techniques but the stable cone is the spray geometry of most interest as it produces small, uniformly sized and shaped droplets [92].

A needle is placed above a conductive substrate at a certain separation distance and a high voltage charge is applied across the gap. PZT slurry is then forced through the needle by syringe at a constant flow rate. The separation distance between needle and electrode has been found to be key [92]. Repeated spray passes can be used to deposit thick films, with a thickness on the order of tens of microns being achievable. Films produced by this method have been shown to be crack free, have good density and to have piezoelectric properties comparable

to those film produced by composite spin coating.

2.3.3.2 Thick Film and Substrate Patterning Techniques

Once a film has been deposited patterning and material removal is often required to form the film into a functional AE device. Film patterning and material removal can be carried out by several routes including; micro-moulding, wet etching, Reactive Ion Etching (RIE) and powder blasting. Sometimes it is also necessary to remove or pattern the device substrate, for example in the creation of thick film membranes or in the complete release of devices from the substrate. This can be achieved by chemical wet etching as well as Deep Reactive Ion Etching (DRIE).

Powder blasting

Powder blasting is a fully mechanical technique for the patterning of thick film MEMS [117]. The substrate is masked with a polymer able to resist the effects of the powder blasting, this can be a photoresist, metal or a self-adhesive polyvinyl layer. Powder is then propelled at the unprotected surface of the film at velocities of up to 290m/s [91, 117]. The powder impact causes micro-cracking in the film material, when the micro-cracks link the material is released from the film exposing the film underneath to powder impacts [91]. This process is continued until all of the exposed film material is removed.

There is very little selectivity between brittle materials in powder blasting [91], this means that once the PZT film has been removed the powder blasting process will begin to remove the substrate material; for example the material removal rate for silicon has been found to be 25μm/min [117]. The removal rate is determined by the mechanical properties of the material to be removed and the kinetic properties of the powder used for blasting.

The material removal rate also varies with distance from the mask edge. The mask edge may obstruct the path of some of the powder particles which are deflected away from the underlying film and so the etch rate is slowed. This slower etch rate causes a gradient to develop. As the etch rate is also influenced by the angle of incidence of the particle onto the surface of the film material the etch

rate is further slowed on the gradient near the mask edge when compared to the flat area well away from the mask [117]. Powder blasting can be carried out which results in very high wall angles and aspect ratios of 2.5:1 have been observed [117].

This process can be used to attain feature sizes on the order of 30μm [91] with good wall angles and is low cost both in terms of equipment and consumables [117]. However the low selectivity between brittle materials and the rough surface finish are both drawbacks [117] which limit the use of powder blasting. Where film material must be removed without damaging the underlying substrate, another technique must be employed.

For AE applications powder blasting is an ideal technique. In integrated applications the substrate is often metal and therefore is relatively undamaged by powder blasting. The relative low cost and ease of implementation of this technique compared to other patterning methods is also advantageous in the manufacture of low cost AE devices

Micro-moulding

Micro-moulding is a process for depositing patterned devices without the need for the removal of excess material. This technique involves the development of a mould with features of micro-scale resolution. This mould is then filled by depositing the piezoelectric material over the whole surface before removing the areas masked-off by the mould material, which can be photoresist [106, 44, 118] or a metallic mask [93]. Micro-moulding can produce features of a greater resolution than other techniques whilst lowering sintering temperatures and not employing hazardous etchant chemicals [93].

Chemical wet etching of PZT films

Chemical wet etching is a technique for chemically removing material, which can be used for the removal of PZT films. PZT etching is usually carried out using a HF/HCl solution [119, 105, 91], the HF component of the etchant attacks Ti and Zr while the HCl attacks the Ti and Pb [91]. The speed of the etch process can be increased by heating the etchant to 60°C [105].

Patterning can be achieved by applying a photoresist mask to the surface of the PZT film and then selectively exposing the photoresist to UV light in the same fashion as described for micro-mould creation above. In this case the photoresist acts to protect the PZT from the etchant which will remove the unprotected PZT. When a photoresist mask is employed it is important to take into account the effects of undercutting during the etch process. Due to the isotropic nature of the PZT film being etched the material will be etched at the same rate in both the vertical and horizontal directions [91].

The isotropic etch rate results in the undercutting of the photoresist by the same distance as the thickness of the film and thus results in a 45° wall angle. This also means that the feature size attainable by wet etching techniques is limited by the thickness of the film being etched. For example the mask width needed to result in a 10μm wide feature when etching a 10μm isotropic thick film is 30μm.

In practice the wall angle of wet etched thick film PZT is often greater than 45°. This is because of the structure of the PZT, multiple layers and sol-infiltrations produce varying film density in the thickness direction. The denser PZT is etched more slowly and so a stepped "pyramid" is produced [105]. Undercutting can be reduced by using a thicker photoresist layer [105].

Wet etching is a useful process for quick and low cost removal of large areas of PZT film. It is not possible to achieve the small feature sizes that can be produced using micro-moulding or reactive-ion etching techniques due to the large undercut and therefore poor wall angle inherent with the use of chemical wet etching on near-isotropic films. This is not an issue for AE device manufacture as the device dimensions are on the order of hundreds of microns.

Reactive Ion Etching of PZT films

Dry etching of PZT can be carried out by RIE or DRIE. The techniques are widely used in the etching of thin film PZT [91]. Photoresist masking is used to protect the sections of the film which are not to be removed. The photoresist material used for the mask is chosen to have a much lower etch rate than the film material to be etched, this is termed a high etch selectivity. Once the masking is complete the etching is carried out. The RIE process is a chemo-mechanical one.

Ions, such as Ar and CF_4 [101], are fired at the surface of the film to be etched and the combination of the chemical and mechanical effects of the ions combine to remove material from the film [106].

RIE processing, unlike chemical wet etching, exhibits an anisotropic etch rate meaning that much higher wall angles can be achieved by this technique than in wet etching [91]. RIE requires expensive equipment which, due to lead contamination concerns, must be either bespoke for PZT etching or be subject to extensive cleaning after each PZT etching run [91]. The etching process is also considerably slower than other processes, this adds to the operational costs and usually limits the application of RIE to thin film processing [91, 106].

Wet etching of substrates

The removal of silicon by wet etching is a well known process [120]. The most widely used wet etchant chemicals are potassium hydroxide (KOH) and tetramethyl ammonium hydroxide (TMAH) [113]. In much the same way as in the selective removal of films, any silicon which is to remain un-etched must be protected by a suitable mask which is resistant to the etchant, usually a UV sensitive photoresist. In silicon wet etching processes the silicon dioxide (SiO_2) etch rate is considerably slower than the etch rate of silicon, 35% KOH at 75°C etches these materials at 0.073μm/h and 43.03μm/h respectively [47]. Due to the much slower etch rate for SiO_2, the oxide is usually removed prior to the etching process by HF.

Once the SiO_2 has been removed, KOH can be used to etch the Si. The surface finish of the Si after etching depends on the crystallographic plane which is exposed by the etchant and the concentration of the KOH [121]. As in the case of etching the PZT film, heating the etchant can increase the etch rate [120]. The removal of silicon by KOH etching becomes more complex when there is a PZT film on the surface of the silicon, particularly if there is a bottom electrode between the Si and the PZT.

When an electrode is present between the film and the silicon, the KOH attacks the interface between the silicon and the electrode [113]. This area is particularly susceptible to attack following sintering without a diffusion barrier as the damage caused to the substrate by lead diffusion results in areas of porosity. These areas

of porosity enable the etchant to penetrate into the interfacial later and to etch the silicon. This process can cause the PZT film to separate from the substrate in flakes, destroying the film [113]. The KOH may also undercut any fine features of the film but the PZT itself is not attacked.

TMAH etching requires special care to ensure that all of the natural oxide later is removed from the Si. TMAH etching exhibits all the properties of KOH etching. TMAH has been found to damage the structure of PZT and has an effective etch rate of 90nm/min [113] which is considerably slower than that of KOH. TMAH damages the PZT film and as such has limited application in the removal of substrates for AE sensor production applications.

Deep Reactive Ion Etching of substrates

DRIE is a vital technique in MEMS production because it has high etch selectivity and the etch is consistent regardless of crystallographic orientation [122, 123]. DRIE works by alternating between etching and the deposition of a polymer which coats all faces of the etched trench. SF_6 is a typical etchant, C_4F_8 is a typical polymeric passivation layer. The high selectivity of the DRIE process means that photoresist can be employed as a mask material, allowing for the patterning of fine detailed features.

The ion etching step quickly removes the polymer at the bottom of the trench due to the incidence angle being 90°, the polymer on the side of the trench etches more slowly due to the low incidence angle. The etching step timing matches the etch rate of the polymer on the trench side wall to avoid a build up of the polymer [122]. As the aspect ratio of the etched feature increases the etch rate at the bottom of the trench decreases due to the interference to the ion incidence rate by the mask material. This slower etch rate causes the wall angle to increase. Undercuts are apparent in high resolution etching applications where a hard mask is used. Undercutting occurs because of the isotropy of the SF_6 etching process [123].

Etch rates of up to 2.4μm/min are possible [120] and final wall angles of up to 89° have been achieved with minimal undercutting by using an O_2 passivation stage to produce a SiO_2 layer in addition to the polymer protection for the side

wall [123]. DRIE is a very effective silicon etching technique, however, both the equipment and running costs are high in this method. This technique is useful for specialised applications or applications where accuracy is essential, for other applications other techniques may be more effective to reduce cost.

2.3.4 Metal Substrates and PZT Film Integration

Traditionally PZT has been deposited on noble metal or conductive oxide bottom electrodes to limit the reactions which take place at the interface between the PZT and the electrode during processing [97]. Platinised silicon and alumina substrates have been widely employed in MEMS processing as they are compatible with PZT processing and exhibit superior PZT/substrate adhesion properties than other substrate materials. The films deposited onto these substrate materials also exhibit superior electrical properties to those deposited onto other substrate materials [111].

Metal substrates have been found to exhibit some properties that are advantageous, compared to platinised silicon or alumina, in MEMS device development. Metal substrates exhibit elastic properties compatible with AE testing applications. Material selection must be carried out carefully to ensure that the metal selected for use as a substrate exhibits sufficient adhesion to the PZT and low reactivity. Low reactivity ensures that there is limited diffusion of material between the substrate and the film [124]. The thermal expansion of the substrate material must also be considered as a large thermal expansion mismatch reduces the electrical properties of the deposited PZT film.

Metals which are of interest for use as substrates in MEMS processing include stainless steel; glass sealing alloy, also known as Kovar; titanium and copper [125, 111, 126, 96, 127]. These metals exhibit properties which are of use in MEMS processing. As metals are widely used in engineering structures, the deposition of PZT onto metal substrates is of great interest in the development of integrated AE devices. PZT has also been integrated with nickel, however, nickel is neither widely employed as structural material or in integrated electronics. As such PZT integration with nickel is not relevant to the development of structurally integrated MEMS AE devices.

Steel and Kovar

Steel is one of the most widely employed of structural elements. As such the integration of PZT with steel substrates is of great interest for integrated AE sensor applications. Integration of PZT thick films on stainless steel is favourable over integration with non-stainless steel. Stainless steel is favoured due to lower reactivity reducing the diffusion of materials, such as the ions of Fe, Cr, Mn and Ni, between the PZT and the substrate [128]. Diffusion takes place during the sintering of the PZT film and reduces the electrical properties of the film substantially [129]. The reduction in the electrical properties of the PZT is due to the diffused ions forming a semi-conducting layer which exhibits poor ferroelectric properties thus reducing the macro scale properties of the film.

Diffusion barriers are of use in reducing the diffusion of material between the PZT and the substrate. ZrO_2, a diffusion barrier commonly utilised with silicon substrates, is effective at preventing diffusion between PZT and the stainless steel substrate. If the diffusion barrier is on the order of hundreds of nanometers in thickness then the use of the stainless steel substrate as a bottom electrode is still viable [128]. The inclusion of a diffusion barrier will decrease the overall properties of the film but this reduction in properties is small compared to the reduction of properties resulting from diffusion.

A further issue with deposition of PZT onto stainless steel is that of thermal expansion. One of the properties which makes the deposition of PZT onto silicon favourable is the similarity of the material thermal expansion coefficients, $\sim$6x10^{-6}/K [130] and 4x10^{-6}/K for PZT and silicon respectively. The thermal expansion coefficient of stainless steel is 18x10^{-6}/K, considerably larger than that of PZT [129]. As the thermal expansion mismatch increases, the ϵ_r of the PZT film is reduced due to stress in the film [129]. This is one of the main limiting factors in the use of stainless steel as a substrate material for the deposition of PZT

Kovar is a glass sealing alloy composed of 29% Ni, 17% Co and a balance of Fe. This composition of alloy exhibits a thermal expansion coefficient of 6x10^{-6}/K. This thermal expansion coefficient is similar to that of PZT. Therefore the use of Kovar as a substrate avoids stress in the film and the resultant reduction in ϵ_r observed with the use of a stainless steel substrate. The electrical properties of

PZT on Kovar are thus superior to those of PZT on steel whilst being inferior to those of PZT on silicon [111].

While Kovar is resistant to oxidation, exposure to the processing temperatures required for the deposition of thick film PZT results in the formation of an oxide layer which exhibits high loss. Sintering of the PZT film on a Kovar substrate under an argon atmosphere reduces the formation of this oxide layers and thus improves the properties of the PZT film [111]. This makes Kovar a very attractive metal for use as a substrate material for the structural integration of PZT AE devices.

Titanium

Titanium has found use as a substrate material for both thin and thick film PZT. The thermal expansion coefficient of titanium is $8.6\text{x}10^{-6}$/K, higher than Kovar, lower than steel and similar to the thermal expansion coefficient of PZT [126]. The small thermal expansion mismatch results in little stress being introduced into the PZT film during processing and therefore the electrical properties of the PZT are not adversely affected.

The adhesion between titanium and PZT is also good. However, there is an issue with diffusion of titanium from the substrate into the PZT film. This diffusion has been shown to alter the composition of the PZT and, with PZT compositions close to the MPB, may result in a phase change from rhombohedral to tetragonal. Diffusion of lead also occurs and may result in a lead deficiency in the PZT leading to the formation of a pyrochlore phase and therefore a reduction in the electrical properties of the PZT film [124].

Diffusion barriers may limit the diffusion of material between the PZT and the substrate whilst also limiting the formation of an oxide layer - an oxide layer results in the film exhibiting reduced ferroelectric properties. $LaNiO_3$ has been employed as a diffusion barrier. $LaNiO_3$ is conductive, providing processing temperatures are limited to below 900°C [124]. This is of benefit as the conductive layer of $LaNiO_3$ acts as a diffusion barrier without the drawback of reducing film properties by the addition of a non-conductive, non-ferroelectric layer between the PZT film and the titanium substrate which is employed as the bottom elec-

trode.

The deposition of PZT films on metals such as stainless steel, Kovar and titanium is a compromise. PZT films deposited on silicon or alumina substrates exhibit superior properties to those deposited on metallic substrates, however metallic substrates exhibit mechanical properties which are more suited for some AE sensing applications. The deposition of PZT onto metallic substrates is of interest for the integration of AE sensors with structural elements as many structural elements are metal. In such AE sensing applications the disadvantages of depositing onto metal substrates are outweighed by the advantages of being able to deposit directly onto the element which requires AE monitoring.

Copper

Unlike steel, Kovar and titanium; copper is not a material which is widely used in structural components. Copper is a low cost material with higher conductivity and is extensively integrated with Printed Circuit Boards (PCB), the integration of PZT with PCBs is desirable to increase component density and therefore the ability to deposit PZT onto copper is of interest [96, 127].

In the context of AE sensing technology, the ability to integrate the AE device onto a PCB enables the pre-amplifier circuit to be mounted with the device, greatly reducing the risk of external noise masking AE events. The mounting of an AE device with the pre-amplifier also reduces the need for external components which may add weight or increase the overall system dimensions.

Additionally, the integration of PZT with copper is of interest for AE applications as copper is a material which is easily removed by etching. Therefore copper is of interest in applications where the release of PZT films from the substrate material is required.

There are issues with the deposition of PZT onto copper. The high temperatures required to sinter PZT in oxidising conditions and the high volatility of PbO [97] combined with the relatively low melting point of copper ($\sim$1085°C) [96] make the control of thermodynamic equilibrium of the process complicated [97]. Typically the the conditions in which copper is stable are incompatible with

PZT which, in this system, can be represented by the reduction of PbO_2 [131].

The processing of PZT on copper requires careful temperature and atmospheric control during sintering to avoid the development of a Pb/Cu alloy interfacial layer. This layer migrates into the film and causes the PZT to decompose into ZrO_2 and lead titanate rich PZT. Decomposition takes place at sintering temperatures greater than 950°C even under controlled atmospheric conditions [96] and as such low temperature PZT processing, such as that of the composite spin coating, is essential.

For the processing of PZT on Cu to be effective it is vital to eliminate the development of this Pb/Cu alloy. This can be achieved by controlling the partial pressure of oxygen (pO_2) and the temperature during the sintering process to fully sinter the PZT while keeping the Cu metallic. The temperature and pO_2 must be high enough to ensure that PbO_2 reduces to form Pb [131] whilst being low enough that the Cu remains as Cu and does not oxidise into CuO_2. Figure 2.12 shows the partial pressure requirements to achieve the desired oxidation conditions [131].

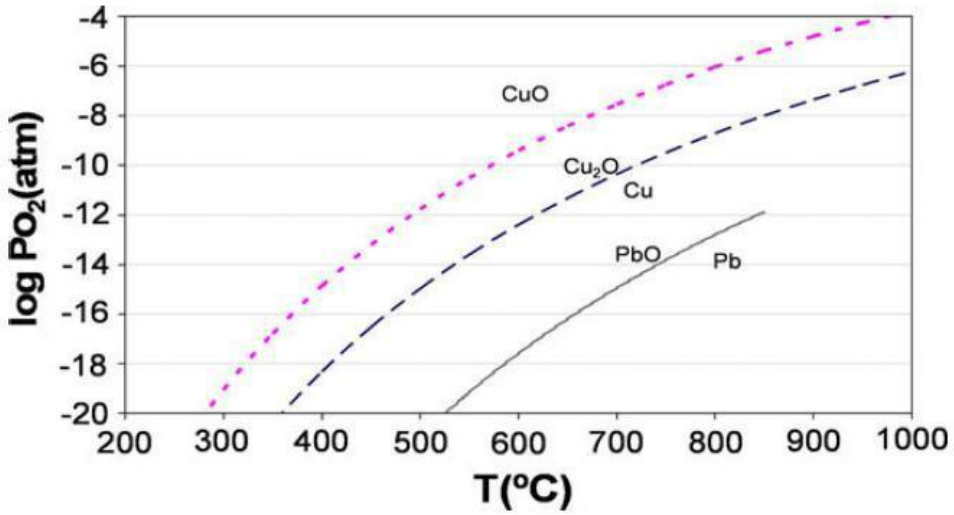

Figure 2.12: Plot of oxygen partial pressure against temperature showing the conditions which are conducive to formation of metal oxides during processing.

The pO_2 required to keep the Cu oxidising varies with temperature, the most appropriate conditions include a pO_2 of between 10^{-8} and 10^{-11} atmospheres and a

temperature of between 850°C and 900°C [96]. If the pO_2 is set by sintering in a dry atmosphere consisting of constant amounts of N_2 and O_2 then the pO_2 may be appropriate for the sintering temperature but not for the heating and cooling process, causing the formation of the Pb/Cu layer [131]. This can be avoided by adjusting the pO_2 during the heating and cooling process. This clearly requires tight atmospheric control in the furnace employed for sintering.

By this method it is possible to deposit thick film PZT onto copper foil and to successfully integrate PZT with PCB technology. High cost equipment is required for the tight control of atmospheric conditions. Once this equipment has been purchased the cost of consumables is low, this makes the process viable for industrial production of integrated PZT/Cu PCBs. One further issue with the deposition of PZT on Cu is the thermal mismatch between the materials causing micro-cracking in the PZT film [131] thus significantly reducing the properties of the film.

Once integration of PZT and copper has been achieved there is the potential to either integrate other components with the PZT element on a PCB. Alternatively the copper may be employed as a sacrificial substrate, releasing the PZT film from the substrate as part of the manufacture of MEMS AE devices which can then be bonded directly to the structural element which requires monitoring.

2.4 Summary

The review of relevant literature carried out in this chapter demonstrates that there is a lack of knowledge concerning the use of thick film MEMS technology for the manufacture of low cost AE sensors. The majority of current AE monitoring technology relies on bulk piezoelectric elements. This leads to costly sensors, unsuitable for use in continuous monitoring applications where the devices may need to be in situ for extended periods or even indefinitely.

Work has been carried out on the miniaturisation of AE devices through thin film technology. Thin film technology does have the potential to result in low cost, disposable devices but the devices produced lack the piezoelectric properties to be effective in detecting AE in many applications.

Another area in which there is a lack of knowledge is the integration of AE sensors with the structural element requiring monitoring. Direct integration is not possible with current AE monitoring technology in which the devices are mounted onto the component surface using a coupling agent. The use of a coupling agent and the need for a wear-plate to protect the piezoelectric element reduces the amplitude of the AE. Direct integration of the element onto the surface of the component is, therefore, of interest.

The need for a compromise between the high cost and lack of flexibility inherent with bulk devices and the poor detection properties of thin film devices has been identified. This can be achieved through the use of thick film manufacturing techniques to provide low cost, disposable AE devices which have the flexibility to be integrated with the structural element under observation, thus improving device performance.

Chapter 3

Methodology

3.1 Metrics

The need for a low cost device with the capability to fulfil the role of a compromise between bulk and thin film AE monitoring technology was established in the literature review carried out during this work. Thick film technology was identified as a solution to this need. The focus of this work was on the deposition and benchmark testing of thick film AE sensors. The development of thick film AE sensors required the use of manufacturing techniques which are described in this chapter.

To adequately assess the performance of the thick film devices in this work against each other, two key dimensionless figures of merit (FOM) were identified. The FOMs which were identified were the relative signal to noise (S/N) ratio (equation 3.1) and the ratio of relative maximum amplitude to the relative volume of the sensing element (A/V) (equation 3.3), compared to the commercial device used for benchmarking in each case. Direct comparison of the thick film devices in this work with each other was not possible due to the transmission media composition, dimensions and the transmission paths all varying in the tests carried out on each device. As such, the amplitude of the AE which was used for the calculation of both metrics also varied. Because of this the commercial devices were employed as a consistent benchmark to which the thick film devices could be compared.

$$FOM_{S/N} = \frac{\left(\frac{S_{MEMS}}{N_{MEMS}}\right)}{\left(\frac{S_{Commercial}}{N_{Commercial}}\right)} \tag{3.1}$$

(3.2)

$$FOM_{A/V} = \frac{\left(\frac{S_{MEMS}}{V_{MEMS}}\right)}{\left(\frac{S_{Commercial}}{V_{Commercial}}\right)} \tag{3.3}$$

Where "S" it the signal amplitude, "V" is the volume of the sensing element and N is the amplitude of noise in the signal.

The S/N ratio of the thick film relative to that of the commercial benchmark was chosen to assess the comparative ability of the thick film device to distinguish the AE from the background noise caused by external interference. The A/V ratio of the device under test relative to the A/V ratio of the commercial device employed for benchmarking was chosen to compensate for sensing element volume and variation in transmission media and paths when assessing the performance of the thick film sensors compared to each other.

3.2 Active Element Materials Production

The manufacture, deposition and poling of piezoelectric elements was vital to this work, as a poled piezoelectric material forms the active element of the AE sensing device. AE sensing devices have previously been manufactured using bulk and thin film technologies. Thick films between 1μm and 100μm thick are of interest as this technology provides a compromise between the properties of bulk and thin film materials. The thick films employed in this work require the production of PZT sol-gel which can then be used to manufacture a composite slurry through the addition of PZT powder. The film, which formed the active element, was then deposited by spin coating and patterned by powder blasting. The active element was poled by contact or corona poling. A description of these techniques are detailed below.

3.2.1 PZT Manufacture

A 1.1 molar PZT sol-gel was synthesised as described by Corker *et al.* [90]. The lead acetate solution was produced by refluxing 52.5g of lead acetate trihydrate (Fisher) with 30ml of 99.9wt% acetic acid (Fisher) for 3 hours at 120°C. Distillation was then carried out between 102°C and 104°C to remove the water.

The 2-ME solution was synthesised by mixing 27.328g of 76wt% zirconium propoxide (Aldrich), 17.685g of 99.99wt% of titanium isopropoxide (Aldrich), 0.629g of 98wt% niobium (V) ethoxide (Inorgtech), 0.508g of antimony (III) ethoxide (Inorgtech) and 0.342g of 98wt% of manganese (III) acetate (Aldrich) with 50ml of 99.8wt% 2-ME (Aldrich) under a nitrogen atmosphere. The 2-ME solution was then refluxed for 3 hours at 120°C under a nitrogen atmosphere.

The lead acetate solution and the 2-ME solution were mixed by refluxing at 120°C for 3 hours under a nitrogen atmosphere. A distillation phase was carried out to remove by-products and to stabilise the solution. The distillation was carried out under nitrogen with heat being increased steadily to 84°C to remove the alcohol from the solution.

Once the alcohol had been removed the temperature was increased to between 102°C and 104°C to remove the water from the solution. This water removal distillation phase was continued until the cloudy solution became clear and then for 30 minutes longer before the heat was removed. Once the solution had cooled 2-ME was added in the same volume as the waste product evolved during distillation resulting in a sol-gel capable of yielding PZT with a composition of $Pb_{1.1}[Nb_{0.015}Sb_{0.015}Mn_{0.015}Ti_{0.472}Zr_{0.481}]O_3$. 5g of ethylene glycol was added to the solution which was then passed through a 0.5μm filter.

PZT sol was prepared for use in infiltrating PZT thick films to increase the density of the film. The infiltration sol was prepared by diluting the manufactured PZT sol-gel with 2-ME in a 1:1 volume ratio.

3.2.1.1 PZT Slurry Production

The PZT slurry utilised in the manufacture of the thick film PZT films was a suspension of PZT powder. PZ26 PZT powder was supplied by Ferroperm Ltd. 0.3105g of Cu_2O and 1.926g of PbO were used as sintering aids and added to 45g of PZ26. 0.9g of KR55 (Ken-React Lica 38, isopropanol isooctyl-alcohol) and 30ml of the PZT sol were added to the PZ26 and sintering aids under a nitrogen atmosphere. The slurry was then ball milled for 24 hours in preparation for deposition. A process flow diagram for the production of PZT sol-gel and slurry is presented in figure 3.1.

3.3 PZT Deposition Techniques

Once produced the PZT was deposited onto a substrate material in order to form a thick film which was used as an active element in the MEMS AE sensors. The substrate was cleaned prior to the deposition of the PZT which was commonly carried out using a spin coating method before film patterning, sintering and poling were conducted.

3.3.1 Substrate Cleaning

The adhesion of deposited PZT films to the substrate was known to be influenced by the cleanliness of the substrate surface. As such a standard substrate cleaning procedure was developed. The substrate material was placed in a solution of washing-up liquid and warm water in an ultrasonic (US) bath for 5 minutes to remove grease from the surface of the substrate. The substrate was then washed clean using de-ionised water before being placed in acetone in a US bath for 5 minutes. The substrate was removed from the acetone before being placed in IPA in a US bath for a further 5 minutes. The substrate was then removed from the IPA and dried using a flow of nitrogen.

Immediately prior to the deposition of PZT the substrate was placed in a Polaron PT7160 RF plasma barrel etcher for 3 minutes at 12W in a 1:4 mix of O_2 to Ar to remove residual organics from the surface of the substrate. Following barrel etch-

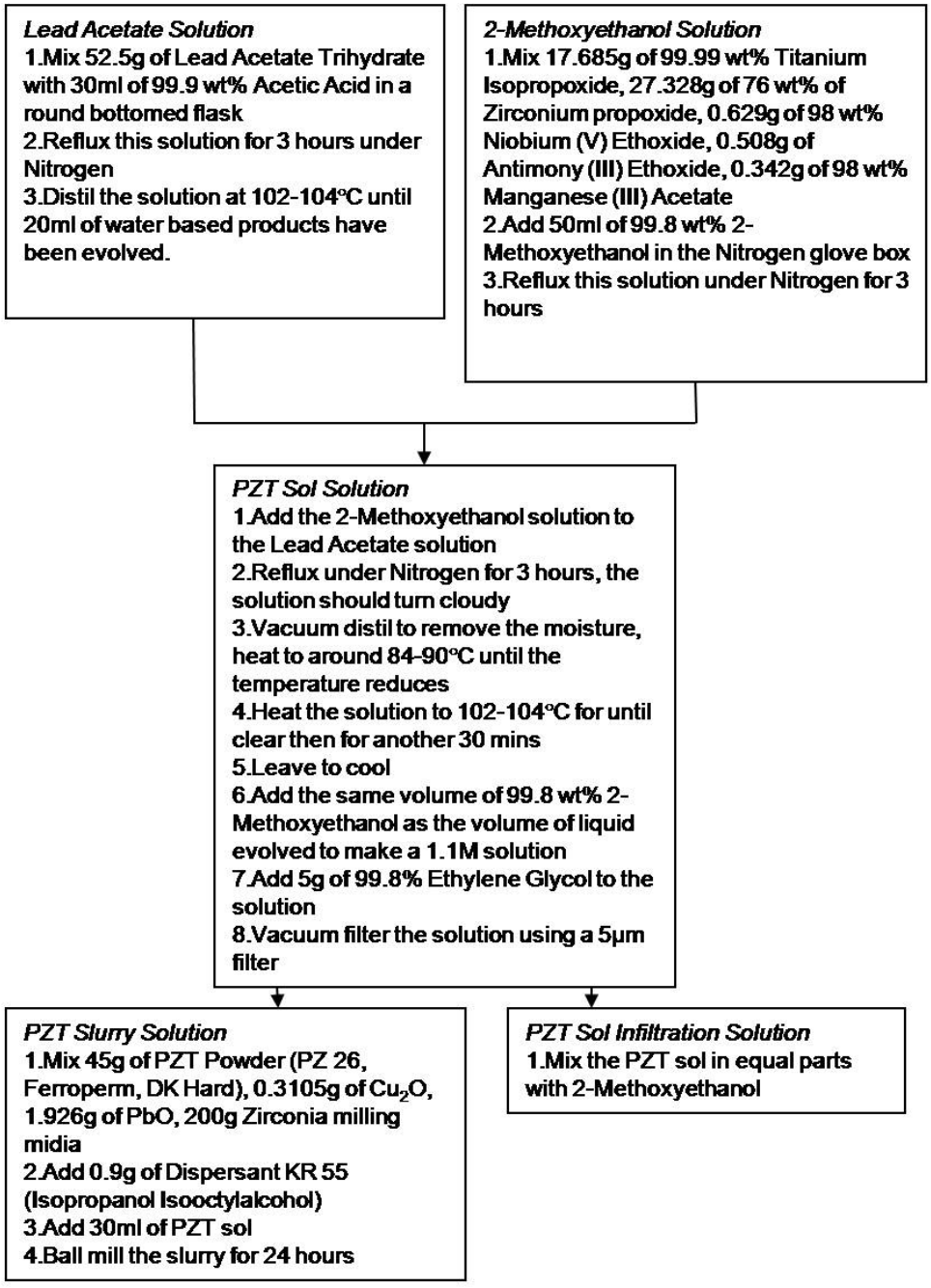

Figure 3.1: Process flow diagram for the production of PZT sol-gel and slurry for use in the manufacture of composite PZT thick films.

ing the surface of the substrate was further cleaned by spraying acetone and IPA onto the substrate whilst the substrate is rotating on the spin coater at 2000rpm. The substrate was then dried on a hotplate at 200°C to evaporate off the solvent.

3.3.2 Spin Coating

Spin coating was carried out on a Cookson spin coater in a clean room environment. The substrate was placed on a chuck and a vacuum was employed to secure the substrate during spinning, it was important to employ a chuck size smaller than that of the substrate to ensure that the liquid being deposited was not sucked into the vacuum system. Sufficient PZT slurry was deposited onto the substrate by pipette to cover 3/4 of the substrate surface area. This was then spun, dried and pyrolysed to form one "C" layer in the x(yC+zS) system. The sol infiltrations which form the "S" component of that system were deposited by dripping sol onto the surface of the deposited slurry layer by syringe through a 0.2μm filter. The sample was then spun, dried and pyrolysed; this process was repeated until the desired film composition had been attained.

Acceleration to full spin speed was carried out over 0.5s. The maximum spin speed employed was dependant on the desired final film thickness, 2000rpm and 3000rpm resulted in PZT thickness of 2.2μm and 1.7μm per composite slurry layer respectively. Deceleration from the maximum spin speed to standing was carried out over 1s. Once the spinning process had been completed the film was dried at 200°C for 60s and then pyrolysed at 450°C for 30s. The substrate was then left to cool before subsequent layers were spun onto the substrate. Once the desired number of layers had been deposited the film was placed in a furnace and sintered at 720°C for 20mins. A heating ramp rate may be employed if required.

3.4 Film Patterning and Electrode Deposition

Film patterning and electrode deposition were required following the deposition of PZT thick films by spin coating to form functional MEMS devices. Low cost methods of patterning were employed in this work to reduce the final cost of the resultant AE devices.

Film patterning was required to remove the excess PZT from the substrate around the active element. Film patterning in this work was carried out by powder blasting using 50μm alumina powder, the impact of the alumina powder on the surface of the PZT causes micro-cracks which link causing the PZT to break away. The film area which required protecting was coated with a self adhesive poly-vinyl layer which was removed following the powder blasting process.

Electrode deposition was carried out by two different methods depending on the composition of the desired electrode. The film was masked with a shadow mask. Electrodes which were deposited before film sintering, such as blanket bottom electrodes, were required to withstand temperatures over 720°C, Ti/Pt electrodes were employed for this application. Ti/Pt electrodes were deposited by Nordiko RF sputtering. The standard thickness of deposited electrodes was 8nm Ti and 100nm Pt. The Ti acted as an adhesion layer, ensuring that there was adequate adhesion between the platinum layer and the substrate material.

Electrodes which were not exposed to the sintering process were composed of Cr/Au. Cr/Au electrodes were deposited by evaporation in an Edwards E480 evaporator. Evaporation is a lower cost process than sputtering and as such was employed when possible. A standard Cr/Au electrode thickness was 10nm Cr and 50nm of Au. In this case Cr was used as the adhesion layer to ensure that the Au was well adhered to the PZT film.

3.5 Silicon Substrate Removal

Silicon was employed as a sacrificial substrate for the release of MEMS AE devices. The deposition and processing of PZT films onto silicon substrates is very well understood and there are also several methods facilitating the removal of silicon, including chemical wet etch and DRIE.

3.5.1 Chemical Wet Etching

Chemical wet etching of silicon is well understood and the etchants employed in this work were potassium hydroxide (KOH) and tetra-methyl ammonium hydroxide (TMAH). Prior to etching, a 17.6μm thick PZT film was deposited onto a cleaned, platinised silicon wafer by spin coating. 2mm diameter Cr/Au electrodes were deposited by evaporation. The PZT film was masked using DET466 photoresist then selectively exposed to a UV source for 84 seconds at an intensity of 12mW/m^2. Excess PZT was removed by etching in 0.5%/4.5% volume HF/HCl. The photoresist mask was subsequently removed using sodium hydroxide.

The patterned PZT sample was protected from the etchant employed in removal of the silicon film by the application of an epoxy backing. This epoxy backing also acted as a structural support for the film once the silicon substrate had been removed. The silicon oxide layer was mechanically removed from the bottom of the sample to speed the etch process as the etch rate of silicon oxide etch rate is several orders of magnitude slower than that of silicon. The sample was suspended in 38% KOH solution at 70°C for 3 hours. The KOH attacked the epoxy backing, reducing the backing structural integrity and resulted in the loss of the sample into the etchant.

A second sample was prepared using black wax to protect the epoxy backing from damage caused by the etchant. The black wax protected sample was suspended in the KOH as described above. The black wax successfully prevented degradation of the epoxy backing. The etchant attacked the silicon. This led to removal of the silicon undercutting the black wax and the epoxy (figure 3.2). The undercutting resulted in the silicon and PZT being attached to the epoxy backing by the top surface of the PZT alone. The epoxy was attacked by the etchant, damaging the structural integrity of the epoxy backing and reducing the adherence between the PZT and the epoxy. The excitation of the etchant caused movement in the silicon which pulled the substrate away from the epoxy backing.

The PZT was adhered to the silicon more strongly than to the epoxy and as such the PZT came away with the silicon and was lost into the etchant. The etch process did not reduce the adhesion between the silicon and the PZT due to the presence of reaction sites [113] where the PZT had reacted with the silicon wafer during processing. Combined with the presence of silicon oxide which was etched

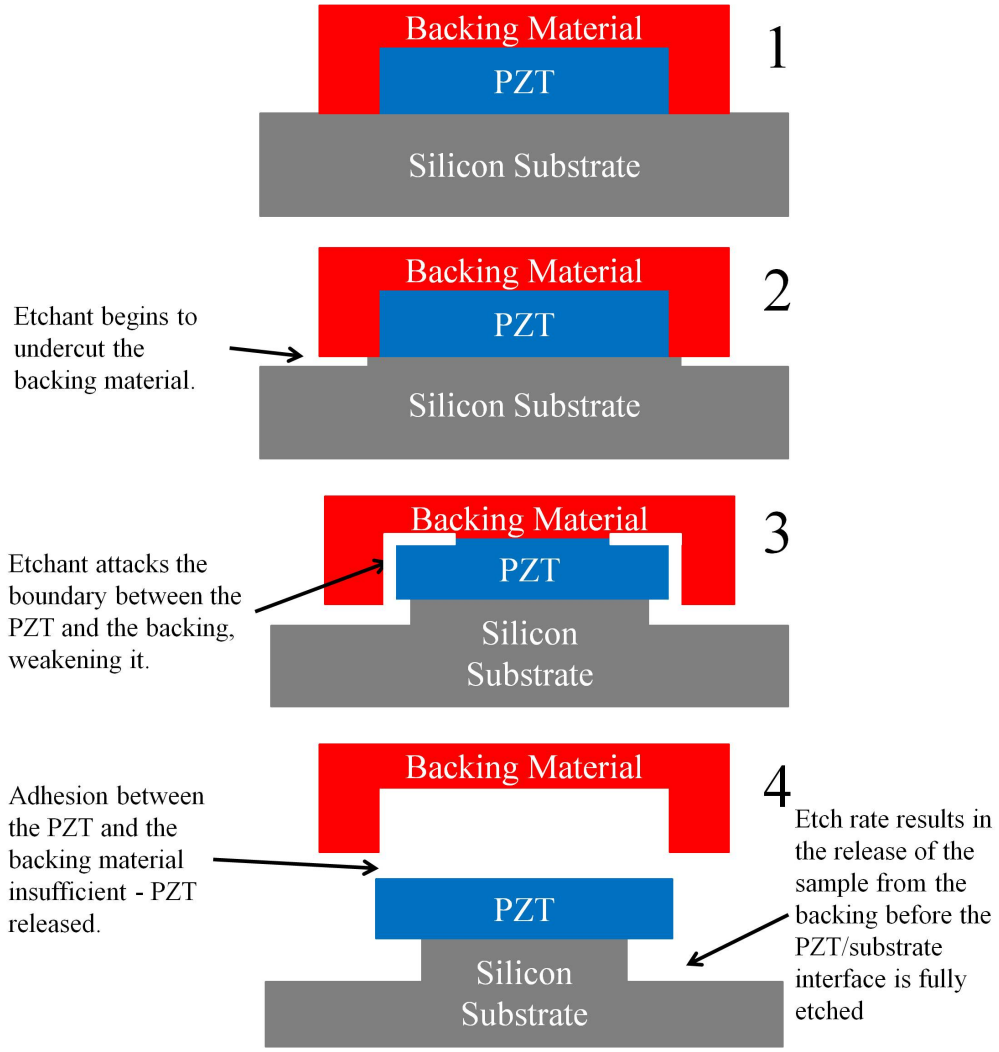

Figure 3.2: Schematic showing the undercutting between the protective backing layer and the substrate.

two orders of magnitude slower by KOH [121], the etchant was unable to remove the substrate layer adhered to the PZT before the substrate broke away from the epoxy backing, destroying the PZT film in the process.

TMAH was employed as an etchant in place of KOH. TMAH was not a harsh etchant and did not attack the interface between the epoxy and the PZT as KOH. 12.5% TMAH was heated to 60°C and the sample was suspended in the etchant. The etchant did not damage the epoxy backing and undercutting between the substrate and the epoxy backing was minimal. One disadvantage of this etch process was that the etch rate was slow and the removal of the silicon substrate was an impractically slow process. The lengthy nature of the process was exacerbated by the need to continually re-seat the sample in the black wax protecting the epoxy backing.

3.5.2 Deep Reactive Ion Etching

DRIE is a common method employed in the micro-machining of silicon. DRIE can be employed to selectively etch through the silicon substrate below the sample to be released. The process has good etch selectivity which ensures that only the silicon is removed and the PZT is not damaged. A process flow diagram for the DRIE process is shown in figure 3.3.

A 17.6μm thick 4(2C+5S) PZT film was deposited by spin coating onto the surface of a platinised silicon wafer cleaned using the standard method. The film was masked using AZ4562 photoresist (Clariant, UK) and selectively exposed to 12mW/m^2 UV light. An 8nm/100nm Ti/Pt top electrode was deposited by sputtering. The electrode areas were masked using a self-adhesive polymer film and the PZT around the electrode area was removed. The film, following the mask removal, is shown in figure 3.4.

The PZT was coated with two layers of AZ4562 photoresist which was used to adhere a backing wafer to the sample for the purposes of cooling during the etch process. The photoresist was spun onto the film surface and the backing wafer placed on the photoresist layer. The photoresist was then dried. The bottom of the sample wafer was coated with a 21μm thick layer of AZ4562 photoresist. The resist was selectively exposed for 90s, using a mask matched to the electrode mask

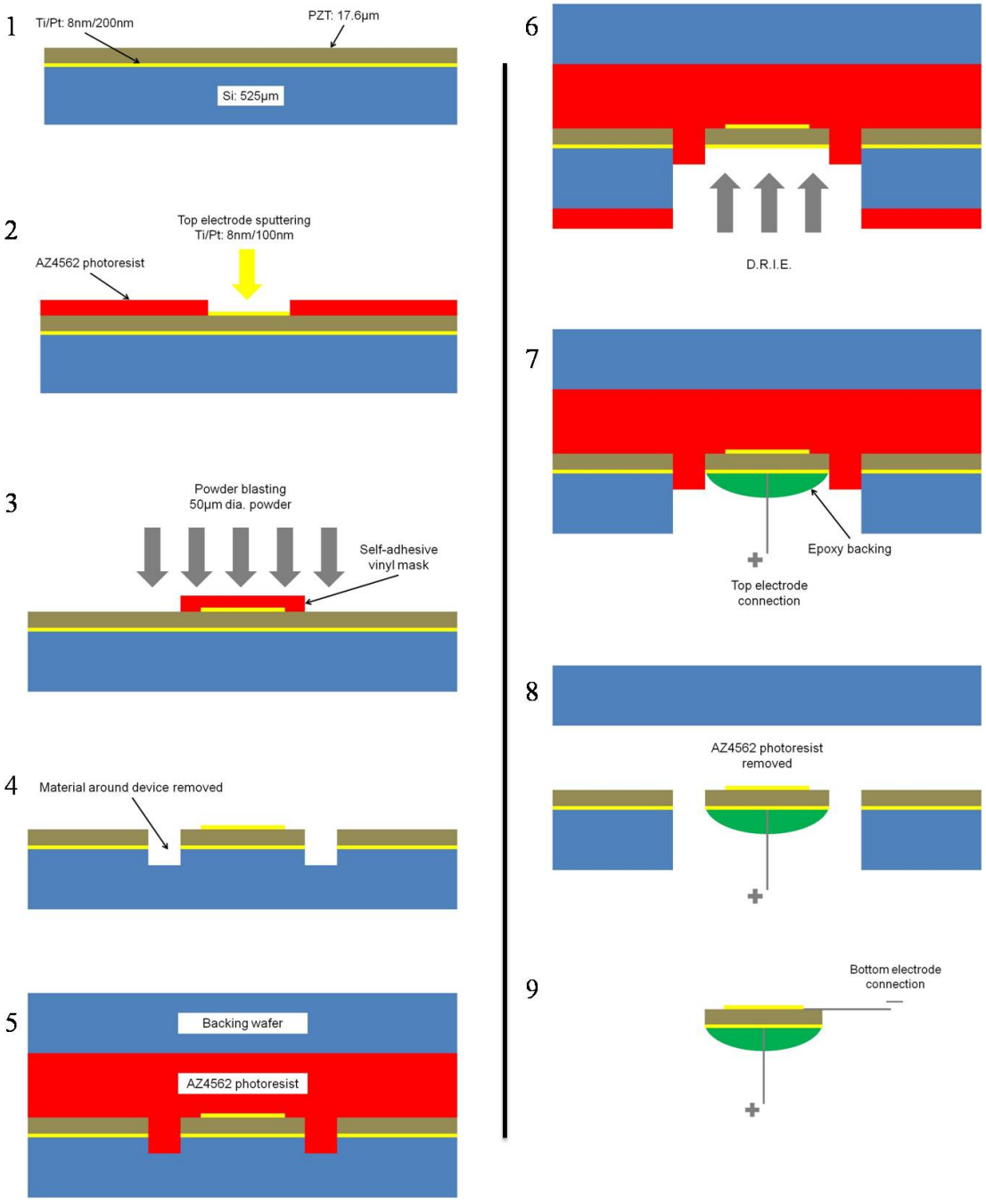

Figure 3.3: Process flow diagram of the release of PZT devices by DRIE etching of silicon.

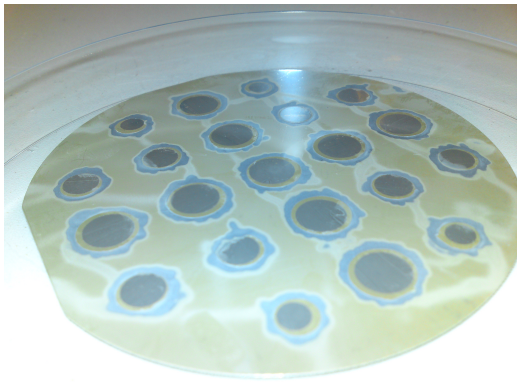

Figure 3.4: Image showing the top surface of the PZT film on silicon following the deposition of top electrodes by sputtering and the patterning of the PZT film.

employed for the top electrodes, to 12mW/m^2 UV light before being developed.

The silicon was etched by DRIE for 95 minutes to remove all silicon. The automatic pressure controller was set to 65.8%. Alternating etch and passivation cycles were used. The etch cycle was 130sccm SF_6 and 13sccm O_2 with a coil and platen power of 600W and 15W respectively for a 13s duration. The passivation cycle was 85sccm of C_4F_8 with a coil power of 600W for an 8s duration.

The DRIE etch process successfully removed the silicon substrate from the rear of the samples (figure 3.5). Several of the samples, which were insufficiently adhered to the backing wafer, came away from the wafer resulting in free 17.6μm thick PZT discs with top and bottom electrodes. The top electrodes of these discs were coated in a layer of baked photoresist used to adhere the film to the backing wafer as shown in figure 3.6.

The photoresist covered sample was immersed in acetone to remove the photoresist. The separated 17.6μm thick PZT was unable to survive the process required in the removal of the photoresist and fractured during the removal process. A released sample was backed with epoxy to act as a structural support during photoresist removal. Despite immersion in acetone for an hour the acetone was unable to remove the photoresist.

The removal of the baked photoresist coating the top electrode of the sample was problematic as the high temperature baking of the photoresist which occurred during the DRIE process and created cross-bonds in the material which resulted

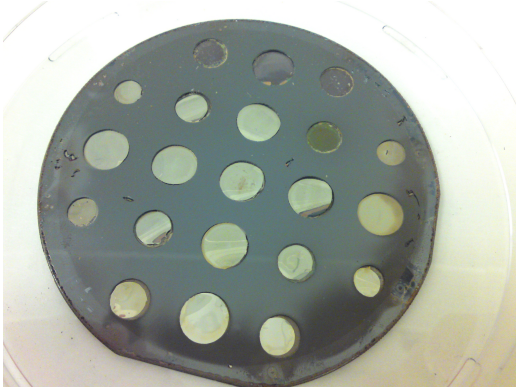

Figure 3.5: Image showing the rear of the PZT wafer following the selective removal of silicon by DRIE. The back surface of the PZT film can be seen where the silicon has been etched to reveal the shiny platinised bottom electrode. It can also be seen that four of the free PZT disks had come away from the backing wafer.

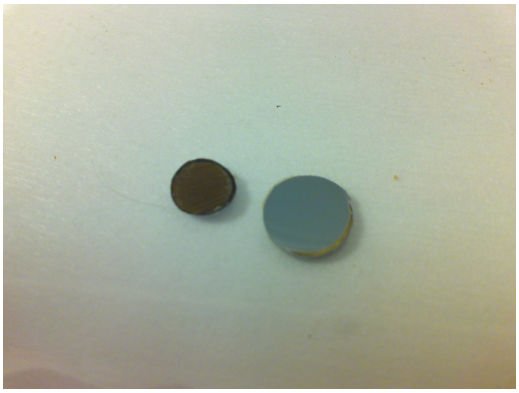

Figure 3.6: Image showing the top (left) and bottom (right) of the PZT disks released from the silicon substrate by DRIE. The persistence of photoresist on the top electrode can be seen.

in the photoresist being resistant to removal by acetone. N-Methylpyrrolidone (NMP) was employed in the removal of the photoresist on the surface of the top electrode. The sample was immersed in NMP for 2 minutes at 70°C. The epoxy was destroyed by this exposure and the PZT became detached from the backing and fractured in the etchant.

The remaining fragments of PZT showed a persistence of photoresist on the top surface of the film. The exposure time required to remove photoresist baked to the surface in this fashion was known to be 8 hours. For the sample to survive in the NMP solution long enough for the photoresist to be removed the sample would have to be reseated in a backing material repeatedly. This reseating of the fragile PZT samples would be impractical and would result in the destruction of the samples.

3.6 Poling

Once a thick film had been manufactured, patterned and electrodes had been deposited; poling was required to produce a functional MEMS device. Poling was carried out by two methods; contact and corona. Contact poling was carried out by heating the sample to 130°C. Once the sample had reached the required temperature, spring-loaded probes were placed in contact with the top and bottom electrodes. A field of 4V/μm was applied across the thick film for 10mins. The sample was then cooled to below 75°C whilst still under electric field.

When films were fragile and at risk of being damaged by the spring-loaded probes employed in contact poling, corona poling was employed. Corona poling was carried out by heating the sample to 130°C. Electrical connections were made to the bottom electrode and a pin suspended 25mm above the top electrode of the sample. Masking was employed to ensure that there was no shorting between the pin and the bottom electrode. A corona poling set up can be seen in figure 3.7. A field of 16kV was applied between the pin and the bottom electrode for 15 minutes. The sample was then cooled to below 75°C under field. The pin to sample separation and the field strength can be varied depending on the individual sample poling requirements.

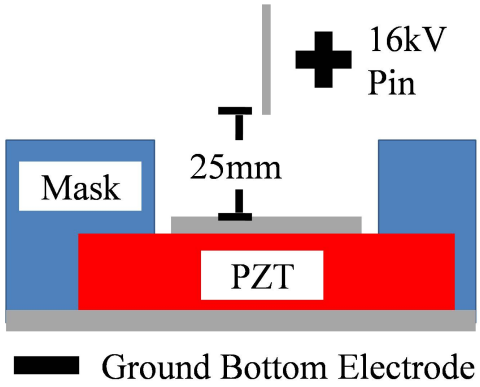

Figure 3.7: Schematic showing a corona poling set up.

3.7 Electrical Characterisation

Characterisation of the electrical properties of the film was carried out both before and after poling. The d_{33} of the film was measured using a Berlincourt type PM25 Piezometer System. It was important to ensure that electrical contact was made between the electrodes and the Berlincourt probes, conductive paint was employed to make a contact between the bottom probe of the Berlincourt and the bottom electrode.

A Wayne Kerr Precision Component Analyser 6425 was employed, with a probe station providing the electrical connection to the electrodes, to measure the ϵ_r, resistance and loss of the film. Measurement was carried out at 1kHz. Impedance measurements between 50kHz and 2MHz were also carried out on samples using a Hewlett-Packard 4192A LF impedance analyser.

3.8 AE Testing

AE devices, which had been poled and characterised, were employed in AE benchmarking tests against PICO or WD sensors from Physical Acoustics Corporation (PAC). The PICO sensor was a single element micro-sensor with a small piezoelectric element and the WD sensor was of a differential design. Impedance testing was carried out on the PICO and WD sensors, the resultant plots are shown in figure 3.8. There was a peak in the PICO sensor response between 450kHz and 600kHz. This peak impedance response was a characteristic of the PICO device and as such the PICO device was suitable as a resonant sensor. The

WD sensor was suitable as a wideband device with a frequency band of 100kHz-1MHz

The MEMS AE device and the commercial AE sensor from PAC to be used for benchmarking were mounted on a metal plate using grease as a coupling agent. A mass of 113 grammes was employed to ensure a good contact between the sensor and the substrate material. The sensors were connected to 2/4/6 pre-amplifiers from PAC enabling pre-amplification of the signal by 20dB, 40dB or 60dB. The pre-amplifiers were connected to a data-logger. AEWin and MI-TRA data-logging programmes from PAC were employed in this work with variable filters and sampling rates.

Hsu-Neilson testing was carried out at a position on the metal plate equidistant from the MEMS and commercial AE sensor. The Hsu-Neilson test involves the fracture of a 0.5mm diameter 2H pencil lead to generate a simulated AE [56]. Multiple Hsu-Neilson pencil breaks were carried out to reduce errors in benchmarking each device.

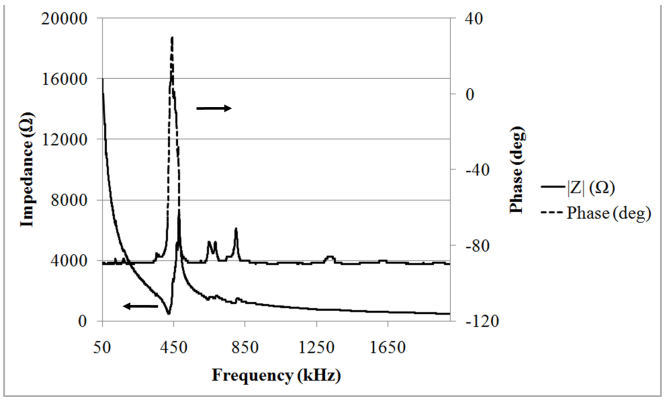

(a)

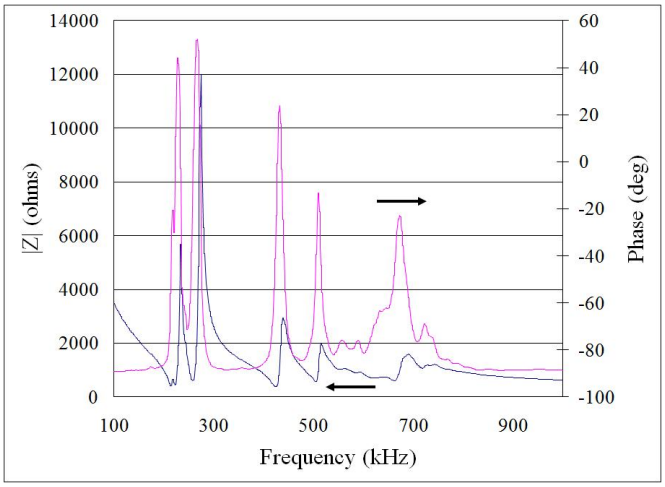

(b)

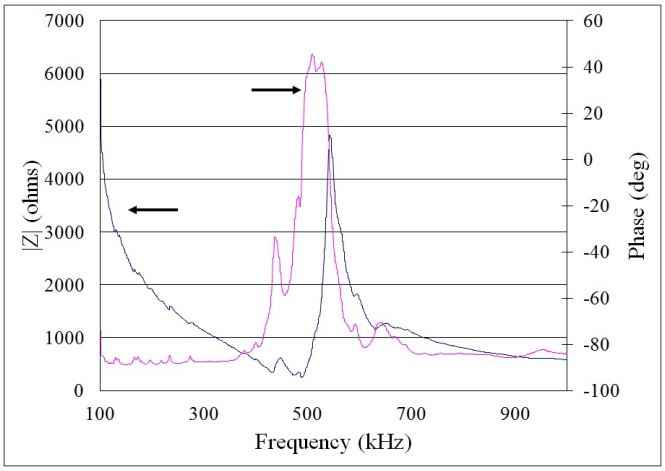

(c)

Figure 3.8: Plots showing the measured impedance and phase angle of the PICO commercial sensor (a), the WD measured between the pin of the dual BNC connector and the common electrode (b) and the WD measured between the hole of the dual BNC connector and the common electrode (c).

Chapter 4

Thick Film AE Sensor Validation Testing

Thick film technology provides a compromise between the superior material properties of bulk piezoelectric materials and the flexibility of MEMS processing. As such, the use of thick film technology in the development of MEMS AE devices was an area of interest. Initial testing work was carried out to assess the viability of using thick film PZT as an AE sensing element.

Pre-prepared PZT thick film devices on silicon substrates were employed in the initial testing work. The experimental work carried out at this stage was for concept proof only and as such the devices and techniques employed for AE stimulation were relatively crude. The aim of the initial work was to validate the ability of the thick film PZT to detect simulated AE and to confirm the potential of thick film PZT for AE monitoring applications.

The thick film sensing elements used in the initial work consisted of a 10μm thick PZT film deposited onto a 525μm thick silicon wafer with a blanket bottom electrode. The 1mm diameter active element was found to have a ϵ_r and measured loss of 1150 and 0.016 respectively. The d_{33} was measured at 40pC/N.

4.1 Acoustic Emission Testing

The PZT thick film device was benchmarked against a WD sensor from PAC. The WD sensor was of a differential design, widely used for dynamic applications with a specified frequency band of 100kHz-1MHz. Impedance sweeps were carried out on both elements of the WD sensor and the impedance and phase angle plots of these elements can be seen in figure 4.1. The impedance and phase angle plots taken between the dual BNC pin and the common electrode can be seen in figure 4.1a.

From these plots it can be seen that this WD sensing element had a maximum amplitude response to signals at 263kHz, high amplitude response to frequencies of 220kHz, 425kHz, 509kHz and 668kHz was also observed. Impedance and phase angle plots are shown in figure 4.1b, which were taken between the dual BNC connector hole and the common electrode. A peak amplitude response for this element can be seen at a frequency of 540kHz. The remainder of the sweep showed a relatively flat frequency response, with a minima at 488kHz.

Both sensors were mounted on the surface of a wood/polymer composite, high attenuation transmission medium. The silicon substrate of the thick film device and the wear plate of the WD sensor were coated in grease and held onto the transmission medium by a mass of 0.02kg, care was taken to ensure an even coupling layer.

Contact was made to both the top and bottom electrode of the thick film by spring loaded probes. A co-axial cable was employed to connect the probes to an oscilloscope for the initial testing of the thick film device. A simulated AE signal was generated by impacting a metal hammer onto the transmission medium. The signal detected by the oscilloscope was a classic transient waveform behaviour indicating that the thick film device was capable of detecting AE. A 50Hz electrical noise signal was detected, with the co-axial cable and probes acting as an aerial. The electrical noise signal amplitude was sizeable and increased with movement of the probes. The noise caused by movement of the probes resulted from a current induced in each probe as it was moved through the Electro-Magnetic (EM) field of the other probe.

Once the thick film device had been validated by use of the oscilloscope, benchmarking was carried out by comparing the response of the thick film device and

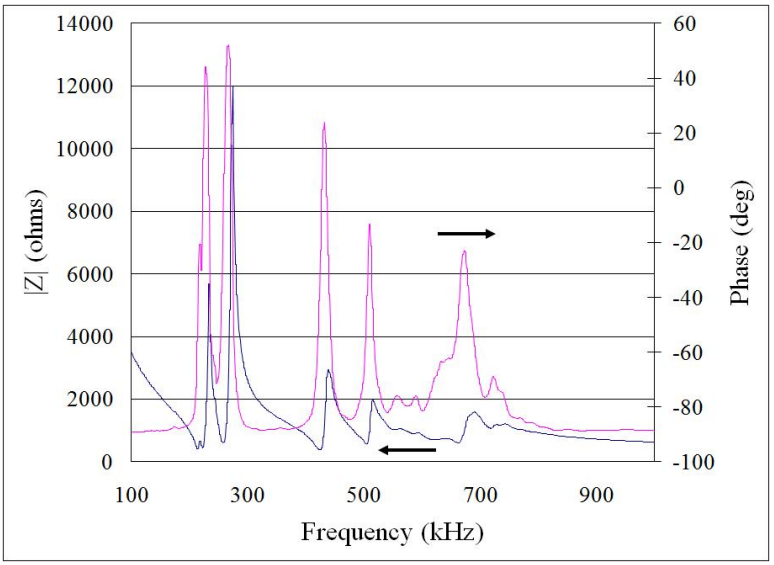

(a)

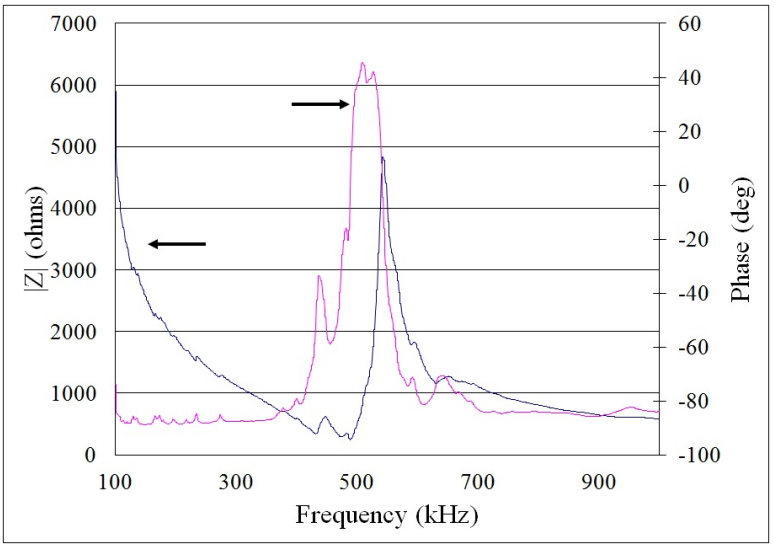

(b)

Figure 4.1: Impedance and phase angle plots between 100kHz and 1MHz of the WD commercial sensor between (a) the pin of the BNC connector and the common electrode and (b) the hole of the BNC connector and the common electrode.

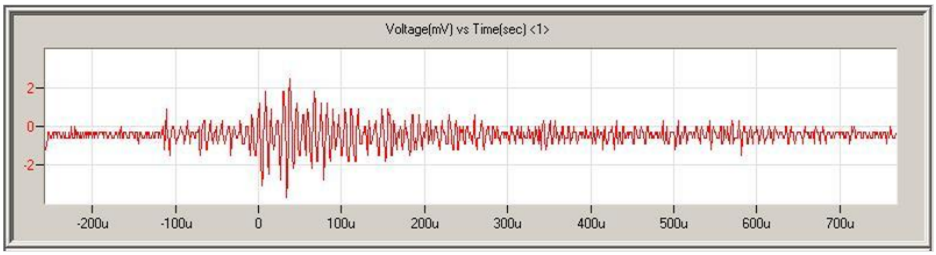

(a)

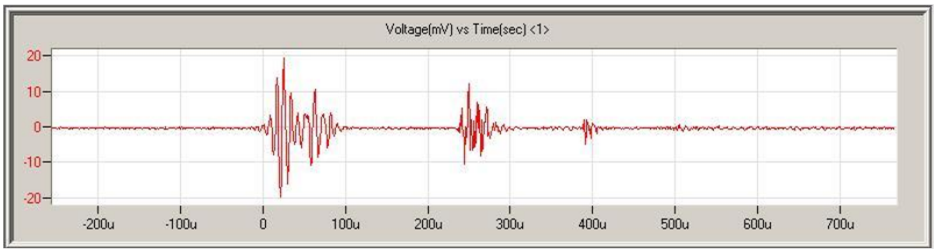

(b)

Figure 4.2: AE time domain waveforms emitted by (a) the thick film device and (b) the WD commercial sensor following emission stimulation in a high attenuation substrate material

the WD sensor to simulated AE. The detected signal was pre-amplified using a 2/4/6 pre-amplifier before being logged by AEWin data logging software from PAC. A pre-amplification of 40dB was employed for both devices with no internal gain. A threshold value of 25dB was used. Several AE events were simulated in the same fashion used previously. Representative time domain plots from the thick film sensor are shown in figures 4.2a and 4.3a and representative plots from the WD sensor are shown in figures 4.2b and 4.3b.

4.2 Discussion and Conclusions

The time domain plot from the WD sensors in figures 4.2b and 4.3b showed that the signal generated by the impact of the metal hammer resulted in several transient signals, this was due to the hammer bouncing upon impact with the surface and therefore generating multiple AE. These bounces were not observed in the time domain plots from the thick film sensors in figures 4.2a and 4.3a. This was due to the poor sensitivity of the thick film device coupled with a low signal to noise ratio.

The thick film sensor detected the AE before the WD sensor due to a the higher

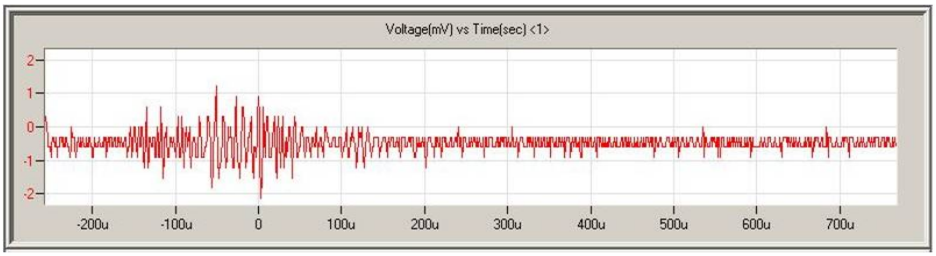

(a)

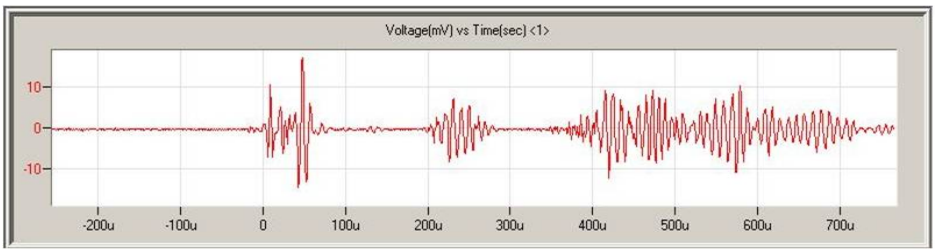

(b)

Figure 4.3: AE time domain waveforms emitted by (a) the thick film device and (b) the WD commercial sensor following emission stimulation in a high attenuation substrate material

relative d_{31} of the thick film PZT compared to the bulk PZT element in the commercial device. The improved d_{31} resulted in the thick film sensor being more sensitive to the faster propagating extensional component of the AE. The amplitude of the extensional component of AE detected by the thick film device was not sufficient to cross the threshold level and trigger the data-logging software. This resulted in a sizeable proportion of the AE signal detected by the thick film device being detected before the zero second mark in the time domain plots.

It was clear from the time domain plots that the output signal from the thick film device exhibits an amplitude an order of magnitude lower than that from the commercial WD sensor. The amplitude of the signal was reduced by attenuation before it activated the piezoelectric element. The effect was more apparent in the commercial sensor. This was caused by a mismatch in the acoustic impedance between the coupling layer, the wear plate and the element itself.

Table 4.1: Table showing the acoustic impedance values of materials employed in the benchmarking of MEMS AE devices.

Material	Mild Steel	Silicone Grease	Silicon	Alumina	PZT
Acoustic Impedance (MRayls)	46.0	~ 1.0	19.6	40.6	32.6

From the values the acoustic impedance values in table 4.1, the percentage of signal amplitude transmitted from the structural element to the PZT element was calculated. It was found that 0.0144% of the AE signal amplitude was transmitted to the MEMS element. Only 0.0077% of the AE signal amplitude was transmitted to the commercial device element. Despite the superior transmission of acoustic energy between the structural element and the thick film sensor, a lower signal to noise ratio was apparent.

There are several reasons for the lower amplitude and therefore lower signal to noise ratio. The thick film device had a thinner active element than the bulk commercial sensor, this resulted in a lower voltage output. The piezoelectric properties of the thick film material were also much lower than that of the bulk material in the commercial device, a d_{33} of 40pC/N compared to 330pC/N for bulk materials such as PZ26 from Ferroperm [132], due to the stresses induced in the films resulting from shrinkage during drying, pyrolysing and sintering, and the constraining effects of the silicon substrate.

These effects caused the amplitude of the signal emitted by the thick film sensor to be lower than that emitted by the commercial device. The commercial device was of a differential design which reduced the effects of electrical noise, thus further improving the signal to noise ratio. The commercial sensor also has a matched backing layer, which reduced reflections from the top surface of the active element. The backing layer also affects the ring down properties of the device, reducing ringing considerably. For these reasons it was unsurprising that the signal from the thick film device was poor when compared to the commercial sensor.

The FOMs employed for the assessment of device performance in this work were calculated for the thick film on silicon sensor. The relative S/N ratio and the relative A/V ratio were calculated to be 7 and 914×10^3 respectively. The low volume of the device compared to the commercial sensor employed resulted in a very high relative A/V ratio. The relative S/N ratio was low, however this FOM was skewed by the high noise amplitude in the WD signal and the wideband nature of the WD sensor. These high noise amplitudes were a result of the suboptimal conditions under which testing was carried out and greatly reduced the effectiveness of this FOM in the assessment of the MEMS device.

Chapter 5

Embedded Thick Film PZT For Use In AE Sensing Applications

The integration of PZT with various substrate materials was important in the production of miniaturised, low cost AE devices. Device integration enables AE devices to be deposited directly onto the structural element requiring monitoring. This type of "embedded" sensor reduces signal attenuation and distortion as the waveform propagates from the transmission medium to the sensing element without passing through any other interfacial layers.

In this chapter the deposition of a PZT thick film - between 1μm and 100μm thick - directly onto a structural element by a composite spin coating method is discussed. The electrical properties of the resultant embedded film are examined and the film is benchmarked against commercial AE devices. The embedding of thick film PZT onto a tungsten carbide/cobalt cutting tool is also presented.

5.1 Embedded Thick Film Sensors on a Kovar Test Plate

The initial testing phase of the work validated the application of thick film PZT for use as an AE sensing device. There were several issues with the device employed in the validation of MEMS AE sensors, many of which were common to many AE sensors. The transmission of the AE signal from the structural element,

through the coupling layer and the silicon substrate into the thick film active element theoretically reduced the signal amplitude by 98.4% due to the acoustic impedance mismatch between the layers through which the AE must travel. The direct integration of the embedded thick film element onto the structural element to be monitored resulted in the much smaller theoretical signal amplitude reduction of 1.4%. The embedding of the thick film element also reduced the distortion of the AE signal. As such the embedding of PZT onto a structural element was of great interest.

There were several factors limiting the integration of PZT directly onto a structural element. Polymer structural elements were largely incompatible with the 720°C sintering temperature required in thick film processing, this ruled out the integration of PZT with polymer components and so a metallic component was employed in this work.

There were also issues with integrating PZT and metallic substrates. The thermal expansion coefficient was much higher in metals than in the ceramic PZT; steel, copper and aluminium exhibit thermal expansion coefficients up to 200°C of $12x10^{-6}$/K, $18x10^{-6}$/K and $23x10^{-6}$/K [133] compared to a PZT thermal expansion coefficient of $\sim 6x10^{-6}$/K [130]. The sizeable differential between the thermal expansion coefficients of PZT and structural metals led to PZT film cracking during processing and a subsequent reduction of film properties.

Kovar was a glass sealing alloy typically composed of 29% Ni, 17% Co and a balance of Fe. The thermal expansion coefficient up to 200°C of Kovar was $6x10^{-6}$/K. This thermal expansion was much more closely matched to that of PZT and as such Kovar was an ideal substrate material for studying the effect of embedding sensors by direct integration.

5.1.1 Device Manufacture and Characterisation

A Kovar test plate was 100mm square and 3.2mm thick. A 4(2C+5S) PZT thick film was deposited onto the surface of the Kovar by spin coating. The substrate had a significantly larger mass than a standard silicon wafer. As such the heating times and temperatures during processing were adjusted accordingly. Drying and pyrolising were carried out for 3 minutes at 310°C and 60 seconds at 525°C. The

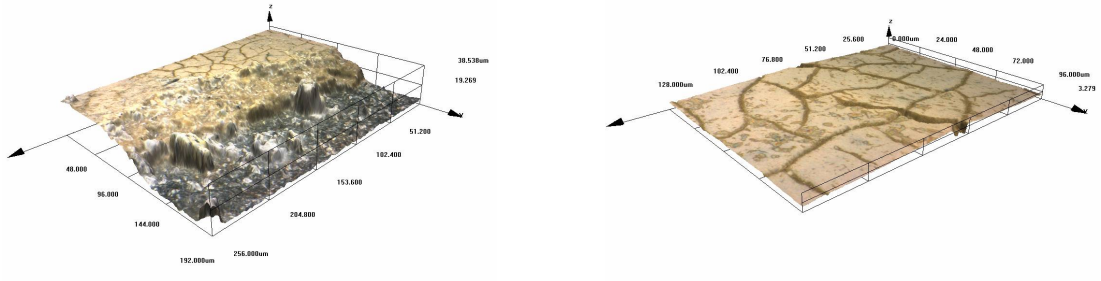

(a) (b)

Figure 5.1: Confocal laser scanning microscopy images of thick film PZT on a Kovar substrate showing (a) a 3D image of the edge of a PZT device following patterning by powder blasting and (b) a 3D image showing cracking on the surface of the PZT film.

PZT was sintered at 720°C for 20 minutes with a 5°C/min temperature ramp rate following deposition. The ramp rate was employed in an attempt to reduce the stress in the film caused by temperature gradients across the system.

The film was patterned and the Kovar substrate was used as the bottom electrode. The film thickness was measured using a confocal laser scanning microscope (figure 5.1) and was found to be 17.6μm. Figure 5.1a shows the damage caused to the edge of the PZT film during the removal of the material by powder blasting. The powder blasting removed the PZT but also caused some damage to the Kovar substrate material.

Cracking of the film surface was observed with crack depths up to 1.5μm (figure 5.1b). Each 1C layer in the 4(2C+5S) deposition had a thickness of 2.2μm, from this it was clear that the cracks had not propagated throughout the film thickness. This indicates that the film cracking was caused during the drying, pyrolysing and sintering stages. The active element was poled by corona poling. The active element was found to have a ϵ_r and a dielectric loss of 86.2 and 0.102 respectively. The d_{33} was measured to be 38pC/N. Impedance testing was carried out on the thick film device and the PAC PICO sensor it was to be benchmarked against and the resultant plots are shown in figure 5.2. The thick film device showed a capacitance response as expected. The thick film device is expected to exhibit a resonance response at a frequency of 247MHz. The resonance is calculated from the thickness of the film and the speed of sound in PZT - 4350m/s.

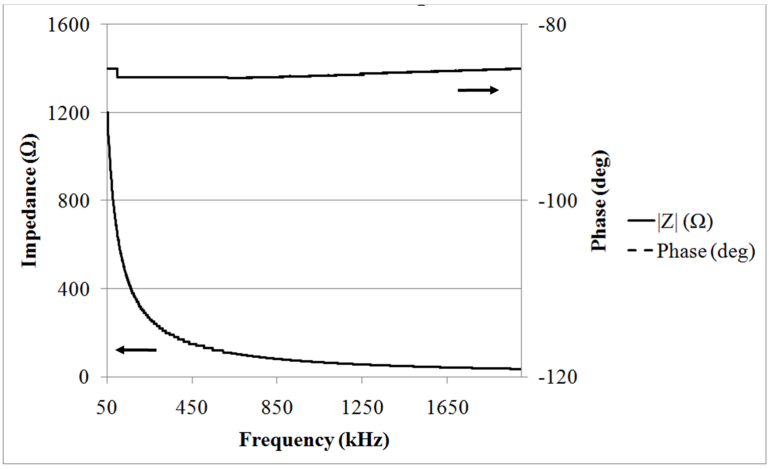

(a)

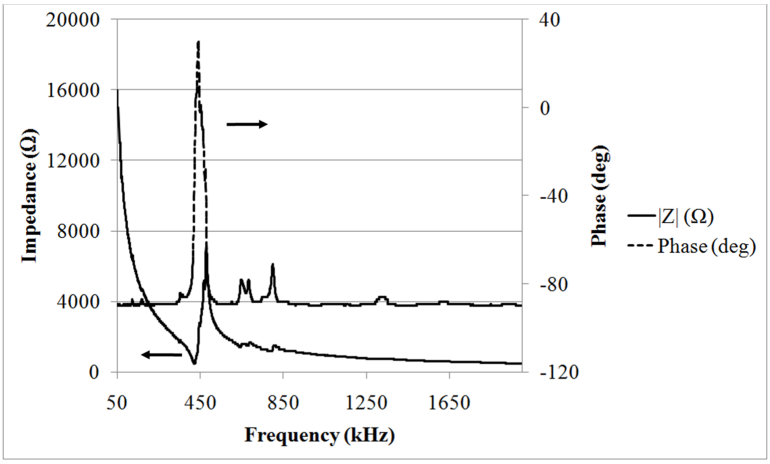

(b)

Figure 5.2: Impedance sweeps of (a) the thick film device and (b) the PICO sensor showing impedance and phase angle.

This resonance is outside the frequency range employed in AE testing. A peak in the response of the PICO sensor was observed between 450kHz and 600kHz. This peak in impedance response was a characteristic of the PICO device and due to this the PICO device was suited for use in a resonant sensor mode across this frequency range. This resulted in the PICO sensor demonstrating greater sensitivity to lower amplitude AE events.

The flat, capacitance-type, response of the thick film device made the thick film more suitable for the characterisation of the AE signal properties but causes a damping effect which reduced the effectiveness of the device in detecting low amplitude AE signals.

5.1.2 Acoustic Emission Testing

The PICO sensor employed was a micro-sensor produced by PAC, it was of a single element design. The PICO sensor was chosen for benchmarking purposes as it was a small device, employed in roles similar to those for which the MEMS AE sensors were designed. The PICO sensor was mounted on the same 64mm pitch circle diameter (PCD) as thick film device on the Kovar substrate. Grease was used as a coupling layer and the sensor was firmly pressed onto the Kovar.

Both sensors were connected to PAC 2/4/6 variable pre-amplifiers. The thick film device pre-amplifier was set to 60dB gain, while the PICO device gain was set at 40dB. Data gathering was carried out using MI-TRA, a commercial transient recorder-analyser system from PAC (2001). Signal filtering was carried out, filter levels were set with upper and lower limits of 100kHz and 1.2MHz. A sampling rate of 10MHz was employed. Hsu-Neilson testing was carried out to simulate AE. This involved a 2H pencil lead being broken at the central point of the sensor PCD. 15 simulations were carried out.

5.1.3 Results

A representative sample of test data from the tests carried out on the embedded thick film device and the PICO sensor are shown in table 5.1. Tests 1, 3, 4, 5 and 6 are representative of one type of response of the thick film and PICO sensors.

In these tests the rise time between 10% and 90% was 3.66μs longer in the thick film device than the PICO sensor, the standard deviation in the rise time variation was 0.33μs. Table 5.1 indicates that the maximum amplitude and the signal energy of the the thick film device were approximately 18.5 and 12 times lower than that of the PICO sensor respectively. The data also shows that there was greater ringing in the thick film device signal, measured as the duration the AE signal amplitude was above 10% of maximum amplitude, than the PICO sensor.

The time and frequency domain plots of representative AE signals detected by both the thick film and PICO sensors are shown in figure 5.3. In this figure the initial 500μs of the time domain is shown on the left and the frequency spectrum of the time domain signal, calculated by use of FFT, is shown on the right. The thick film signal is shown here above the signal detected by the PICO sensor.

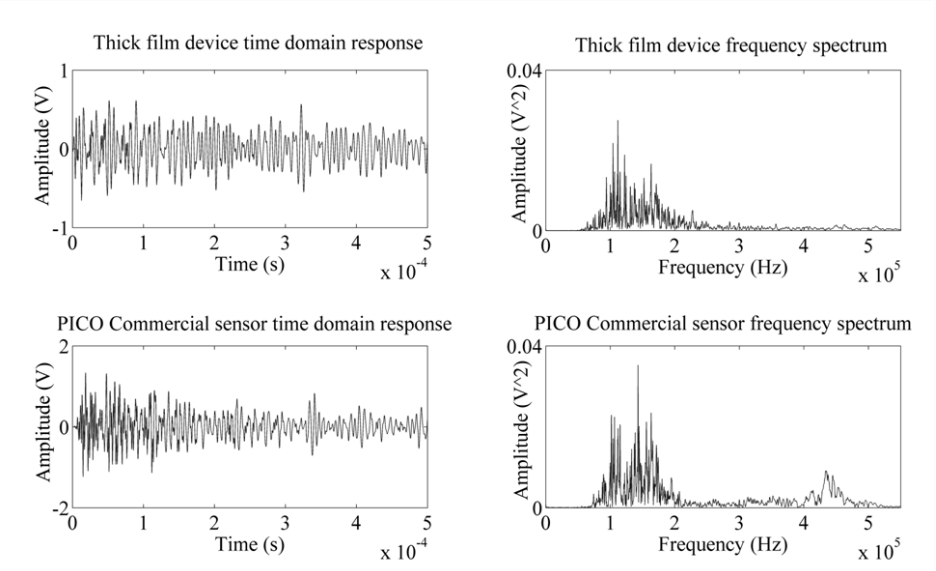

Figure 5.3: Plot showing the initial 500μs of the time domain (left) and frequency domain (right) signals detected by the thick film device (top) and the PICO commercial sensor (bottom). The signal to noise ratios of the thick film and commercial devices were 63.1 and 120.6 respectively.

Spectrograms of the initial 20μs of the time domain signals from the thick film and PICO sensor were calculated using AGU Vallen Wavelet software (release A2009.1027) from Vallen Systeme GmBH. The AGU Vallen Wavelet software operates on a Gabor transform with a transform window of 20μs. Vallen Systeme GmBH Vallen Dispersion software (release A2009.1027) was used to calculate dispersion curves for Lamb waves in the Kovar plate, based on the dimensions and physical properties of the plate material. These plots can be seen in figure

Table 5.1: Table showing representative responses of the thick film device and the PICO sensor to AE generated by Hsu-Neilson pencil lead breaks.

	Test Number	1	2	3	4	5	6	7
Thick Film	Peak amplitude (mV)	0.693	1.035	0.534	0.615	0.659	0.654	0.474
	Rise time (μs)	11.6	10.9	11.4	11.4	11.4	11.9	10.4
	Duration (ms)	2.055	2.806	1.983	2.626	2.007	1.996	2.001
PICO	Peak amplitude (mV)	12.842	17.042	10.352	11.866	11.866	13.379	8.301
	Rise time (μs)	7.9	11.9	7	7.8	8	8	11.8
	Duration (ms)	1.899	2.552	1.663	2.048	1.435	1.375	1.656
Differential between Thick Film and PICO devices	Peak amplitude (mV)	-12.149	-16.007	-9.818	-11.251	-11.207	-12.725	-7.827
	Rise time (μs)	3.7	-1	4.4	3.6	3.4	3.9	-1.4
	Duration (ms)	0.156	0.254	0.32	0.578	0.572	0.621	0.345

5.4.

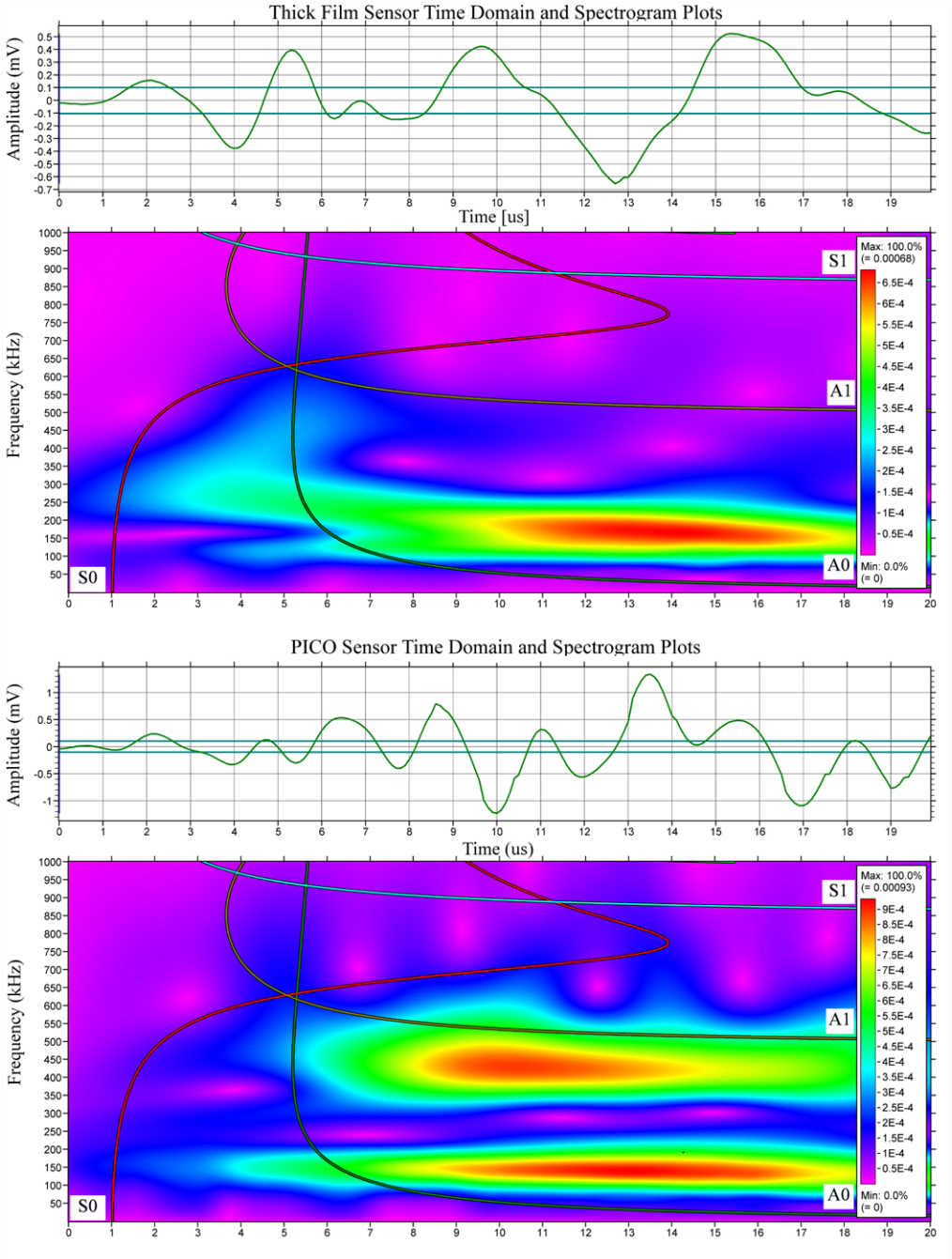

Figure 5.4: Gabor transform spectrograms of the initial 20μs of the time domain signal from the thick film device (top) and the PICO sensor (bottom) with overlaid zeroth and first order Lamb wave dispersion curves calculated using software from Vallen Systeme GmBH

The data from tests 2 and 7 (table 5.1) were unusual in that the PICO sensor showed a longer rise time than the thick film device. In these tests the response

of the thick film device was consistent with the thick film sensor responses from tests 1, 3, 4, 5 and 6. The response of the PICO device showed a dominance of A_0 rather than the A_1 as in the test data from tests 1, 3, 4, 5 and 6. An example of this can be seen in figure 5.5 which compares the Gabor transforms of tests 1 and 2 for both the thick film device and the PICO sensor.

5.1.4 Discussion and Conclusions

It is clear from figure 5.3 that there was a smaller high frequency component amplitude in the thick film device when compared to the PICO sensor. This observation was verified by the spectrogram of the time domain data for each sensor (figure 5.4). The maximum amplitude of the signal emitted by the thick film device resulted from the A_0 waveform. The spectrogram shows that the faster rise time in the signal emitted by the PICO sensor was caused by the interaction of the asymmetric first (A_1) order Lamb wave with the resonant sensitivity peak between 450kHz and 600kHz. This interaction was not present in the thick film device. The A_1 waveform arrived before the A_0 waveform, resulting in a shift in the peak amplitude of the signal. The time to 10% of maximum amplitude was not shifted and therefore the interaction of the PICO sensor with the A_1 wave component reduced the rise time.

The duration of the signal detected by the thick device was greater than that of the PICO sensor. This was explained by the lack of an acoustically matched backing material on the thick film devices. The top surface of the PZT element was in direct contact with the surrounding atmosphere and so the acoustic impedance differential was high causing a large degree of signal reflection. The acoustically matched backing material in the PICO sensor was of a suitable thickness and a small enough acoustic impedance mismatch to minimise reflections and therefore reduce the signal duration caused by these reflections.

The lower peak amplitude and signal energy of by the thick film device can be explained by a combination of factors. One important factor influencing the signal amplitude was the piezoelectric properties of the sensing element. The typical d_{33} of bulk PZT [132] is an order of magnitude greater than that of the measured thick film device d_{33}. The superior material properties of bulk PZT lead to the

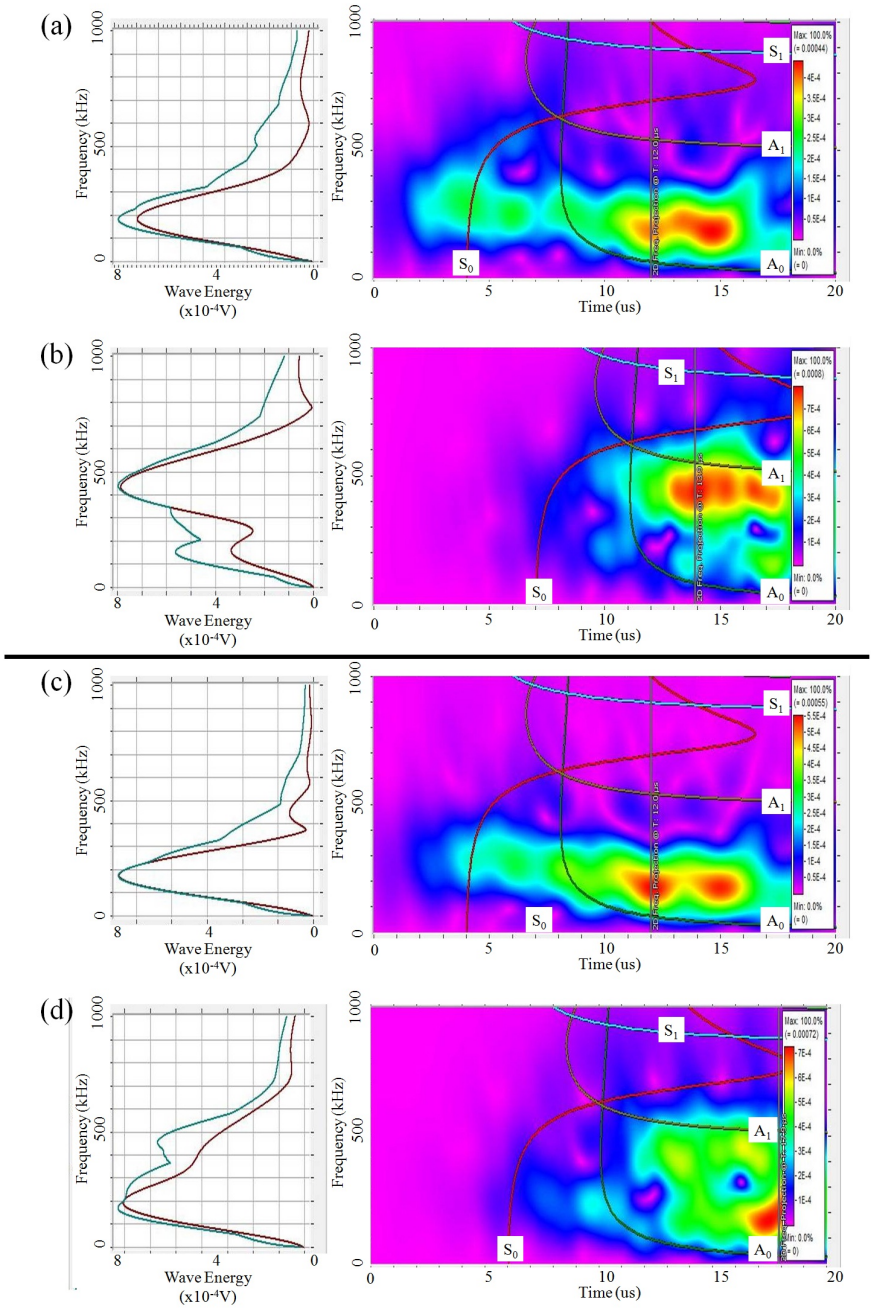

Figure 5.5: Gabor transform spectrograms of the thick film and PICO sensor test 1 (a and b respectively) and the thick film and PICO sensor test 2 (c and d respectively). The A_1 wave component dominated waveforms a and b while c and d were dominated by the A_0 wave component as can be seen from the overlaid dispersion curves.

commercial device exhibiting greater piezoelectric properties than the thick film device. The poorer properties of the thick film device are due to stresses resulting from the manufacturing process.

The amplitude in the thick film sensor was not reduced by acoustic impedance mismatch resulting from the transmission of the AE across several interface layers. The embedded nature of the thick film device theoretically resulted in the transmission of 98.6% of the acoustic energy between the Kovar plate and the thick film. The transmission of the acoustic energy from the Kovar test plate to the active element of the commercial device required the energy to be transmitted through a grease coupling layer and a wear plate. Transmission through these layers theoretically resulted in the transmission of 0.0085% of the acoustic energy between the Kovar test plate and the active element.

The wideband nature of the thick film device when compared to the resonant behaviour of the PICO device means that the response of the thick film device to different frequency components was proportional and not influenced by resonant responses as in the PICO device. It was seen from the spectrogram that the thick film sensor was initially more sensitive, as a proportion of maximum amplitude, than the PICO device to the symmetric zeroth order (S_0) Lamb wave. At frequencies above 700kHz the thick film sensor sensitivity was reduced.

Both the thick film and the PICO sensors showed a similar response to the zeroth order asymmetric (A_0) Lamb wave after 6μs. After this point the A_0 wave component was largely low frequency in nature. Before 6μs the A_0 waveform had frequency components above 700kHz and as such sensitivity to this component was reduced. The PICO device was more sensitive to the A_0 component between 450kHz and 600kHz due to the sensor resonance.

The resonant sensitivity of the the PICO sensor to the 450kHz to 600kHz frequency band resulted in a high sensitivity to the A_1 which, after 6μs, was at a frequency of approximately 500kHz, coinciding with the peak response of the PICO resonant band. This sensitivity was not present in the thick film device, the flat response of the thick film device led to the device producing a signal with an amplitude representative of the input signal over a broader frequency spectrum; the amplitude A_1 waveform was not artificially increased by the sensor. This was desirable in applications where the objective is to characterise the source of the

AE.

Neither device was sensitive to the S_1 waveform predicted by the dispersion curve due to the high frequency of this wave mode which was above 800kHz for the duration of the first 20μs of the signal. The lack of sensitivity was due to a combination of factors. The S_1 component of the AE was of a low amplitude compared to the asymmetric components. The S_1 mode of propagation was also parallel to the plane of the Kovar plate, resulting in the activation of the AE sensors in the d_{31} mode. The poor d_{31} properties of the thick film device reduced the sensitivity to the S_1 wave mode. The low amplitude S_1 was at a frequency above the resonant frequency of the PICO device and as such the commercial sensor also showed reduced sensitivity to this wave mode.

The data from tests 2 and 7 were not included in the signal analysis as they were inconsistent with the data from other tests. These inconsistencies were in the minority in the test data. These inconsistencies are due to a reduced A_1 component in the AE signal which was a property of the AE generated by the pencil break.

The lack of a significant A_1 component means that the PICO resonant frequency band between 450kHz and 600kHz was not excited to the same extent in test 2 and 7 as in other tests. The lack of a significant resonant response resulted in the maximum amplitude of the PICO signal being a product of the A_0 waveform and therefore the peak amplitude shifted to a later time in the signal. When the A_1 component of the signal was not dominant the rise time of the PICO device was greater than that of the thick film. This was expected due to the fact that the signal must travel through the coupling layer and the wear plate to reach the active element of the PICO sensor. The PICO element was also thicker than the thick film element and so requires a greater time for the signal to fully activate the element.

From the experimental results it was clear that the thick film device performed well and showed qualitative similarity with the commercial PICO device between 39kHz and 1.25MHz. The thick film device showed a quantitative similarity with the commercial device at lower frequencies between 39kHz and 313kHz. The thick film sensor lacked sensitivity above 700kHz but this was not a concern as AE monitoring is usually carried out at lower frequencies. The flat response of

the structurally integrated thick film sensor made the device ideal for use in wide-band applications.

5.2 Tungsten Carbide/Cobalt Substrate

The validation of embedded thick film sensing devices on the Kovar test plate demonstrated that the reduction in the number of layers through which the AE signal was transmitted resulted in a significantly higher transfer of AE energy between the transmission media and the active element of the sensor. The embedding of thick film sensors directly onto other substrate materials was, therefore, of great interest. The embedding of thick film AE sensors on tungsten carbide/cobalt cutting tools was of interest. For this application the deposition of a thick film PZT element 5mm by 4mm onto the surface of a substrate approximately 15mm long by 4.5mm wide by 0.5mm thick was required.

Before the film was deposited the pre-prepared tungsten carbide/cobalt substrates, which were brought in from an external source, were cleaned by an ultrasonic bath in washing up liquid, a US bath in acetone and a US bath in IPA sequentially. Following cleaning in the ultrasonic baths the substrates were barrel etched to remove organic deposits on the material surface.

A 3(C+4S) PZT film was deposited on the surface of the substrate by spin coating at 3000rpm before drying and pyrolising at 200°C for 60s and 450°C for 30s respectively. The substrate dimensions were too small for spin coating without a suitable supporting substrate. As such the WC/Co substrates were mounted on a silicon wafer using Kapton tape for the duration of the spinning process before being removed for the drying and pyrolising stages. Once the film had been deposited on the substrate the samples were sintered at 720°C. The thick film PZT was masked to form a 4mm by 3mm Cr/Au top electrode of 14nm/61nm thickness which was deposited by evaporation.

Energy Dispersive X-Ray (EDX) analysis was carried out by an external body and it was found that following sintering there was a lead rich layer 1μm to 2μm thick below the PZT film. Analysis also showed a layer of oxidised substrate below the lead rich layer. This layer was found to be between 8μm to 13μm thick

in the centre of the film to 40μm thick at the film edge. This oxide was found to inhibit the conductivity of the substrate and therefore it's use as a bottom electrode for the sensing device.

Following the analysis of the samples it was desirable to reduce the oxide layer. It was suspected that the oxide layer developed during the sintering process. To counter this oxide layer formation, sintering was carried out under an argon atmosphere. The spin coating process was repeated as previously described. The sintering process was carried out in a tube furnace with an Ar flow over the samples throughout sintering. To act as a control a set of samples were retained and sintered in the same tube furnace without the Ar flow to match the temperature profile of the sintering process.

EDX analysis indicated that lead rich and oxide layers, similar to those in the first set of samples, were also present in the the control samples. The samples sintered in Ar showed a thinner layer of oxidised substrate than samples sintered in air. The lead rich layer was also found to be thinner than that found in the air sintered sample. The analysis also found that there was a porous layer present at the interface between the PZT and the lead rich layer. This porous layer was not found to decrease film adhesion.

Electrical testing was also carried out to characterise the capacitance and loss of the film on the WC/Co substrate. As the bottom electrode was non-conductive due to the oxide layer, testing was carried out by scraping away the oxide layer on the bottom of the substrate. This resulted in the capacitance and loss measurements being carried out across the oxide layer as well as the PZT film.

The resistance and capacitance of the film sintered in air were found to be 377Ω and 285μF respectively when measured at 100Hz. The capacitance and loss were found to vary over a wide range which indicated that the film was of a poor quality. The electrical properties of the film sintered in an argon atmosphere were superior to those of the film sintered in air. The resistance and capacitance were measured as 265kΩ and 1.39nF, respectively. The increased thickness of the lead oxide layer in the air sintered samples affected the stoichiometry of the film and resulted in poorer electrical properties than the film sintered under an argon atmosphere. As such, the reduction in the thickness of the substrate oxidation layer, which acts as a dielectric, was a contributing factor to improved film elec-

trical properties in the samples sintered in the Ar atmosphere.

While the use of an argon atmosphere during sintering reduced the oxidation of the substrate and the production of a lead rich layer these issues were not completely eliminated. The oxide layer which persists in the Ar sintered samples was produced during the pyrolisation of the film at 450°C. Tungsten carbide oxidises between 500°C and 600°C [134] and as such heating to 450°C may result in a partial oxidation reaction. Another cause of the persistent oxide layer was the lack of adequate sealing on the Ar filled tube furnace, resulting in a partial oxygen pressure which may induce an oxidation reaction.

Another approach to reducing these issues was the deposition of a Ti/Pt electrode on the substrate before sintering. The substrates were cleaned as previously described before a Ti/Pt electrode 10nm/100nm thick was deposited by sputtering. The Ti/Pt electrode had poor adhesion to the WC/Co substrate and as such PZT deposition was impossible.

With these issues unresolved it became clear that a flexible low temperature deposition technique was required. Low temperature was required to prevent the formation of oxide layers in substrates such as WC/Co. A flexible deposition technique that would eliminate the need for a difficult and time consuming spin coating technique was also desirable.

5.3 Conclusions

PZT based films have been shown to be effective in detecting AE signals generated by Hsu-Neilson testing. PZT based AE devices have also been successfully integrated with metallic substrate materials. Spin coating was used to deposit a structurally integrated PZT thick film onto a Kovar sheet. The embedded nature of the thick film device resulted in the percentage of AE energy transferred from the Kovar test plate to the sensor active element from less than 1% to more than 98%. AE testing was carried out using Hsu-Neilson testing to generate artificial AE.

The thick film device performed well when compared to a commercially avail-

able PICO sensor. The thick film device frequency response was found to be flat making this type of device ideal for characterisation of the physical properties of the AE source. The thick film PZT AE sensor was able to successfully detect AE signals generated by Hsu-Neilson testing and identify signal characteristics resulting from the wave interaction with the transmission media.

Work was also carried out to embed thick film PZT onto tungsten carbide/cobalt cutting tools. Issues found with processing the thick film on the tungsten carbide/cobalt substrate indicated that the development of low temperature processing techniques, for the manufacture of MEMS AE sensors embedded directly onto the structural element under observation, was necessary.

The FOMs used to assess device performance were calculated for the thick film device on Kovar and were compared to the FOMs calculated for the thick film on silicon employed for initial testing. The relative S/N and relative A/V ratios were calculated to be 1.9 and 0.74×10^3. The relative S/N ratio was lower than that calculated for the thick film on silicon, despite the FOM for the thick film on silicon being skewed by poor results from the commercial device. This indicated that the embedded nature of the thick film on Kovar was effective in reducing the S/N ratio. The relative A/V ratio was much lower than that calculated for the thick film on silicon. This was due to the d_{33} of the thick film on Kovar being lower than that of the thick film on silicon.

Chapter 6

The Release Of MEMS AE Devices From Substrate Materials

The testing previously carried out on thick film devices embedded with substrate materials, specifically a Kovar test plate, has validated the use of thick film PZT for AE sensing purposes. It was found that the percentage of AE energy transferred from the Kovar test plate to the embedded thick film element was significantly greater than the percentage of the energy transferred from the Kovar test plate to the active element of the PICO commercial AE sensor - 98% compared to less than 1%. This was due to the embedded nature of the thick film device reducing the number of acoustically mismatched material interface layers between the Kovar test plate and the device active element when compared to the commercial device.

The embedding of thick film PZT active elements into structural elements which require AE monitoring was not always possible. There were several reasons why the deposition of a thick film device onto a structural element was not achievable in every case. Large substrates were not compatible with the composite spin coating technology previously employed in this work. Other techniques, such as screen printing, required high temperatures to achieve a film with properties appropriate for use in AE monitoring. High temperature processing was not compatible with many structural elements as damage to the structural element may occur. High processing temperatures may have also caused the PZT thick film to react with the structural element, reducing the PZT properties and possibly

causing damage to the film.

One solution to the limitations on the embedding of a thick film PZT device was the manufacture of the thick film sensor on a substrate which was then removed. The removal of the substrate removes the acoustically mismatched material interface layers between the coupling layer and the substrate and the substrate and the thick film. This removal of two acoustically mismatched material interface layers resulted in an increase in the percentage of AE energy transmitted between the structural element and the AE sensor active element.

The release of thick film PZT from silicon substrates by chemical wet etching and DRIE were discussed in the methodology of this work. These state of the art techniques were inadequate for the development of a thick film AE sensor. KOH etching was inappropriate for the removal of the silicon sacrificial substrate due to the infiltration of the etchant between the substrate and the epoxy backing which weakened the backing and resulted in the adhesion between the epoxy and the PZT reducing and the PZT and silicon substrate separating from the epoxy. The TMAH etch was also inappropriate due to the impractically long processing time.

It was shown that DRIE was an effective method of removing the silicon substrate and releasing the PZT film. However there were issues with the method, whilst the silicon was effectively removed the photoresist required to bond the cooling wafer to the sample wafer persisted; the removal of the photoresist was not possible without the destruction of the sample. Another issue with the DRIE process is the cost involved in the silicon removal. The cost of the DRIE process is conferred to the cost of the individual devices, reducing the disposability of the devices.

As the state of the art technology was inappropriate the employment of other sacrificial substrates or substrate release layers. The techniques explored in this chapter were the deposition of thick film PZT onto, and the subsequent etching of, titanium foil and copper foil. Work was also carried out on the use of sodium silicate as a release layer for the removal of PZT from a silicon substrate.

6.1 Metal Substrates

Metallic substrates have been shown to be compatible with the deposition of a film which was effective in AE testing applications. Metals are also easily etched using electro-chemical processes which are well understood. As such metals were attractive substrate materials for use in the release of PZT from the substrate support employed during processing. This chapter will explore the use of titanium and copper foil as sacrificial substrates for the release of PZT thick films.

6.1.1 Titanium Foil Etching

The removal of the titanium foil substrate from the reverse of PZT films was of interest as a means to improve the capabilities of the PZT film as an AE sensor. The removal of the substrate material resulted in reduced attenuation caused by the transmission of AE across several acoustic impedance differential interfaces.

A 2C+5S PZT film was deposited by spin coating onto titanium foil 0.11mm thick which had been thoroughly cleaned and barrel etched. As the PZT film thickness increased during deposition the magnitude of the bending during drying and pyrolising also increased. A 4(2C+5S) film deposition had been attempted on a test substrate under identical deposition conditions to assess the maximum possible film thickness attainable by this deposition method.

Significant dishing was apparent in the film and substrate following the first 2C+5S deposition stage (figure 6.1). Following subsequent depositions cracking was observed and large portions of the film began to flake away after the deposition of a 2(2C+5S) film. As such the attainable film thickness was limited to a maximum of 4.4μm when depositing under these conditions.

The film was then sintered at 720°C for 20 minutes with heating carried out at a ramp rate of 5°C/min. Following sintering a tape test was carried out to check the film adhesion, the film was fully adhered to the Ti foil substrate and there was no lift-off in the tape test.

The top surface of the film was masked using Kapton tape and the titanium was placed opposite a metal sheet in a 25% volume solution of HCl which was

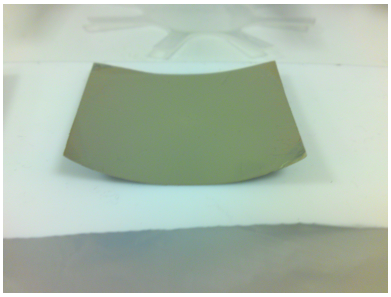

Figure 6.1: Dishing of the titanium substrate caused by PZT film shrinkage during the drying and pyrolising stages of production.

then agitated. Care was taken to ensure that the separation of the titanium sample anode and the metallic cathode was uniform. Both the metal sheet and titanium substrate were connected to a power supply and a field was applied. A voltage of 19V was required to initiate the etch process before the field strength was reduced to 8.5V for the remaining 15 minutes of the etching process. This higher initial field strength was required to etch through the titanium oxide layer before the field was turned down for the etching of the titanium.

The etch process resulted in the removal of the titanium substrate material from the rear of the film. The etch rate was heterogeneous. The etch removed the titanium at the edge of the substrate, the titanium from the raised section which was an imprint of the PZT devices on the reverse of the substrate was also removed. This heterogeneous etch rate resulted in areas of weakness in the substrate material. This weakness, combined with etchant agitation, resulted in cracking of the substrate and sections falling away into the etchant.

Cross-sectional SEM images were taken of a section where the titanium foil had broken away (figure 6.2). It can be seen from the SEM image in figure 6.2a that the PZT thick film has been undermined by the removal of the titanium foil during etching. The patterning of the titanium substrate is due to the movement of the agitated etchant. From figure 6.2b it is evident that the etching process removes the titanium foil but a layer persists on the lower surface of the PZT film. The persistent layer was formed of a titanium oxide. Due to the insulating nature of this layer it was not possible to remove it using electrode etching.

More substantial protection for the thick film PZT was required to prevent the PZT from flaking away following the undercutting due to removal of the titanium substrate. To achieve this protection a layer of DET466 photoresist was applied

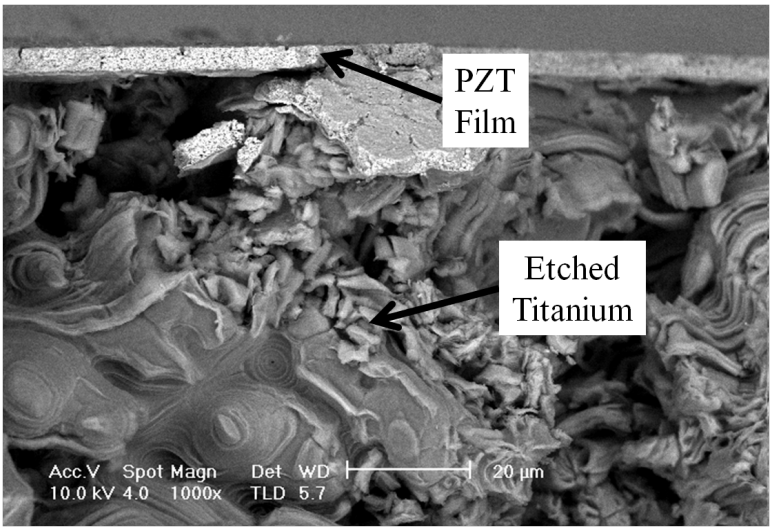

(a)

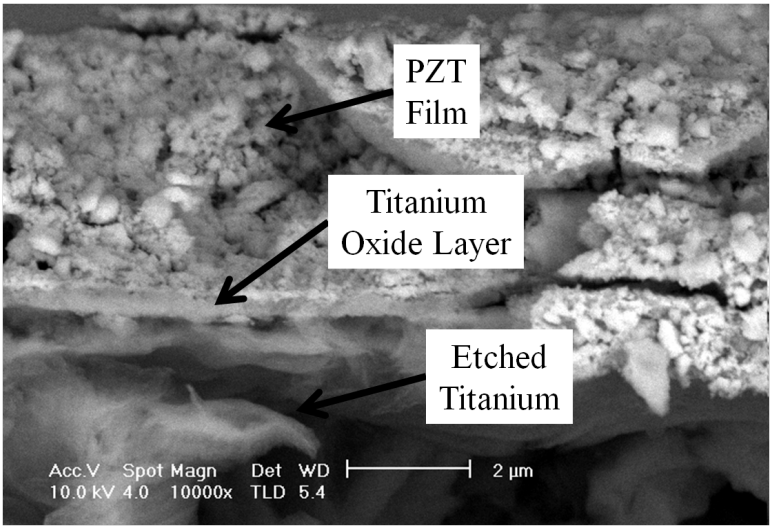

(b)

Figure 6.2: (a) SEM images of the PZT thick film on titanium foil substrate following the etching of the substrate using a 25% volume solution of HCl and a field strength of 8.5V and (b) a SEM image showing the titanium oxide layer which persisted on the underside of the PZT film following etching.

to the surface of the PZT following the deposition, patterning and electrode deposition stages. Once the photoresist layer had been deposited tape was used to protect the top surface and edges of the titanium foil.

The process used for etching was identical to the previously employed process. Once again the etch was found to be heterogeneous and the edges of the raised imprint of the titanium caused by the patterned thick film on the reverse of the titanium foil was removed at a greater rate than the rest of the exposed titanium. Despite the added structural support for the PZT the film still delaminated when undercut by the removal of titanium substrate. This is due to the PZT thick film being a brittle ceramic material and exhibiting poor structural strength when not supported by a substrate material.

6.1.2 Copper Substrates

There were problems with achieving a homogeneous etch rate across the surface of the titanium foil substrate. A solution to this issue was the use of a substrate material which does not require an electric field to etch. The material chosen as a substrate was copper. There has been work carried out previously on the integration of thin film PZT with copper substrates. The partial pressures required to co-process PZT and copper have been thoroughly investigated [97, 131].

The etching of copper was also very well understood [135]. Chemical etches can be used to remove copper and these processes result in an isotropic etch which was advantageous compared to the titanium etching process. Combined with the availability of copper foil this process was an attractive method for the release of the PZT from the substrate.

6.1.2.1 Processing

0.1mm thick copper foil was employed as a substrate material, the substrate was cleaned using a washing up liquid/IPA/acetone US bath and then barrel etched to remove residual organics. A 13.2μm, 3(2C+5S) PZT film was deposited by spin coating and sintered at 720°C with a 5°C/min temperature ramp rate. An oxide layer was apparent on the bottom surface of the Cu foil post-sintering this

layer was scraped away to allow access to the copper foil for use as a bottom electrode.

A Cr/Au top electrode was deposited by evaporation and contact poling was carried out with a field strength of 8V/μm at 120°C for 10 minutes and then cooled to below 80°C under field. Electrical measurements were carried out. The loss and d_{33} were measured as 0.0195 and 11pC/N, respectively, and the ϵ_r was calculated as 97.09. These properties are not as favourable as those of PZT deposited on either Kovar or titanium foil substrates. This is due to the relatively high thermal expansion coefficient of copper, which is double that of titanium, causing cracking in the film during sintering. This film cracking was imaged by confocal microscopy and is shown in figure 6.3. Crack depths were determined to be on the order of 10μm suggesting that the cracking was through the whole film thickness.

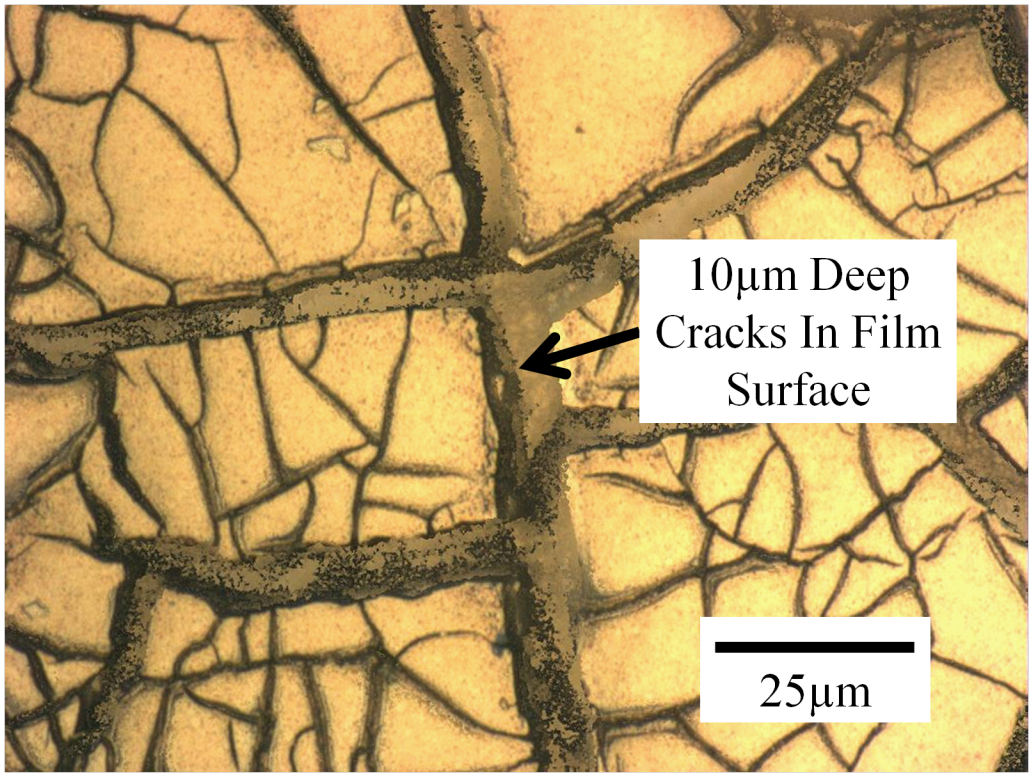

Figure 6.3: Confocal image showing surface cracking of the PZT film deposited onto a copper foil substrate.

The PZT was masked and then patterned by powder blasting to produce 5mm diameter PZT features. The features were protected using a layer of epoxy before

etching was carried out. The PZT on copper was immersed in 10.5M nitric acid for 20 minutes. This etch process successfully removed the copper substrate and resulted in released PZT supported by an epoxy backing.

A picture of the released device is shown in figure 6.4a. A black layer was present on the reverse of the sample, this was consistent with the oxide layer present on the copper following sintering. Confocal microscopy and SEM (figure 6.4c) images were taken of the interface between the PZT and the copper foil. The confocal image showed that the PZT was inset into the epoxy backing by 18μm (figure 6.4b). This was caused by the powder blasting patterning removing some of the copper foil substrate from around the device before the epoxy was applied.

EDX spectroscopy was used to identify the composition of the components. It was found that the black layer was comprised of lead and copper oxide, whilst the PZT below the oxide layer was found to be lead-depleted. The lead/copper oxide layer was non-conductive. This resulted in a dielectric layer between the lower electrode and the PZT film causing an apparent reduction in the measured film properties.

It is possible to avoid the formation of this Pb/Cu oxide layer by careful control of the atmosphere in which the sample is sintered. Preventing the formation of the lead/copper oxide layer was important to remove the dielectric layer and improve the measured electro-mechanical properties of the film. As the tight atmospheric controls required to prohibit the formation of the Pb/Cu oxide layer did not lend themselves to low cost, large scale fabrication another solution was sought.

6.1.2.2 Barrier Layers

Barrier layers were investigated as a low cost method of prohibiting the formation of the Pb/Cu oxide layer. ZrO_2 has previously been shown to be effective at prohibiting oxidation and interfacial reactions. ZrO_2 producing sol was produced by mixing 47ml of ethyl anhydride with 3ml glacial acetic acid and 4.344g of zirconium (IV) propoxide. A 60nm thick ZrO_2 layer was deposited by spin coating at 3000rpm in a clean room environment then sintered at 850°C for 25mins with no heating ramp rate. Four copper substrates were prepared; one with a 60nm ZrO_2 diffusion barrier, one with a 8nm/200nm Ti/Pt diffusion layer, one with

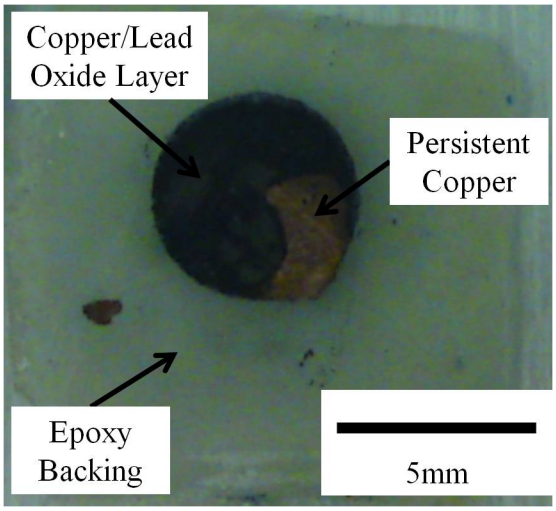

(a)

(b)

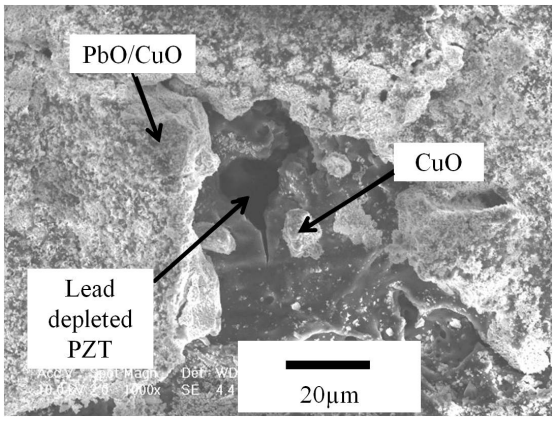

(c)

Figure 6.4: An image of the interface between the PZT and copper showing the black copper/lead oxide layer which persisted following the etch, a small amount of copper also persisted (a). Confocal microscopy profile showing the 18μm which the PZT film is inset into the surrounding epoxy backing (b). SEM image showing the surface of the PZT film following the removal of the copper substrate. The composition of the copper/lead oxide layer and the lead rich lead titanate was identified by EDX (c).

60nm of ZrO_2 and 8nm/200nm Ti/Pt and one control with no diffusion barrier.

The PZT was deposited using the method previously described. Sintering was carried out using a process consistent with that previously used. Images were taken of the surface of the films deposited on the Cu substrate. These images are shown in figure 6.5. It was clear from the macro surface morphology that the ZrO_2 barrier layers were not effective as the quality of the film deposited on the ZrO_2 barrier layer was poor. There was cracking of the film surface and the PZT was found to delaminate from the substrate and as such the use of ZrO_2 as a barrier layer was not conducive to the deposition of a PZT film suitable for use in AE sensing applications.

The Ti/Pt deposited on the ZrO_2 boundary layer was dull and non-conductive indicating that the ZrO_2 was not a suitable boundary layer for use in this system. The PZT deposited directly onto the Ti/Pt on copper substrate was found to be conductive through the film. This indicates that the cracking, caused by thermal expansion, penetrated through the entire film, suggesting that copper was an inappropriate substrate layer for the deposition of PZT using the low cost processing methods presented.

6.1.2.3 Copper Sacrificial Layer

The etching of the copper foil substrate material to release the thick film PZT was successful, however the high thermal expansion resulted in the process being inappropriate for use in the manufacture of thick film AE devices. Therefore a thin layer of copper on a silicon substrate with more suitable thermal expansion properties was investigated. This layer was then to be etched away releasing the film from the substrate below and allowing the re-use of the substrate.

Copper was deposited by electroplating where a copper sulphate solution was produced by mixing 50g of $CuSO_4$-$5H_2O$ with 18g of H_2SO_4 in 200ml of water. A 50mm by 50mm, 0.5mm thick section of copper foil was placed into the copper sulphate solution. This foil was used as the cathode whilst a platinised silicon wafer anode was cleaned and placed into the copper sulphate solution. Care was taken to ensure a consistent separation of 25mm between the anode and cathode.

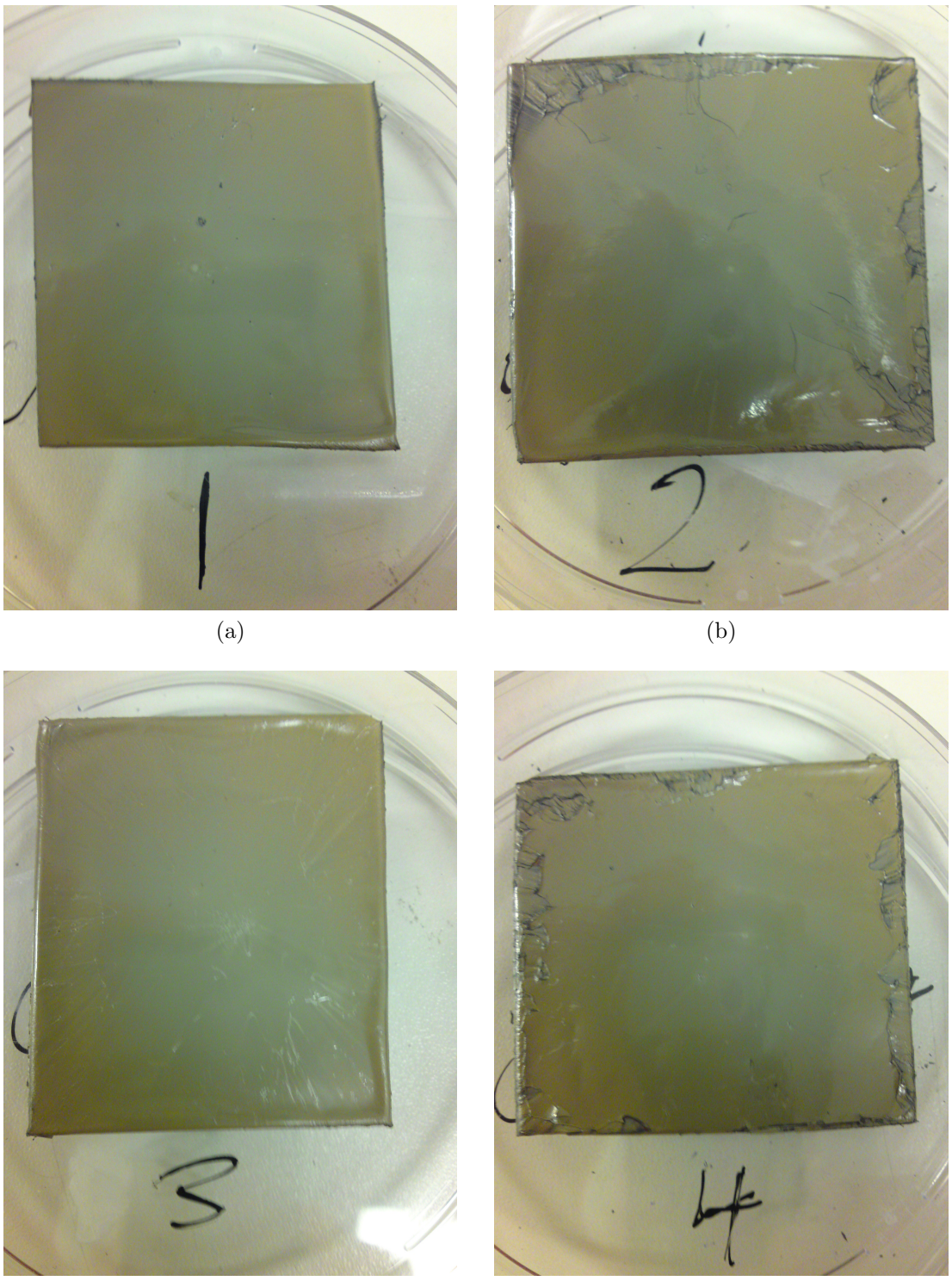

(a) (b)

(c) (d)

Figure 6.5: Images showing the top surface of (a) a PZT film deposited onto copper foil substrates which were coated with no barrier layer, (b) a ZrO_2 barrier layer, (c) a Ti/Pt barrier layer and (d) a ZrO_2 and Ti/Pt barrier layer.

A field of 9V was applied for 30s. Following the coating of the anode the samples were removed from the copper sulphate, washed in de-ionised water and then dried. Confocal microscopy was carried out to assess the thickness and surface roughness of the copper layer on the platinised silicon wafer. The copper layer was found to be of a mean thickness of 6.44μm with a root mean squared surface roughness of 4.51μm. It was clear from these parameters that the deposition of PZT onto this surface would result in a poor quality film inappropriate for use in AE sensing applications. The surface roughness can be reduced by tighter controls on the electroplating process. These closer processing controls can result in a film which is of suitable surface roughness for the deposition of a PZT film.

6.1.3 Conclusion

It was clear from the work carried out that the copper foils were inappropriate as sacrificial substrates or release layers. Copper processing required close control of the atmosphere and temperature to inhibit the formation of a copper/lead oxide layer at the interface between the PZT film and copper substrate. Even with close control the temperatures required for the processing of the PZT film combined with the thermal expansion differential of the copper and PZT and the shrinkage of the PZT during sintering may result in the film cracking.

6.2 Sodium Silicate Release Layer

Sodium silicate, also known as water glass, was a water soluble material which exhibited properties attractive for use as a substrate material for PZT deposition. Sodium silicate was inert, reducing reactions with the PZT film; exhibiting a low thermal expansion, similar to that of PZT; and was easily dissolved, enabling effective release of the PZT film. Sodium silicate, when dry, was a glass-like material. When deposited on a silicon substrate, sodium silicate would act as a soluble release layer to release the PZT film from the structural support of the substrate. Sodium silicate has the advantage of exhibiting a thermal expansion coefficient much lower than that of metal substrates, so there are fewer concerns with cracking caused by thermal expansion mismatch.

As sodium silicates have many forms, an understanding of the phase equilibria of the Na_2O-SiO_2 was essential. The phase equilibria of the sodium silicate system had been thoroughly investigated [5, 136, 6]. The phase diagram of sodium silicate can be seen in figure 6.6a. It was clear from the phase diagram that the nature of the resultant film will be related to the composition of the starting solution and the temperature to which the film is heated during processing. The commercially available sodium silicate (Aldrich) employed in this work was of a starting solution of 0.714 SiO_2 and was composed of 62.9wt.% water. This composition of sodium silicate would partially melt during heating at temperatures above 834°C (figure 6.6b). As such, PZT co-processed with sodium silicate may be processed at temperatures of 834°C and above to potentially release stress in the PZT film.

For the sodium silicate to be effective as a substrate release layer it must be smooth during the PZT deposition and processing and the layer must be soluble following processing. As such, it was important to ascertain the effects of both low temperature drying and the effects of high temperature calcination on both the surface morphology and the solubility of the sodium silicate layer. Precalcination of the film was also investigated as previous work [137] showed that, when calcined at temperatures below 800°C, the sodium silicate transforms on the surface of the silicon substrate to a white powder which is inappropriate for the effective deposition of a PZT film.

6.2.1 Sodium Silicate Drying

Silicon substrates were cleaned using the sequential washing-up liquid, IPA and acetone US bath method previously employed. Once the substrates were cleaned they were inclined, aqueous sodium silicate was deposited onto the substrate by pipette and dried at room temperature for 48 hours, resulting in a smooth sodium silicate later. Confocal microscopy was employed to ascertain the thickness of the sodium silicate following drying. The layer was found to exhibit a mean thickness of 22.28μm with a standard deviation of 1.54μm.

Drying was carried out for 5 minutes at temperatures ranging between 70°C and 400°C. Photos of samples dried at room temperature, 70°C, 100°C and 200°C are shown in figure 6.7. It can be seen from the images in figure 6.7 that as the drying

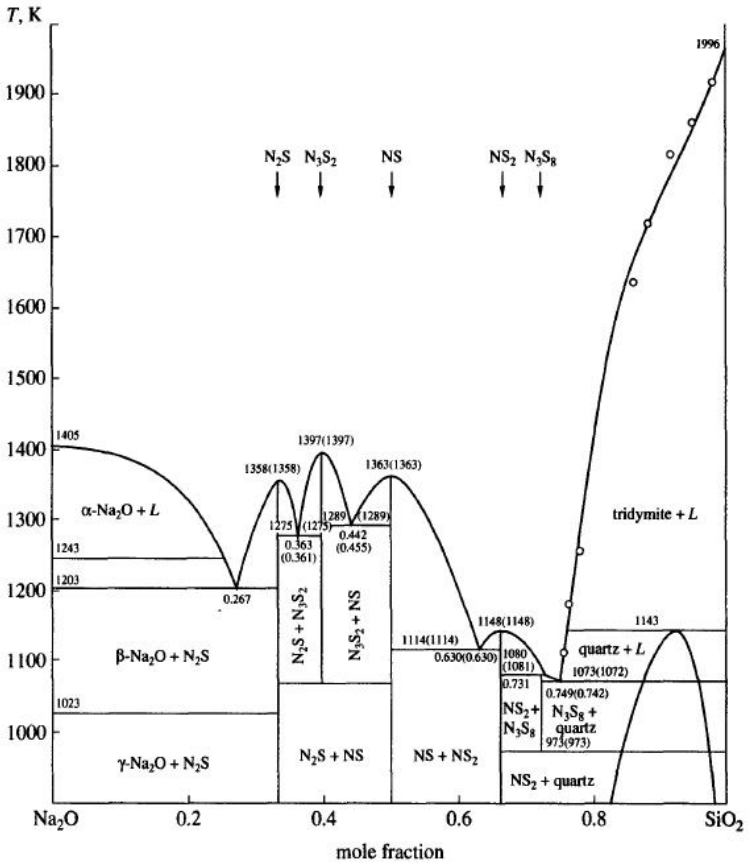

(a)

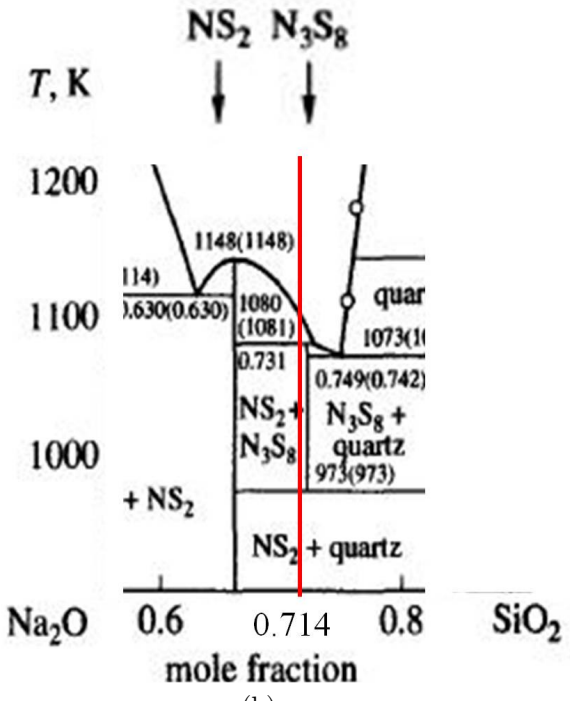

(b)

Figure 6.6: (a) Figure showing the phase diagram of sodium silicate, in this diagram N and S represent Na_2O and SiO_2 respectively [5]. (b) Magnified phase diagram showing the composition of sodium silicate employed in this work.

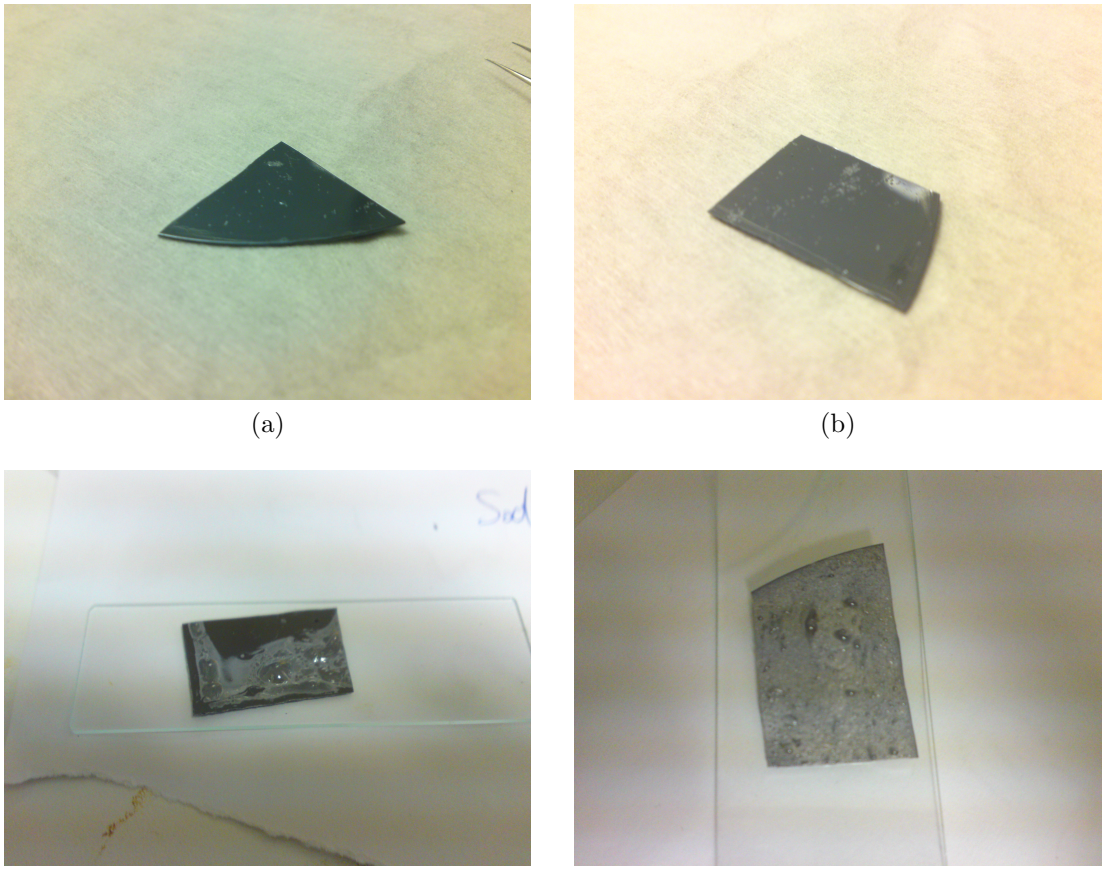

(a) (b)

(c) (d)

Figure 6.7: Images showing sodium silicate dried at room temperature(a), 70°C (b), 100°C (c) and 200°C (d). The increase in bubbling present in the layer can clearly be seen.

temperature increases the occurrence of bubbling in the layer also increases. As the sodium silicate dried a skin was formed on the surface of the layer. The bubbles, caused by the expansion of the water in aqueous solution with the sodium silicate out-gassing when heating was carried out, pushed through the surface skin which then dried resulting in a rough surface finish. At higher temperatures the bubbling was violent and resulted in a very rough surface finish. A flow of nitrogen across the surface of the layer during drying was employed to reduce the bubbling in the layer. Using the nitrogen technique the layer dried without bubbling on the layer surface. However, rippling in the sodium silicate layer was apparent when the blown nitrogen method was employed.

Thermo-gravimetric analysis (TGA) was carried out on aqueous sodium silicate to identify the variation in mass with temperature change over time. The results of the TGA can be seen in figure 6.8. From the TGA it was clear that there was

an initial low temperature drying stage in which the water from the aqueous solution was evaporated. At a temperature of 126°C there was an inflection point (figure 6.8), indicating that the water chemically in solution with the sodium silicate had been removed, this corresponded to a 30.4wt.% reduction in mass. The removal of water continued as the temperature increased. At 450°C, the temperature employed in PZT pyrolising, the mass of the sample had reduced by 61.6wt.%. At 800°C the mass had reduced by 62.1wt.% indicating the removal of the majority of the initial 62.9wt.% water present in the sodium silicate sample. The TGA showed clearly that significant water loss would take place in the sodium

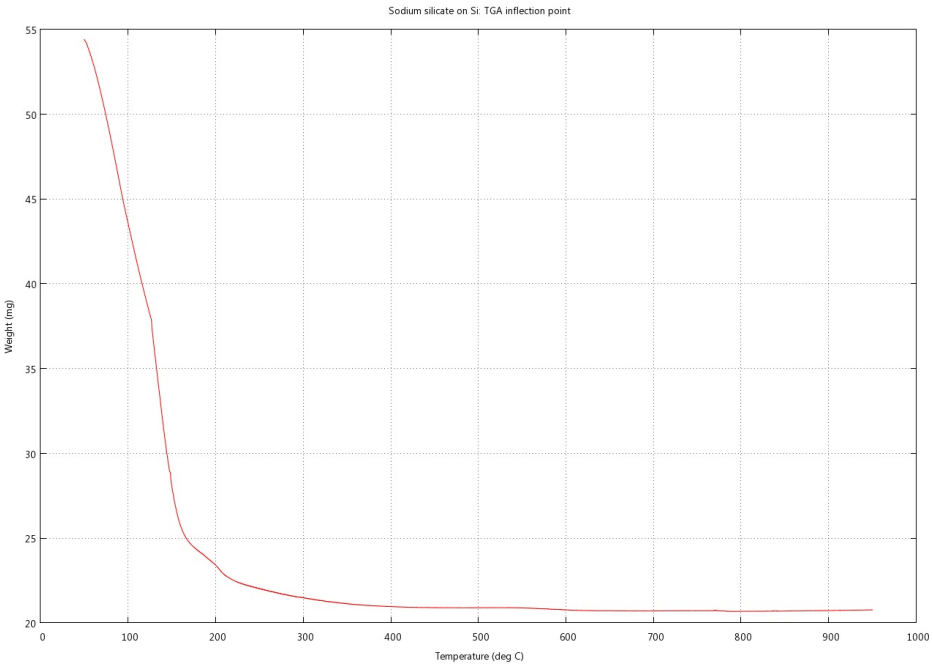

Figure 6.8: Figure showing the thermo-gravimetric analysis of sodium silicate between room temperature and 900°C.

silicate layer at temperatures employed during the pyrolising stage of PZT deposition, in which 99.2% of the total water removal occurred. This indicated that the sodium silicate may not be stable at temperatures employed for the processing of PZT due to the removal of the aqueous water and the associated bubbling resulting in a surface morphology incompatible for co-processing with PZT.

Due to the bubbling caused by the out-gassing of the water during the heating employed to dry the sodium silicate layer, the hotplate dried sodium silicate had a rough surface finish which was not compatible with PZT deposition. High temperature drying carried out at 400°C resulted in the sodium silicate crystallising upon contact with the hotplate, as predicted by a literature XRD trace (figure

6.9), to form β-$Na_2Si_2O_5$ which was white and powdery in appearance due to the volatile out-gassing of the aqueous water combined with the rapid crystal growth. The β-$Na_2Si_2O_5$ was well adhered to the substrate.

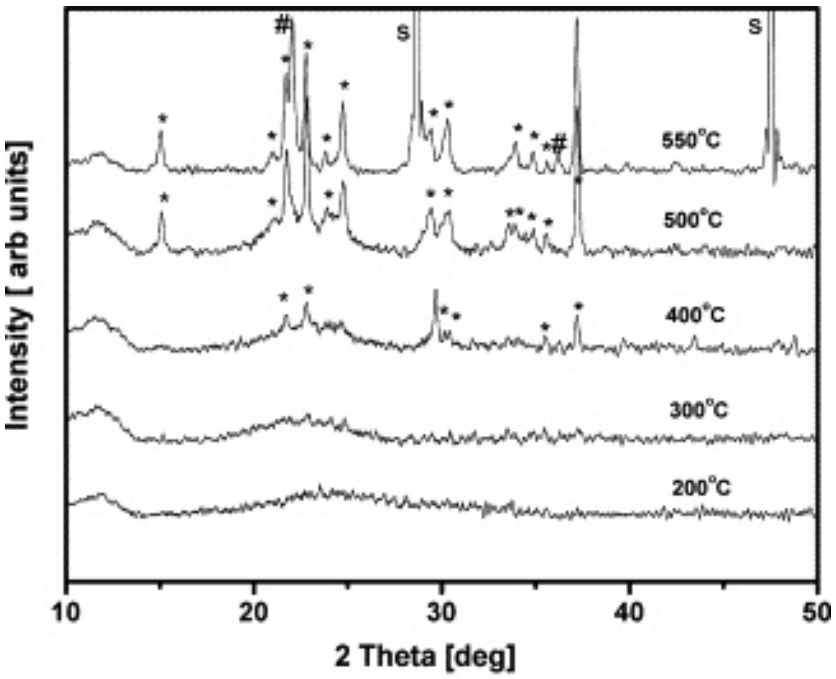

Figure 6.9: XRD trace of sodium silicate crystallisation at temperatures between 200°C and 550°C. The β-$Na_2Si_2O_5$ peaks are indicated by "$*$", the cristobalite by "#" and silicon by "S" [6].

6.2.1.1 The Effect of Thickness on Sodium Silicate Layer Drying

The effect of sodium silicate thickness was investigated by casting. A 1mm thick layer of the aqueous solution was deposited onto a silicon wafer surrounded by a wall of self-adhesive aluminium tape. The cast layer drying was carried out in the same way as the film drying described above and experienced similar issues with bubbling when drying was carried out above room temperature.

Drying in a vacuum oven was investigated to prevent the formation of the bubbles in the layer due to the out-gassing of aqueous water passing through the dried skin of the sodium silicate. The vacuum oven was set to 75°C and 500mbar below atmospheric pressure. Drying times of 20 minutes, 40 minutes, 60 minutes and 120 minutes were employed. It was found that a drying time below 120 minutes resulted in a layer which was not fully dried. The sodium silicate layer

was smooth when removed from the vacuum oven, however, rippling occurred on the surface of the cast layer following removal from the vacuum oven. This may be due to the temperature gradient experienced during the rapid cooling experienced by the film upon removal from the vacuum oven. This resulted in a contraction of the surface of the sodium silicate layer which cools quicker than the sodium silicate in proximity to the substrate. There were similar issues with higher temperature drying causing bubbling as in the drying of the thinner layers on silicon indicating that thickness did not affect the surface morphology of the layer.

From the experimental work carried out it was clear that the drying process needed to be carefully controlled to ensure that the deposited film was of a quality which would enable a PZT film to be deposited onto the surface. The surface roughness of the film increased as the drying temperature increased due to the bubbling caused by water release during drying and at temperatures of 400°C and above the crystallisation of the film. The release of bubbles within the sodium silicate layer during drying were not affected by the thickness of the film and can be mitigated by the drying of the film at room temperature prior to careful heating of the layer with a slow temperature ramp rate. Another explanation for the surface roughness was the phase separation into the silica and β-$Na_2Si_2O_5$ during the heating process. This resulted in a rough surface regardless of film thickness.

Once a drying process had been identified, films were produced for use in the investigation of the effects of calcination at temperatures up to 900°C. An understanding of the changes which took place in the layer during calcination was essential as the sodium silicate layer would be subjected to a temperature of 720°C during the processing of PZT films.

6.2.2 Sodium Silicate Layer Calcination

Layers were prepared for calcination by depositing sodium silicate onto a silicon wafer which had been cleaned using the standard cleaning procedure. The sodium silicate was deposited by pipette onto an inclined wafer with the excess being allowed to run off. One film was then dried at 100°C and another at 150°C prior to calcination. Calcination was initially carried out at 720°C with no ramp

rate to match the processing conditions utilised in the processing of thick film PZT deposited onto platinised silicon by composite spin coating.

X-ray diffraction (XRD) was carried out on the sodium silicate films before and after calcination, these comparative XRD traces can be seen in figure 6.10a and 6.10b, respectively. The trace for the non-calcined sodium silicate can be compared to literature traces which are shown in figure 6.9 [6]. It can be seen that, while increasing the drying temperature had an effect on the appearance of the sodium silicate prior to calcination, the XRD trace did not alter significantly and the layer was still amorphous prior to calcining at 720°C.

The XRD traces of the sodium silicate layers dried at 100°C and 150°C and then calcined at 720°C matched that of the literature values for β-$Na_2Si_2O_5$, which was expected, as shown on the sodium silicate phase diagram (figure 6.11). The comparative XRD traces of the sodium silicate layers which were dried by different methods indicated that the drying process had a negligible effect on the sodium silicate layer composition after calcining had been carried out. This was important as it demonstrated that a drying process could be selected to result in the desired surface finish without adversely affecting the properties of the film following calcination. The peak at 32.5° was was due to the silicon substrate onto which the sodium silicate film was deposited.

The phase diagram (figure 6.6b) indicated that a $Na_6Si_8O_{19}$ phase formed at a temperature above 701°C. Upon cooling, following the calcination process, $Na_6Si_8O_{19}$ decomposed back into β-$Na_2Si_2O_5$ and quartz. This decomposition resulted in a white powder forming on the layer surface, this powder has been previously observed to be quartz crystals [6]. The phase diagram indicated that at 807°C and above, the $Na_6Si_8O_{19}$ decomposed into $Na_2Si_2O_5$ and a liquid phase. This process has been shown to be irreversible [6].

The sodium silicate is entirely liquid at temperatures above 834°C and has been shown to cool from this phase to form a cracked, transparent layer [6]. Two sodium silicate layers were deposited by pipette and dried at room temperature before being calcined at 800°C and 900°C, respectively. Figure 6.12 shows the surface morphology of the calcined sodium silicate layers.

It can be seen that the layer calcined at 800°C exhibited a white powdery surface

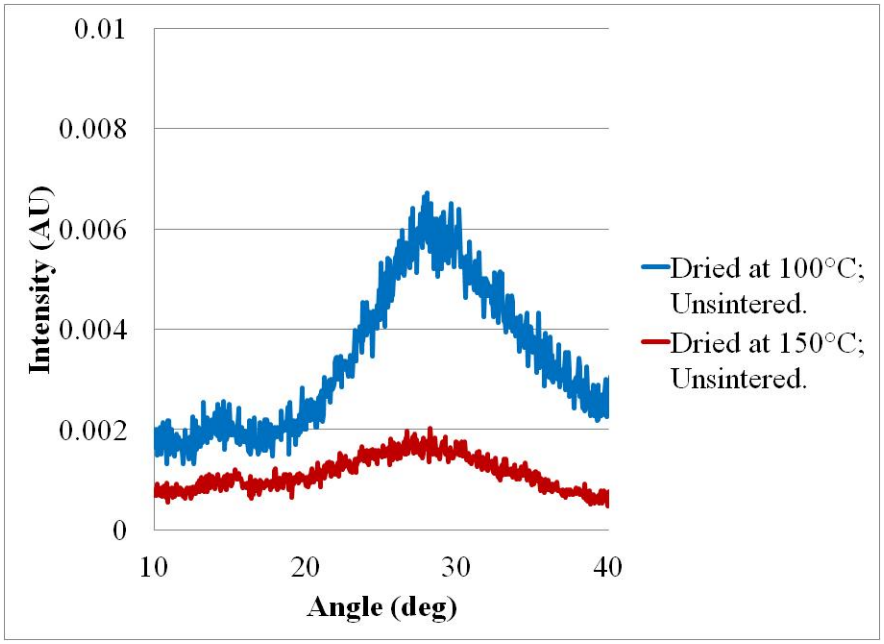

(a)

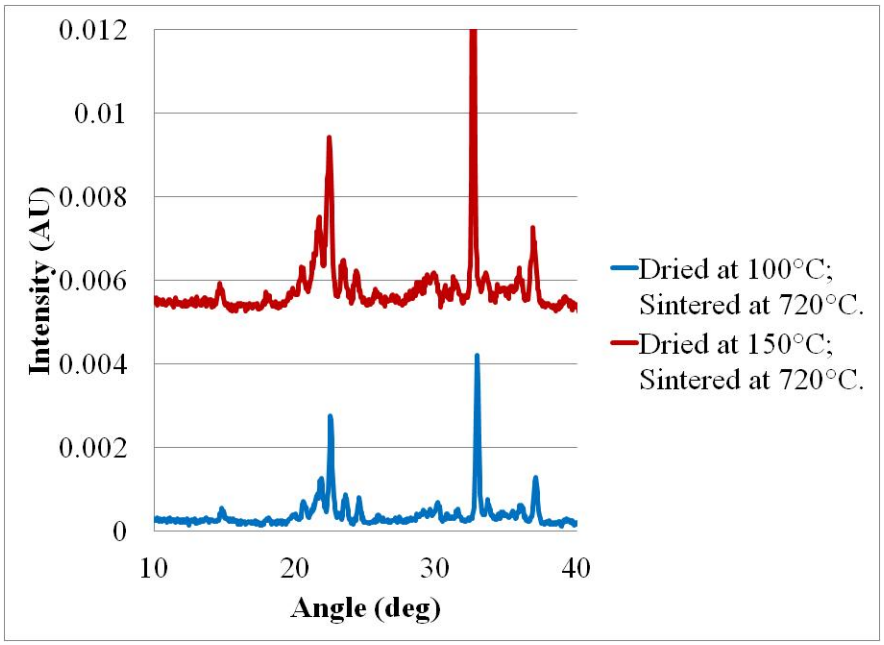

(b)

Figure 6.10: XRD traces of sodium silicate (a) before and (b) after calcining at 720°C. The upper trace on each XRD is of the sodium silicate layer pre-dried at 150°C with the lower trace being pre-dried at 100°C.

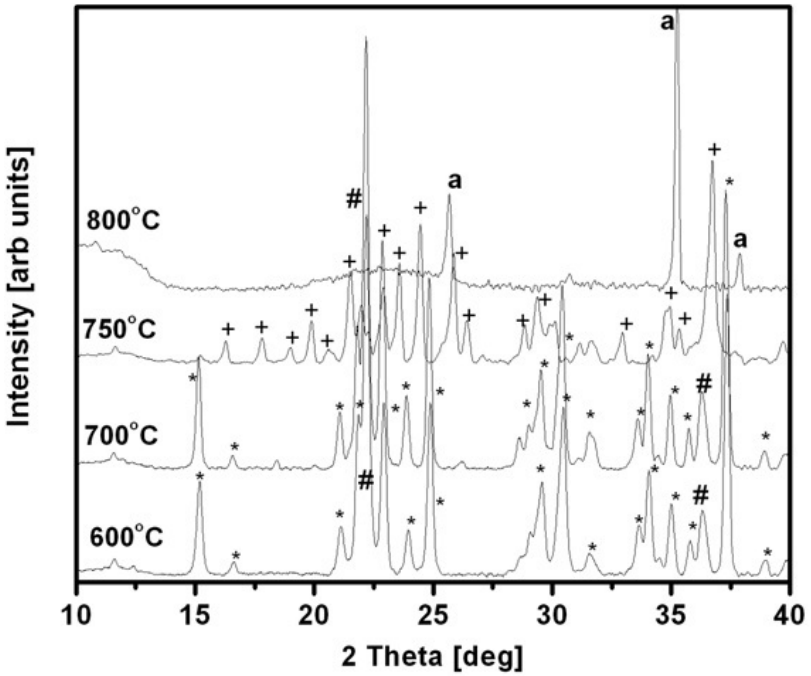

Figure 6.11: XRD trace of sodium silicate crystallisation at temperatures between 600°C and 800°C. The β-$Na_2Si_2O_5$ peaks are indicated by "$*$", $Na_6Si_8O_{19}$ by "+", the cristobalite by "#", silicon by "S" and alumina by "a" [6].

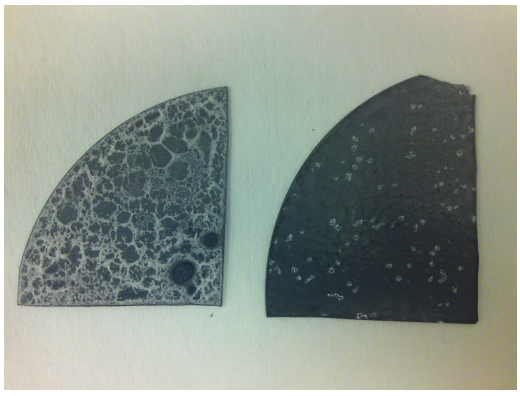

Figure 6.12: Image showing the surface morphology of sodium silicate calcined at 800°C (left) and 900°C (right). The powdery surface finish of the 800°C calcined sample is clear.

finish which may be the quartz crystals previously observed. The white powder deposit was present around what appeared to be bubble formations which arose during the calcining process, similar to those seen during drying at temperatures above 150°C and possibly resulting from the layer being heated through those temperatures. The degassing of water in aqueous solution through a dried skin on the surface of the sodium silicate resulted in bubbling. The white powder deposit may have formed on the skin of these bubbles which subsequently burst resulting in the patterning observed. A reduction in temperature ramp rate has been shown to have no effect on the formation of the white powder layer [6].

The sodium silicate layer calcined at 900°C did not exhibit the white powdery surface finish seen in the layer calcined at 800°C. The 900°C calcined layer was completely crystalline and a smooth surface finish which may have been suitable for use as a substrate for PZT deposition. The surface morphology was consistent with the the calcination of sodium silicate at a temperature resulting in an entirely liquid phase as predicted by the phase diagram.

Whilst the surface of the sodium silicate was suitable for PZT deposition, the sodium silicate which had been calcined to 900°C was not readily soluble. The cracked sodium silicate layer was removable by force; this method was not compatible with the release of PZT. This reduced the effectiveness of the sodium silicate prepared by this method as the release layer could not be removed without damaging the film. One reason the sodium silicate layer calcined to 900°C was less soluble than the sodium silicate calcined to 800°C was a reduction in the surface area of the layer due to the layer being smoother. The sodium silicate calcined to 900°C was less soluble than the un-calcined film due to the crystalline structure resulting from the calcination process. An increase in water temperature and pressure has previously been shown to be effective in removing these layers.

6.2.3 Sodium Silicate Release Layer Conclusions

Work was carried out on the development of a process for the deposition of a sodium silicate layer for use as a release layer for the separation of the PZT thick film from the substrate material. Drying processes were investigated between room temperature and 400°C. It was found that 99.2% of the water content of

the starting sodium silicate solution was removed by drying at a temperature of 450°C. The removal of water, which degassed as bubbles through a skin which forms on the surface of the sodium silicate, resulted in a rough surface finish which may result in damage to PZT thick films to be co-processed with sodium silicate.

Due to the rough surface morphology resulting from the drying process being unsuitable for co-processing with PZT thick films, work was carried out on pre-calcining the sodium silicate layer. It was found that a calcining temperature of 900°C was required to produce a surface morphology suitable for the deposition of PZT, the sodium silicate solubility was reduced following calcining. This reduction in solubility limited the application of sodium silicate as a release layer resulted from a reduction in surface area. The surface area was lower due to the liquid phase prohibiting the formation of a rough powdery surface.

6.3 Conclusions

The release of PZT AE devices from the substrate was an essential area of investigation. Removal or release of the substrate from the PZT film enables the PZT element to come into direct contact with the structural element under observation. This was of benefit for AE detecting applications where any layer between the AE transmission media and the PZT element may result in signal attenuation and distortion.

Metal foils were employed as sacrificial substrates. The etching of titanium foil substrates was not successful. This was due to an inhomogeneous etch rate combined with insufficient structural support for the PZT. This resulted in delamination of the PZT film and the subsequent destruction of the film in the etchant. This delamination may be avoided by the improvement of the structural support provided by the PZT backing layer. Copper was also employed as a sacrificial substrate. The copper foil was successfully etched away from the PZT film with only a lead oxide/copper oxide layer persisting. The processing of PZT on copper foil resulted in severe cracking to the film and ruled out the use of copper foil as a sacrificial substrate. Copper was also investigated for use as a release layer, however, the deposition of a copper film suitable for co-processing with PZT was

not achieved.

There were issues associated with the use of metal as a sacrificial substrate and as a device release layer. Sodium silicate was a non-metallic release layer. The drying and calcining of sodium silicate was carried out to identify a process compatible with the conditions required for the deposition of PZT thick films. The drying process of sodium silicate was found to significantly affect the surface morphology with higher temperature drying resulting in an increase in bubbling within the layer and therefore a rougher surface finish.

The drying process did not affect the composition of the film following calcining at temperatures of 720°C and above. It was found that a calcination temperature of 900°C was required to produce a film of suitable surface morphology for co-processing with PZT. This was supported by literature which suggested that a suitable surface morphology would be present following calcination at temperatures of 834°C and above. The sodium silicate layer was found to exhibit reduced solubility following calcination at 900°C and as such further work on the removal of the sodium silicate without causing damage to a co-processed PZT film was required.

It was clear from the results presented in this work that, while device release by way of release layer or sacrificial substrate was a promising avenue for investigation, significant future work was required to refine the device release process to a point where it would be suitable for application to MEMS AE sensor manufacture. The successful deposition of PZT thick films onto metal foils was of interest as this technique allows for the manufacture of MEMS AE sensors on a material which exhibits acoustic properties similar to those of the structural elements requiring monitoring. These devices may then be mounted onto a structural element without the need to remove the substrate material.

Chapter 7

Thick Films On Metal Foils For Integrated AE Sensing Applications

Integrated MEMS AE sensors may be produced separately and situated alongside the structural element by adhesive. This method of integration provides many advantages common to embedded MEMS sensors. This type of sensor does require a coupling layer between the active element and the structural component under observation. This coupling layer may adversely effect the detected signal, introducing a possible source of signal attenuation and distortion.

7.1 Deposition of an Integrated PZT Thick Film on a Kovar Foil Substrate

The deposition and validation of a structurally integrated AE sensor has shown that thick film PZT can be successfully used for AE sensing applications. Unfortunately the spin coating deposition technique utilised in the manufacture of the integrated AE device on Kovar was incompatible with structural elements greater than 100mm in diameter. There were two possible solutions to this issue; use a processing method compatible with the deposition of PZT sensors onto large structural components as discussed in section 8.1 or the deposition of thick film PZT devices onto a substrate with an acoustic impedance closer to that of

the structural element than the traditional silicon substrate and the subsequent attachment of the device to the structure.

As many structures which require AE monitoring are metallic the acoustic impedance can be best matched by the use of a metallic substrate for the PZT thick film element. The acoustic impedance of mild steel was 46.02MRayls. The acoustic impedance of Kovar was more closely matched to this - 41.53MRayls - than silicon with an acoustic impedance of 19.63MRalys. As the work in section 5.1 has shown, Kovar has thermal expansion properties conducive to the deposition of PZT without causing damage to the film through thermal expansion induced cracking. As such Kovar foil was selected as a substrate material.

PZT deposition was carried out by spin coating onto Kovar foil 0.25mm thick. The objective of this procedure was to assess the practicality of depositing thick film PZT onto a metal foil. PZT 17.6 μm thick was deposited onto the Kovar foil substrate by spin coating a 4(2C+5S) composite film.

Confocal laser scanning microscopy was carried out to characterise the cracking of the surface of the film. An image of the film surface is shown in figure 7.1a. Figure 7.1b shows a cross-sectional profile of the image in figure 7.1a. The cross sectional profile shows limited cracking on the surface of the PZT, the cracks are shown to be several microns in width but, importantly, only a maximum of two microns deep. This indicates that while the cracking is extensive the cracks do not penetrate more than one "C" layer. This type of cracking may reduce the d_{31} of the film and thus may reduce the sensitivity of the film to S_i waveforms. This type of cracking will not reduce the d_{33} of the material significantly.

A 2mm diameter Cr/Au electrode 10μm/50μm thick respectively was deposited onto the surface of the PZT and the film was poled by contact poling at a field strength of 2.27V/μm for 10 minutes at 130°C before being cooled to 75°C whilst still under field. The d_{33}, capacitance, resistance and loss were measured. The ϵ_r of the PZT was 260, the loss and d_{33} were measured as 0.1406 and 38pC/N respectively.

The film properties of the PZT on Kovar are sufficient to enable the use of the PZT film for AE sensing applications. The loss of the film on Kovar foil was 3.86% greater than that of the PZT on the Kovar sheet, the ϵ_r is much greater

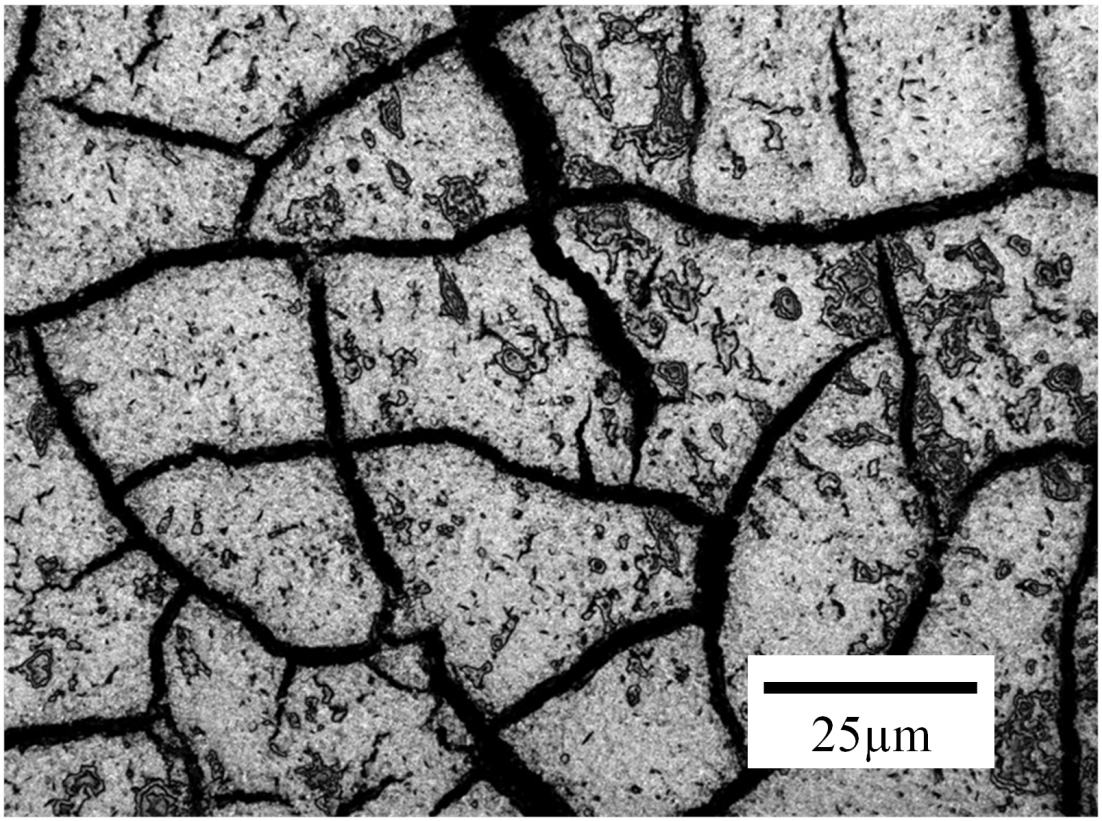

(a)

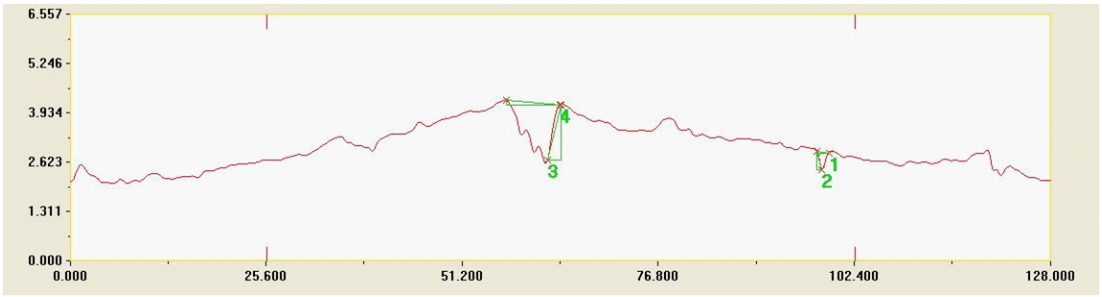

(b)

Figure 7.1: Confocal image of cracking on the surface of the PZT film deposited onto Kovar foil following sintering showing (a) an image of cracking present the film surface and (b) a cross sectional profile of the cracking; points 1 and 2 correspond to a width and depth of 1.65μm and 0.48μm respectively, points 3 and 4 correspond to a depth and width of 1.47μm and 7.11μm respectively.

on the foil than the sheet. The d_{33} of both the PZT on the foil and on the sheet were identical.

The improvement in properties observed when the thick film PZT was deposited onto Kovar foil compared with Kovar sheet was due to the Kovar foil being thinner and therefore more compliant. This resulted in bending of the sheet during the drying, pyrolising and sintering which reduced the stress induced in the film. This did not occur when the thick film was deposited onto the Kovar sheet as the sheet did not bend but constrained the thick film to a greater extent, increasing the stress in the film and reducing the film properties as a result. As a result of these improved film properties an investigation was carried out into the deposition of thick film PZT onto thinner metal foil substrates.

7.2 Integration of Thick Film PZT with a Titanium Foil Substrate

The properties of the PZT film on Kovar foil demonstrated that the deposition of thick film PZT onto metal foil was viable and resulted in improved film properties. As such, deposition onto a thinner substrate was carried out. Titanium foil was employed as a substrate material as the high material strength means that a thinner substrate can be employed.

The density of titanium was approximately half that of Kovar, despite this the speed of sound through these materials is similar, 5090m/s and 4968m/s for titanium and Kovar respectively. The Young's modulus of titanium was slightly lower than that of Kovar, 116GPa to 159GPa. Both titanium and Kovar are stable at temperatures required for PZT processing.

7.2.1 Device Manufacture

A 2C+5S PZT film was deposited onto the titanium foil by spin coating and patterned by powder blasting. 5mm diameter Cr/Au electrodes 12nm/62nm thick were deposited by evaporation and the film was masked and then patterned by

powder blasting. The non-conductive oxide layer produced during film sintering was removed and then contact poling was carried out with a field strength of 8V/μm at 130°C for 10 minutes before the film was cooled under the field.

The electrical properties of the film were measured. The d_{33} was found to be 51.9pC/N, the ϵ_r and loss were found to be 235.2 and 0.0423 respectively. The loss compares favourably with that of the thick film PZT on Kovar foil. Despite comparing well to thick film PZT on Kovar, the loss is considerably higher than the measured loss of the PICO sensor, which was 0.0065.

Electrical contact was made from the Ti foil substrate and the Cr/Au top electrode to a BNC connector. A 1mm thick layer of epoxy resin (Buehler) was deposited on the top surface of the device to act as a supporting structure around the electrode/wire interface. An impedance sweep was carried out on the thick film device on Ti foil, the response was found to be flat over a wide frequency band. The impedance sweep is shown in figure 7.2.

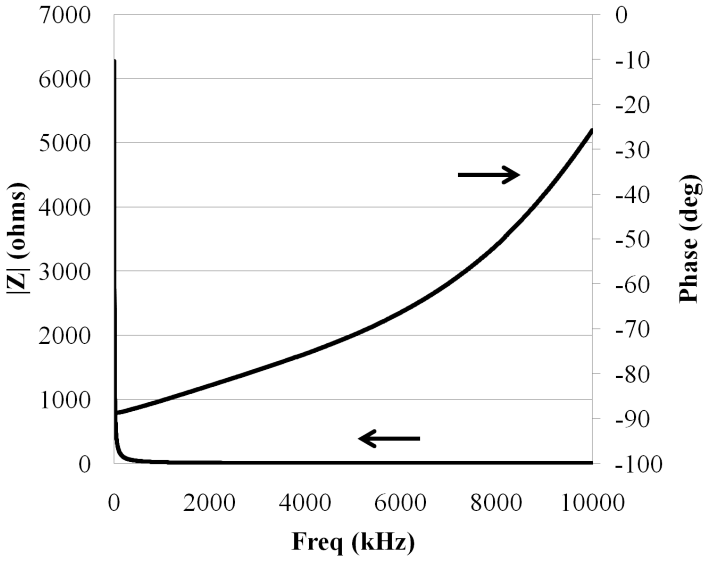

Figure 7.2: Plot showing the impedance and phase angle of the thick film device on the Ti substrate.

7.2.2 Static Applications

Validation of the thick film device on titanium foil was carried out by benchmarking the device against a PICO commercial sensor from PAC. The benchmarking

was carried out on a static system.

7.2.2.1 Acoustic Emission Testing

Hsu-Neilson testing was employed to simulate AE in a 250mm square steel plate with a thickness of 5mm. The thick film and PICO sensors were mounted on the plate as shown in figure 7.3a. Grease was used as a coupling layer and a 113 gram weight was used to press the sensors onto the plate surface. The separation between the sensors was 106mm.

2/4/6 pre-amplifiers from PAC were employed. The pre-amplification values were set to 60dB and 40dB for the thick film and PICO sensors respectively. The thick film threshold level was set to 30dB while the threshold level for the PICO sensor was set to 25dB. For both devices lower and upper filters of 1kHz and 3MHz were used, a sampling rate of 5MHz was employed. 15 Hsu-Neilson, 0.5mm diameter 2H pencil breaks were carried out at a point equidistant between the two AE sensors. The results were recorded using AEWin software from PAC.

Following these Hsu-Neilson tests the sensors were relocated on the plate and were arranged as shown in figure 7.3b. The distance between the devices was 150mm. The coupling, pre-amplification and detection software settings were consistent with the previous tests. 50 Hsu-Neilson tests were carried out and the detected AE recorded by the AEWin software.

7.2.2.2 Results and Discussion

The mean detected signal amplitudes in both testing runs were 42mV and 240mV for the thick film and PICO commercial sensors, respectively. The standard deviation of the mean amplitudes was 3mV for the thick film and 4mV for the PICO device. The thick film sensor signal was pre-amplified by an order of magnitude more than the signal from the PICO sensor. The signal energy of the thick film device signal was three orders of magnitude lower than that of the signal detected by the PICO sensor. The duration of the signal detected using the thick film sensor was similarly an order of magnitude shorter than the signal detected by the PICO sensor.

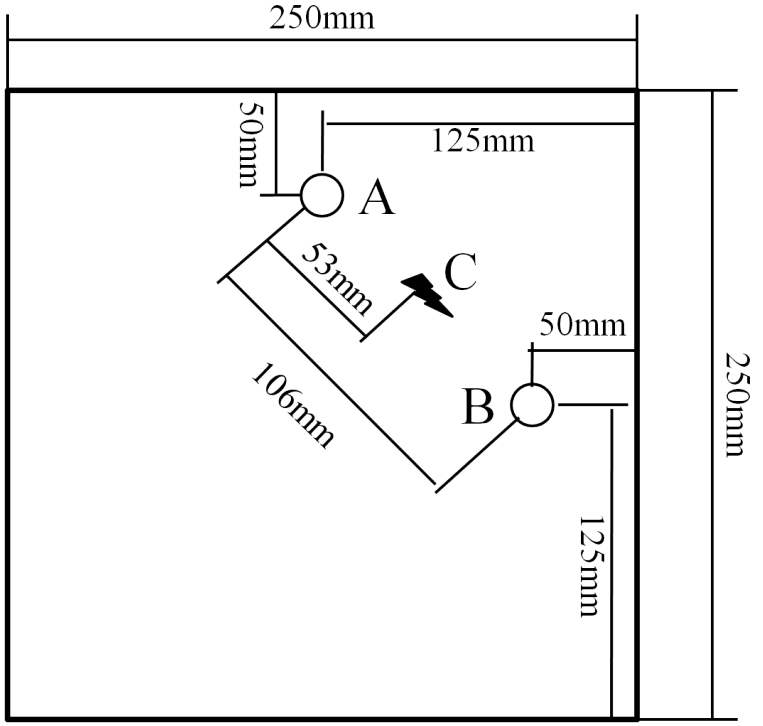

(a)

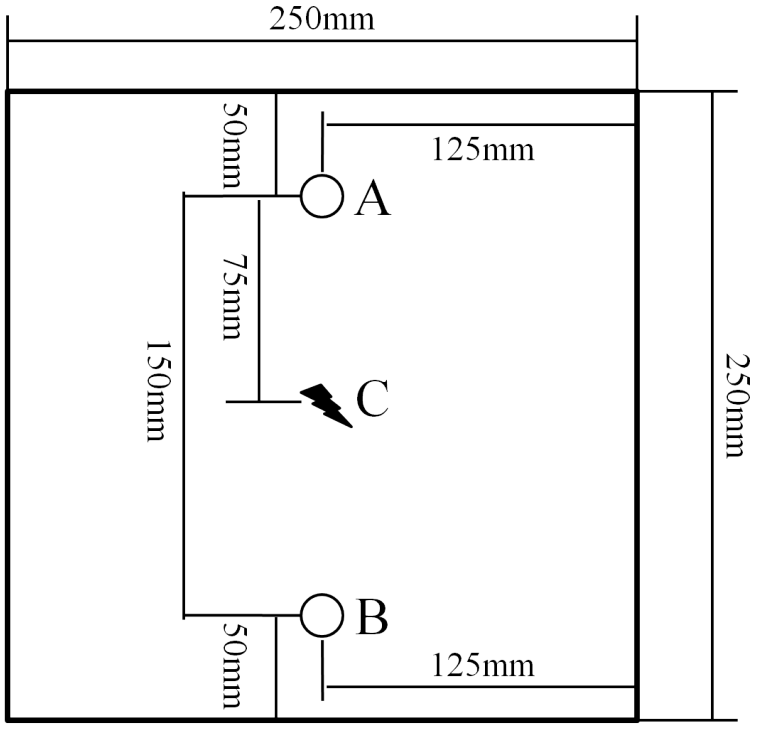

(b)

Figure 7.3: Schemes showing the mounting positions of the thick film sensor [A], PICO sensor [B] and the position of the simulated AE [C] during static testing run (a) conditions one and (b) condition two.

The time and frequency domain responses from both the thick film and the PICO commercial sensor under Hsu-Neilson testing runs one and two are shown in figure 7.4a and figure 7.4b, respectively. It can be seen from these plots that the time domain and frequency domain response to the simulated AE was consistent in both run conditions. It can also be seen that PICO sensor exhibited the characteristic resonant peak at 500kHz as seen in section 5.1.1.

It can be seen from the frequency spectra that the thick film device detected signals with a frequency between 100kHz and 500kHz. Amplitude spikes were also present at 691kHz and 912kHz in signals from both test run conditions. The 691kHz frequency spike was also detected by the PICO sensor. The spike detected in the signal emitted by the PICO sensor was similar in amplitude to the spike detected in the signal emitted by the thick film sensor.

The spike at 912kHz was not detected by the PICO sensor, possibly due to the combination of greatly reduced response to frequencies above 800kHz and a loss of more signal energy due to acoustic impedance than in the thick film device. 1.13% of acoustic energy was theoretically transmitted from the steel to the thick film, compared to only 0.77% theoretically between the steel and the PICO sensor. The spikes were not present on the spectrogram of the signal, this can be explained due to the resolution of the spectrogram being lower than than the bandwidth of the frequency spike.

Both the 691kHz and 912kHz frequency spikes correspond to a wavelength of 5mm for the asymmetric and symmetric Lamb wave components respectively. The excitation of these frequency components was caused by the AE waves reflecting and causing the plate to resonate. AGU Vallen Wavelet software (release A2009.1027) was used to carry out Gabor transforms on the waveforms detected under run conditions one and two. The spectrograms of these waveforms are shown in figure 7.5 and figure 7.6.

The spectrogram of the initial 50μs of the signals detected by the thick film and the PICO sensors under run condition one are shown in figure 7.5a and figure 7.5b respectively. These clearly show that there was high amplitude frequency content between 300kHz and 700kHz detected by the PICO sensor and 100kHz to 800kHz detected by the thick film sensor. The dispersion curve offset time in the spectrograms also showed that the wave forms reached the active element of

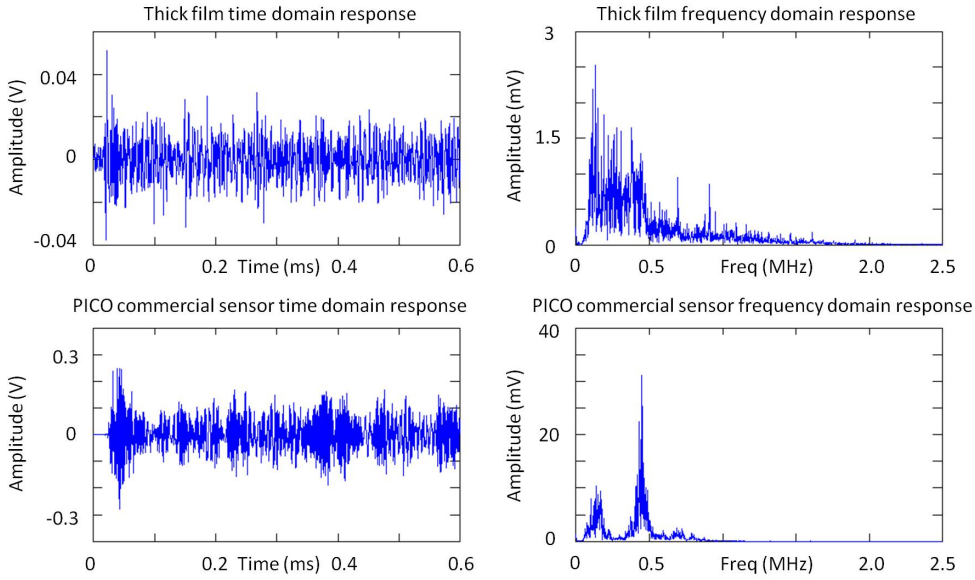

(a)

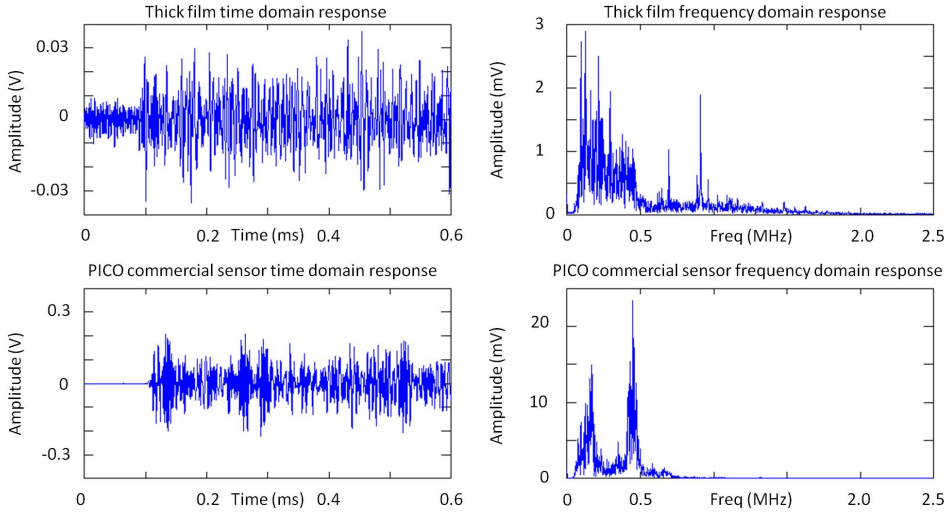

(b)

Figure 7.4: Representative plots showing the initial 600μs of the time domain (left) and frequency domain (right) signals detected by the thick film device (top) and the PICO commercial sensor (bottom) following Hsu-Neilson tests under run conditions (a) one and (b) two. The thick film and commercial device signal to noise ratios were observed to be 4.2 and 240 respectively.

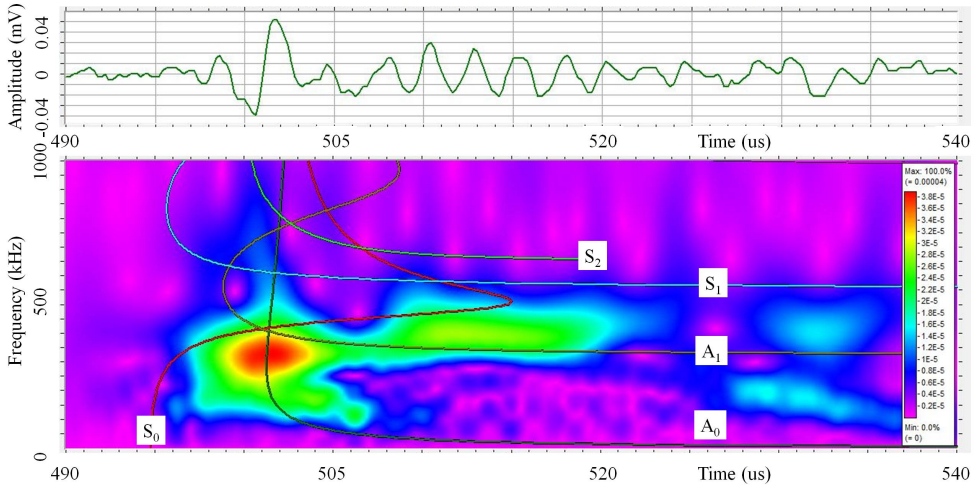

(a)

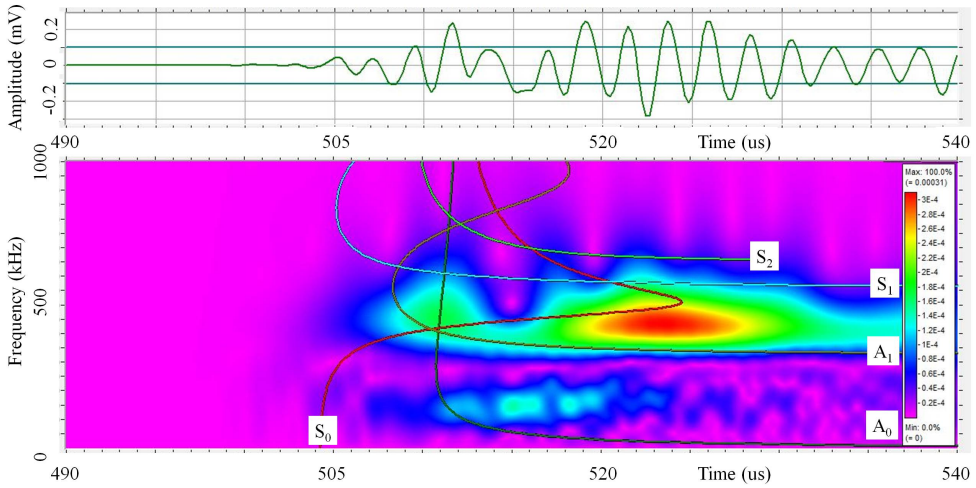

(b)

Figure 7.5: Gabor transform spectrogram of the initial 50μs of the waveform, with dispersion curves overlaid, carried out using AGU Vallen Wavelet software on waveforms detected by the (a) thick film and (b) PICO sensors following Hsu-Neilson testing on a steel plate under run condition one.

the thick film sensor 11.2μs before the active element of the PICO sensor. The delayed arrival time resulted from the alumina wear plate on the PICO sensor which was thicker than the titanium foil substrate of the thick film sensor and also transmitted sound at a lower velocity.

The maximum amplitude of the signal detected by the thick film device occurred at the point where the zeroth and first order asymmetric Lamb waves intersect with the zeroth order symmetric Lamb wave, 7μs after the signal was initially detected. This intersection takes place at a frequency of 340kHz and therefore falls within a frequency band at which the PICO sensor was shown to exhibit a reduced response to excitation (figure 5.2b). The maximum amplitude for the signal detected by the PICO sensor occurred 21μs after the signal was initially detected and was caused by the zeroth order symmetric waveform exciting the PICO sensor resonant response at a frequency between 450kHz and 500kHz.

The triple point where the A_0, A_1 and S_0 waveforms intersect occurred 7μs after the initial signal detection. The triple point occurred at a frequency to which the PICO sensor exhibits a reduced sensitivity. This resulted in a lower amplitude signal from the waveform interactions. The apparent lower amplitude of the intersection of the A_0, A_1 and S_0 wave components, combined with the S_0 wave component, exciting the highly sensitive resonant response of the PICO sensor, 21μs after the initial signal detection, resulted in a shifting of the time to maximum amplitude by 14μs.

Figure 7.6a and figure 7.6b show the Gabor spectrograms of the initial 50μs of the waveform signals detected by the thick film and the PICO sensor respectively under run condition two. Both the signals detected by the thick film and PICO sensors showed significant amplitude frequency responses between 100kHz and 750kHz. Waveform arrival times show that the thick film sensor element was activated 15μs before the PICO commercial sensor. This delay resulted from the increased thickness of the wear plate which was made alumina which exhibits a lower speed of sound than that of the titanium foil substrate of the thick film device. The initial 10μs of the signals emitted from the PICO and the thick film devices were very similar under both run conditions.

As under run condition one, the maximum amplitude of the signal detected by thick film sensors coincided with the intersection of A_0, A_1 and S_0 waveforms at a

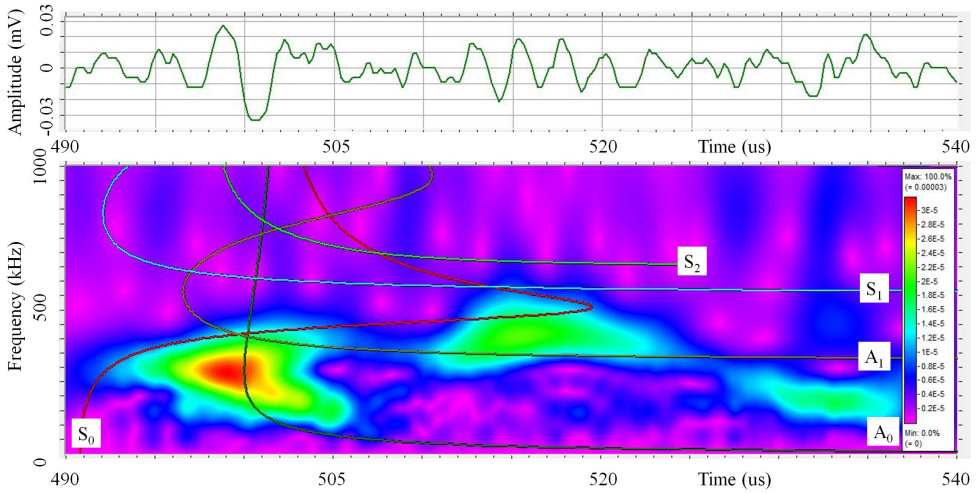

(a)

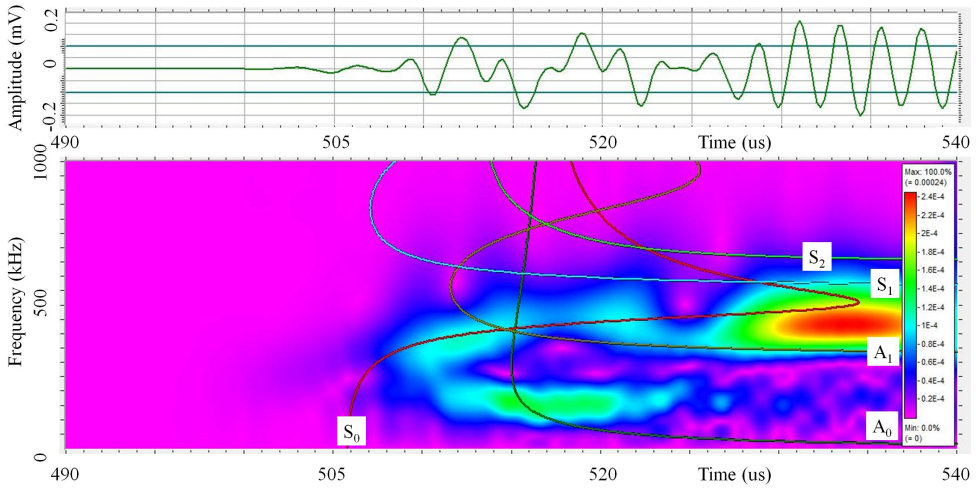

(b)

Figure 7.6: Gabor transform spectrogram of the initial 50μs of the waveform, with dispersion curves overlaid, carried out using AGU Vallen Wavelet software on waveforms detected by the (a) thick film and (b) PICO sensors following Hsu-Neilson testing on a steel plate under run condition two.

time of 7μs after the initial waveform detection and a frequency of 300kHz. The maximum amplitude fell within the low sensitivity frequency band of the PICO sensor and, as under run condition one, explained why the rise time of the PICO sensor was 17μs longer than that of the thick film. The maximum amplitude of the signal detected by the PICO sensor was shifted to the point where the symmetric, longitudinal, wave interacted with the PICO sensor resonance peak between 450kHz to 500kHz.

Possible reflection paths were identified for the thick film and the PICO commercial sensors under run condition one (figure 7.7a) and run condition two (figure 7.7b). The longitudinal and transverse speeds of sound in steel from the Vallen database - 5960m/s and 3240m/s respectively - were used, along with the changes in distance identified for each transmission path under both run conditions, to calculate the variation in time of flight for each transmission path. The reflection arrival times have been indicated on Gabor transform spectrograms of PICO sensor and thick film sensor signals under run condition one and run condition two in figures 7.8 and 7.9 respectively. The notation employed in the identification of the reflection arrival times was "L_n" and "T_n" for longitudinal and transverse waves respectively; the numeric subscript indicating the associated transmission path in figure 7.7a for run condition one and figure 7.7b for run condition two.

It was clear from the analysis of these results that the thick film on titanium foil functions effectively as a wideband AE sensor. The signal to noise ratio for the thick film sensor was just over three which is within the range recommended by industry for sensor operation. The thick film sensor exhibits a flat response over a wide frequency range making it ideal for wideband sensing applications.

The thick film device on titanium foil was comparable to the thick film deposited directly onto the 3.2mm thick Kovar sheet (section 5.1). The amplitudes of the signals detected before pre-amplification by the thick film on titanium were 57 times lower in amplitude than those detected by the PICO sensor. The thick film device on titanium foil is compared to the thick film device embedded in Kovar and the PICO commercial device, in table 7.1. The thick film on titanium demonstrated a superior performance than the thicker and larger thick film sensor on Kovar largely because the thick film on titanium exhibits greater film properties. The d_{33} of the thick film on titanium was 1.37 times greater than that of the thick film on Kovar. This was due to the bending of the titanium foil

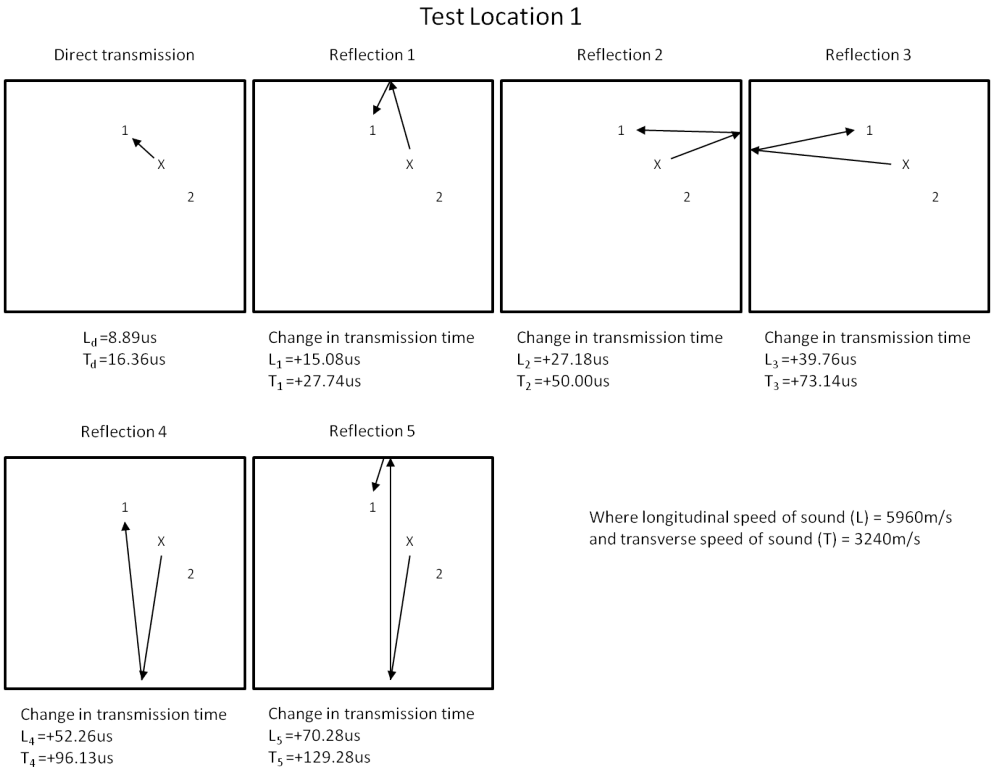

(a)

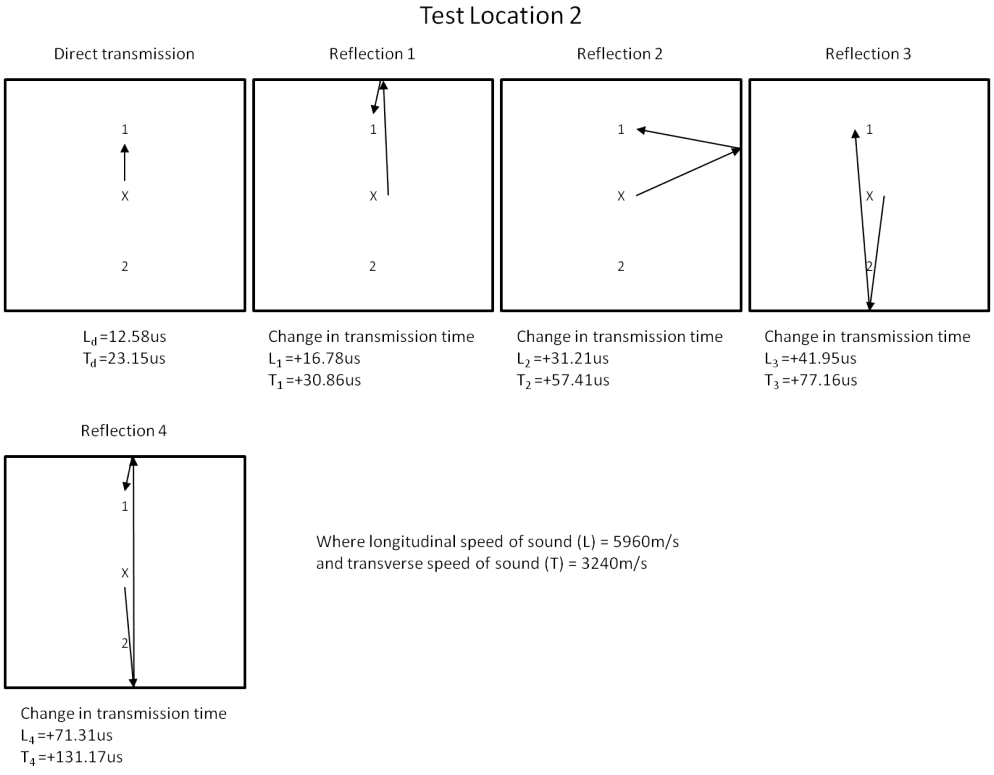

(b)

Figure 7.7: Identified paths of transmission and related times of flight for longitudinal and transverse waves under testing condition one (a) and two (b).

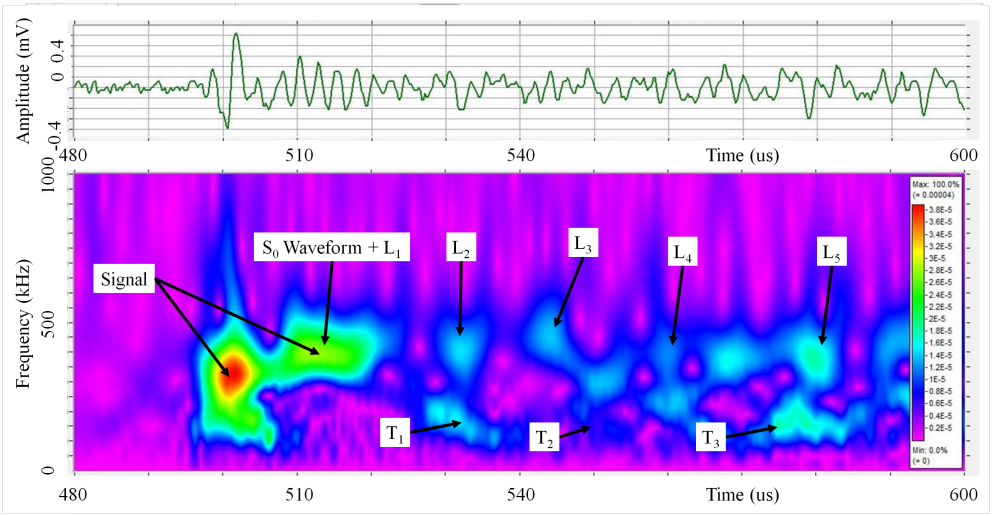

(a)

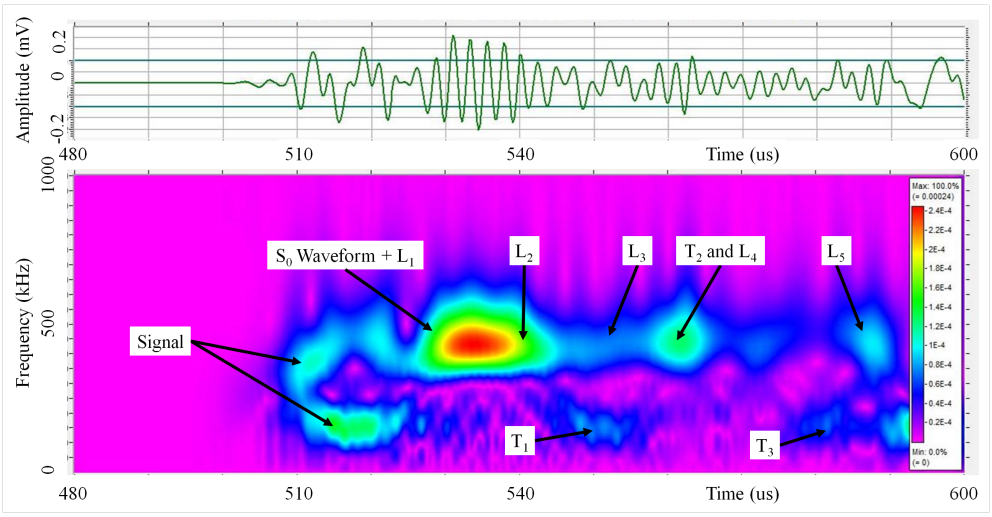

(b)

Figure 7.8: Gabor transform spectrograms of the initial 120μs of the waveforms detected by the (a) thick film and (b) PICO sensors following Hsu-Neilson testing on a steel plate under run condition one. Calculated reflection arrival times are indicated. Gabor transforms were carried out using AGU Vallen Wavelet software.

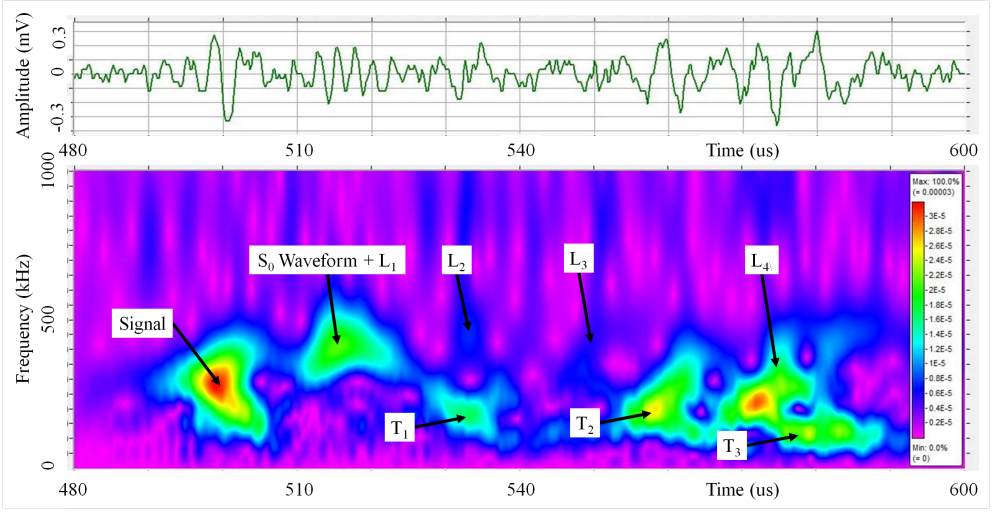

(a)

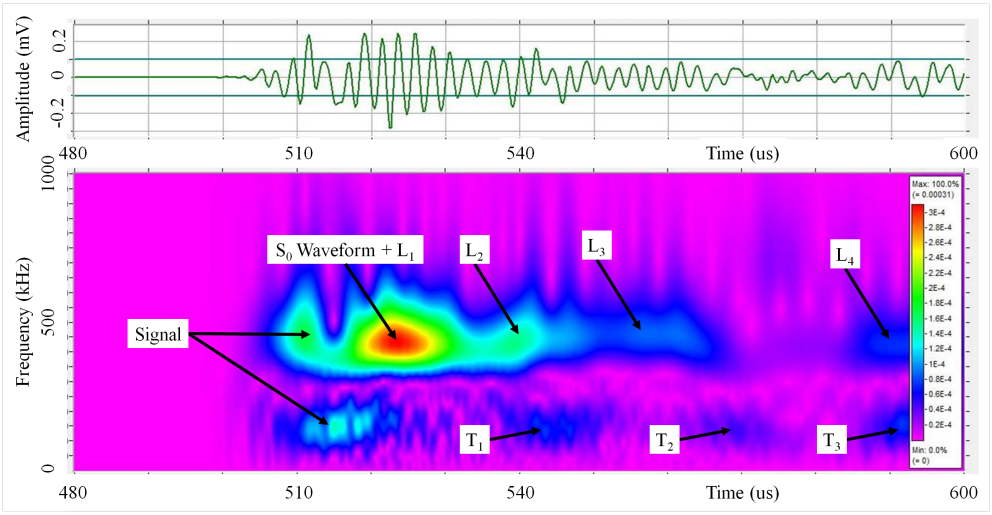

(b)

Figure 7.9: Gabor transform spectrograms of the initial 120μs of the waveforms detected by the (a) thick film and (b) PICO sensors following Hsu-Neilson testing on a steel plate under run condition two. Calculated reflection arrival times are indicated. Gabor transforms were carried out using AGU Vallen Wavelet software.

Table 7.1: Table showing a comparison of the thick film device on titanium foil, the thick film device embedded in Kovar and the PICO commercial AE sensor.

Sensor	PICO	Thick film embedded in Kovar	Thick film on titanium foil
Relative signal amplitude before pre-amplification	1	0.0541	0.0192
Relative thickness	∼1	0.176	0.044
Relative sensing area	∼1	4.00	1.56
Relative d_{33}	1 (N.B. bulk material property)	0.115	0.157

during processing which released stress in the film. This bending was not possible in the Kovar sheet and despite the thermal expansion of Kovar being $6x10^{-6}$/K compared to $8.5x10^{-6}$/K for titanium, the stress in the thick film on Kovar was still greater than that in the thick film on titanium [133]. Another reason for the relatively poor performance of the thick film on titanium was the lack of electrical impedance matching between the thick film device and the commercial data logging software. This may affect the properties of the signal output from the thick film sensor, reducing signal amplitude.

7.2.3 Dynamic Applications

Following the validation of the thick film device on the Ti foil substrate by static AE testing on a metal plate, dynamic testing was carried out. The devices were mounted on the bearing housing of a rotating shaft system. These tests were carried out to assess the ability of the PZT thick film device to detect bearing faults in rotating systems. The thick film device was again benchmarked against a commercially available sensor.

7.2.3.1 Acoustic Emission Testing

Benchmarking of the thick film device on titanium foil in dynamic situations was carried out by mounting both a thick film and a WD, wideband, sensor from PAC

(a) (b)

Figure 7.10: (a) Bearing test-bed used for the benchmarking of the thick film PZT sensor on titanium foil against the WD commercial sensor and (b) the mounting locations of the sensors.

on a bearing test rig. The bearing test rig can be seen in figure 7.10a and the mounting position of the thick film and WD sensor on the bearing housing can be seen in figure 7.10b. The test rig consisted of a shaft suspended by one artificially damaged and two undamaged bearings. The damaged bearing was a Cooper Split 01C/40GR bearing. The Cooper Split 01C/40GR bearing had a 72mm rolling pitch diameter and consisted of 10 bearing elements of 12mm diameter with a 0° contact angle.

The shaft was connected to an electric motor which enabled the shaft to be driven at speeds between 500rpm and 6000rpm. A hydraulic ram with a maximum load of 6.89MPa was also connected to the shaft to create a load on the bearing during the testing cycle. The sensors were permanently mounted on the bearing housing using Super Glue as a coupling agent. The sensors were connected to pre-amplifiers set at 40dB and the signal was analysed by AEWin software from PAC with a sampling rate of 2MHz.

Three testing runs were carried out under various loading conditions. Initially the shaft was rotated at 1000rpm, 2000rpm and 3000rpm under zero load. In the second testing condition the shaft was rotated at 1000rpm with a load of 2.07MPa. The third testing condition was carried out at 2000rpm at a load of 1.17MPa. Under each testing condition manual triggering for data collection was employed.

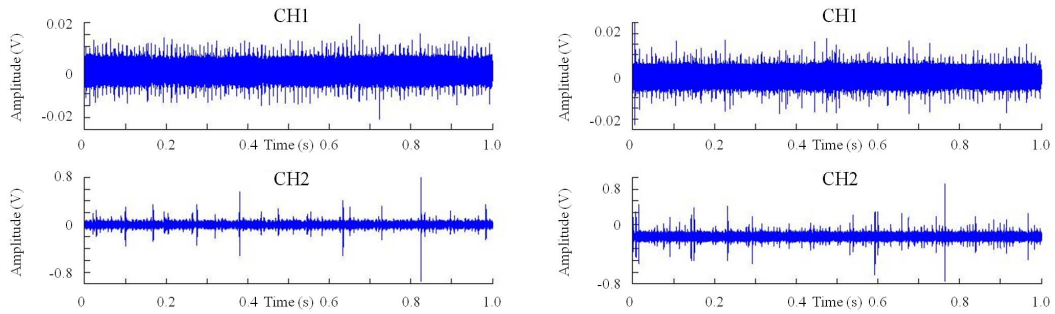

(a) (b)

Figure 7.11: Two time domain responses of the thick film PZT on titanium foil (CH1) and WD commercial sensor (CH2) to a shaft with a damaged bearing rotating at 2000rpm under a load of 1.17MPa. A rattling sound was heard emanating from the bearing housing during the recording of these hits.

7.2.3.2 Results and Discussion

Initial test runs carried out for the purposes of sensor calibration indicated that the noise in the signal detected by the thick film sensor was of such high amplitude that the signal to noise ratio was less than one. The noise signal was an order of magnitude greater in amplitude when the titanium substrate was mounted directly onto exposed metal sections of the test rig. This was due to the rig acting as an aerial for RF interference generated by a large transformer located 15 meters away from the test bed.

The titanium bottom electrode was isolated from the rig by a polymer film, this reduced the amplitude of the noise. The signal to noise ratio was still below one when testing was carried out. A representative response can be seen in figure 7.11, this response was recorded with the shaft rotating at a speed of 2000rpm and with a load on the shaft of 1.17MPa. During this testing situation a rattling sound was observed emanating from the bearing hub on which the sensors were mounted. The time domain responses for each of the testing situations can be seen in Appendix A.

It was clear that as the shaft rotational speed and applied loading increased the number of peaks detected by the WD sensor increased, as did the amplitude of those peaks. With the low signal to noise ratio of the thick film sensor it was impossible to detect any emissions resulting from a mechanical source.

The response of the WD commercial sensor was as expected from a system containing a damaged bearing. The AE events are caused by the damaged section of the bearing interacting with the other bearing components. The signal response expected from a damaged bearing is well understood and the frequency of the signal caused by the damage could be used to assess which component of the bearing was damaged [35]. The signal to noise ratio of by the thick film sensor was such that use of the current device for the detection of AE was impractical on dynamic systems.

7.2.4 Thick Film/Titanium Foil Integration Conclusions

A thick film sensing element was integrated with a titanium foil substrate for use in detecting AE in both static and dynamic situations. This active element was effective at detecting AE in static situations. The amplitude of the thick film device response was 20 times lower than that of a commercial PICO sensor before pre-amplification. The thick film sensor had a similar sensing element area and an element thickness three orders of magnitude less than that of the commercial device.

The thick film device on titanium also performed well compared to the thick film integrated into the Kovar sheet which only exhibited a comparative response 3.08 times greater in amplitude than that of the thick film on titanium despite the thick film on titanium being 4 times thinner and having a sensor element area 2.5 times lower than that of the device integrated with the Kovar. There was also an extra transmission medium inter-facial layer to cause attenuation of the signal present in the thick film on titanium foil sensor system. However, the properties of the thick film on titanium were greater than the properties of the thick film on Kovar. This was due to the bending of the substrate during processing reducing the stress in the film compared to the Kovar sheet which constrained the film and caused increased stress, thus reducing the film properties.

The signal to noise ratio of the titanium foil sensor limited the devices use in dynamic applications and in situations where the external interference from RF sources was high. The commercial sensor used for the dynamic application benchmarking was of a differential design to aid in eliminating external noise. The commercial sensor also had electrical shielding to reduce the effects of external noise.

Had the PICO sensor been employed the signal amplitude would have been lower, owing to the reduced dimensions of the PICO sensor active element when compared to the WD sensor. The amplitude of noise in the signal from the PICO sensor would also be greater than that in the signal from the WD sensor. This is due to the PICO sensor consisting of a single active element. As such, the interference from external EM noise sources cannot be eliminated from the signal. The performance of the PICO sensor in the dynamic testing application would have been poorer than that of the WD sensor.

7.3 Integrated MEMS AE Sensors on Metal Foil Conclusions

Thick films were deposited onto Kovar foil and it was found that the properties of the film deposited onto the foil were superior to those of the thick film deposited onto the Kovar sheet. This was due to the reduction in film stress in the film resulting from the reduced constraints on the film during heating. These reduced constraints are due to the flexibility of the foil which enabled the stress in the film to be released which caused the film to bend instead of cracking and reducing the film properties, as was apparent in the case of the thick film on the Kovar sheet. As such the deposition of PZT onto thin metallic foils was investigated.

Thick film PZT was deposited onto titanium foil by spin coating. The thickness of the deposited film was limited by substrate bending caused by film contraction due to liquid loss during the heating stages of film production. The bending, while limiting film thickness, resulted in a relaxation of stress in the thick film compared to the tightly constrained thick film deposited onto Kovar; resulting in improved film properties. The amplitude response of the thick film on titanium was lower than that of the thick film on Kovar, however, signal characteristics caused by wave interaction with the transmission media were still clear. The frequency response of the thick film device on titanium was flat and performed well when compared to the PICO sensor.

The thick film on titanium was shown to operate effectively as a wideband static AE sensor in static testing situations. An investigation was carried out to assess

the effectiveness of the thick film on titanium for detecting AE in dynamic testing situations. The thick film on titanium sensor was mounted on a bearing housing containing a damaged bearing alongside a commercial WD differential AE sensor. The damaged bearing was rotated at various speeds and under various loads to assess the ability of the thick film on titanium to identify damage to the bearing. It was found that the thick film on titanium foil was unable to identify the damage to the bearing. This was due to a signal to noise ratio lower than one, meaning that the signal was masked by excessive noise.

The FOMs employed in this work were used to assess the performance of the thick film on titanium foil compared to the thick film on a Kovar plate substrate. The relative S/N and relative A/V ratios were calculated as 57.1 and 2.6×10^3 respectively. The relative S/N ratio of the device was poor compared to that of the thick film on Kovar which was 1.9. This was due to the titanium substrate and the metal test plate, to which it was in contact, acting as an aerial for EM noise from the surrounding environment. The S/N ratio can be improved by the use of electrical shielding of the thick film on titanium and the grounding of the test plate. Despite the greater issues with the processing of thick film PZT on titanium compared to processing on Kovar, the thick film on titanium exhibited superior properties relative to the volume of the sensing area.

Chapter 8

Piezoelectric/Polymer Composite Materials For Integrated AE Applications

8.1 PZT/Polymer Composite

There were difficulties with integrating thick film PZT directly with structural elements which require monitoring by AE sensors. Some difficulties included the limits on substrate dimensions imposed by the spin coating method utilised in this work. Other deposition methods can be employed spray coating, EPD [91] or EHDA [92] for example. However, the films deposited by these methods do still require sintering at temperatures above 700°C. Sintering at these temperatures may be possible by halogen lamp but these temperatures may damage the structural element which is being monitored, reducing the structural integrity of the element, or causing an undesirable oxidation reaction.

The integration of sensors was important as it reduced the distortion of signal due to transmission through coupling layers. As such it was important to find a solution to these issues. PZT paint was one such solution. PZT paint was comprised of PZT inclusions in a polymer matrix and combined flexible deposition techniques with processing temperatures below 150°C.

8.1.1 Materials and Methodology

The PZT paint was a composite of PZT powder in a polymer matrix. The PZT powder chosen for the initial material manufacture was PZ26 from Ferroperm. This was the same powder used in the production of PZT slurry for composite film deposition. A liquid polymer matrix was required to enable the deposition of a film onto a substrate which was then dried to form a PZT/polymer composite film.

8.1.1.1 PDMS Matrix Material

Several polymers were considered for use as a matrix material. Initially Sylgard 184 polydimethylsiloxane (PDMS) was explored as a matrix material. The resin and hardener were mixed in a volume ratio of 10:1 as instructed by the manufacturer. As the volume of the resin was an order of magnitude greater than that of the hardener the PZT powder was mixed into this component. PZT powder volume loadings of 1%, 2.5%, 5%, 10% and 15% were introduced into the PDMS. Samples with these powder loadings were prepared with Igepal-630 dispersant volume loadings of 0%, 0.5%, 1%, 1.5%, 2% and 2.5%.

It was found following mixing that in the higher PZT volume loading samples, 5vol.% and above, the polymer was insufficient to coat the powder. This was due to the high viscosity of the PDMS resulting in issues with mixing the PZT into the PDMS. It was possible to mix the lower volume loaded samples, below 2.5vol.%, with PZT however the viscosity of the final PZT/PDMS was too high to enable deposition of a uniform film. The dispersant had a negligible effect on the dispersion of the PZT powder within the PDMS matrix regardless of volume loading.

8.1.1.2 PVAc Matrix Material

To reduce the viscosity of the composite a solvent was required to dilute the matrix material. The solvent was then evaporated off following the composite deposition resulting in a PZT/polymer film of a desired volume loading. The polymer used in this case was polyvinyl acetate (PVAc). Both acetone and toluene were used as solvents to dissolve the PVAc. Varying volume ratios were used including

25, 20, 15, 10 and 5 to 1 ratios of solvent to PVAc.

The PVAc was left to dissolve over night in varying volumes of solvent. PZT was added in volume loadings of 48%, 30%, 20%, 15%, 10% and 5% and the viscosity, which dictates the feasibility of depositing a uniform layer, was assessed. It was found that the choice of solvent had little effect on the deposition properties of the composite and as such acetone was chosen as the solvent over toluene because it was more readily available and there were fewer associated health concerns.

A solvent to polymer ratio of 25 to 1 was found to exhibit a suitable viscosity to be employed in combination with a 48% volume loading of PZT. Lower solvent to polymer ratios, when combined with PZT powder were found to be too viscous for the deposition method employed in this work. 0.05g of Igepal-630 dispersant was added to the composite to ensure dispersion of powder following mixing. The PZT powder was mixed with the PVAc/acetone matrix using a Silverson high shear mixer operating at 4000rpm for 10 minutes.

The PZT/PVAc composite was deposited by pipette onto the surface of a platinised silicon wafer masked using an 80μm thick self-adhesive polymer within 30 minutes of mixing. A doctor blade was drawn across the surface of the mask to remove the excess material. The solvent in the deposited composite was then left to dry at room temperature. A second sample was deposited 3 hours after mixing to assess the effects of ageing on the composite solution. Confocal laser scanning microscopy was carried out on the samples deposited at different times after mixing.

The confocal images of these two cases can be seen in figure 8.1. The confocal image showed that it was essential to deposit the composite onto the substrate as soon as possible following mixing, a delay of 3 hours resulted in the PZT powder agglomerating of the matrix solution. This led to a surface of large particles in the film with a thin layer of matrix material between particles (figure 8.1b). This effect was not present in the films deposited within 30 minutes of mixing (figure 8.1a). A SEM image of the film deposited 3 hours after mixing can be seen in figure 8.1c. This image confirms the presence of agglomerates within the deposited film. SEM micrograph of a film deposited within 30 minutes of mixing was trammelled by high levels of film charging.

Table 8.1: Table showing variation of electrical properties pre- and post-poling with percentage volume PZT powder loading in a PVAc matrix.

PZT % vol. loading	Poling condition	ϵ_r	R(MΩ)	loss	d_{33}(pC/N)
20	No	12.8	1.73	0.042	-
30	No	19.1	2.11	0.016	-
40	No	26.9	1.23	0.055	-
48	No	28.9	29.80	0.099	-
	Yes	20.9	158.75	0.026	5.35

8.1.2 Effects of PZT Volume Loading

25 to 1 volume matrix solutions of acetone to PVAc were produced. PZT powder was added to these solutions to form composite slurries which would result in powder loading percentages of 20vol.%, 30vol.%, 40vol.% and 48vol.% following the evaporation of the acetone. 0.05g of Igepal-630 was added to each composite slurry. The slurries were mixed for 10 minutes at 4000rpm using a Silverson high shear mixer. Following mixing the slurries were deposited onto self-adhesive polymer sheet masked platinised silicon wafers by pipette and a doctor blade was used to remove the excess material. The films were left to dry in air at room temperature.

Confocal microscopy was used to assess the mean film thickness of each of the deposited films. The mean film thickness measurements for 20vol.%, 30vol.%, 40vol.% and 48vol.% powder loadings were 7.8μm, 10.5μm, 13.3μm and 14.9μm respectively. Electrical testing was carried out on the films and the variation of ϵ_r, loss and resistance with powder volume loading and the results can be seen in table 8.1. Corona poling was carried out on the 48vol.% PZT loaded film. A field strength of 16kV was employed with a pin to sample separation of 25mm at 130°C for 15 minutes. The sample was then cooled to 60° under field.

The relative permittivity values of the PZ26/PVAc films with varying powder volume percentage loading are plotted in figure 8.2 along with Bruggeman non-symmetric, Sen-Scala-Cohen, Jylha-Sihvola, Looyenga and Lichtenecker models of permittivity variation with inclusion volume fraction variation. The ϵ_r of PVAc

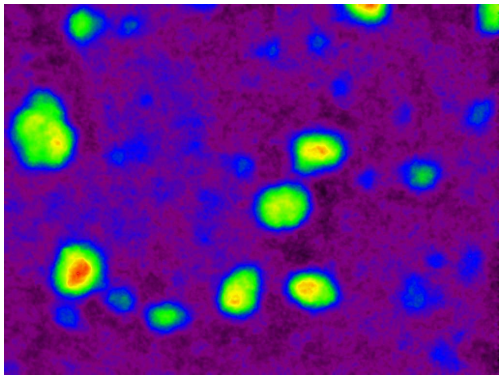

(a)

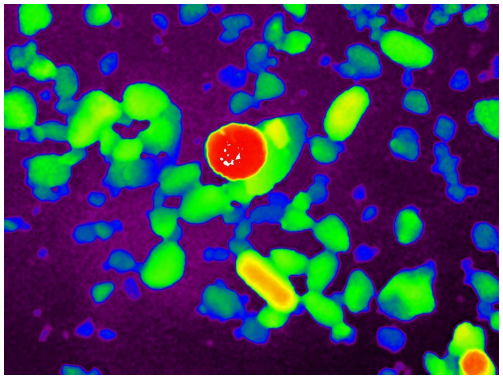

(b)

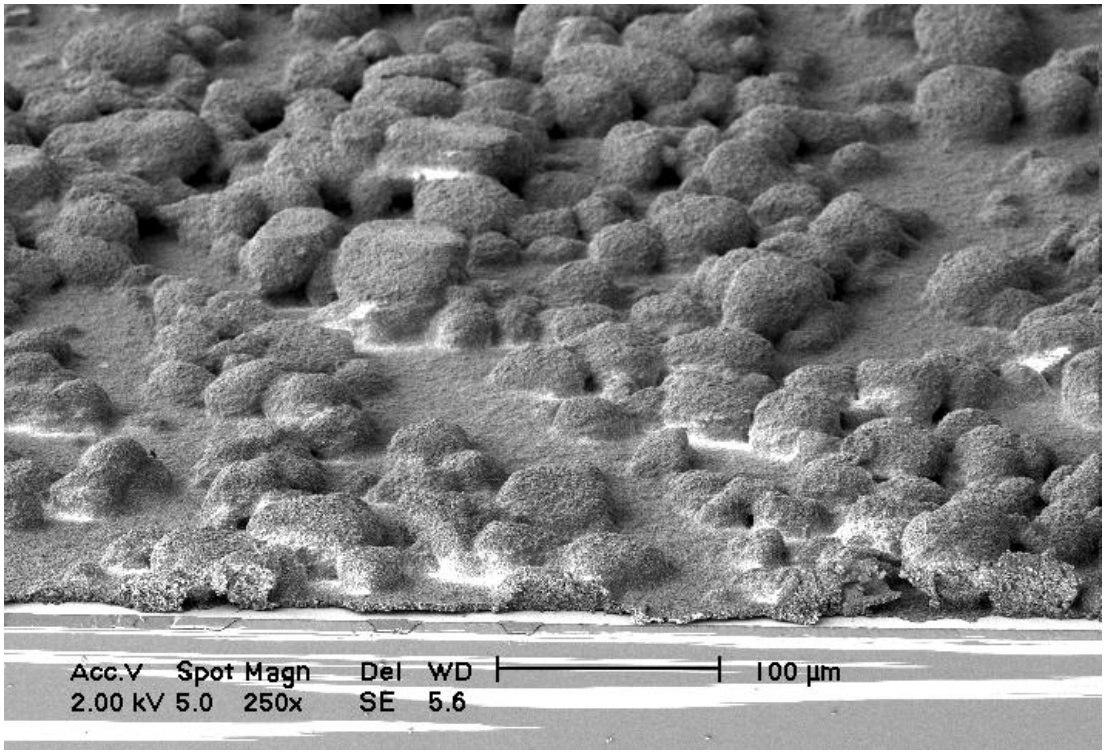

(c)

Figure 8.1: Images showing the effects of agglomeration of the PZT/PVAc composite with time after mixing showing the surface a 480μm by 640μm surface area of the PZT/PVAc composite film deposited (a) 30 minutes and (b) 3 hours after mixing using a Silverson high shear mixer. (c) A cross-sectional SEM image showing the surface of the PZT/PVAc composite film deposited 3 hours after mixing is also shown.

and bulk PZT were used for calculation of the permittivity models, these values were 3.4 and 1330 respectively. It can be seen that for powder volume loadings of 20vol.%, 30vol.% and 40vol.% the Lichtenecker model provides a good approximation.

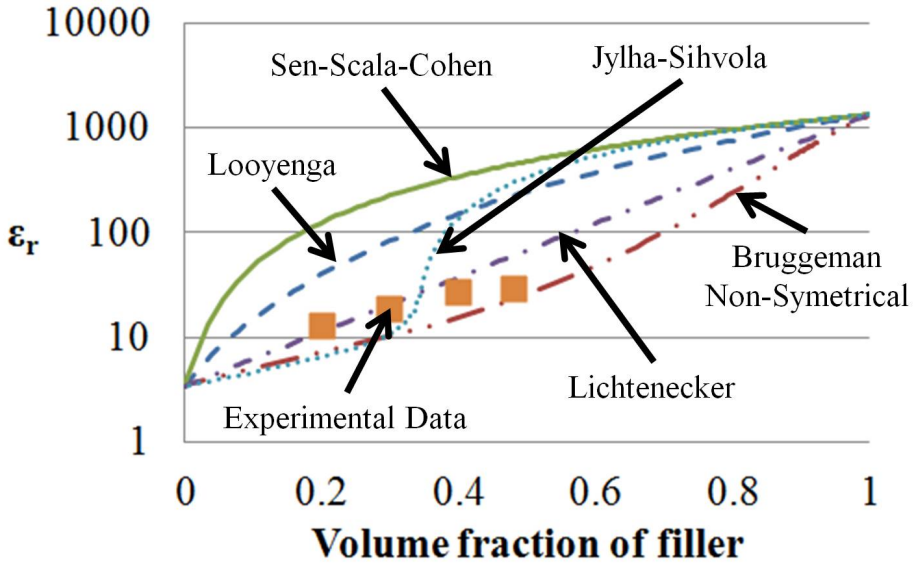

Figure 8.2: Plot showing the variation of the PZ26/PVAc relative permittivity with volume fraction of powder loading and comparing results with theoretical models of permittivity variation.

The Lichtenecker model was expected to provide a good approximation to the ϵ_r of the system when the R_ϵ was greater than 100. The R_ϵ of the PZT/PVAc composite system was 391. The 48% powder volume loading film case was more closely estimated by the Bruggeman non-symmetric equation, whilst the Sen-Scala-Cohen equation was a poor estimate of the experimental data. This indicated that the volume loading was below the percolation threshold. This was unexpected as the Bruggeman non-symmetric model was traditionally employed in powder percentage loading situations lower than 35% and indicates that the inclusions were near symmetrically distributed in the matrix material.

The lower than expected ϵ_r resulted from a reduced measured capacitance whilst the thickness of the film was consistent with the thickness observed for the other volume loading cases. This supported the conclusion that the distribution of PZT inclusions in the polymer matrix was close to symmetric indicating that the shear mixing process was effective and that deposition within 30 minutes of mixing was sufficient to avoid the formation of agglomerates. This conclusion was further

supported by SEM micrograph of a 48vol.% loaded film deposited within 30 minutes of mixing (figure 8.3). This image shows the distribution of PZT inclusions to be near symmetric.

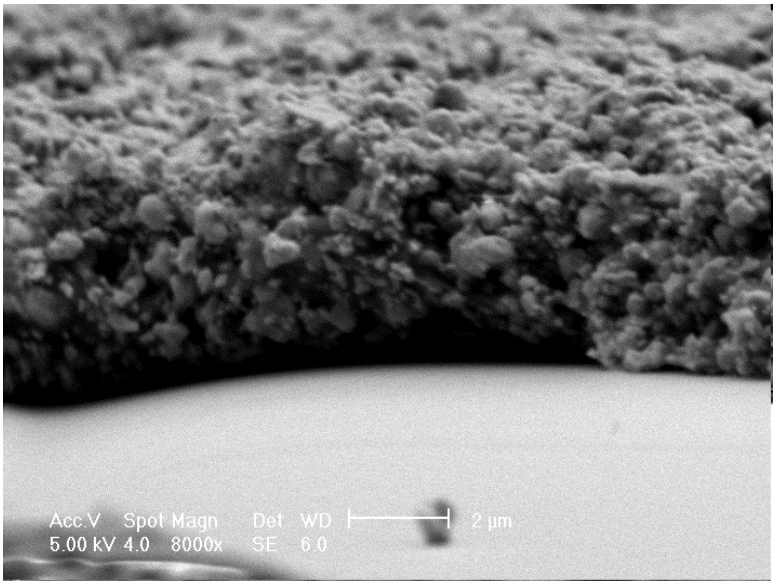

Figure 8.3: SEM image showing the near symmetric distribution of 48vol.% loading PZT inclusions in a PVAc matrix, the PVAc matrix can clearly be seen.

8.1.3 Improvement of Material Properties

A 48% volume powder loaded film was deposited onto a platinised silicon wafer as described previously. A Cr/Au top electrode 16μm/54μm thick and 2mm in diameter was deposited by evaporation. The film was then poled by contact poling under a field of 9V/μm for 10 minutes at 130°C then cooled under field until the temperature was below 50°C. Following poling the electrical properties were measured using a Wayne Kerr and a Berlincourt d_{33} meter. The film resistance and loss were measured as 159MΩ and 0.026 respectively. The ϵ_r was calculated to be 21 and the d_{33} was measured at 5.35pC/N.

The relatively low d_{33} of the PZT/PVAc composite film when compared to thick films deposited by other methods was explained by several factors. The force applied to the film may be absorbed by deformation of the PVAc matrix and as such the force applied to the PZT inclusions may be lower than that of the overall force on the film. The PVAc matrix material may also act as a dielectric, reducing

the net charge transfer in the material. The d_{33} of the PZ26 powder inclusions in the composite was poorer due to damage caused by the material processing involved in the powder production. In traditional PZT composite systems this powder was heat treated during sintering. This allows film recrystallisation to take place which increases the electro-mechanical properties of the film.

Molten Salts Annealing

Annealing of the PZT powder by molten salts processing was one method of reducing the damage of PZT powders caused during material processing. Molten salts annealing improved material properties by ensuring that the particles of PZT were isolated. The molten salts process was attractive as the materials involved were non-reactive and were easily removed from the desired product following treatment. Molten salts processing was carried out on the PZ26 powder before the powder was added to the PVAc/solvent solution. A 1:1 molar ratio of NaCl powder and KCl powder was produced. PZT powder was placed in a furnace with the salt mix in a 1:1 ratio by weight. The molten salts mix was then heated to 700°C for 2 hours using a ramp rate of 10°C/min. Once cooled the mix was washed and dried to remove all of the salt leaving annealed PZT. The molten salts treated PZT was added to the PVAc/solvent solution in sufficient quantities to result in a 48% volume powder loaded film following the removal of the solvent by drying. Igepal-630 dispersant was employed and the slurry was mixed in the same fashion as previously described.

The molten salts PZT/PVAc slurry was deposited onto platinised silicon as previously described resulting in a homogeneous, 10μm thick film. Cr/Au top electrodes were evaporated onto the top surface of the dried film and the electrical properties of both samples were measured. An ϵ_r, resistance and loss of 50.6, 9.6MΩ and 0.1205 were recorded

Corona poling was carried out to avoid damage caused to the film by the use of sprung probes. Poling was carried out under a field of 16kV for 15 minutes at 135°C before cooling to below 50° under field. A sample to pin separation of 25mm was employed. Electrical testing was carried out on the molten salts PZT/PVAc film following poling. The ϵ_r of the film was calculated to be 48.0; resistance and loss were found to be 4.9MΩ and 0.0242 respectively. The d_{33} of

Table 8.2: Table showing the effect of molten salts treatment on a PZ27 powder in a PZT/PVAc composite film before and after poling.

PZ27 treatment	Poling condition	ϵ_r	R (MΩ)	loss	d_{33} (pC/N)
Un-treated	No	178.8	50.7	0.046	-
	Yes	219.1	95.6	0.020	0.0
Molten Salts Annealed	No	35.5	37.9	0.034	-
	Yes	24.7	91.0	0.019	2.3

the film was found to be 8pC/N.

The d_{33} and an ϵ_r of the PZT/PVAc, in which the PZT had been treated using the molten salts process, was 1.45 and 2.30 times greater than the PZT/PVAc in which the PZT was untreated. This indicates that the molten salts process was effective in recrystallising the PZT powder. However, the d_{33} was still an order of magnitude lower than that of thick films deposited by other processing techniques.

PZ27/PVAc Composite Films

The effects of changing the composition of the PZT powder used in the manufacture of the PZT/PVAc slurry were investigated. The hard PZ26 previously employed was replaced by PZ27, also from Ferroperm. PZ27 was a soft PZT with a considerably greater d_{33} than PZ26, 425pC/N and 330pC/N respectively [138]. PZ27 also exhibited a greater ϵ_r than PZ26, 1800 compared to 1300, and a Q-factor three orders of magnitude lower.

Half of the PZ27 was heat treated using the molten salts process described previously. Two PZ27/PVAc composite slurries with 48% volume powder loading were prepared, one containing molten salts treated powder one containing untreated powder. These slurries were then deposited onto a platinised wafer following the masking/doctor blade process described previously. Cr/Au top electrodes were evaporated onto the dried films and electrical measurements were carried out (table 8.2).

Both films were poled at 130°C for 25 minutes under a 16kV field with a pin to sample separation of 15mm and then cooled to below 65°C whilst under the

field. Electrical measurements were carried out on the poled films. The molten salts treated PZ27/PVAc film ϵ_r was calculated to be 24.7, the resistance and loss were measured as 91.1MΩ and 0.019 respectively. The d_{33} was measured as 2.3pC/N. The ϵ_r of the untreated film was calculated to be 219.1 with a resistance of 95.6MΩ and a loss of 0.020. The d_{33} of the untreated PZ27/PVAc film was negligible. The field strength used for poling the untreated PZ27/PVAc was increased to 17.5kV, however this resulted in widespread shorting across the film.

The physical structures of the films were investigated using confocal microscopy and SEM to image the films. Comparative average surface profiles obtained through confocal microscopy can be seen in figure 8.4. It was seen that the untreated PZ27/PVAc slurry resulted in a much greater film thickness than the molten salts treated PZ27/PVAc slurry. A more detailed cross section of the untreated PZ27/PVAc film (figure 8.4c) indicated the presence of large powder agglomerates in the film which were separated by areas in which the substrate was covered by a sub-micron thickness layer of PVAc with no PZ27 powder present.

The poor electrical properties of the untreated PZ27/PVAc film were explained by the physical structure of the film. The areas of substrate which were coated by the thin layer of PVAc limited the strength of field which could be applied before shorting occurred. The limited field strength was not great enough to successfully pole the considerably thicker agglomerates which made up the remainder of the film. In addition to this, any shorting which occurred during poling would damage the substrate covering meaning any charge generated by the PZT was earthed. As such the d_{33} of the untreated PZ27/PVAc composite film was measured as zero.

Investigation of the molten salts PZ27/PVAc film by SEM showed a homogeneous film which consisted on thin flakes of PZ27 stacked on top of each other (figure 8.5). These flakes appeared to be separated by dielectric layers of PVAc. This layered structure explained why the d_{33} of the molten salts treated PZ27/PVAc film was four times lower than that of the molten salts treated PZ26/PVAc film which was of similar dimensions.

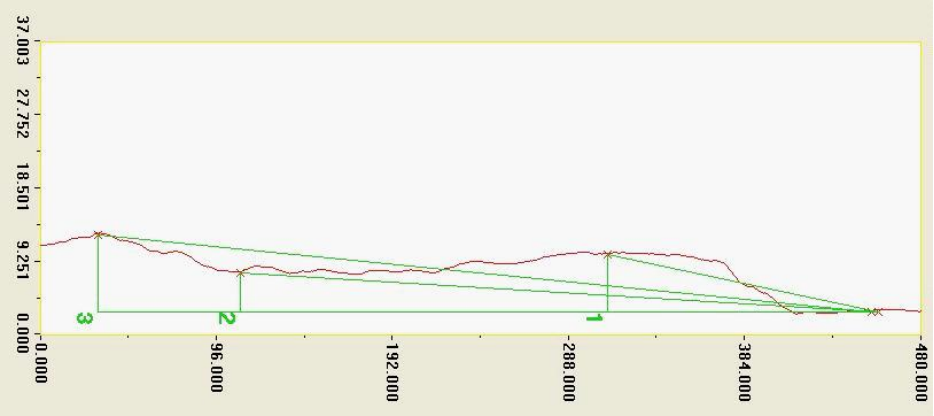

(a)

(b)

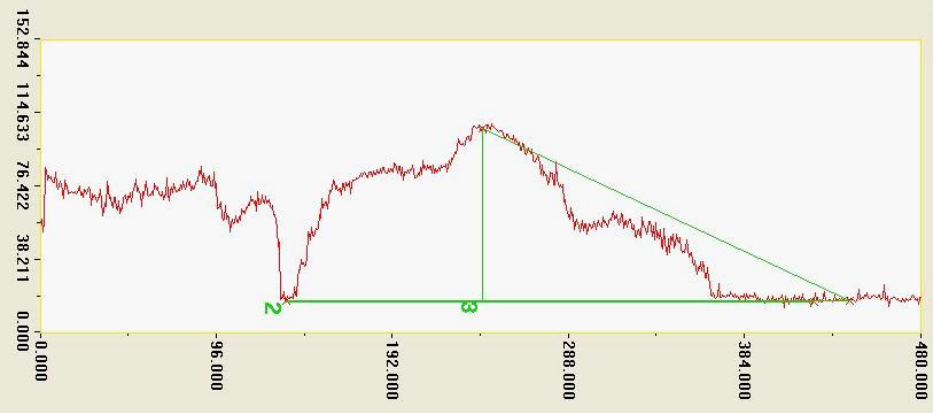

(c)

Figure 8.4: The effects treating PZT using a molten salts method on the surface profiles of PZT/PVAc composite films measured by confocal microscopy. (a) Surface profile of the molten salts treated PZT/PVAc composite film. The film thickness at points 1, 2 and 3 were measured as 7.15μm, 4.82μm and 9.73μm respectively. (b) Surface profile of the untreated PZT/PVAc composite film. The film thickness at point 1 was measured as 72.846μm. (c) Surface profile of the untreated PZT/PVAc composite film. The film thickness at points 2 and 3 were measured as 0.79μm and 89.784μm respectively.

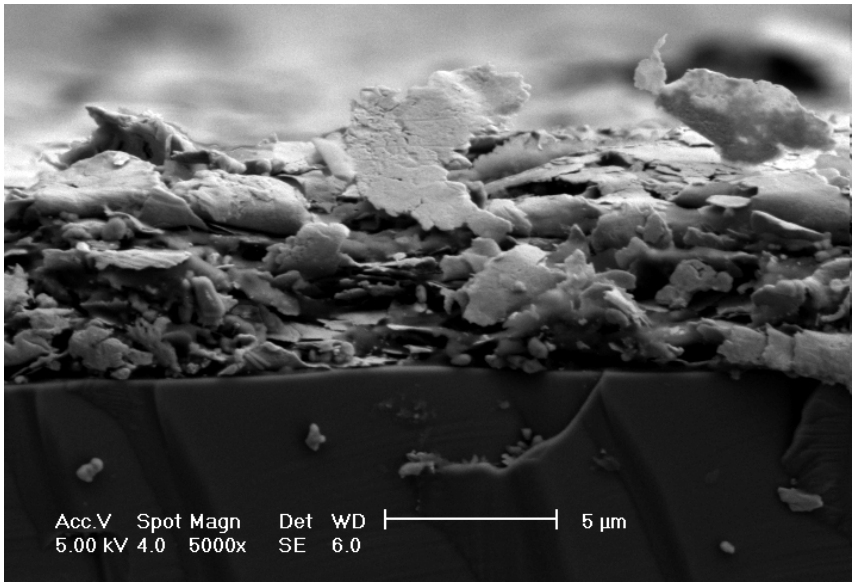

Figure 8.5: SEM image showing the stacked PZT-flake/polymer structure of the molten salts treated PZ27/PVAc composite film.

Materials Selection Conclusions

It was clear from the characterisation and improvement of PZT/PVAc composite films that the film properties were considerably poorer than those of films of similar dimensions deposited by spin coating. The greatest film properties were observed in the molten salt treated PZ26/PVAc composite. The ϵ_r of the film was calculated as 48.0 and the d_{33} of the film was found to be 8pC/N. This compared poorly to the PZT film deposited on Kovar in section 5.1 which was of a similar thickness and exhibited a ϵ_r and d_{33} of 86.2 and 38pC/N respectively.

These reduced properties are to be expected as the PVAc matrix, in which the PZT was suspended, comprises approximately 50% of the film by volume and exhibited a ϵ_r of 3.2; the relative permittivity variation with inclusion volume loading of the various PZT/polymer composites can be seen in figure 8.6. The PVAc matrix also reduces the force transmission to the PZT inclusions by deforming. These issues may limit the effectiveness of PZT/PVAc as an AE sensor element.

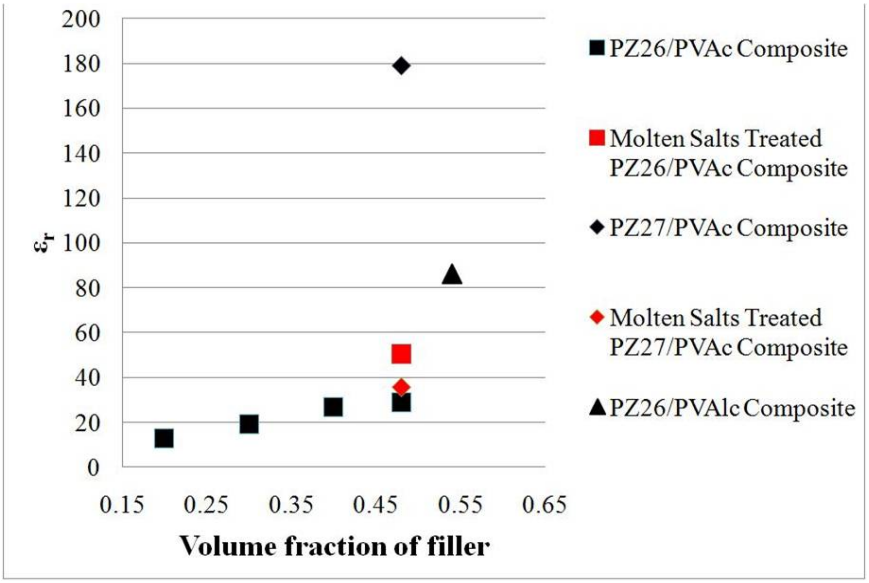

Figure 8.6: Plot showing the permittivity of the various PZT/polymer composite materials with respect to volume fraction of powder loading.

8.1.4 Acoustic Emission Testing

A PZ26/polyvinyl alcohol (PVAlc) film was produced by the following method: PVAlc was dissolved in de-ionised water in a volume ratio of 13.5:1 water to PVAlc. PZ26 powder had been treated in a zinc acetate solution and then added to the polymer solution to produce a slurry which would result in a film with 54% volume PZT powder loading following removal of the water by drying. The slurry had been deposited onto an aluminium foil substrate and 2mm diameter Cr/Au top electrodes were deposited once the film had dried.

The Zn acetate treated PZ26/PVAlc had been poled under a field of 10kV with a sample to pin separation of 10mm for 60 minutes at a temperature of 100°C. Electrical properties of the film were measured. The composite film was reported to exhibit an average ϵ_r of 86.3, a loss of 0.058 and a d_{33} of 15.2pC/N. The d_{33} was superior to molten salts treated PZ26/PVAc due to the Zn acetone treatment ensuring improved bonding to the polymer, thus improved force transfer to from the matrix to the PZT inclusions.

The Zn acetate treated PZ26/PVAlc was mounted onto the same 250mm square, 5mm thick steel plate as used in section 7.2.2.1, in the same position as the thick film device on the titanium substrate in figure 7.3b in section 7.2.2.1. A commercial PICO sensor was again used for benchmarking purposes. Grease was used as

a coupling material for both devices. Pre-amplification values of 60dB and 40dB were applied to signals from the PZT/PVAlc and PICO sensors respectively using a 2/4/6 pre-amplifier from PAC. Threshold values of 30dB and 40dB were applied to the PICO and PZT/PVAlc polymer devices respectively. A sample rate of 5MHz was employed and upper and lower filters were set at 3MHz and 1kHz respectively. AE signals were generated using the Hsu-Neilson test, with a 0.5mm diameter 2H pencil, at the centre of the plate which was a distance of 75mm from each sensor.

8.1.4.1 Results

Several simulated AE tests were carried out and time domain plots which were representative of both the PZT/PVAlc and the PICO devices are shown in figure 8.7. The maximum amplitude, following pre-amplification, of the representative signal was 140mV and 345mV for the PZT/PVAlc and PICO devices, respectively. The AE signal was detected by the PZT/PVAlc sensor 20μs earlier than the PICO sensor.

Gabor transforms were carried out on the time domain signals using the AGU Vallen Wavelet software (release A2009.1027) and are shown in figure 8.8. A frequency resolution of 100Hz and a wavelet window of 10μs were employed. The PICO sensor response to the simulated AE was much the same as the sensor response observed in the thick film on titanium foil tests (section 7.2.2.1). The response to the intersection between the S_0, A_0 and A_1 Lamb wave components, at the PICO sensor low sensitivity point of 340kHz, was present but the maximum amplitude was again offset due to the sensitivity of the PICO sensor between 450kHz and 500kHz. The PICO sensor signal also detected reflections due to interaction with the plate boundary.

The Gabor transform of the PZT/PVAlc showed a periodicity at frequencies between 200kHz-400kHz of 13μs and at frequencies between 600kHz and 1.2MHz of 5μs. It was also clear from the Gabor transform in figure 8.8a that these periodicities were present at lower amplitudes before the AE signal was detected. This indicates that this periodicity was related to noise induced between the sensor and pre-amplifier rather than a physical characteristic of either the sensor or the steel plate on which the AE testing was carried out.

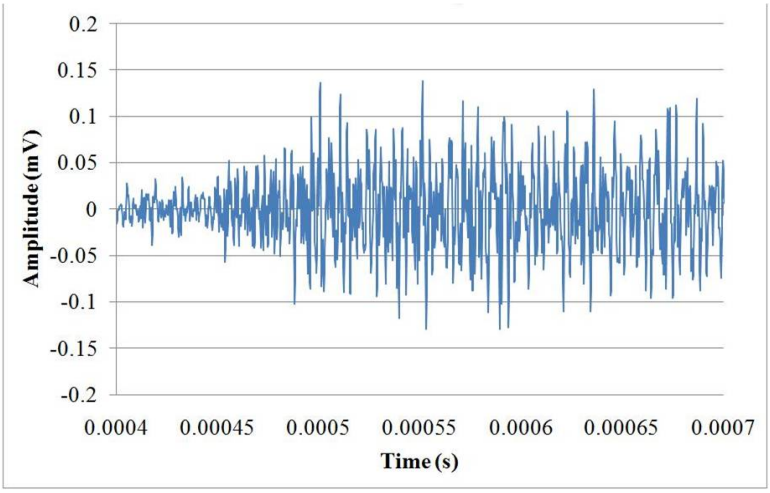

(a)

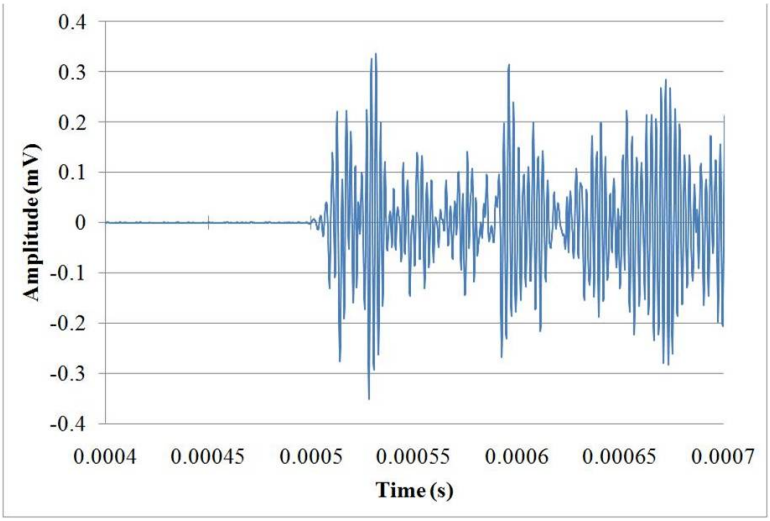

(b)

Figure 8.7: Plots showing the the time domain response between 400μs and 700μs of (a) Zn acetone treated PZT/PVAlc composite film and (b) PICO commercial device to simulated AE generated by Hsu-Neilson testing. The signal to noise ratios of the PZT/PVAlc and commercial devices were observed to be 5.6 and 690 respectively.

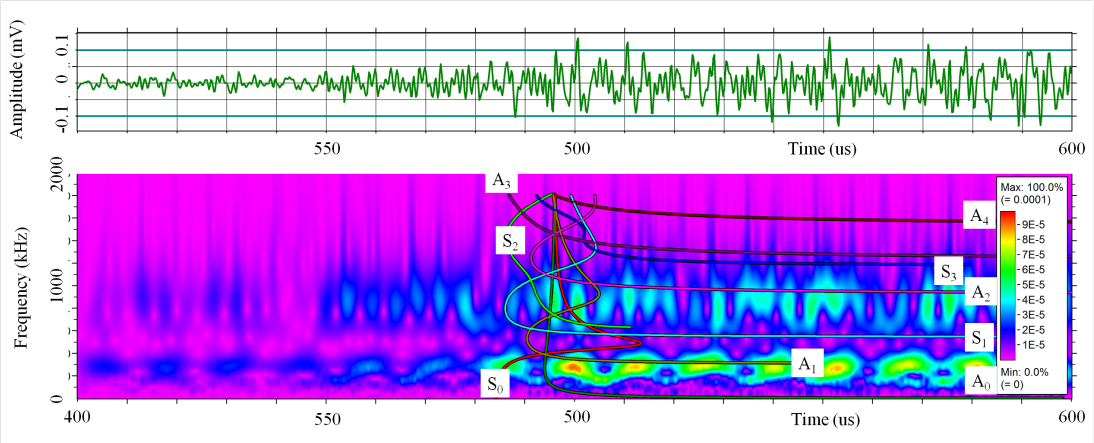

(a)

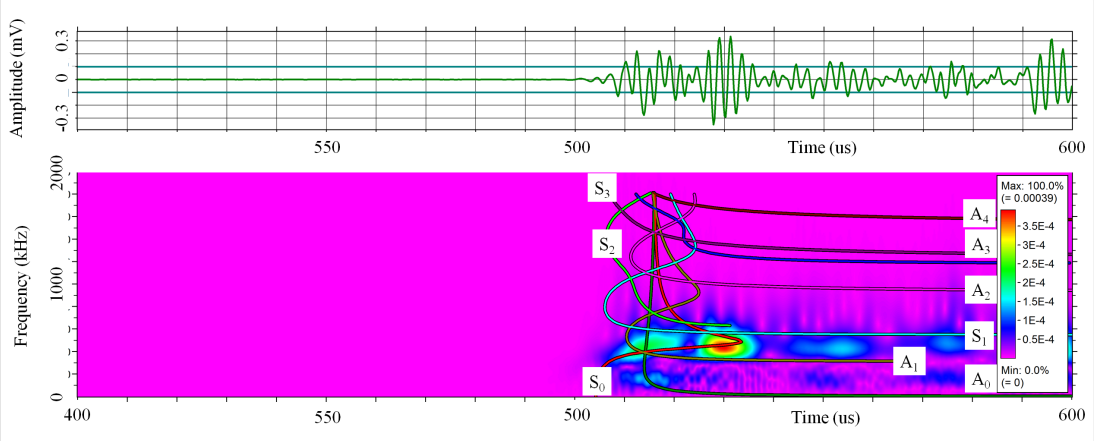

(b)

Figure 8.8: Gabor transform plots plots between 400μs and 600μs showing the the frequency response of (a) Zn acetone treated PZT/PVAlc composite film and (b) PICO commercial device to simulated AE generated by Hsu-Neilson testing.

The amplitude of the noise was intensified by interaction between the lower frequency noise and the S_0 and A_1 Lamb wave components. The higher frequency noise amplitude was supplemented at the higher frequency range by the interaction of the noise with the A_2 Lamb wave component. The signal to noise ratio of the PZT/PVAlc sensor was 2.5. This was below the recommended minimum for use in industrial applications and the noise in the sensor masked the signal features which were discernible when using PZT thick films deposited onto metal substrates by other methods.

Table 8.3: Table showing a comparison of the thick film device on titanium foil, the thick film device embedded in Kovar and the PICO commercial AE sensor.

Sensor	PICO	Thick film embedded in Kovar	Thick film on titanium foil	PZT/PVAlc composite
Relative signal amplitude before pre-amplification	1	0.0541	0.0192	0.04
Relative thickness	∼1	0.176	0.044	0.172
Relative sensing area	∼1	4.00	1.56	0.25
Relative d_{33}	1 (N.B. bulk material property)	0.115	0.157	0.046

8.1.4.2 Conclusions

The 17.22μm thick PZT/PVAlc composite film sensor signal amplitude was 25 times lower than that of the PICO commercial device before signal pre-amplification was employed. This can be compared to the 17.6μm thick film PZT deposited by spin coating directly onto Kovar sheet and the 4.4μm thick PZT film on titanium foil with signal amplitudes 18 and 50 times lower than that of the PICO commercial sensor respectively. This was partially explained by the PZT/PVAlc composite film exhibiting a d_{33} 0.4 times that of the thick film PZT on Kovar. Comparitive properties of the MEMS AE sensors compared to the PICO commercial sensor are shown in table 8.3

However, despite having a response amplitude double that of the thick film on titanium foil the signal to noise ratio of the signal detected by the PZT/PVAlc composite film sensor was lower and wave characteristics resulting from the physical properties of the structural component under observation were not apparent. The rise time, wave energy, duration and ringing characteristics of the signal were not quantifiable due to noise which was high in amplitude compared to the signal. The noise also resulted in the reflections from the edges of the transmission media being impossible to identify. This was due to the noise in the signal masking the characteristics and was also due to the deformable PVAlc matrix distorting the wave signal and diffusing the energy of the AE, reducing the detected AE signal

amplitude further.

8.2 PZT/Polymer AE Device Integration Conclusions

There was a need to integrate PZT AE sensors onto substrate materials at low temperatures. This was achieved through a PZT/polymer composite material which was deposited onto various substrates for processing purposes but could easily be deposited and processed directly onto structural elements. The PZT/polymer composite materials were developed to attain favourable properties for AE sensing applications. Sensor benchmarking was then carried out by comparing the PZT/polymer sensors to the PICO commercial sensor.

The PZT/polymer composite was found to exhibit properties which were poor in comparison to the thick film deposited onto both Kovar and titanium substrates. However, when compared to the PICO commercial sensor the amplitude response of the PZT/polymer composite was twice that if the thick film on titanium. Despite this greater amplitude response the PZT/polymer composite sensor was unable to identify the wave characteristics relating to the interaction of the wave with the medium of transmission. This was due to a low signal to noise ratio and the deformable nature of the polymer matrix which distorted the AE signal.

The relative ratios of S/N and A/V were calculated to be 123.2 and 9.3×10^3, respectively. These FOMs show that the PZT/polymer composite devices exhibited a relative S/N ratio which was high compared to that of both the thick film on Kovar and the thick film on titanium foil - 1.9 and 57.1 respectively. This indicated that the S/N ratio of the PZT/polymer device was poorer than the S/N ratio of the other devices. Electrical shielding and grounding may reduce the noise and therefore improve the S/N ratio. The relative A/V ratio showed the PZT/polymer composite to be superior to the thick film on titanium and the thick film on Kovar - 2.5×10^3 and 0.74×10^3 respectively.

Chapter 9

Summary

9.1 Device Performance

The relative performance of the MEMS AE monitoring devices developed in this work was tracked by two figures of merit (FOM): the relative signal to noise (S/N) ratio and the relative maximum amplitude to sensing element volume (A/V) ratio. The FOM for each device are presented in table 9.1.

The FOMs in table 9.1 showed a trend of both increasing relative S/N ratio and relative A/V ratio. These increasing FOM ratios indicated that each new MEMS AE device developed in this work showed a poorer S/N ratio than the previous device. This was explained by the trend towards a smaller sensing volume and therefore a smaller maximum signal amplitude whilst the noise signal amplitudes remained consistent due to test conditions. The relationship between maximum signal amplitude and sensing element volume was not linear, as demonstrated by the A/V ratio. The trend in this FOM showed that each new device tested showed a greater maximum signal amplitude for the sensing element volume of the device relative to a commercial device benchmark when compared to the previously developed MEMS devices.

The thick film on silicon device did not follow these trends, this was due to several contributing factors. The commercial sensor against which the thick film on silicon was tested was not consistent with the other MEMS device benchmarking tests. The WD sensor used for benchmarking the thick film on silicon

Table 9.1: Table showing a summary of the figures of merit for each MEMS AE device produced in this work.

Device	Relative Signal to Noise Ratio	Relative Maximum Amplitude to Sensing Element Volume
Thick film on silicon substrate	7	914×10^3
Thick film on Kovar	1.9	0.7×10^3
Thick film on titanium foil	57.1	2.6×10^3
PZT/polymer composite on aluminium foil	123.2	9.4×10^3

had different characteristics than the PICO sensor employed in benchmarking the other MEMS devices. The WD was a wideband sensor and as such the frequency response was much flatter than the resonant PICO sensor. The sensing element volume of the WD sensor was also much greater than that of the PICO sensor. The lack of resonant response and the larger sensing element area resulted in the A/V ratio of the WD sensor being lower than it would have been with the PICO sensor. This in turn resulted in an increase in the relative A/V ratio of the thick film on silicon compared to the WD device than would be expected were the thick film on silicon compared to the PICO commercial device.

The flatter response of the WD sensor also resulted in a reduced S/N ratio. The noise in the benchmarking of the thick film on silicon was due to the mechanical properties of the test and as such was not filtered out by either the differential WD sensor or the thick film device. The noise combined with the relatively low signal amplitude of the WD signal resulted in the S/N ratio of the WD sensor being low. The S/N ratio of the thick film on silicon was 5 which was comparable to the S/N ratios of both the thick film on titanium and the PZT/polymer MEMS devices which were 4.2 and 5.6, respectively. However, when the low thick film on S/N ratio was compared to the low benchmark S/N ratio it appeared to be more comparable to the embedded thick film on Kovar - S/N ratio of 63.1 - than to the thick film on titanium and the PZT/polymer composite.

The trends in the FOMs employed show that the thick film MEMS devices developed in this work do act as a compromise between the expense of bulk devices and the performance of thin film devices as expected from the literature review.

The trend in A/V ratio is one of the main reasons that thin film devices perform poorly at detecting AE. The reduction of the A/V ratio combined with a consistent noise amplitude results in a poor S/N ratio in thin film devices thus limiting AE detection capabilities. Thick film devices are a compromise with better S/N properties than thin films but poorer S/N properties than bulk devices.

The embedding of the thick film PZT onto Kovar also showed that it was possible to attain a significant improvement in S/N ratio, this improvement of S/N ratio may be useful in future MEMS devices. The improvement in S/N ratio was shown to be a compromise as the embedding of the device also reduced the A/V ratio significantly.

9.2 Summary of Work Carried Out

Work was carried out to integrate PZT thick films, manufactured by MEMS processing techniques, with metallic substrates to produce a structurally integrated thick film AE sensor. PZT was deposited onto a 3.2mm thick Kovar sheet by composite spin coating. Electrical and physical properties of the film on Kovar plate were identified. The d_{33} of the bulk material from which the commercial device was produced was an order of magnitude greater than that of the MEMS device. This was due to the thick film element being thinner, being exposed to greater stresses during manufacture and exhibiting a significantly different micro-structure. The MEMS device was shown to be a wideband sensor, lacking in resonance peaks, and was sensitive to AE with a frequency between 39kHz and 700kHz.

AE signals were generated in the Kovar plate following Hsu-Neilson testing. The AE signal was detected by the thick film on Kovar plate and the commercial sensor. The max amplitude of the signal output from the thick film device was 18.5 times lower than that of the signal output from the commercial PICO sensor. This was explained by the commercial device sensing element being two orders of magnitude thicker than the MEMS device and exhibiting greater piezoelectric properties. The rise times of the AE signals detected by the PZT thick films on the Kovar plate were a longer than the PICO commercial sensor against which it was benchmarked. The wideband nature of the MEMS device was show to be the cause of the longer rise time when compared to the PICO commercial sensor.

Theoretical dispersion curves were calculated based on the physical properties of the Kovar plate. The detected AE signal was transformed to the frequency domain using a Gabor transform and the dispersion curves were overlaid. The detected signal corresponded to the dispersion curves showing that the signal detected by the MEMS AE device was capable of identifying physical properties of the plate through which the emitted AE was transmitted.

With the success of structurally integrated thick film AE devices in detecting artificially generated AE signals, work was carried out to investigate the release of thick film from the substrate material. The release of the film by sacrificial substrate and sacrificial release layer were both investigated. PZT was deposited onto metal substrates which were then etched. Titanium was etched to release the PZT film however an inhomogeneous etch process resulted in the film fracturing and breaking away into the etchant.

Copper was employed as a substrate material, the copper was then etched away from the PZT. It was found that the non-conductive lead/copper oxide layer was not removed by the nitric acid employed in the removal of the copper substrate. The copper substrate was successfully removed, however the issues with processing PZT on copper, such as film cracking, meant that the resultant released devices were unsuitable for AE processing applications.

Sodium silicate was a material of great interest for the release of thick film PZT films due to the material being water soluble. Drying and sintering processes were investigated to manufacture a uniform sodium silicate layer which was readily soluble in water. It was found that during the drying process 50% of the water was removed from the sodium silicate solution. The removal of the water at temperatures above ambient caused bubbling in the sodium silicate layer and at temperatures above 100°C the bubbling resulted in a surface finish with a roughness inappropriate for the deposition of PZT.

Calcining of the sodium silicate at the temperatures required in the processing of PZT resulted in a white powder deposit on the surface of the sodium silicate layer. The formation of this deposit was avoided by calcining the sodium silicate at a temperature above 850°C. This resulted in the crystallisation of sodium silicate from β-$Na_2Si_2O_5$ to $Na_6Si_8O_{19}$. At temperatures above 834°C the sodium

silicate entered a liquid phase and when subsequently cooled this resulted in a $Na_6Si_8O_{19}$ layer with a surface finish suitable for the deposition of PZT. However the $Na_6Si_8O_{19}$ film was not readily soluble in water and therefore not appropriate for use as a film release layer.

Work was carried out on the integration of PZT with metal foils. PZT was deposited onto Kovar and titanium foil by composite sol-gel spin coating. The physical properties of the films deposited onto various metal foil substrates were observed and compared to the properties of the PZT deposited previously onto other metal substrates. It was found that as the thermal expansion coefficient of the metal foil substrate increased the cracking of the film surface increased. The PZT film deposited on copper, which had the highest thermal expansion coefficient of materials used in this work, severe cracking was observed such that when the oxide layer was reduced by the use of conductive Ti/Pt the PZT was conductive.

PZT film properties were also measured and it was found that the increase in film cracking correlated with a reduction in ϵ_r. Films deposited on Kovar and titanium foil, which have thermal expansion coefficients of 6x10^{-6}/K and 8.5x10^{-6}/K, exhibited ϵ_r of 260 and 235.2 respectively. This compares to PZT on silicon - thermal expansion of $\sim$1x10^{-6}/K - with an ϵ_r of 1150. The thickness of the substrate material also had a major affect on the ϵ_r of the PZT film deposited upon it. The ϵ_r of PZT previously deposited on Kovar plate was significantly lower than the PZT film deposited on Kovar foil, 86.2 compared to 260. This reduction was explained by the thicker substrate constraining the film during the production process and inducing stress which reduce the film properties.

PZT thick film deposited on the titanium foil was employed in static AE sensing applications. The thick film on titanium was mounted on a steel plate along with a PICO commercial sensor. AE was then artificially generated by Hsu-Neilson pencil breaks on the steel plate. The thick film on the titanium foil was successful in detecting signals generated by Hsu-Neilson tests and benchmarking was carried out against the PICO sensor. The max amplitude of the signal output by the thick film on titanium foil was 57 times lower than that output of the commercial PICO sensor. The signal previously output by the thick film on Kovar sheet was 3.08 times greater than that from the titanium foil. This is explained by the d_{33} of the film on being 1.37 times greater than that of the film on Kovar resulting

from the lack of cracking induced by thermal expansion due to the foil substrate bending to release stress during processing.

Signal reflections were resulted from the interaction of the AE with the boundary of the steel plate onto which the sensors were mounted. These signal reflections were detected by the MEMS and commercial AE devices. A Gabor transform was used to transform the AE signal from the time domain to the frequency domain and dispersion curves were overlaid. The reflected signals enabled the identification of the physical dimensions of the steel plate through which the emitted AE is transmitted.

The thick film on titanium was also benchmarked against a WD differential sensor from PAC in a dynamic application. Both devices were mounted on the bearing housing of a rotating shaft system. It was found that the S/N ratio of the thick film sensor was lower than one. It was impractical to increase the signal amplitude as this would require an increased film thickness or density, both of which were limited by the constraints placed on film development by the use of the titanium foil substrate. The deposition of a thicker film was not possible due to cracking caused by the stresses produced in the film during manufacture. The sensor was, therefore, ineffective at detecting AE in dynamic situations.

The development and deposition of a piezoelectric paint at temperatures below 150°C was carried out for use in integrated AE applications. The effects of varying the solvent and the type of PZT on the film properties were identified. A molten salts processing technique was used to improve the d_{33} of the film. The variation of film properties with volume loading were compared with theoretical values. It was found that the ϵ_r of the film increased with film volume loading as expected from the theory.

PZT treated with ZnO was combined with a polymer on a substrate of aluminium foil then the ability of the device to effectively detect AE generated by Hsu-Neilson testing was benchmarked against the PICO commercial sensor. It was found that the amplitude of the AE signal output from the PZT/polymer was 25 times lower than that from the commercial sensor. It was also found that, while the PZT/polymer sensor was capable of detecting the AE signal generated by Hsu-Neilson testing, the physical properties of the transmission media were indiscernible from the detected signal due to the deformation of the polymer ma-

trix distorting the signal. This limited the effectiveness of the PZT/polymer AE device.

Chapter 10

Future Work

Avenues for future work have been identified with the aims of solving some of the existing issues with the manufacture of structurally integrated MEMS AE devices and further refining the MEMS AE devices presented in this work.

10.1 Signal Noise Reduction

The active element of a MEMS AE device is considerably thinner than that of a commercial bulk device, in addition the piezoelectric properties of the MEMS active element are often significantly lower than those of the bulk material. These properties result in a reduction in the amplitude of the signal output response to AE compared to that of bulk commercial sensors. This lower signal amplitude results in a reduction in the signal to noise ratio. A signal to noise ratio of at least three is recommended by industry for effective AE detection applications. As the amplitude of the signal output response to AE is often limited due to the constraints of MEMS production techniques the reduction of noise is important.

10.1.1 AE Device Backing

The thick film AE sensor structurally integrated into the Kovar plate presented in this work performed well when benchmarked against commercial AE sensors. As the thick film device showed a repeatable response to simulated AE with no variation due to coupling or substrate geometry, the thick film on Kovar could be

employed in identifying the effects of acoustically matched backing layers.

Backing materials must exhibit several properties to be effective. The material must be of a similar acoustic impedance to that of the active element, thus limiting the reflection of acoustic energy from the interface between the active element and the backing layer. Reflection of acoustic energy from the top surface of the backing layer must also be avoided by employing a material which successfully dissipates acoustic energy. It is important that the backing layer is not conductive to eliminate possible electrical shorting between the top and bottom electrode.

Noise generated by the reflection of AE within the device itself is a major cause of poor signal to noise ratio. A backing layer which exhibits the properties described above has the effect of reducing noise and thus improving the signal to noise ratio. Without a backing layer the AE wave transmits through the piezoelectric element and is reflected back off the interface between the piezoelectric element and the surrounding environment as the interface exhibits a high acoustic impedance mismatch. An acoustically matched backing greatly reduces these reflections. The AE is transmitted through the piezoelectric element and across an acoustically matched boundary into a backing layer where the AE wave is damped to reduce reflections.

Various materials merit investigation for use as acoustically matched backings. These materials consist of a polymer matrix with inclusions to alter the acoustic properties of the material on a macro-scale. Alumina powder [139], tungsten powder [75], PZT powder or other dense materials may be employed as inclusions in an epoxy matrix to form a material which is suitable for use as a backing. As such these materials should be employed as backing layers for thick film AE devices on Kovar. The various acoustic backings should be applied to several devices on the same Kovar plate, one device remaining without backing and one device being backed by epoxy with no inclusions to act as control devices. AE simulation should then be carried out by Hsu-Neilson testing to enable direct comparison of the properties of the backing materials.

In addition to the inclusion material, variation of the volume loading of the inclusions is also of interest as the macro-scale properties of the material are related to the volume loading of inclusions. Another parameter which is of interest is the

thickness of the backing layer. The effects of various combinations of these parameters should be identified to ensure the selection of the most appropriate backing layer. Once an appropriate layer has been identified it should be employed in subsequent MEMS device manufacture and benchmarking of the backed devices should be carried out.

10.1.2 Electrical Shielding

In addition to noise resulting from reflections back off the top surface of the piezoelectric element, noise may also result from interference from the environment in which the device is employed. Interference from the surrounding environment may be electrical or mechanical in nature. Mechanical noise results from vibration of the structural element under observation and is typically of a frequency significantly lower than that of AE. As such interference from mechanical vibration is rarely an issue in AE monitoring.

The EM interference from the surrounding environment may be caused by several sources. Proximity to electrical equipment may induce EM interference into the cable between the sensor and the data-logger or directly into the sensor. The effect of interference induced into the cable can be reduced by employing shielded co-axial cable and by ensuring that the pre-amplification of the signal takes place as close to the sensor as possible. This pre-amplification boosts the AE signal before significant noise is introduced thus increasing the signal to noise ratio in the cable between the pre-amplifier and the data-logger.

The reduction of induced EM interference in the MEMS device is important in increasing the signal to noise ratio. One method by which the EM interference may be reduced is shielding of the MEMS AE device. Commercial AE device elements are surrounded by a grounded metal case. The grounded case isolates the charged electrode from the EM noise, the same approach is of interest for MEMS AE devices.

A MEMS AE device consisting of an active element with a suitable backing material electrically isolating the top electrode should be manufactured and poled. A conductive layer should be used to completely coat the backing material and contact the bottom, ground electrode - conductive paint may be used for this.

Care must be taken to ensure that the top electrode and the connection to the top electrode are isolated from the coating. Electrical contact between the device and the pre-amplifier should then be made using the conductive coating as ground. During operation this coating effectively isolates the charged top electrode from noise.

The electrically shielded device should be benchmarked against an sensor of identical design without the shielding. AE testing should be carried out and the signal to noise ratio of each sensor should be identified. The shielding may be applied to the thick film on titanium foil devices. The reduction in EM interference may increase the signal to noise ratio such that the thick film on titanium is suitable for dynamic AE sensing applications.

10.1.3 Dual Element MEMS AE Devices

Noise reduction may also be achieved through a variation in the design of the MEMS sensor. Differential sensors are employed where noise from external EM interference is an issue. Differential sensors are composed of one active element alongside another. This design is easily achieved using MEMS technology.

Another possible differential sensor design requires one element stacked upon another with a common central electrode. A substrate must be chosen with a thermal expansion close to that of PZT to reduce cracking of the film during production. This is important for a MEMS differential sensor as the combined thickness of both elements will be several microns. A blanket bottom electrode should be deposited onto the substrate. A PZT film and a patterned electrode should be deposited. Onto this a second PZT film should be deposited, sandwiching the patterned electrode between the two PZT films. An electrode should be deposited onto the top surface of the final film.

The top PZT film should then be selectively patterned to enable contact to be made to the central, common ground electrode. The common ground electrode may be connected to the electrical shielding of the device. Care should be taken to ensure that the top and bottom electrodes do not come into contact with the grounded shielding. Poling should be carried out by applying an electric field to the top and bottom electrodes while using the common central electrode as

ground. This will result in oppositely poled top and bottom active elements.

During AE testing the signal generated by the the top device is subtracted from the signal generated by the bottom device, this has the effect of doubling the AE signal whilst eliminating any EM noise induced from external sources. This design of sensor should be benchmarked against a MEMS sensor with a single element. The thickness of the single element used for benchmarking should be equal to that of both the elements in a differential device.

10.2 Device Release Technology

The technology involved in releasing the MEMS AE devices from the substrate, which provides structural support during the manufacturing process but may hinder the operation of the device, is an important avenue for further investigation. The release of the MEMS AE device from the substrate may improve device functionality by reducing attenuation and wave distortion caused by the transmission of the AE through the substrate. Released devices, when combined with a suitable backing material and electrical signal may then be used with the structural element only separated from the active element by the bottom electrode and a coupling layer.

10.2.1 Metal Foil Substrate Etching

The complete removal of metal foil substrates has been employed in this work. The etching of a titanium foil substrate resulted in the PZT film breaking up due to the etch rate being inconsistent across the substrate. This inconsistent etch rate was due to a variation in the separation of the anode and the cathode across the device. As a result some areas of the titanium broke away, fracturing the PZT in the process.

One solution to this problem is selective etching. The process carried out in this work employed a rectangular cathode which, due to the uneven rear surface of the titanium substrate, resulted in an inconsistent etch as previously noted. A point cathode should be employed, when multiple devices are being etched an

array of point cathodes may be appropriate.

A point cathode consists of a pin, electrically connected in the same fashion as the rectangular foil cathode. The pin should be located directly above the area of the substrate - the anode - which requires etching. The etching process will then remove the desired substrate material on which the MEMS device was manufactured while leaving the remainder of the substrate intact and preventing the PZT from fracturing.

In addition to point cathodes, variation of the backing employed to provide structural support to the PZT film during the etch process should be carried out. A stronger material which could provide more support and better adherence to the PZT than the currently employed photoresist and tape is required. The material must be resistant to the etch process to avoid the need to reseat the device. Variation of the metal foil employed as a substrate is also of interest. Nickel has previously been shown to be an effective substrate for the deposition of PZT [140]. As such the deposition of PZT onto a nickel substrate which will then be etched to release the PZT device is of interest.

10.2.2 Sodium Silicate Release Layers

The use of a sodium silicate release layer merits further work. There were issues with the deposition of a sodium silicate layer suitable when co-processing with PZT. The work carried out on sodium silicate either resulted in an uneven film surface or a layer which was not soluble and therefore incompatible with the release of the PZT. These issues may be related to the composition of the sodium silicate and, as such, work should be carried out to identify the effects of varying the starting composition of the sodium silicate.

Varying the starting composition of the sodium silicate will alter the composition of the layer during and following processing resulting in a variation in the physical properties of the layer including the surface finish and the film solubility. Work should be carried out to identify the optimal sodium silicate composition, resulting in properties conducive with co-processing sodium silicate and PZT. Various sodium silicate drying and heat treatments should be carried out prior to the deposition of the PZT to identify the effects of each process on the sodium

silicate.

PZT should be deposited onto sodium silicate layers of varying compositions produced and heat treated as previously described. The physical and electrical properties of the PZT films co-processed with the sodium silicate layer should be identified prior to release. The release of the PZT film should then be carried out, using water to remove the sodium silicate. The properties of the released PZT film should then be identified and compared with the non-released film properties and the properties of thick films integrated with other substrate materials. The sodium silicate film release process found to exhibit the greatest piezoelectric properties should then be employed in the manufacture of released MEMS AE devices for benchmarking.

10.3 MEMS Sensor Development

The development of MEMS AE sensing technology is an important area in which future work should be conducted. MEMS sensors should be developed to carry out the same roles as commercially available bulk AE sensors currently do. This development will offer a lower cost, disposable solution to the detection of AE which may be employed in situations where commercial, bulk sensors are inappropriate. Important areas of interest are the development of sensor arrays and wireless sensing technology.

10.3.1 MEMS Sensor Arrays

An area of interest in the field of AE is the use of sensor arrays [1]. AE sensor arrays are useful for identifying the location of the source of an AE. MEMS technology offers the potential for the integration of a sensor array onto a single substrate which can then be integrated into the structural element in a similar fashion to individual MEMS AE devices.

Either multiple sensors may be deposited upon the same substrate in an array which can then be mounted on the structural element or multiple individual sensors may be arranged on a structural element. The arrival time of the AE gen-

erated in the structural material at each sensor varies depending on the distance between the source of the AE and each individual sensor. The arrival time data from an array with three or more sensors can be used to triangulate the location of the emission.

Work should be carried out varying the number of MEMS AE sensors in the array and the array geometry to identify the optimum arrangement for the location of the source of the AE. Arrays should be applied to structural elements of varying geometry such as plates and pipes along with dynamic applications such as rotating bearing systems to assess the suitability of MEMS arrays for the detection of AE in each application.

10.3.2 Wireless MEMS Sensors

A further area of interest in the field of AE monitoring is that of wireless sensing technology. Wireless sensors enable the monitoring of difficult to reach components without the need for a complex, lengthy and costly network of wires, particularly when an array of AE devices is employed. Wireless technology is currently employed alongside bulk AE devices resulting in the same issues with wireless AE monitoring as have already been identified with standard AE monitoring.

The use of wireless MEMS technology has previously been demonstrated [76]. The combination of MEMS wireless technology with MEMS AE technology has many advantages. Wireless MEMS technology is small and may be powered by the vibration of the structural element under observation. This means that disposable wireless MEMS AE sensors may be mounted on difficult to reach components during the component manufacturing process. The sensors may then remain in situ for the life cycle of the component, providing a continuous structural health monitoring solution.

There are issues with the integration of wireless technology and MEMS AE technology. The signal output of the MEMS AE device will require pre-amplification, introducing the need for a integrated MEMS pre-amplifier. This pre-amplifier must also be self-powered, eliminating the need for access to the device to replace the power supply.

The integration of the MEMS AE sensor, pre-amplifier and wireless transmitter must be carried out on a common substrate. This introduces further issues with device release and structural integration. All of the components must be structurally supported by a backing material if the substrate is to be removed to allow direct contact of the active element of the MEMS AE device with the structural element under observation. The effects of a backing layer on the functionality of the MEMS wireless transmitter must be identified.

A method by which an array of MEMS AE sensors may be integrated with pre-amplifiers and wireless transmitters and deposited directly onto a structural element would be of great interest [141]. Screen printing is one possible manufacturing technique which may be appropriate and this may be combined with the development of PZT/polymer materials enabling low processing temperatures which allows the integration of MEMS devices with a wider range of structural elements.

Chapter 11

Conclusions

The aim of this work was to design and develop a structurally integrated AE sensor using MEMS manufacturing techniques. To achieve this aim initial testing was carried out on a PZT film deposited on a silicon wafer as a proof of concept. The initial validation testing showed that thick film PZT on silicon was a suitable material for AE testing and merited further investigation.

This work has shown the successful integration of MEMS AE devices with structural elements by deposition directly onto the element. PZT was integrated with a Kovar plate, representative of a structural element, by composite sol-gel spin coating. The PZT film was patterned and poled to create a structurally integrated thick film AE device. The structurally integrated device was benchmarked against a commercially available AE sensor and was found to perform well, detected simulated AE successfully. This confirmed that structurally integrated thick film devices are comparable to commercially available AE sensors with the advantages of reduced size and material costs.

This work has also shown the development of metal foil as a substrate for AE devices to be integrated with structural elements. Titanium and aluminium foils were employed as substrates, thick film PZT and PZT/polymer films were deposited onto these substrates respectively. The MEMS devices were then mounted on a structural element for AE benchmarking. Both types of MEMS devices were comparable with commercial devices at detecting simulated AE. The PZT/polymer device was unable to characterise properties of the AE source or the transmission. The thick film on titanium was successfully able to detect AE reflections from the edge of the structural element demonstrating that the MEMS

sensor is a viable AE sensing solution.

PZT films were deposited on metal foils to enable the release of AE devices. The foils were etched to release the PZT film. The etching of titanium foil resulted in the PZT film breaking up; the copper foil was successfully removed resulting in the release of the PZT film. The PZT film which had been deposited onto copper required a diffusion barrier to prevent the formation of a non-conductive oxide layer. Film cracking during processing resulted in the PZT on copper being conductive and therefore inappropriate for use in AE sensing applications. The etching of metal substrates requires significant refinement before the process is appropriate for the release of MEMS devices for AE detection applications.

Sodium silicate was employed as a non-metallic substrate release layer. Work was carried out to identify drying and sintering conditions which were conducive to the integration of sodium silicate into the PZT manufacturing process. Drying at room temperature was found to be suitable for film preparation. Sintering of the sodium silicate at a temperature above 850°C was shown to produce a layer suitable for the deposition of PZT; this layer was not soluble in water and as such was not appropriate for use as a substrate release layer.

This work has shown that the release of MEMS devices requires further development to be successfully implemented as a manufacturing process. The integration of MEMS devices directly onto structural elements has been shown to be comparable to commercial devices in the detection of AE. The integration of MEMS devices with metal foils which can be mounted on structural elements has also been shown to be successful in the detection of AE. Both of these techniques merit further development to produce a commercially viable MEMS AE sensor.

Appendix A

.1 Thick Film Sensor on Titanium Foil Dynamic Validation Tests

Time domain responses of the thick film sensor on titanium foil substrate and the WD commercial sensor are presented. The sensors were mounted on a bearing housing which contained an artificially damaged bearing. Hits were recorded at 1000rpm (figure 1), 2000rpm (figure 2) and 3000rpm (figure 3) with no load on the shaft.

For the second testing situation the time domain responses of the thick film sensor on titanium foil substrate and the WD commercial sensor are presented. The sensors were mounted on a bearing housing which contained an artificially damaged bearing. Hits were recorded at 1000rpm with a load of 2.07MPa on the shaft (figure 4).

For the third testing situation the time domain responses of the thick film sensor on titanium foil substrate and the WD commercial sensor are presented. The sensors were mounted on a bearing housing which contained an artificially damaged bearing. Hits were recorded at 2000rpm with a load of 1.17MPa on the shaft with and without a rattling sound being emitted from the bearing housing (figure 5 and 6).

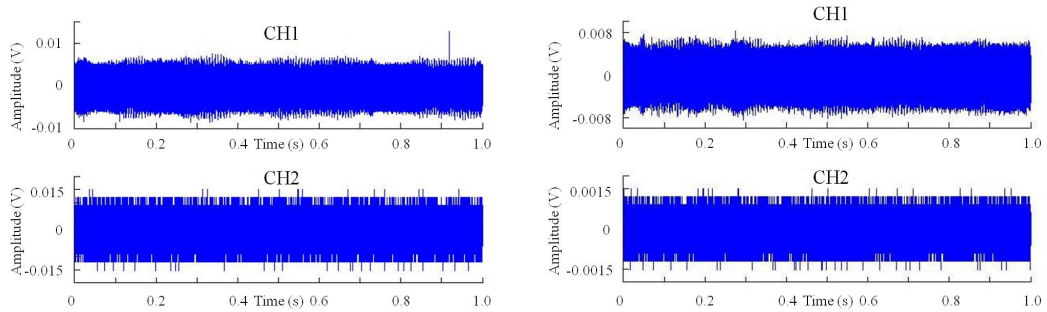

(a) 1st manually instigated hit. (b) 2nd manually instigated hit.

Figure 1: Time domain responses of the thick film PZT on titanium foil (CH1) and WD commercial sensor (CH2) to a shaft with a damaged bearing rotating at 1000rpm under no load.

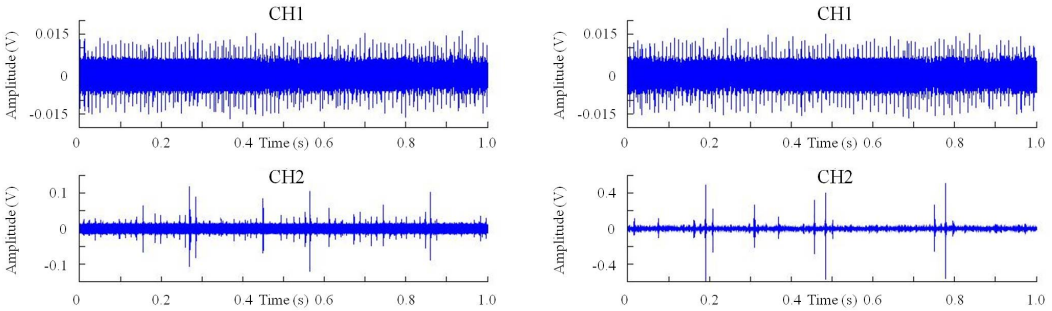

(a) 1st manually instigated hit. (b) 2nd manually instigated hit.

Figure 2: Time domain responses of the thick film PZT on titanium foil (CH1) and WD commercial sensor (CH2) to a shaft with a damaged bearing rotating at 2000rpm under no load.

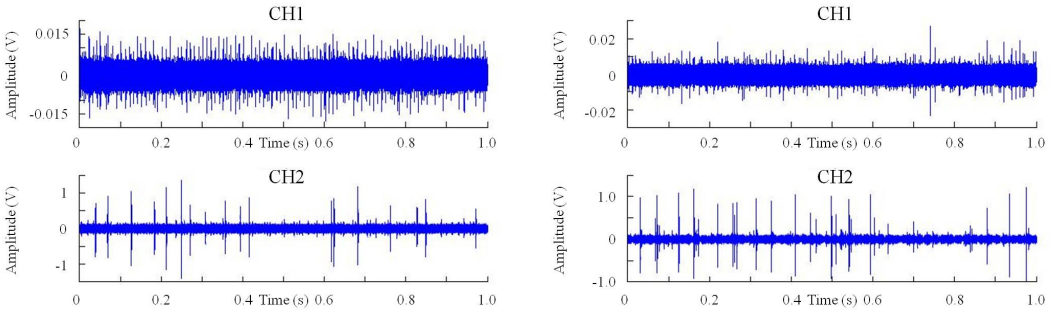

(a) 1st manually instigated hit. (b) 2nd manually instigated hit.

Figure 3: Time domain responses of the thick film PZT on titanium foil (CH1) and WD commercial sensor (CH2) to a shaft with a damaged bearing rotating at 3000rpm under no load.

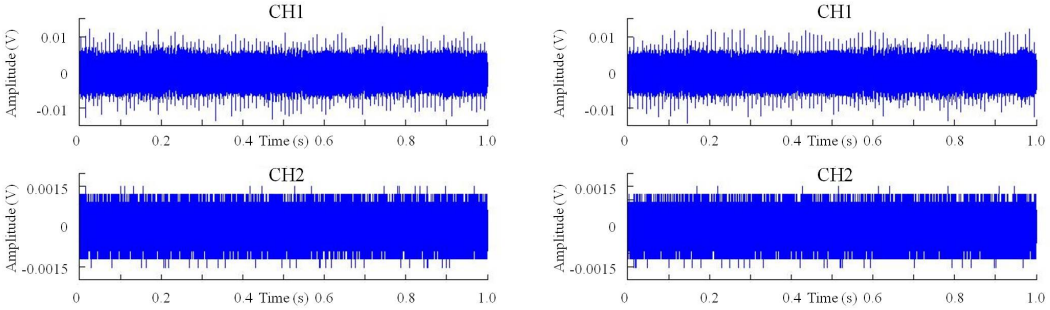

(a) 1st manually instigated hit.

(b) 2nd manually instigated hit.

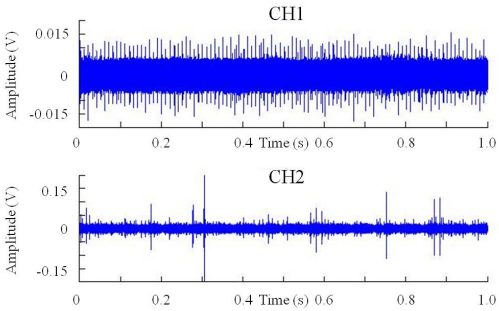

(c) 3rd manually instigated hit.

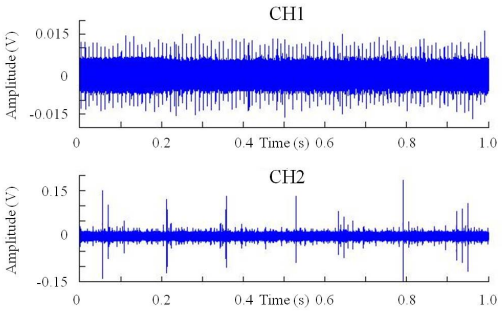

(d) 4th manually instigated hit.

Figure 4: Time domain responses of the thick film PZT on titanium foil (CH1) and WD commercial sensor (CH2) to a shaft with a damaged bearing rotating at 1000rpm with a load of 2.07MPa.

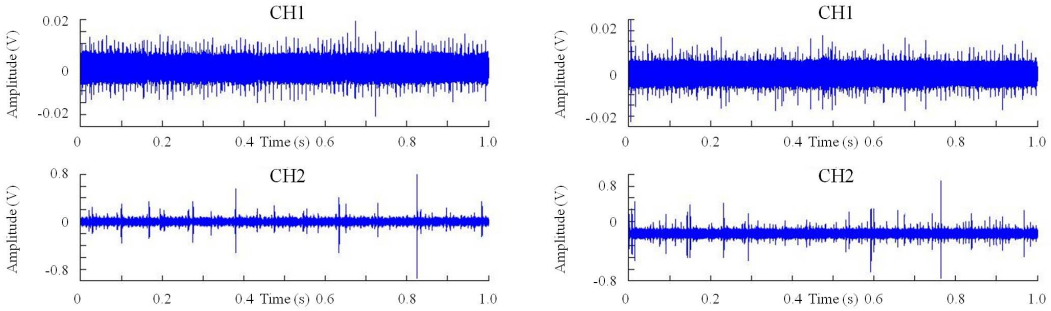

(a) 1st manually instigated hit. (b) 2nd manually instigated hit.

Figure 5: Time domain responses of the thick film PZT on titanium foil (CH1) and WD commercial sensor (CH2) to a shaft with a damaged bearing rotating at 2000rpm under a load of 1.17MPa. A rattling sound was heard emanating from the bearing housing during the recording of these hits.

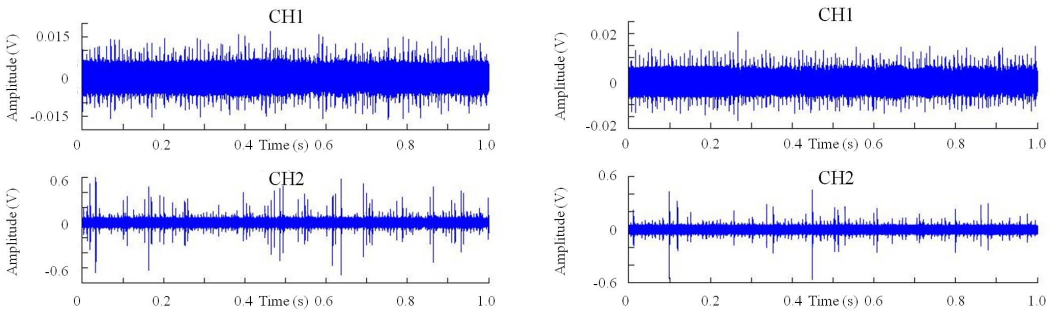

(a) 1st manually instigated hit. (b) 2nd manually instigated hit.

Figure 6: Time domain responses of the thick film PZT on titanium foil (CH1) and WD commercial sensor (CH2) to a shaft with a damaged bearing rotating at 2000rpm under a load of 1.17MPa. No rattling was observed during the recording of these hits.

Appendix B

.2 Journal Papers

A.J. Pickwell, R.A. Dorey, and D. Mba, "Thick-film acoustic emission sensors for use in structurally integrated condition monitoring applications", *Ultrasonics, Ferroelectrics and Frequency Control, IEEE Transactions on*, vol. 58, no. 9, pp. 1994-2000, 2011.

.3 Conference Papers

A.J. Pickwell, R.A. Dorey, and D. Mba, "Thick film, Acoustic Emission sensors for embedded structural health monitoring systems", *COMADEM 2010 - Advances in Maintenance and Condition Diagnosis Technologies Towards Sustainable Society, Proc. 23rd Int. Congr. Condition Monitoring and Diagnostic Engineering Management*, pp. 677-684, 28/06/2010-02/07/2010, 2010.

A.J. Pickwell, R.A. Dorey, and D. Mba, "Structurally Integrated Thick Film Acoustic Emission Sensors", *Engineering Asset Management and Infrastructure Sustainability: Proceedings of the 5th World Congress on Engineering Asset Management (WCEAM 2010)*, pp.739-747, 25/10/2010-27/10/2010, 2012.

.4 Oral Presentations

.4.1 Conferences

Electroceramics XII Trondheim, Norway (13/6/10): Thick film acoustic emission sensors for embedded structural health monitoring systems.

COMADEM 2010 Nara, Japan (28/6/10): Thick film, Acoustic Emission sensors for embedded structural health monitoring systems.

.4.2 Symposia

Microsystems and Nanotechnology Centre Seminar Cranfield, UK (6/10/10): Design and development of MEMS Acoustic Emission sensors.

.5 Poster Presentations

Piezo 2011 Sestriere, Italy (28/2/11): Integrated thick film acoustic emission sensor for structural health monitoring.

ISIF 2011 Cambridge, UK (31/7/11): Integrated thick film acoustic emission sensor for structural health monitoring.

Thick-Film Acoustic Emission Sensors for Use in Structurally Integrated Condition-Monitoring Applications

Andrew J. Pickwell, Robert A. Dorey, and David Mba

***Abstract*—Monitoring the condition of complex engineering structures is an important aspect of modern engineering, eliminating unnecessary work and enabling planned maintenance, preventing failure. Acoustic emissions (AE) testing is one method of implementing continuous nondestructive structural health monitoring. A novel thick-film (17.6 μm) AE sensor is presented. Lead zirconate titanate thick films were fabricated using a powder/sol composite ink deposition technique and mechanically patterned to form a discrete thick-film piezoelectric AE sensor. The thick-film sensor was benchmarked against a commercial AE device and was found to exhibit comparable responses to simulated acoustic emissions.**

I. Introduction

Acoustic emission (AE) sensors are an important tool in nondestructive testing (NDT). NDT is used in many fields, including structural and process monitoring and biomedical research, with industries such as aerospace, nuclear, and civil engineering making widespread use of NDT by AE monitoring [1]–[4]. AE monitoring is now being applied to both static and nonstatic systems [5]. The drive for smaller, more cost-effective devices is paramount and one solution to this challenge is the use of micro-electromechanical systems (MEMS). MEMS devices enable AE technology to be deployed in space- or weight-critical applications for which the commonly used commercial bulk-piezoelectric AE sensors [1], [2], [6] are inappropriate. MEMS manufacturing methods also enable devices to be low cost and disposable, enabling deployment in situations where device recovery is difficult.

In this work, an 8-mm-diameter, 17-μm-thick film acoustic emission sensor is deposited directly onto a Kovar (Carpenter Technology Corp., Reading, PA) plate acting as the test structure. The diameter of 8 mm was chosen because it is comparable to the existing commercial sensor. The response of the thick-film device to these simulated acoustic events was compared with responses of one of the smallest commercially available sensors for benchmarking purposes. The thick-film and commercial devices were then exposed to simulated acoustic emissions. The thickness of 17 μm is 1/140 the thickness of some of the smallest available commercial devices [7].

Manuscript received December 8, 2010; accepted June 11, 2011.

The authors are with Cranfield University, Cranfield, Bedfordshire, UK (e-mail: r.a.dorey@cranfield.ac.uk and d.mba@cranfield.ac.uk).

Digital Object Identifier 10.1109/TUFFC.2011.2043

II. Method

Lead zirconate titanate (PZT) sol and composite slurry (PZT sol and powder) were produced with a Zr/Ti ratio of 52/48 [8], [9]. A Kovar substrate with dimensions 100 × 100 × 3.2 mm was cleaned in an acetone/isopropyl alcohol ultrasonic bath. A 17.6-μm PZT thick film was deposited onto the Kovar using a 4(2C+5S) composite spin-coating technique [10]. A spin speed of 2000 rpm was used. After each deposition, the film was dried at 310°C for 180 s and pyrolised at 525°C for 60 s. Once the composite film was complete, sintering was carried out at 720°C for 20 min, following a ramp rate of 5°C/min. The PZT was masked and then patterned by powder blasting. To produce the final sensing elements, a mask was applied and an 8-mm-diameter top electrode, of 11.2-nm-thick Cr and 150-nm-thick Au, was sputtered onto the PZT surface. The PZT was then heated to 135°C and poled by a corona poling process at 16 kV with a needle-to-sample gap of 30 mm for 15 min. The PZT was left to cool under the electric field to prevent stress depoling. A BNC connector was connected to the top electrode and to the Kovar base plate. The BNC was connected directly to the commercial pre-amplifier. This was done to minimize the signal loss and interference caused by electrical resistance in the system before amplification. The poled thick-film device had a piezoelectric constant (d_{33}) of 38 pC/N, a capacitance of 2.18 nF, and a dielectric loss of 0.102, measured at 100 kHz. The relative permittivity of the film was calculated to be 86.21.

The thick-film device deposited on the Kovar plate consists of a circular single element; this provides high sensitivity to AE regardless of the sensor orientation relative to the incoming wave [11]. As such, a single-element PICO sensor from Physical Acoustics Corporation (PAC; Princeton Junction, NJ), with an operating frequency range of 200 to 750 kHz, was chosen for comparative testing. Another reason for selecting the PICO sensor was the small size (4 × 5 mm) of the device, because it is often used in situations similar to those for which the thick-film sensor is designed. A commercial PICO sensor was mounted 32 mm from the center of the Kovar plate using grease as a coupling agent, see Fig. 1. Signals from both the PICO and the thick-film PZT sensors were monitored using MISTRA, a commercial transient recorder-analyzer system from PAC (2001). The PICO and thick-film sensor signals were pre-amplified by 40 and 60 dB, respectively, using variable gain 2/4/6 pre-amplifiers from PAC. A lower-

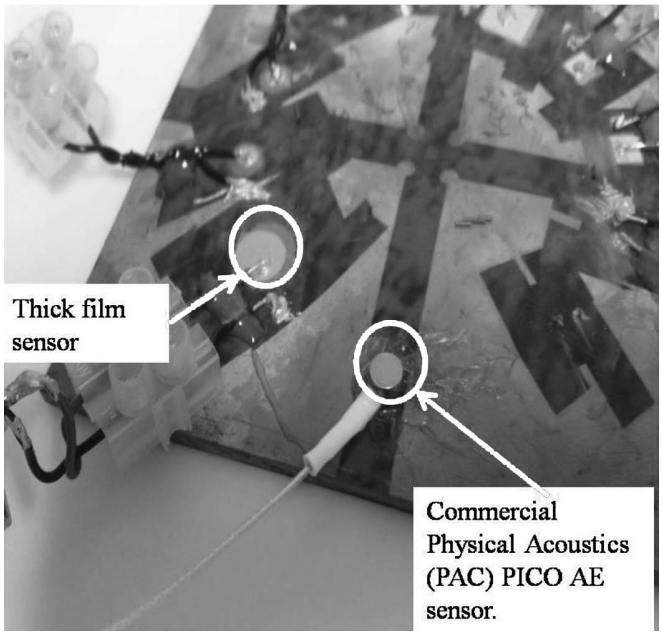

Fig. 1. A thick-film PZT acoustic emissions device (left) alongside a commercially available PICO sensor (right).

frequency filter of 100 kHz and an upper filter of 1.2 MHz were used, and AE waveforms were recorded at a sampling rate of 10 MHz.

III. Results

An AE event was simulated by the Hsu–Nelson test: breaking a 0.5-mm-diameter 2H pencil lead at the center of the Kovar plate [12]. A variation in the waveform arrival times between the PICO and the thick-film sensor suggests that the simulated acoustic source was not exactly equidistant from the sensors; this effect is apparent in all tests performed using the Hsu–Nelson test. A total of 15 simulations were undertaken and representative time-domain responses and corresponding frequency spectra are shown in Fig. 2.

From initial observations, it is clear the PICO sensor signal exhibits a greater concentration of higher-frequency wave components within the initial 100 μs of the waveform. The maximum amplitude of the waveform detected by the thick-film device is 0.054 times that of the PICO

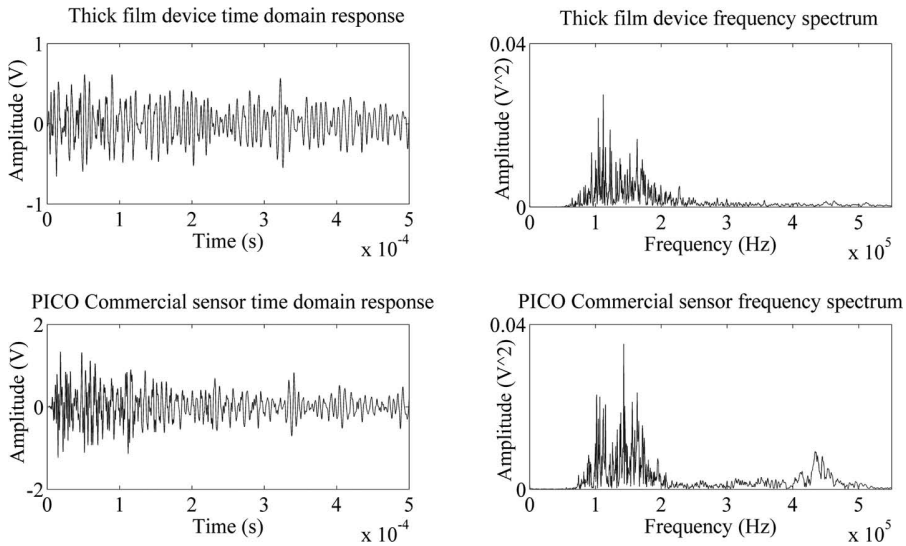

Fig. 2. Time domain plot showing the initial 500 μs of waveforms received by the thick-film and PICO sensors (top and bottom, respectively) and the corresponding frequency domain plots following a Hsu–Nelson simulated acoustic emission event.

TABLE I. Data Collected From Hsu–Nelson Tests Before Pre-Amplification.

	Test number						
	1	2	3	4	5	6	7
Thick-film							
Peak amplitude (mV)	0.693	1.035	0.534	0.615	0.659	0.654	0.474
Rise-time (μs)	11.6	10.9	11.4	11.4	11.4	11.9	10.4
Duration (ms)	2.055	2.806	1.983	2.626	2.007	1.996	2.001
PICO							
Peak amplitude (mV)	12.842	17.042	10.352	11.866	11.866	13.379	8.301
Rise-time (μs)	7.9	11.9	7	7.8	8	8	11.8
Duration (ms)	1.899	2.552	1.663	2.048	1.435	1.375	1.656
Differential between thick-film and PICO devices							
Peak amplitude (mV)	−12.149	−16.007	−9.818	−11.251	−11.207	−12.725	−7.827
Rise-time (μs)	3.7	−1	4.4	3.6	3.4	3.9	−1.4
Duration (ms)	0.156	0.254	0.32	0.578	0.572	0.621	0.345

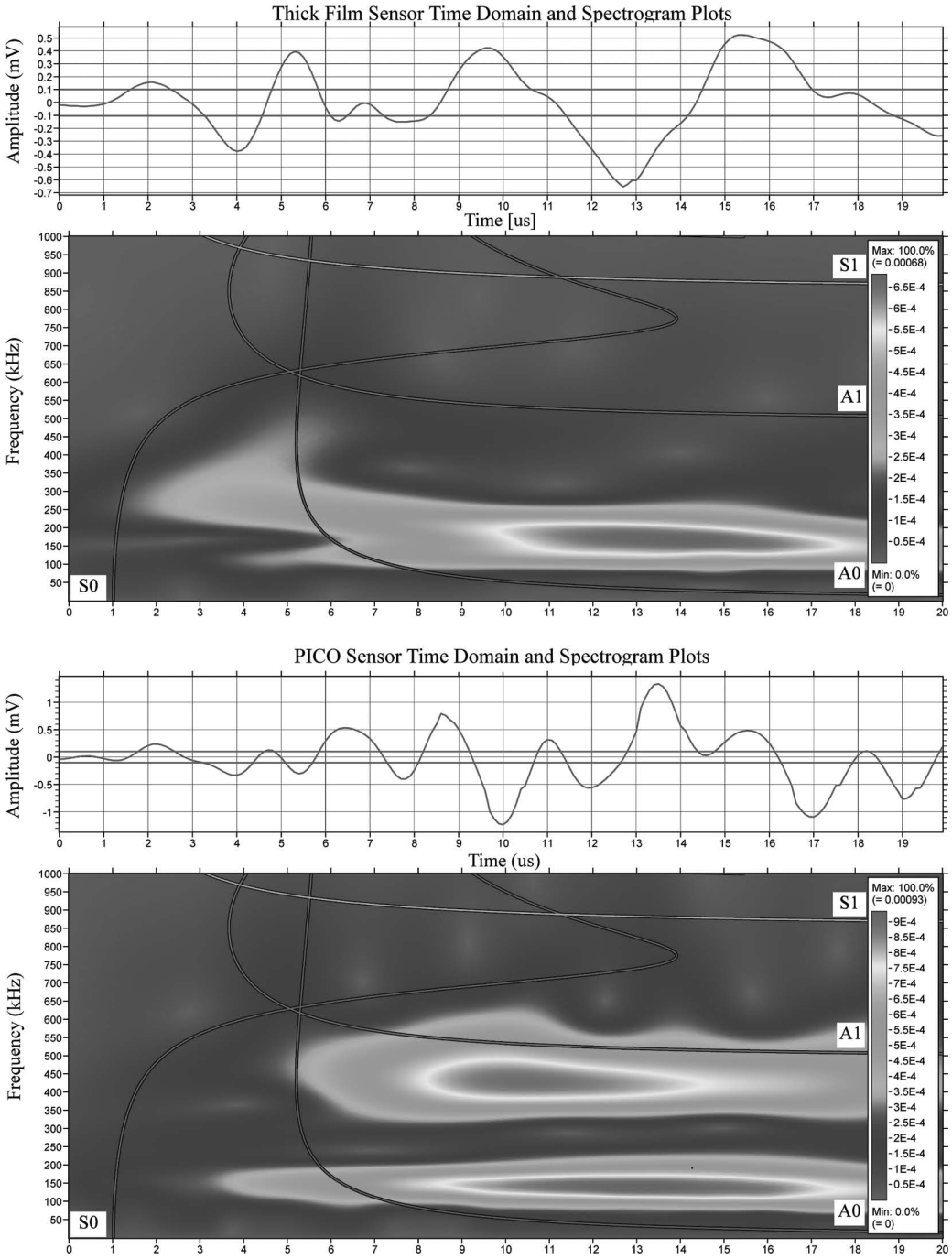

Fig. 3. Time domain plot and Gabor transform spectrogram of the initial 20-μs waveform received by thick-film (top) and PICO (bottom) devices following a simulated acoustic emission event with waveform dispersion curves of zero- and first-order symmetric and asymmetric Lamb waves overlaid using the Vallen GmBH software.

sensor (see Table I), whereas the overall signal energy for the thick-film sensor is 0.083 times that of the PICO sensor. The signal amplitude of the thick-film waveform takes longer to drop below 10% of the peak amplitude than the PICO commercial device, as shown in Table I.

The waveform detected by the thick-film sensor in tests 1, 3, 4, 5, and 6 (see Table I) has a mean rise-time from 10% to 90% peak amplitude of the initial signal which is 3.66 μs slower than that of the waveform detected by the PICO sensor (11.54 μs and 7.74 μs for the thick-film device and the PICO sensor, respectively) with a standard deviation of 0.33 μs. In tests 2 and 7, the rise-time values for the PICO sensor were inconsistent with the data collected from the other tests; for reasons explored in Section IV, the data from these tests was excluded from the rise-time analysis. The calculation of the average and standard deviation of rise times was only carried out using the differential data between the thick-film and the PICO

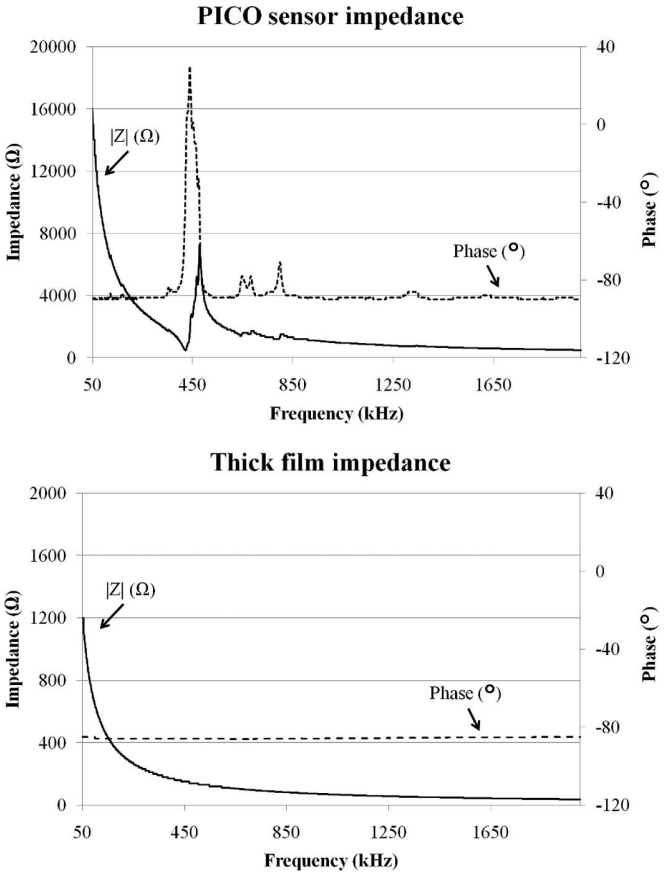

Fig. 4. Impedance measurement plots showing impedance and phase angle for the PICO commercial sensor (top) and the thick-film device (bottom). The resonance peak of the PICO sensor between 400 and 650 kHz can clearly be seen.

devices to provide a comparison between the devices. The average and standard deviation of the raw data for each device is not presented because this only provides information about the pencil break and not about the qualities of the devices in comparison to each other.

IV. Discussion

The greater signal duration exhibited by the thick-film sensor waveform, measured as the differential of the time for the signal amplitude to rise above 10% of the maximum amplitude to the time when the signal drops below 10% of the maximum amplitude, is explained by the lack of an acoustically matched backing to attenuate any signal reflections from the top surface of the sensor and by signal distortion caused by mismatching of the electrical impedance of the device amplifier circuits in the device studied [13]. However, it must be noted that the waveform detected by the PICO commercial sensor must travel through coupling media and wear plates before reaching the active element, consequently the AE signal will be distorted and attenuated while traversing these obstacles [14]. The direct coupling of the thick-film device greatly reduces these effects.

The lower amplitude response to the raw input signal is similarly explained by the electrical impedance matching. Lower piezoelectric properties also adversely affect the response of the thick-film device to the raw input signal. Because of the use of bulk manufacturing techniques, the piezoelectric active element in the PICO device does not have the same microstructure or stress state as the thick-film device. Such stresses in the thick-film device are known to result in a reduction of the piezoelectric properties compared with bulk materials [15]. Poorer piezoelectric properties result in a reduction in the response that the thick-film device exhibits under excitation. The thick-film device had a d_{33} of 38 pC/N compared with a reported bulk value of 330 pC/N for PZ26 [16]. Work is ongoing to improve the film piezoelectric properties because the output amplitude is directly proportional to the d_{33}. It should be noted that a change to the d_{33} value would also result in a change to both the electrical and acoustic matching properties of the material, altering the device response. The device with the highest d_{33} may not, therefore, be the most appropriate for AE sensing.

The fast Fourier transform (FFT) frequency spectra of the PICO and thick-film sensors are comparable (Fig. 2); they have similar frequency responses to the simulated emission between 50 and 250 kHz. Although FFT analysis has been employed for more than a century to aid in the characterization of frequency content within a signal, FFT is limited in applications in which the signal frequency content varies over time [17]. To provide more information about the composition of the detected signal, a different approach must be taken. A spectrogram presents relative frequency intensity plotted against time, enabling observation of the changing frequency composition of the signal. A Gabor transform is an efficient way of calculating the spectrogram of the detected signal. The reduced spectrogram calculation time requires a compromise between loss of time and frequency resolution [17], [18].

The variation in frequency response to different components of the Lamb wave is demonstrated by superimposing Lamb wave distribution curves for the AE signal in the Kovar plate onto a spectrogram of the initial 20 μs of time domain waveform detected by each device as shown in Fig. 3. The spectrogram was calculated using the AGU Vallen Wavelet software (release A2009.1027, Vallen Systeme GmBH, Icking, Germany) which runs on a Gabor transform; the overlaid waveforms were calculated using the Vallen Dispersion software (release A2009.1027, Vallen Systeme GmBH). A transform window of 20 μs was used.

The spectrogram in Fig. 3 shows that the thick-film sensor initially exhibits a stronger response to zero-order symmetric Lamb waves (S_0) than the PICO sensor, but above 700 kHz, the thick-film device is subject to greater attenuation than the PICO sensor and the S_0 signal amplitude decreases. The response to the lower-frequency zero-order asymmetric wave (A_0) is comparable in the devices. The thick-film device lacks the peak at 400 to 500 kHz that is characteristic of the frequency response of the PICO sensor. This peak is caused by resonance in the

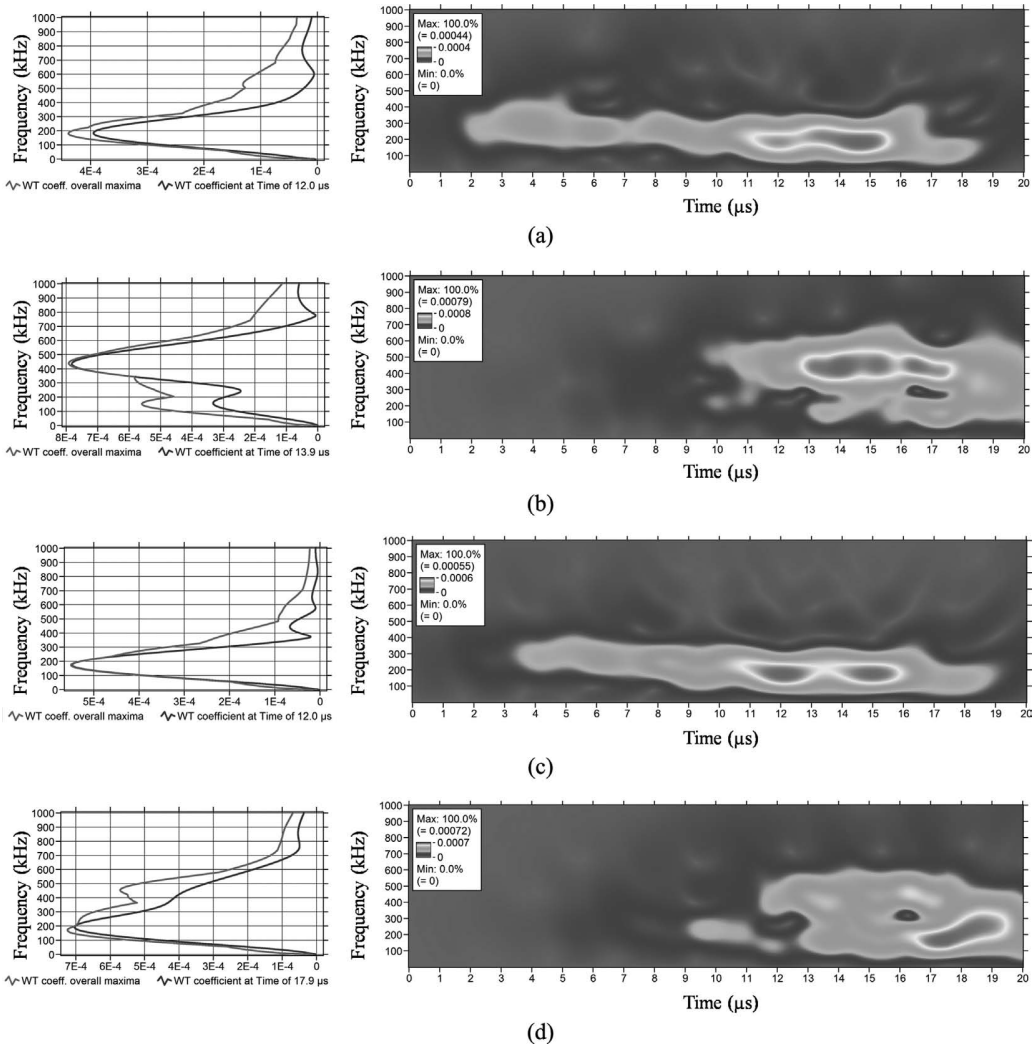

Fig. 5. Gabor transform spectrograms of representative detected waveforms with corresponding wavelet transform coefficient plots for pencil-break tests in which, for test 1, the first-order asymmetric Lamb wave dominates: (a) and (b) for thick-film and PICO sensor responses, respectively, and, for test 2, the zero-order asymmetric Lamb wave dominates: (c) and (d) for thick-film and PICO sensor responses, respectively, using the Vallen GmBH software.

400 to 650 kHz band, as shown by electrical impedance measurements carried out on both devices *in situ* (Fig. 4). A flatter frequency response is more desirable in an AE sensor [19], and therefore the lack of a sensitivity peak between 400 and 650 kHz exhibited by the thick-film sensor is of benefit to the thick-film device. When stimulated by the Hsu–Nelson pencil break test, the large amplitude signal detected by the PICO sensor in the 400 to 500 kHz range is actually caused by the larger response at resonance of the PICO sensor with the first-order asymmetric Lamb wave (A_1) component of the pencil-break emission, which exhibits a frequency of 500 kHz. The thick-film sensor lacks this resonant peak, and so the amplitude of the response to the A_1 waveform is more representative of the actual waveform amplitude, relative to the other waveform component amplitudes, than the data gathered by the PICO sensor.

The two results (test numbers 2 and 7), in which the commercial PICO sensor exhibited a longer rise-time than the thick-film device, can be explained by the domination of the A_0 waveform in the initial stages of the pencil break signal rather than the A_1 waveform, as in the bulk of the test data. This is due to variation in the pencil break. This issue is not observed with the data for the thick-film devices because thick-film devices have a flat frequency response across a larger bandwidth, meaning that no one waveform dominates the overall response disproportionately. This can be seen in the 2-D frequency projection plots in Fig. 5, which compare spectrograms of a representative waveform responses to a pencil-break test which is dominated by the A_1 waveform [Figs. 5(a) and 5(b)] and a response dominated by the A_0 waveform [Figs. 5(c) and 5(d)]. A 2-D frequency projection of the representative waveforms is also presented, showing both the frequency projection at the maximum amplitude and the frequency projection at 90% of the maximum amplitude, which was used for calculating the rise time. The representative waveforms chosen were the full waveforms from the

thick-film and PICO sensors in tests 1 and 2 (see Table I). Without the domination of the A_1 waveform resonance in the PICO sensor, the rise time for the PICO devices would be longer than that of the thick-film device, as expected, because the thick-film device is directly bonded to the surface of the Kovar plate.

V. Conclusions

The PZT thick-film device performed well and exhibited several beneficial characteristics compared with the PICO commercial sensor. The thick-film device showed qualitatively similar acoustic properties to those exhibited by the PICO commercial device between 39 kHz and 1.25 MHz and was quantitatively similar between 39 and 313 kHz. This indicates that the thick-film PZT device is well suited to acoustic emission monitoring, especially in the lower-frequency AE band. This was expected because both the thick-film and PICO sensors are of a similar single-element type. The thick-film sensor lacks sensitivity at frequencies in excess of 700 kHz. This is not a significant concern because the majority of acoustic emission monitoring is carried out below this frequency. The flatter frequency response of the thick-film sensor compared with the PICO sensor is a benefit because it ensures a representative amplitude response to all Lamb wave components within the operating range usually required for AE monitoring. This is not achieved by the commercial device, which exhibits a resonant peak at in the range of 400 to 650 kHz. The addition of an acoustically matched backing could improve the properties of the thick-film device by minimizing waveform reflection from the device-to-air interface. Further work could also be carried out to minimize the impedance mismatch and therefore improve the signal-to-noise ratio.

Work has previously been carried out on using PZT as an active element in AE devices [20], including bulk PZT fibers [21], [22] and thin-film materials [23]. However, this is the first known attempt to deposit a structurally integrated PZT acoustic emissions sensor directly onto the element requiring monitoring, using thick-film processing techniques. The successful manufacture of a viable thick-film acoustic emission device could lead to commercial uptake and deployment of thick-film devices in continuous nondestructive structural health monitoring applications.

References

[1] S. Dolinsek, J. Kopac, Z. J. Viharos, and L. Monostori, "An intelligent AE sensor for the monitoring of finish machining process," in *Proc. 2nd Int. Conf. Intelligent Processing and Manufacturing of Materials*, Honolulu, HI, Jul. 10–15, 1999, vol. 2, pp. 847–853.

[2] R. K. Miller and P. McIntire, *Non-Destructive Testing Handbook; Vol. 5: Acoustic Emission Testing,* 2nd ed., Columbus, OH: American Society of Non-Destructive Testing, 1987.

[3] A. Berkovits and D. Fang, "Study of fatigue crack characteristics by acoustic emission," *Eng. Fract. Mech.*, vol. 51, no. 3, pp. 401–409, 1995.

[4] P. Sedlak, J. Sikula, T. Lokajicek, and Y. Mori, "Acoustic and electromagnetic emission as a tool for crack localization," *Meas. Sci. Technol.*, vol. 19, no. 4, art. no. 045701, 2008.

[5] D. Mba and R. B. K. N. Rao, "Development of acoustic emission technology for condition monitoring and diagnosis of rotating machines: Bearings, pumps, gearboxes, engines, and rotating structures," *Shock Vib. Dig.*, vol. 38, no. 1, pp. 3–16, 2006.

[6] G. Gautschi, *Piezoelectric Sensorics: Force, Strain, Pressure, Acceleration and Acoustic Emission Sensors, Materials and Amplifiers.* New York, NY: Springer-Verlag, 2002.

[7] European Physical Acoustics SA, (2010, Sep. 7) Complete line of standard acoustic emission sensors. [Online]. Available: http://www.epandt.com/us/Catalog_AE%20sensor_us.htm

[8] G. De Cicco, B. Morten, and M. Prudenziati, "Piezoelectric thick-film sensors," in *Handbook of Sensors and Actuators*, vol. 1, Amsterdam, The Netherlands: Elsevier Science, 1994, pp. 209–228.

[9] R. A. Dorey, S. B. Stringfellow, and R. W. Whatmore, "Effect of sintering aid and repeated sol infiltrations on the dielectric and piezoelectric properties of a PZT composite thick film," *J. Eur. Ceram. Soc.*, vol. 22, no. 16, pp. 2921–2926, 2002.

[10] R. A. Dorey, F. Dauchy, D. Wang, and R. Berriet, "Fabrication and characterisation of annular thickness mode piezoelectric micro ultrasonic transducers," *IEEE Trans. Ultrason. Ferroelectr. Freq. Control*, vol. 54, no. 12, pp. 2462–2468, 2007.

[11] European Physical Acoustics SA, (2010, Jan. 26) Acoustic emission products. 2004. [Online]. Available: http://www.epandt.com/us/capteur_ea_us.html

[12] *Standard Guide for Determining the Reproducibility of Acoustic Emission Sensor Response.* ASTME 976-94, 1996.

[13] J. L. San Emeterio, A. Ramos, P. T. Sanz, and A. Ruiz, "Evaluation of impedance matching schemes for pulse-echo ultrasonic piezoelectric transducers," *Ferroelectrics*, vol. 273, no. 1, pp. 297–302, 2002.

[14] J. M. Park and H. C. Kim, "The effects of attenuation and dispersion on the waveform analysis of acoustic emission," *J. Phys.*, vol. 22, no. 5, p. 617–622, 1988.

[15] P. Glynne-Jones, S. P. Beeby, P. Dargie, T. Papakostas, and N. M. White, "An investigation into the effect of modified firing profiles on the piezoelectric properties of thick-film PZT layers on silicon," *Meas. Sci. Technol.*, vol. 11, no. 5, pp. 526–531, 2000.

[16] R. A. Dorey and R. W. Whatmore, "Apparent reduction in the value of the d_{33} piezoelectric coefficient in PZT thick films," *Integr. Ferroelectr.*, vol. 50, no. 1, pp. 111–119, 2002.

[17] B. Boashash, Ed., *Time Frequency Signal Analysis and Processing—A Comprehensive Reference*, 1st ed., Oxford, UK: Elsevier, 2003.

[18] A. Moreno-Munoz, Ed., *Power Quality—Mitigation Technologies in a Distributed Environment*, 1st ed., London, UK: Springer-Verlag, 2007.

[19] M. Johnson and P. Gudmundson, "Experimental and theoretical characterization of acoustic emission transients in composite laminates," *Compos. Sci. Technol.*, vol. 61, no. 10, pp. 1367–1378, 2001.

[20] M. Barbezat, A. J. Brunner, P. Flüeler, C. Huber, and X. Kornmann, "Acoustic emission sensor properties of active fibre composite elements compared with commercial acoustic emission sensors," *Sens. Actuators A*, vol. 114, no. 1, pp. 13–20, 2004.

[21] H. Cho, T. Abe, and T. Matsuo, "Quantitative evaluation of the blocking ratio of a blockage inside a pipe utilizing film-type PZT elements," *J. Solid Mech. Mater. Eng.*, vol. 3, no. 2, pp. 278–286, 2009.

[22] M. Eaton, R. Pullin, K. Holford, S. Evans, C. Featherston, and A. Rose, "Use of macro fibre composite transducers as acoustic emission sensors," *Remote Sens.*, vol. 1, no. 2, pp. 68–79, 2009.

[23] C. R. Cho, L. F. Francis, and M. S. Jang, "Piezoelectric properties and acoustic wave detection of $Pb(Zr_{0.52}Ti_{0.48})O_3$ thin films for microelectromechanical systems sensor," *Jpn. J. Appl. Phys.*, vol. 38, no. 7A, pt. 2, pp. L751–L754, 1999.

Andrew J. Pickwell is a final-year Ph.D. researcher at Cranfield University. Mr. Pickwell graduated with a first class B.Eng. (Hons) in mechanical engineering from the University of Hertfordshire in 2008.

Mr. Pickwell has industrial experiance with Caterpillar Inc. and Mastenbroek Ltd. He is an associate member of the Institute of Mechanical Engineers (AMIMechE) and a graduate member of the Institute of Materials, Minerals and Mining (Grad IMMM).

Mr. Pickwell is currently carrying out work on the design and development of micro electromechanical solutions in the field of structural

health monitoring and non-destructive testing, including the integration of thick-film micro electromechanical systems with various substrate materials.

Robert Dorey holds a chair in Nanomaterials and is Fellow of the Higher Education Academy (FHEA) and Institute Materials, Mining and Minerals (FIMMM), as well as a Chartered Scientist and Engineer.

Professor Dorey heads the Microsystems and Nanotechnology Centre at Cranfield University, and between 2003 and 2008 he held a prestigious Royal Academy of Engineering/EPSRC Research Fellowship.

Professor Dorey leads the Energy and Environment research team concerned with nano- and micro-scale solutions for energy generation and environmental monitoring, with a particular focus on micro-scale processing and materials integration, fabrication, and microstructure-property relationships.

Professor Dorey joined Cranfield University in 2000 after completing his Ph.D. degree at the University of Surrey for work on the sintering of alumina and the effect of porosity on thermal shock behavior, strength, and Young's modulus of alumina ceramics. Dr. Dorey's research record brings together materials processing and characterization of both mechanical and electrical properties. In June 2003, he was awarded academic status at Cranfield (lecturer position).

David Mba is actively involved with research in machine condition monitoring and prognosis, machine dynamics, and turbo-machinery.

Thick film, Acoustic Emission sensors for embedded structural health monitoring systems.

A.J. Pickwell, R.A. Dorey, D. Mba

Cranfield University, College Road, Cranfield, Bedfordshire, MK43 0AL

ABSTRACT

Structural heath monitoring of engineering structures is of growing interest due to increased complexity of such structures and the ability to schedule maintenance when it is needed thus preventing unnecessary work or preventing failure. One such method for monitoring the structural health of large scale structures is through the detection of Acoustic Emissions (AE). A novel thick film Acoustic Emission sensor is presented. Piezoelectric thick film AE sensors were fabricated by creating and pattering lead zirconate titanate (PZT) thick films using a powder/sol composite ink deposition technique in conjunction with mechanical patterning of the subsequent films. The resultant AE sensors exhibit a response comparable to commercially available AE sensors. Comparative results between the thick film and commercial sensors will be reviewed and discussed.

Keywords: Acoustic Emission, Sensor, PZT, Thick film.

1 INTRODUCTION

Non-destructive testing (NDT) is used in many applications, structural monitoring, process monitoring and biomedical research for example. Industries such as aerospace, nuclear and civil engineering make widespread use of NDT. A vital technique used in NDT is Acoustic Emission (AE) monitoring. Whilst traditionally used for static applications there is a focus on developing miniaturized sensors for use in both static and non-static NDT applications [1]. It is vital that whilst devices are miniaturized cost effectiveness is maintained. One proposed solution to this challenge is micro-electromechanical systems (MEMS). This work details the deposition of a thick film AE sensor directly onto a structural element. An artificial AE event is simulated in the element and the response compared to responses of commercially available sensors for benchmarking purposes.

2 BACKGROUND

2.1 Acoustic Emission Signals

AE waves come in two distinct types, transient and continuous. The most pertinent wave form for AE monitoring is transient. Typically the transient type emission, caused by material phase transformation, crack growth or the movement of dislocations within the material, is a short time period event. The event contains, within its waveform, important information that can provide much information about the signal source. These important characteristics include the event duration, maximum amplitude, rise time and count [2].

The measured area under the rectified signal is related to the magnitude and velocity of the emission source. The maximum amplitude is proportional to the surface area created during a cracking event and the velocity of crack propagation. Event duration can be used to differentiate an AE event from background noise signals and can also be used in conjunction with the rise time and the count information to identify the position and source of the AE.

2.2 Acoustic Emission Sensor Design

Almost all AE sensors are piezoelectric and are similar in design to acceleration sensors [3]. Different types of piezoelectric sensors are available to carry out the task of detecting AE events. Piezoelectric sensors started to appear shortly after the First World War. Förster and Scheil are recognised as the first to use the piezoelectric effect to detect AE signals in 1936 [3]. Originally sensors were piezoelectric crystals. Quartz (SiO2) was the most common single crystal material as it has good piezoelectric properties and a high mechanical strength. Several other crystals showed sufficient qualities to be used in commercial AE sensors including tourmaline, gallium orthophosphate and crystals of the CGG group [3]. Several ceramic material groups were also investigated but none surpassed single crystals for AE applications. Lead zirconate titanate was subsequently invented and was found to show properties that were promising for sensing applications.

Other sensor types include capacitive transducers and active filament sensors. In capacitive transducers the AE wave moves internal conductive elements producing a capacitance change directly related to the amplitude of the input AE. It is known that capacitive transducers can record a good approximation of surface movement however the sensitivity of these sensors is insufficient for actual Acoustic Emission testing according to Miller and McIntire [2]. Active filament sensors are made with uniaxially orientated piezoelectric fibres embedded in a polymer matrix between two interwoven electrodes [4] this structure is also known as an active fibre composite elements or AFC. Barbezat et al. [5] identified that AFC are superior to traditional AE sensors in that they are lighter, more flexible and could be combined with existing polymer products. AFC sensors exhibit anisotropic sensitivity caused by the orientation of the fibres within the material. This combined with the fact that AFC sensors have a lower sensitivity to AE events than traditional piezoelectric sensors does limit the applications that they are suitable for. Work is also being carried out on adapting piezoelectric paint for use as an in-situ Acoustic Emission sensor [6].

A typical piezoelectric element AE sensor design is shown in figure 1. The sensor case acts as the conductive element for the earth and helps to shield the signal from external noise sources. The backing reduces noise caused by reflection of the signal from the back face of the piezoelectric element which would otherwise give a false reading.

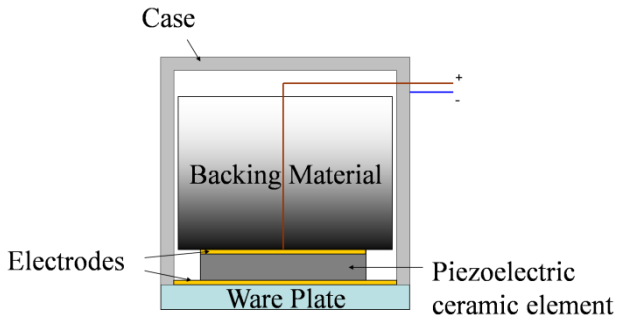

Figure 1. Schematic of traditional single element AE sensor design.

2.3 Material Selection

There are several thick film piezoelectric materials. The material with the best properties for Acoustic Emission devices is lead zirconate titanate (PZT). PZT can be used as a bulk material, as in existing AE devices, or deposited as a thick or thin film. Thick films have the advantage of being more durable than thin films. There are various methods for depositing thick films onto a substrate material

including screen printing, sputtering, direct writing, electrophoretic deposition, micro-stereolithography and composite sol-gel techniques [7]. Composite sol-gel is the intended production method for PZT deposition in this work and so will be presented here.

Composite sol-gel techniques have been researched extensively and provide a promising avenue for advancing thick film technology. In this method firstly a sol is produced. The sol is then mixed with powder to produce a composite slurry. The slurry is spun onto a flat substrate to ensure an even film thickness. Each layer is then heated to remove the solvent. Several layers can then be deposited onto the previous ones. In this way a thick film can be built up [8]. It is possible to increase the density of the porous film by repeated sol infiltrations. These infiltrations fill the pores in the material before being dried. Several infiltrations can be carried out on each layer deposited. These infiltrations can be used to lower the sintering temperature and have previously been investigated [9][10]. Once the required film thickness has been achieved the material is sintered to increase the density and piezoelectric properties [11]. This process produces a film with a consistent thickness and good piezoelectric qualities.

3 DEVICE MANUFACTURE

PZT sol and composite slurry were produced with a Zr/Ti ratio of 52/48 [9][12]. A Kovar substrate with dimensions 100x100x3.2mm was cleaned in an acetone/IPA ultrasonic bath. A spin coating technique was used to deposit a 4(2C+5S) composite PZT film of 17.6µm thickness onto the substrate. 2000rpm spin speed was used. The film was dried at 310°C for 180 seconds and pyrolised at 525°C for 60 seconds after each deposition. Upon completion of the composite film deposition process sintering was carried out at 720°C for 20min. To reduce thermal stress between Kovar and PZT a ramp rate of 5°C/min was employed. A mask was applied to the PZT film and then patterning was carried out by powder blasting. Discrete piezoelectric elements were produced by the application of a mask prior to the sputtering of an 8mm diameter Cr/Au top electrode, of 11.2nm/150nm onto the PZT film surface. The PZT was poled by a corona poling process. The film was initially heated to 135°C before poling was carried out for 15mins at 16kVwith a needle to sample gap of 30mm. To prevent depoling the PZT was left to cool under the electric field. The top electrode and the Kovar substrate was electrically connected using a BNC connecter. The poled thick film device was found to have a capacitance of 2.18nF and a dielectric loss of 0.102, measured at 100kHz. The finished device is shown in figure 2 alongside a Physical Acoustics Corporation (PAC) PICO commercial sensor.

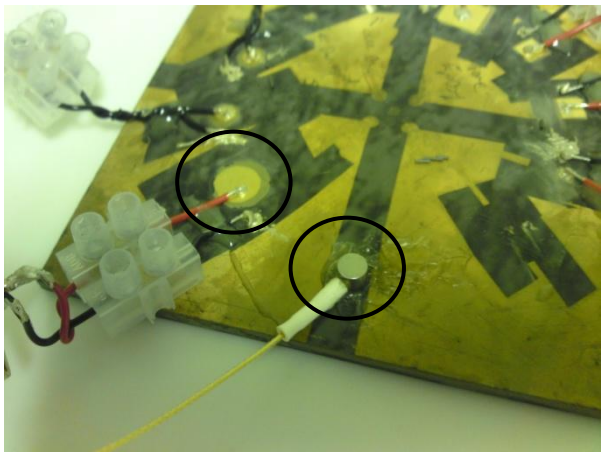

Figure 2. A thick film PZT Acoustic Emissions device (left) alongside a commercially available PICO sensor (right).

4 RESULTS AND DISCUSSION

4.1 Thick Film and Single Element Sensor Comparison

The thick film device deposited directly onto the Kovar substrate is a single element design. This provides high sensitivity to AE signals independent of the sensor orientation relative to the incoming acoustic wave. A PICO sensor from PAC was chosen for comparative testing as it is of a similar design to the thick film device. The PICO sensor has an operating frequency of 200-750kHz. A commercially available PICO sensor was mounted at 32mm from the center of the Kovar substrate with grease used as a coupling agent. Signals produced by the PICO and the thick film PZT devices were monitored using MI-TRA a commercial transient recorder-analyzer system from PAC 2001. Variable gain 2/4/6 pre-amplifiers from PAC were used. Pre-amplifications of 40dB and 60dB were used for the PICO and thick film sensor signals respectively. A 10MHz sampling rate was used to give a good resolution in signal analysis. A schematic of the Acoustic Emission monitoring set up is shown in figure 3.

AE events were simulated using the Hsu Nelson test carried out at the centre of the Kovar substrate. The Hsu Nelson test consists of breaking a 0.5mm diameter HB pencil lead [13].There is a variation in waveform arrival times between the PICO and the thick film sensor suggesting that the simulated acoustic source was not exactly central between the two sensors, this effect is apparent in all tests performed using the Hsu Nelson test. It is clear from figure 4 that, qualitatively, the waveforms exhibit similar properties. The PICO sensor signal exhibits a concentration of higher frequency wave components within the initial 100μs of the waveform compared to the thick film device as shown by the spectrogram in figure 5. The maximum amplitude of the PICO sensor is1.9 times that of the thick film device with the rise time of the thick film sensor being 25μs greater and the signal duration 0.5ms greater than that of the PICO sensor. The signal energy of the thick film waveform is 1.2 times greater than that of the PICO sensor. The properties of the PICO and thick film waveform frequency spectrum, shown in figure 4, are comparable, both exhibiting a frequency response to the simulated emission between 50kHz and 250kHz. The thick film device lacks the sensitivity peak at 400-500kHz which is characteristic of the frequency response of the PICO device.

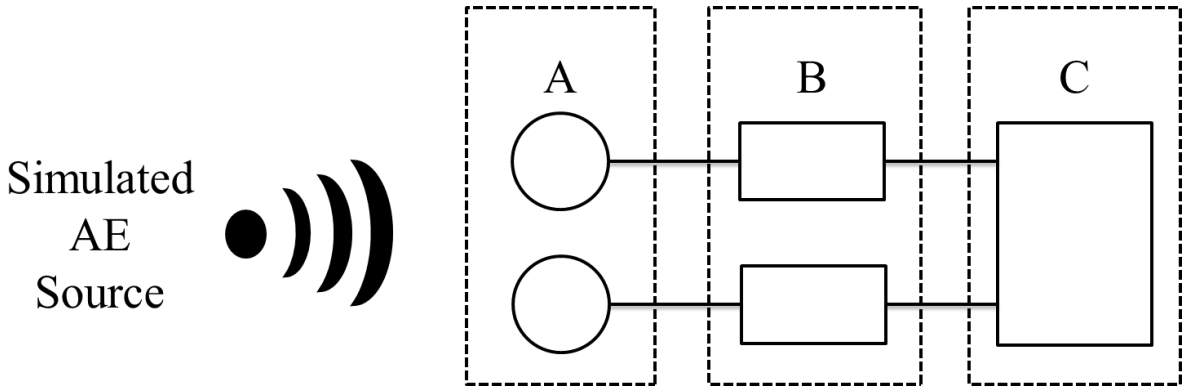

Figure 3. Schematic of the AE monitoring system, Simulated AE signals are received by two different AE sensors at A. The received signals are pre-amplified by 40/60dB as specified at B. The pre-amplified signals are received by the MI-TRA PCI card for analysis at C.

The greater amplitudes of the raw signal and frequency response can be explained as being a result of the relative thickness of the active piezoelectric element in the PICO sensor compared to that of the thick film device and the differences in electrical matching between the sensors and the commercial monitoring system. A flatter frequency response is desired in Acoustic Emissions applications and therefore the thick film frequency response lacking the sensitivity peak between 400kHz and 500kHz

is of benefit. The increased signal duration of the thick film sensor is explained by a lack of acoustically matched backing to attenuate signal reflections from the top surface of the device.

4.2 Thick Film and Dual Element Sensor Comparison

The PICO sensor was replaced on the Kovar substrate by a dual element, differential WD sensor from PAC with an operational range between 100 and 1000kHz. The sensor design alleviates issues of electromechanical interference in the signal. The WD sensor includes a 24dB common-mode rejection giving a signal with reduced interference. The WD sensor was mounted in an identical position on the Kovar substrate as the PICO sensor to ensure that there were no variations in the waveforms due to plate geometry. The signal processing parameters utilized were the same as those used for the thick film/PICO test. Pre-amplifications of 40dB and 60dB were applied to signals from the WD and thick film sensors respectively.

An AE event was simulated using the Hsu Nelson method and the signal was received by the devices. The waveform from the WD sensor has a peak amplitude an order of magnitude greater than that of the thick film waveform as shown in figure 4. The commercial sensor waveform has a rise time 50µs greater than that of the thick film device. The thick film sensor signal duration is 180µs greater than that of the WD device. The signal energy of the WD sensor is 6.6 times that of the thick film waveform. The WD sensor signal frequency spectrum indicates a frequency response intensity of a greater magnitude than both the thick film and PICO sensors. The frequency spectrum also indicates that the WD sensor exhibits sensitivity to the simulated AE between 75kHz and 350kHz. The WD frequency response is flatter than either the PICO or the thick film devices over a greater bandwidth.

The increased frequency response bandwidth present in the WD sensor (figure 4), along with a piezoelectric active element of greater thickness and an electrical impedance matching explain why the commercial WD time domain waveform amplitude is of greater magnitude than the thick film device. The WD sensor exhibits an initial amplitude peak before a second higher peak as a possible result of the dual element sensor design with the element closest to the transmission media being activated initially and then the second element being activated.

4.3 Dual Element and Single Element Sensor Comparison

As control the PICO sensor was tested against the WD sensor. Both devices were mounted on the Kovar plate using grease as a coupling agent. An Acoustic Emission was simulated at 32mm from the centre of both devices. A pre-amplification of 40dB was applied to the signals from both devices. The WD sensor signal had a peak amplitude and a signal energy of 4.3 and 5.7 times that of the PICO sensor respectively. The PICO sensor exhibits a rise time 90µs greater than the WD sensor and an event duration 128µs greater. The signal generated by the PICO sensor exhibits much greater frequency intensity during the first 32µs, particularly between 350kHz and 650kHz. Despite this greater initial intensity, the frequency spectra of the signals show the WD sensor to be sensitive to a greater frequency range than the PICO.

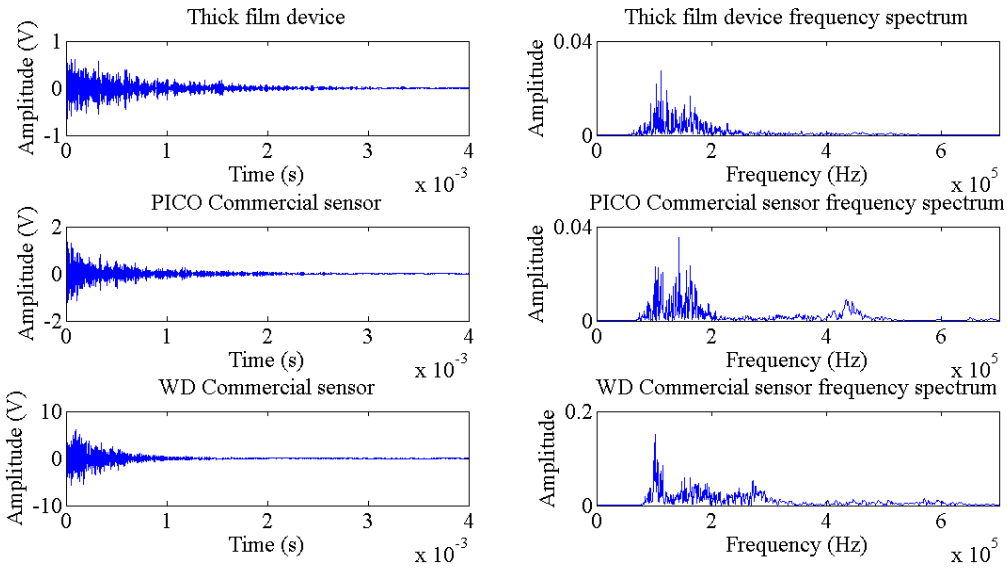

Figure 4. Time domain (left) and frequency domain (right) plots of the simulated AE signal received by thick film, PICO and WD sensors (top to bottom).

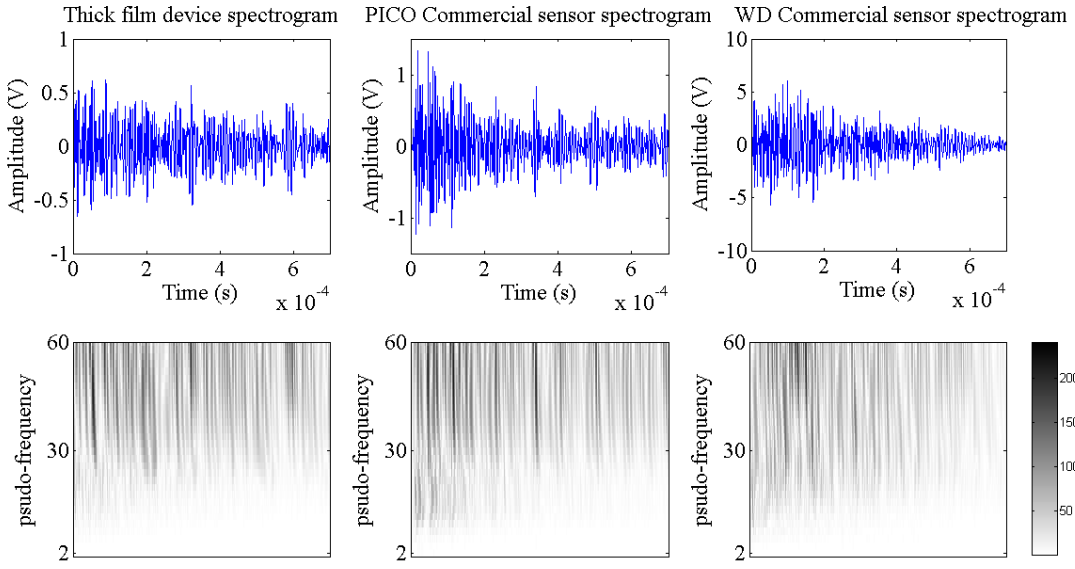

Figure 5. Time domain plot (top) and spectrogram (bottom) of the initial 700µs waveforms received by thick film, PICO and WD sensors (left to right).

5 CONCLUSIONS

The thick film device performed well when compared to the commercial sensors. The thick film device exhibited acoustic properties similar to those of the PICO commercial sensor. This was expected due to the similar design of the thick film and PICO sensors. An active element of greater area in the thick film device partially compensates for the lack active element thickness in the PICO sensor. The active element material in the commercial devices has not been exposed to the same stresses as the thick film PZT during the manufacture process. Stress during manufacture is known to result in the PZT exhibiting poorer piezoelectric properties as a thick film than as a bulk material

utilized in commercial devices [14]. These poorer piezoelectric properties can result in devices having a reduced response to excitation from an external source.

The waveform exhibited by the WD commercial sensor has a far greater response with less noise than the thick film device waveform. This can be explained by the similar area and much greater thickness of the active element within the WD sensor compared to that of the thick film device. The dual element design of the sensor eliminates much of the electrical noise and improves the signal resolution. The rise time of the WD sensor is greater than that of the PICO and thick film devices. Factors affecting the rise time are the electrical properties of the sensor and detection equipment meaning that commercial devices should exhibit better properties than the thick film device. The simulated AE signal is detected earlier by the thick film device. The reason for this that the thick film device is deposited directly onto the surface of the transmission media whereas the commercial sensors both have coupling media and wear plates. These obstacles extend the travel time of the acoustic wave to the active element and may cause distortion in the AE signal as well as signal attenuation [15].

This is the first known attempt at the deposition of an integrated, thick film, piezoelectric Acoustic Emissions sensor directly onto a structural element. The success of this work in producing a thick film device capable of detecting Acoustic Emissions could lead to significant uptake and deployment of thick film devices in the field of continuous non-destructive condition monitoring.

REFERENCES

[1] Mba, D. and Rao, R. B. K. N. (2006), "Development of Acoustic Emission Technology forCondition Monitoring and Diagnosis of RotatingMachines: Bearings, Pumps, Gearboxes, Engines,and Rotating Structures", *The Shock and Vibration Digest*, vol. 38, no. 1, pp. 3.

[2] Miller, R. K. and McIntire, P. (1987), *Non-destructive testing handbook; Volume 5: Acoustic emission testing*, Second edition ed, American society of non-destructive testing, United States.

[3] Gautschi, G. (2002), *Piezoelectric sensorics: force, strain, pressure, acceleration and acoustic emission sensors, materials and amplifiers*, Springer-Verlag, Berlin, Heidelburg, New York.

[4] Corker, D. L., Zhang, Q., Whatmore, R. W. and Perrin, C. (2002), "PZT 'composite' ferroelectric thick films", *Journal of the European Ceramic Society*, vol. 22, no. 3, pp. 383-390.

[5] Barbezat, M., Brunner, A. J., Flüeler, P., Huber, C. and Kornmann, X. (2004), "Acoustic emission sensor properties of active fibre composite elements compared with commercial acoustic emission sensors", *Sensors and Actuators A: Physical*, vol. 114, no. 1, pp. 13-20.

[6] Li, X. and Zhang, Y. (2008), "Analytical study of piezoelectric paint sensor for acoustic emission-based fracture monitoring", *Fatigue and Fracture of Engineering Materials and Structures*, vol. 31, pp. 684.

[7] Dorey, R. A. and Whatmore, R. W. (2004), "Electroceramic Thick Film Fabrication for Mems", *Journal of Electroceramics*, vol. 12, no. 1/2, pp. 19-32.

[8] Dauchy, F. (2007), *Stress Analysis, Dielectric, Piezoelectric, and Ferroelectric Properties of PZT Thick Films. Fabrication of a 50MHz Tm-pMUT Annular Array.* (unpublished PhD thesis), Cranfield University, Cranfield.

[9] Dorey, R. A., Stringfellow, S. B. and Whatmore, R. W. (2002), "Effect of sintering aid and repeated sol infiltrations on the dielectric and piezoelectric properties of a PZT composite thick film", *Journal of the European Ceramic Society*, vol. 22, no. 16, pp. 2921-2926.

[10] Kholkin, A. L., Yarmarkin, V. K., Wu, A., Avdeev, M., Vilarinho, P. M. and Baptista, J. L. (2001), "PZT-based piezoelectric composites via a modified sol–gel route", *Journal of the European Ceramic Society*, vol. 21, no. 10-11, pp. 1535-1538.

[11] Takahashi, S. (1980), "Sintering of $Pb(Zr,Ti)O_3$ Ceramics at Low Temperatures", *Japanese Journal of Applied Physics*, vol. 19, no. 4, pp. 771.

[12] De Cicco, G., Morten, B. and Prudenziati, M. (1994), "Piezoelectric thick-film sensors", in *Handbook of sensors and actuators (vol 1)*, Elsevier Science B.V., Amsterdam, pp. 209.

[13] American Society for Testing and Materials, *ASTM E 976, Standard Guide for Determining the Reproducibility of Acoustic Emission Sensor Response.*, West Conshohocken, USA.

[14] Glynne-Jones, P., Beeby, S. P., Dargie, P., Papakostas, T. and White, N. M. (2000), "An investigation into the effect of modified firing profiles on the piezoelectric properties of thick-film PZT layers on silicon", *Measurement Science & Technology*, vol. 11, no. 5, pp. 526-531.

[15] Park, J. M. and Kim, H. C. (1988), "The effects of attenuation and dispersion on the waveform analysis of acoustic emission", *Journal of Physics*, vol. 22, no. 5, pp. 617.

STRUCTURALLY INTEGRATED THICK FILM ACOUSTIC EMISSION SENSORS

A.J. Pickwell, R.A. Dorey, D. Mba

Cranfield University, College Road, Cranfield, Bedfordshire, MK43 0AL

Interest is growing in the field of structural health monitoring by Acoustic Emission (AE). AE monitoring of component health enables maintenance to be scheduled when it is needed thus preventing frequent and unnecessary servicing or unplanned downtime due to component failure. AE testing has many applications including monitoring civil engineering structures and validating component quality post-production. A novel thick film Acoustic Emission sensor is presented. AE sensors were fabricated by creating and pattering thick film lead zirconate titanate (PZT), a piezoelectric ceramic; using a powder/sol composite ink deposition technique in conjunction with mechanical patterning of the subsequent films. The resultant AE sensors exhibit a comparable response to commercially available AE sensors. Comparative thick film and commercial sensors results will be reviewed and discussed.

Keywords: Acoustic Emission, Sensor, PZT, Thick film.

1. INTRODUCTION

Non-destructive testing (NDT) has many applications; structural monitoring, process monitoring and biomedical research for example. A vital technique used in NDT is Acoustic Emission (AE) monitoring. Whilst traditionally used for static applications there is a focus on developing miniaturized sensors for use in both static and non-static NDT applications [1]. AE monitoring is also used in situations where size and weight are limiting factors, such as in the aerospace sector; or in situations where accessibility is an issue, such as in the nuclear sector. It is vital that, whilst devices are miniaturized, cost effectiveness is maintained. In all of these applications micro-electromechanical systems (MEMS) can provide a useful solution. MEMS AE devices which are up to 250 times thinner than existing commercially available devices can be manufactured. These devices can be manufactured for lower cost than bulk devices and integrated into structural elements.

There are already reported examples of MEMS AE devices in literature. These devices vary widely with sensors of thick film [2], thin film [3-5], active-fibre [6-8] and piezoelectric paint [9] design all being investigated. Many different materials are utilized in these devices including lead-based PZT as well as lead-free materials such as aluminium nitride [5], PVDF [10], BNT, KNN [11] and zinc oxide [3]. However, MEMS devices are reported to suffer from poor sensitivity due low piezoelectric properties and material volumes when compared to commercially available, bulk piezoelectric element devices. The benefits of PZT use in various MEMS device applications have been extensively reported in literature; in spite of the extensive research carried out in these fields thick film, PZT AE devices have remained unexplored. This work details the deposition of a thick film, PZT AE sensor directly onto a structural element. An artificial AE event is simulated in the element and the response compared to responses of commercially available sensors for benchmarking purposes.

2. BACKGROUND

2.1 Acoustic Emission Signals

AE waves come in two distinct types, transient and continuous. The most pertinent wave form for AE monitoring is transient. Typically the transient type emission, caused by material phase transformation, crack growth or the movement of dislocations within the material, is a short time period event. The event contains, within its waveform, important information that can provide much information about the signal source. These important characteristics include the event duration, maximum amplitude, rise time and count [12].

The measured area under the rectified signal is related to the magnitude and velocity of the emission source. The maximum amplitude is proportional to the surface area created during a cracking event and the velocity of crack propagation. Event duration can be used to differentiate an AE event from background noise signals and can also be used in conjunction with the rise time and the count information to identify the position and source of the AE.

2.2 Acoustic Emission Sensor Design

Almost all AE sensors are piezoelectric and are similar in design to acceleration sensors in that they make use of a piezoelectric sensing element [13]. Different types of piezoelectric sensors are available to carry out the task of detecting AE events. Piezoelectric sensors started to appear shortly after the First World War. Förster and Scheil are recognised as the first to use the piezoelectric effect to detect AE signals in 1936 [13]. Originally sensors were piezoelectric crystals. Quartz (SiO_2) was the most common single crystal material as it has good piezoelectric properties and a high mechanical strength. Several

other crystals showed sufficient qualities to be used in commercial AE sensors including tourmaline, gallium orthophosphate and crystals of the CGG group [13]. Several ceramic material groups were also investigated but none surpassed single crystals for AE applications. Lead zirconate titanate was subsequently invented and was found to show properties that were promising for sensing applications.

Other sensor types include capacitive transducers and active filament sensors. In capacitive transducers the AE wave moves internal conductive elements producing a capacitance change directly related to the amplitude of the input AE. It is known that capacitive transducers can record a good approximation of surface movement however the sensitivity of these sensors is insufficient for actual Acoustic Emission testing according to Miller and McIntire [12]. Active filament sensors are made with uniaxially orientated piezoelectric fibres embedded in a polymer matrix between two interwoven electrodes [14] this structure is also known as an active fibre composite elements or AFC. Barbezat et al. [6] identified that AFC are superior to traditional AE sensors in that they are lighter, more flexible and could be combined with existing polymer products. AFC sensors exhibit anisotropic sensitivity caused by the orientation of the fibres within the material. This combined with the fact that AFC sensors have a lower sensitivity to AE events than traditional piezoelectric sensors does limit the applications that they are suitable for. Work is also being carried out on adapting piezoelectric paint for use as an in-situ Acoustic Emission sensor [9].

A typical piezoelectric element AE sensor design is shown in figure 1. The sensor case acts as the conductive element for the earth and helps to shield the signal from external noise sources. The backing reduces noise caused by reflection of the signal from the back face of the piezoelectric element which would otherwise give a false reading.

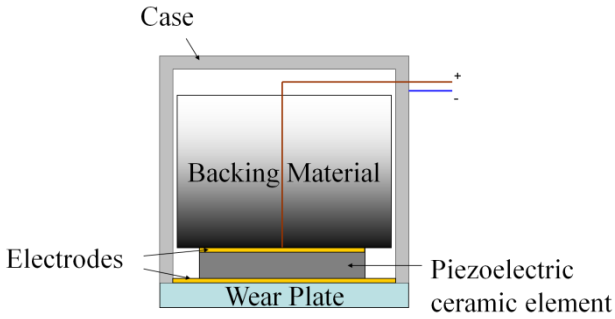

Figure 1. Schematic of traditional single element AE sensor design.

2.3 Material Selection

There are several thick film piezoelectric materials. The material with the best properties for Acoustic Emission devices is lead zirconate titanate (PZT). PZT can be used as a bulk material, as in existing AE devices, or deposited as a thick or thin film. Thick films have the advantage of being more durable than thin films. There are various methods for depositing thick films onto a substrate material including screen printing, sputtering, direct writing, electrophoretic deposition, micro-stereolithography and composite sol-gel techniques [15]. Composite sol-gel is the intended production method for PZT deposition in this work and so will be presented here.

Composite sol-gel techniques have been researched extensively and provide a promising avenue for advancing thick film technology. In this method firstly a sol is produced. The sol is then mixed with powder to produce a composite slurry. The slurry is spun onto a flat substrate to ensure an even film thickness. Each layer is then heated to remove the solvent. Several layers can then be deposited onto the previous ones. In this way a thick film can be built up [16]. It is possible to increase the density of the porous film by repeated sol infiltrations. These infiltrations fill the pores in the material before being dried. Several infiltrations can be carried out on each layer deposited. These infiltrations can be used to lower the sintering temperature and have previously been investigated [17][18]. Once the required film thickness has been achieved the material is sintered to increase the density and piezoelectric properties [19]. This process produces a film with a consistent thickness and good piezoelectric qualities.

3. DEVICE MANUFACTURE

PZT sol and composite slurry were produced with a Zr/Ti ratio of 52/48 [17][20]. A Kovar substrate with dimensions 100x100x3.2mm was cleaned in an acetone/IPA ultrasonic bath. A spin coating technique was used to deposit a 4(2C+5S) composite PZT film of 17.6µm thickness onto the substrate. 2000rpm spin speed was used. The film was dried at 310°C for 180 seconds and pyrolised at 525°C for 60 seconds after each deposition. Upon completion of the composite film deposition process sintering was carried out at 720°C for 20min. To reduce thermal stress between Kovar and PZT a ramp rate of 5°C/min was employed. A mask was applied to the PZT film and then patterning was carried out by powder blasting. Discrete piezoelectric elements were produced by the application of a mask prior to the sputtering of an 8mm diameter Cr/Au top electrode, of 11.2nm/150nm onto the PZT film surface. The PZT was poled by a corona poling process. The film was initially

heated to 135°C before poling was carried out for 15mins at 16kVwith a needle to sample gap of 30mm. To prevent depoling the PZT was left to cool under the electric field. The top electrode and the Kovar substrate was electrically connected using a BNC connecter. The poled thick film device was found to have a capacitance of 2.18nF and a dielectric loss of 0.102, measured at 100kHz. The finished device is shown in figure 2 alongside a Physical Acoustics Corporation (PAC) PICO commercial sensor.

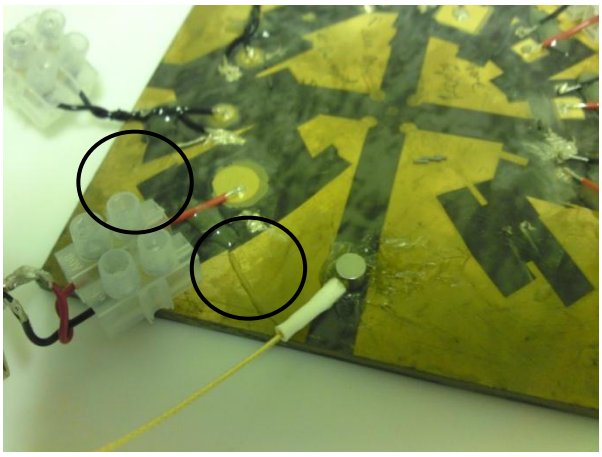

Figure 2. A thick film PZT Acoustic Emissions device (left) alongside a commercially available PICO sensor (right).

4. RESULTS AND DISCUSSION

The thick film device deposited directly onto the Kovar substrate is a single element design. This provides high sensitivity to AE signals independent of the sensor orientation relative to the incoming acoustic wave. A PICO sensor from PAC was chosen for comparative testing as it is of a similar design to the thick film device. The PICO sensor has an operating frequency of 200-750kHz. A commercially available PICO sensor was mounted at 32mm from the center of the Kovar substrate with grease used as a coupling agent. Signals produced by the PICO and the thick film PZT devices were monitored using MI-TRA a commercial transient recorder-analyzer system from PAC 2001. Variable gain 2/4/6 pre-amplifiers from PAC were used. Pre-amplifications of 40dB and 60dB were used for the PICO and thick film sensor signals respectively. A 10MHz sampling rate was used to give a good resolution in signal analysis.

AE events were simulated using the Hsu Nelson test carried out at the centre of the Kovar substrate. The Hsu Nelson test consists of breaking a 0.5mm diameter HB pencil lead [21].There is a variation in waveform arrival times between the PICO and the thick film sensor suggesting that the simulated acoustic source was not exactly central between the two sensors, this effect is apparent in all tests performed using the Hsu Nelson test. It is clear from figure 3 that, qualitatively, the waveforms exhibit similar properties. The PICO sensor signal exhibits a concentration of higher frequency wave components within the initial 100µs of the waveform compared to the thick film device as shown by the spectrogram in figure 4. The maximum amplitude of the PICO sensor is1.9 times that of the thick film device with the rise time of the thick film sensor being 25µs greater and the signal duration 0.5ms greater than that of the PICO sensor. The signal energy of the thick film waveform is 1.2 times greater than that of the PICO sensor. The properties of the PICO and thick film waveform frequency spectrum, shown in figure 3, are comparable, both exhibiting a frequency response to the simulated emission between 50kHz and 250kHz. The thick film device lacks the sensitivity peak at 400-500kHz which is characteristic of the frequency response of the PICO device.

The greater amplitudes of the raw signal and frequency response can be explained as being a result of the relative thickness of the active piezoelectric element in the PICO sensor compared to that of the thick film device and the differences in electrical matching between the sensors and the commercial monitoring system. A flatter frequency response is desired in Acoustic Emissions applications and therefore the thick film frequency response lacking the sensitivity peak between 400kHz and 500kHz is of benefit. The increased signal duration of the thick film sensor is explained by a lack of acoustically matched backing to attenuate signal reflections from the top surface of the device.

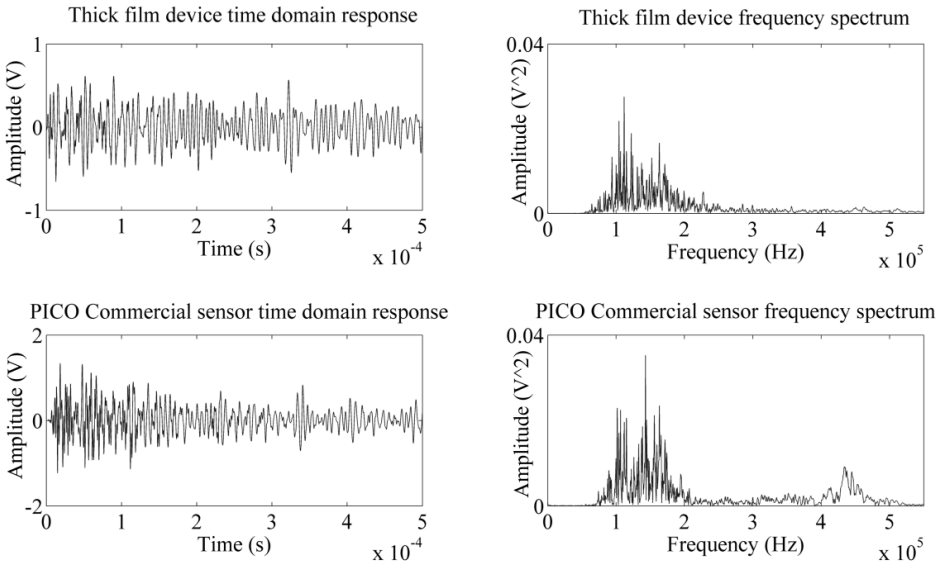

Figure 3. Time domain (left) and frequency domain (right) plots of the simulated AE signal received by thick film and PICO sensors (top and bottom respectively).

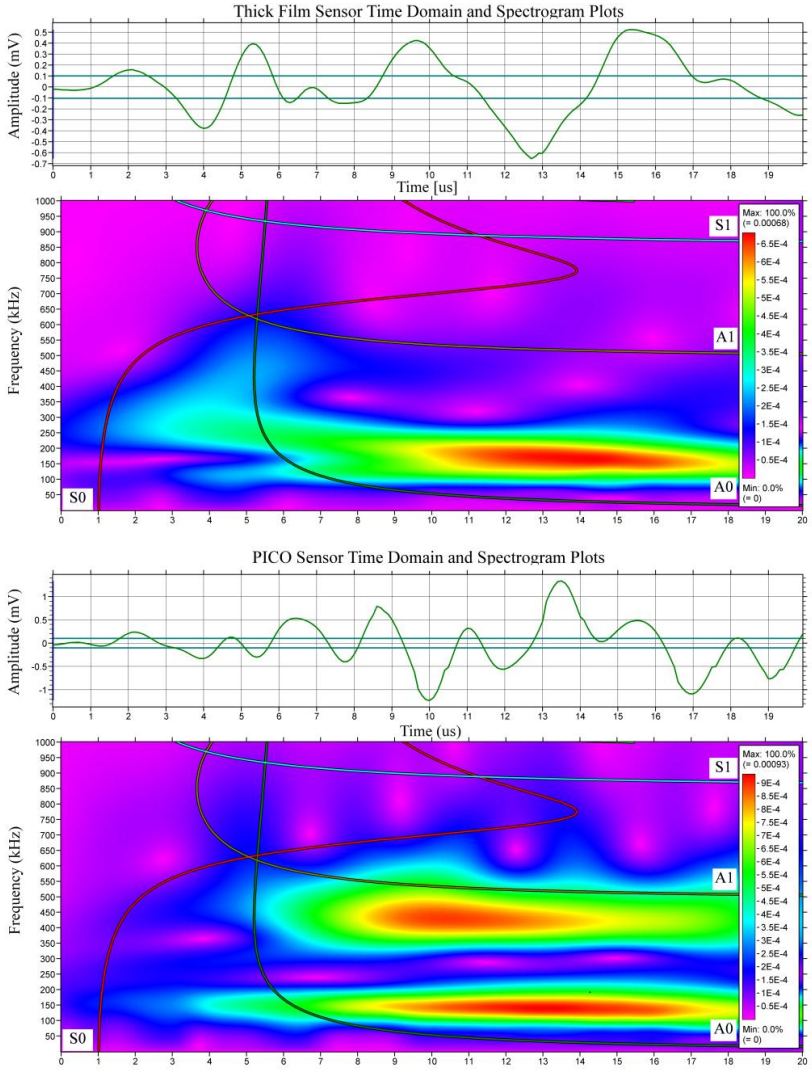

Figure 4. Time domain plot (top) and spectrogram (bottom) of the initial 700µs waveforms received by thick film and PICO sensors (top and bottom respectively).

5. CONCLUSIONS

The thick film device performed well when compared to the commercial sensors. The thick film device exhibited acoustic properties similar to those of the PICO commercial sensor. This was expected due to the similar design of the thick film and PICO sensors. An active element of greater area in the thick film device partially compensates for the lack active element thickness in the PICO sensor. The active element material in the commercial devices has not been exposed to the same stresses as the thick film PZT during the manufacture process. Stress during manufacture is known to result in the PZT exhibiting poorer piezoelectric properties as a thick film than as a bulk material utilized in commercial devices [22]. These poorer piezoelectric properties can result in devices having a reduced response to excitation from an external source.

The rise time of the thick film sensor is greater than that of the PICO sensor. Factors affecting the rise time are the electrical properties of the sensor and detection equipment meaning that commercial devices should exhibit better properties than the thick film device. The simulated AE signal is detected earlier by the thick film device. The reason for this that the thick film device is deposited directly onto the surface of the transmission media whereas the commercial sensors both have coupling media and wear plates. These obstacles extend the travel time of the acoustic wave to the active element and may cause distortion in the AE signal as well as signal attenuation [23].

This is the first known attempt at the deposition of an integrated, thick film, PZT Acoustic Emissions sensor directly onto a structural element. The success of this work in producing a thick film device capable of detecting Acoustic Emissions could lead to significant uptake and deployment of thick film devices in the field of continuous non-destructive condition monitoring.

REFERENCES

[1] Mba, D. and Rao, R. B. K. N. (2006), "Development of Acoustic Emission Technology forCondition Monitoring and Diagnosis of RotatingMachines: Bearings, Pumps, Gearboxes, Engines,and Rotating Structures", *The Shock and Vibration Digest*, vol. 38, no. 1, pp. 3.

[2] Belavic, D., Hrovat, M., Zarnik, M. S., Holc, J. and Kosec, M. (2009), "An investigation of thick PZT films for sensor applications: A case study with different electrode materials", *Journal of Electroceramics*, vol. 23, pp. 1.

[3] Imai, S., Tokuyama, M., Hirose, S., Burger, G. J., Lammerink, T. S. J. and Fluitman, J. H. J. (1995), "A thin-film piezoelectric impact sensor array fabricated on a Si slider for measuring head-disk interaction", *IEEE Transactions on Magnetics*, vol. 31, no. 6, pp. 3009-3011.

[4] Cho, C. R., Francis, L. F. and Jang, M. S. (1999), "Piezoelectric Properties of Acoustic Wave Detection of $Pb(Zr_{0.52}Ti_{0.48})O_3$ Thin Films for Microelectromechanical Systems Sensor", *Japanese Journal of Applied Physics*, vol. 38, pp. L751.

[5] Kirk, K. J., Elgoyhen, J., Hood, J. P., Hutson, D., Dwyer-Joyce, R. S., Zhang, J. and Drinkwater, B. W. (2010), "Ultrasonic condition monitoring using thin-film piezoelectric sensors", *Insight*, vol. 52, no. 4, pp. 184.

[6] Barbezat, M., Brunner, A. J., Flüeler, P., Huber, C. and Kornmann, X. (2004), "Acoustic emission sensor properties of active fibre composite elements compared with commercial acoustic emission sensors", *Sensors and Actuators A: Physical*, vol. 114, no. 1, pp. 13-20.

[7] Feng, G. H. and Tsai, M. Y. (2010), "Acoustic emission sensor with structure-enhanced sensing mechanism based on micro-embossed piezoelectric polymer", *Sensors and Actuators A*, vol. 162, pp. 100.

[8] Lam, T. Y., Lam, K. H. and Chan, H. L. W. (2005), "Micromachined piezoelectric polymer membrane acoustic sensor", *Integrated Ferroelectrics*, vol. 76, no. 1, pp. 31.

[9] Li, X. and Zhang, Y. (2008), "Analytical study of piezoelectric paint sensor for acoustic emission-based fracture monitoring", *Fatigue and Fracture of Engineering Materials and Structures*, vol. 31, pp. 684.

[10] De Rosa, I. M. and Sarasini, F. (2010), "Use of PVDF as acoustic emissions sensor for in situ monitoring of mechanical behaviour of glass/epoxy laminates", *Polymer Testing*, vol. 29, pp. 749.

[11] Lam, K. H., Lin, D. M. and Chan, H. L. W. (2007), "Lead-free acoustic emission sensors", *Review of Scientific Instruments*, vol. 78, pp. 115109.

[12] Miller, R. K. and McIntire, P. (1987), *Non-destructive testing handbook; Volume 5: Acoustic emission testing*, Second edition ed, American society of non-destructive testing, United States.

[13] Gautschi, G. (2002), *Piezoelectric sensorics: force, strain, pressure, acceleration and acoustic emission sensors, materials and amplifiers*, Springer-Verlag, Berlin, Heidelburg, New York.

[14] Corker, D. L., Zhang, Q., Whatmore, R. W. and Perrin, C. (2002), "PZT 'composite' ferroelectric thick films", *Journal of the European Ceramic Society*, vol. 22, no. 3, pp. 383-390.

[15] Dorey, R. A. and Whatmore, R. W. (2004), "Electroceramic Thick Film Fabrication for Mems", *Journal of Electroceramics*, vol. 12, no. 1/2, pp. 19-32.

[16] Dauchy, F. (2007), *Stress Analysis, Dielectric, Piezoelectric, and Ferroelectric Properties of PZT Thick Films. Fabrication of a 50MHz Tm-pMUT Annular Array.* (unpublished PhD thesis), Cranfield University, Cranfield.

[17] Dorey, R. A., Stringfellow, S. B. and Whatmore, R. W. (2002), "Effect of sintering aid and repeated sol infiltrations on the dielectric and piezoelectric properties of a PZT composite thick film", *Journal of the European Ceramic Society*, vol. 22, no. 16, pp. 2921-2926.

[18] Kholkin, A. L., Yarmarkin, V. K., Wu, A., Avdeev, M., Vilarinho, P. M. and Baptista, J. L. (2001), "PZT-based piezoelectric composites via a modified sol–gel route", *Journal of the European Ceramic Society,* vol. 21, no. 10-11, pp. 1535-1538.
[19] Takahashi, S. (1980), "Sintering of $Pb(Zr,Ti)O_3$ Ceramics at Low Temperatures", *Japanese Journal of Applied Physics,* vol. 19, no. 4, pp. 771.
[20] De Cicco, G., Morten, B. and Prudenziati, M. (1994), "Piezoelectric thick-film sensors", in *Handbook of sensors and actuators (vol 1),* Elsevier Science B.V., Amsterdam, pp. 209.
[21] American Society for Testing and Materials, *ASTM E 976, Standard Guide for Determining the Reproducibility of Acoustic Emission Sensor Response.*, West Conshohocken, USA.
[22] Glynne-Jones, P., Beeby, S. P., Dargie, P., Papakostas, T. and White, N. M. (2000), "An investigation into the effect of modified firing profiles on the piezoelectric properties of thick-film PZT layers on silicon", *Measurement Science & Technology,* vol. 11, no. 5, pp. 526-531.
[23] Park, J. M. and Kim, H. C. (1988), "The effects of attenuation and dispersion on the waveform analysis of acoustic emission", *Journal of Physics,* vol. 22, no. 5, pp. 617.

Integrated Thick Film Acoustic Emission Sensor For Structural Health Monitoring

A.J. Pickwell, R.A. Dorey, D. Mba.

Cranfield UNIVERSITY

Fabrication

- 17.6µm thick 4(2C+5S) PZT[2] film deposited onto a Kovar substrate by spin coating[3]
- Film sintered at 720°C
- Film masked and patterned by powder blasting
- Cr/Au electrode deposited on film surface by evaporation
- Corona poling: 140°C, 16kV at 30mm for 15 minutes.

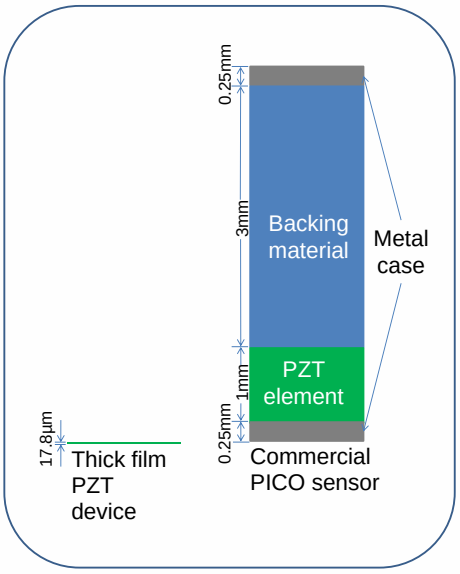

Testing

Simulated Acoustic Emission (AE) event using Hsu-Nelson[1] test

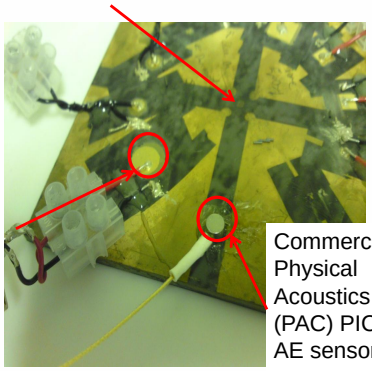

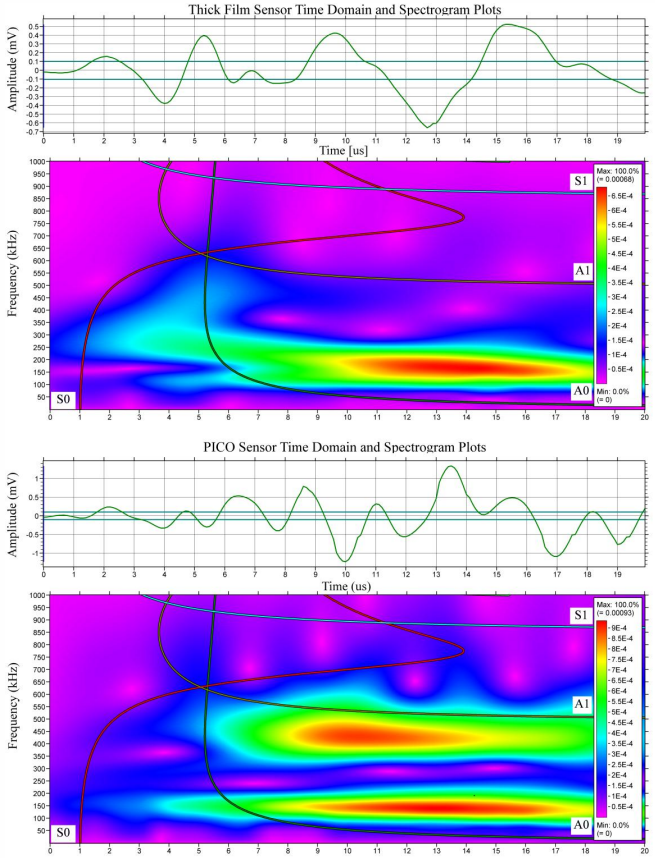

Time domain plot and Gabor transform spectrogram of the initial 200µs waveform received, with waveform dispersion curves of zero and first order symmetric and asymmetric lamb waves overlaid.

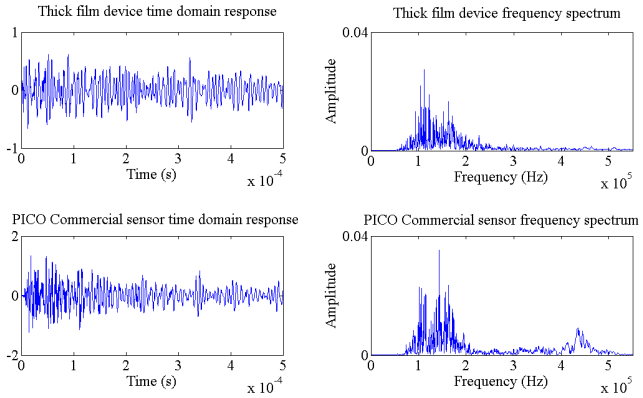

Time domain plot showing the initial 500µs of waveforms received by the thick film and PICO sensors (top and bottom respectively) and the corresponding frequency domain plots following a Hsu-Nelson simulated AE event.

Conclusions

- Qualitatively comparable to the PICO commercial sensor
- Lacks the characteristic 500kHz sensitivity of the PICO
- Lacks sensitivity at frequencies greater than 700kHz
- Less susceptible to high frequency noise
- Good performance at the lower frequencies commonly used for AE monitoring

These results show that the thick film sensor is of suitable bandwidth for use in industrial applications.

1. American Society for Testing and Materials, *ASTM E 976, Standard Guide for Determining the Reproducibility of Acoustic Emission Sensor Response., West Conshohocken, USA.*
2. Dorey, R. A., Stringfellow, S. B. and Whatmore, R. W. (2002), *Journal of the European Ceramic Society, vol. 22, no. 16, pp. 2921-2926.*
3. Dorey, R. A., Dauchy, F., Wang, D. and Berriet, R. (2007), *IEEE Transactions on Ultrasounics, Ferroelectrics, and Frequency Control, vol. 54, no. 12, pp. 2462.*

Contact; a.j.pickwell@cranfield.ac.uk, Tel: +44 (0)1234 750111 ext. 2723, Bld 70, Cranfield University, Cranfield, MK43 0AL, UK.

References

[1] D. Aljets, A. Chong, and S. Wilcox, "Acoustic Emission source location in plate-like structures using a closely arranged triangular sensor array," in *Proceedings of the 29th European Conference on Acoustic Emission Testing*, vol. 2010-10, EWGAE, 8/9/2010 - 10/9/2010 2010. xii, 7, 195

[2] M. Eaton, R. Pullin, K. Holford, S. Evans, C. Featherston, and A. Rose, "Use of macro fibre composite transducers as Acoustic Emission sensors," *Remote Sensing*, vol. 1, p. 68, 2009. xii, 10, 11, 12, 14, 15, 16

[3] Fujitsu, "FRAM - ferroelectric RAM technology." http://www.fujitsu.com/emea/services/microelectronics/fram/technology.html, 20/11 2008. xii, 48

[4] E. Cross, "Materials science: Lead free at last," *Nature*, vol. 432, no. 7013, p. 24, 2004. xiii, 53

[5] A. I. Zaitsez, N. E. Shelkova, and B. M. Mogutnov, "Thermodynamics of Na_2O-SiO_2 melts," *Inorganic Materials*, vol. 36, no. 6, p. 647, 2000. xv, 130, 131

[6] R. Subasri and H. Nafe, "Phase evolution on heat treatment of sodium silicate water glass," *Journal of Non-Crystalline Solids*, vol. 354, p. 896, 2008. xv, 130, 134, 136, 138, 139

[7] C. Scheffer and P. Girdhar, *Machinery Vibration Analysis and Predictive Maintenance*. Oxford, UK.: Elsevier, 1st ed., 2004. 1

[8] C. U. Grosse and M. Ohtsu, *Acoustic Emission Testing*. Berlin: Springer, 2008. 1, 2, 19

[9] F. Ullmann, *Ullmann's Chemical Engineering and Plant Design*, vol. 1-2. Germany: John Wiley and Sons, 2005. 1

[10] A. A. Baker, S. Dutton, and D. Kelly, *Composite Materials for Aircraft Structures*. Reston, VA, US.: American Institute of Aeronautics and Astronautics, 2nd ed., 2004. 1

[11] G. Petrangeli, *Nuclear Safety*. Oxford, UK: Elsevier, first ed., 2006. 1

[12] V. Baranov, E. Kudryavtsev, G. Sarychev, and V. Schavelin, *Acoustic Emission in Friction*. Oxford, UK: Elsevier, 1st ed., 2007. 1

[13] R. K. Miller and P. McIntire, *Non-Destructive Testing Handbook; Volume 5: Acoustic Emission Testing*, vol. 5. United States: American society of non-destructive testing, second edition ed., 1987. 1, 8, 38, 39, 40

[14] S. J. Vahaviolos, *Acoustic Emission*. Baltimore, USA.: American Society for Testing and Materials, 1972. 1, 41

[15] F. Kishinouye, "An experiment on the progression of fracture," *Journal of Acoustic Emission*, vol. 9, no. 3, p. 177, 1990. 1

[16] T. F. Drouillard, "Acoustic Emissions - the first half century," 21 Oct. 1994 1994. 1, 2

[17] C. Hellier, *Handbook of Non-Destructive Evaluation*. New York, USA.: McGraw Hill, 2001. 2

[18] T. Kishi, M. Ohtsu, and S. Yuyama, *Acoustic Emission - Beyond the Millennium*. Oxford, UK.: Elsevier Science, 1st. ed., 2000. 2, 42, 43, 45, 46

[19] Z. Su and L. Ye, *Identification of Damage Using Lamb Waves - From Fundamentals to Applications*. 2009. 3, 11, 13, 15, 16, 20, 22, 23, 35, 38, 42, 43, 44, 45, 50

[20] X. Li and Y. Zhang, "Analytical study of piezoelectric paint sensor for Acoustic Emission-based fracture monitoring," *Fatigue and Fracture of Engineering Materials and Structures*, vol. 31, p. 684, 2008. 6, 15, 16, 18, 20, 23, 27

[21] G. Qi, "Wavelet-based AE characterization of composite materials," *NDT and E International*, vol. 33, no. 3, pp. 133–144, 2000. Cited By (since 1996): 46. 8, 39, 44, 45

[22] WavesinSolids LLC, "Transformer inspection using Acoustic Emission." http://www.wins-ndt.com/-Transformer, 20/11 2007. 8

[23] W. Liu and J. W. Hong, "Three-dimensional Lamb wave propagation excited by a phased piezoelectric array," *Smart Materials and Structures*, vol. 19, no. 085002, p. 12, 2010. 11

[24] J. X. Liu, D. N. Fang, W. Y. Wei, and X. F. Zhao, "Love waves in layered piezoelectric/piezomagnetic structures," *Journal of Sound and Vibration*, vol. 315, pp. 146–156, 8/5 2008. 11

[25] K. Luangvilai, L. J. Jacobs, and J. Qu, "Modal decomposition of double-mode Lamb waves: Numerical verification and discussion on extension to general multi-mode leaky Lamb waves," *Health Monitoring and Smart Nondestructive Evaluation of Structural and Biological Systems IV*, vol. 5768, p. 304, 2005. 11

[26] R. Kumar and T. Kansal, "Propagation of Lamb waves in transversely isotropic thermoelastic diffusive plate," *International Journal of Solids and Structures*, vol. 45, pp. 5890–5913, 11 2008. 11

[27] G. S. Radchenko, "Plated-designed structures: new possibility of obtaining resonance enhancement of piezoelectric properties using Lamb waves," *Journal of Physics D: Applied Physics*, vol. 41, no. 15, p. 155421, 2008. 11

[28] H. Jeong and Y. S. Jang, "Wavelet analysis of plate wave propagation in composite laminates," *Composite Structures*, vol. 49, p. 443, 2000. 11, 13, 45

[29] F. Li, Y. Wu, J. F. Manceau, and F. Bastien, "Temperature compensation of Lamb wave sensor by combined antisymmetric mode and symmetric mode," *Applied Physics Letters*, vol. 92, p. 074101, 2008. 13

[30] B. P. Zhu, Q. F. Zhou, J. Shi, K. K. Shung, S. Irisawa, and S. Takeuchi, "Self-separated hydrothermal lead zirconate titanate thick films for high frequency transducer applications," *Applied Physics Letters*, vol. 94, p. 102901, 2009. 13

[31] C. S. Park, S. M. Lee, and H. E. Kim, "Effects of excess PbO and Zr/Ti ratio on microstructure and electrical properties of PZT films," *Journal of the American Ceramic Society*, vol. 91, no. 9, p. 2923, 2008. 14, 15, 52

[32] J. M. Park and H. C. Kim, "The effects of attenuation and dispersion on the waveform analysis of Acoustic Emission," *Journal of Physics*, vol. 22, no. 5, p. 617, 1988. 17

[33] T. Yan, P. Theobald, and B. E. Jones, "A self-calibrating piezoelectric transducer with integral sensor for in situ energy calibration of Acoustic Emission," *NDT and E International*, vol. 35, pp. 459–464, 10 2002. 17, 34, 35, 40

[34] M. Barbezat, A. J. Brunner, P. Fleler, C. Huber, and X. Kornmann, "Acoustic Emission sensor properties of active fibre composite elements compared with commercial Acoustic Emission sensors," *Sensors and Actuators A: Physical,*, vol. 114, pp. 13–20, 8/20 2004. 18, 32

[35] D. Mba and R. B. K. N. Rao, "Development of Acoustic Emission technology for condition monitoring and diagnosis of rotating machines: Bearings, pumps, gearboxes, engines,and rotating structures," *The Shock and Vibration Digest*, vol. 38, p. 3, January 2006 2006. 19, 161

[36] M. Lukacs, M. Sayer, D. Knapik, R. Candela, and F. S. Foster, "Novel PZT films for ultrasound biomicroscopy," in *Ultrasonics Symposium, 1996. Proceedings., 1996 IEEE*, vol. 2, pp. 901–904 vol.2, 1996. ID: 1. 19

[37] G. Manthei, "Characterization of broadband Acoustic Emission sensors," vol. 2010-10, EWGAE, 2010. 19

[38] Y. Iwasa, *Case studies in superconducting magnets: design and operational issues*. Plenum Press, illustrated ed., 1994. 20

[39] European Physical Acoustics Corporation, "Acoustic Emission products." http://www.epandt.com/us/capteur_ea_us.html, 26/01 2004. 21

[40] P. Theobald and R. Pocklington, "Velocity sensitivity calibration of AE sensors using the through wave method and laser interferometry," 8/10/2010 2010. 22, 34, 35

[41] J. Rodel, W. Jo, K. T. P. Seifert, E. M. Anton, and T. Granzow, "Perspective on the development of lead-free piezoceramics," *Journal of the American Ceramic Society*, vol. 92, no. 6, p. 1153, 2009. 23, 54, 55

[42] K. H. Lam, D. M. Lin, and H. L. W. Chan, "Lead-free Acoustic Emission sensors," *Review of Scientific Instruments*, vol. 78, p. 115109, 2007. 24, 55

[43] C. R. Cho, L. F. Francis, and M. S. Jang, "Piezoelectric properties and acoustic wave detection of $Pb(Zr_{0.52}Ti_{0.48})O_3$ thin films for microelectromechanical systems sensor," *Japanese Journal of Applied Physics*, vol. 38, p. L751, 1999. 24, 25

[44] F. Tyholdt, R. A. Dorey, and H. Raeder, "Novel patterning of composite thick film PZT," *Journal of Electroceramics*, vol. 19, p. 315, 2007. 25, 58, 61, 63, 68

[45] G. H. Feng and M. Y. Tsai, "Acoustic Emission sensor with structure-enhanced sensing mechanism based on micro-embossed piezoelectric polymer," *Sensors and Actuators A*, vol. 162, p. 100, 2010. 25, 26

[46] I. M. D. Rosa and F. Sarasini, "Use of PVDF as Acoustic Emissions sensor for in situ monitoring of mechanical behaviour of glass/epoxy laminates," *Polymer Testing*, vol. 29, p. 749, 2010. 26, 50

[47] T. Y. Lam, K. H. Lam, and H. L. W. Chan, "Micromachined piezoelectric polymer membrane acoustic sensor," *Integrated Ferroelectrics*, vol. 76, no. 1, p. 31, 2005. 26, 70

[48] J. R. White, B. D. Poumeyrol, J. M. Hale, and R. Stephenson, "Piezoelectric paint: Ceramic-polymer composites for vibration sensors," *Journal of Materials Science*, vol. 39, no. 9, pp. 3105–3114, 2004. Cited By (since 1996): 13. 27, 28

[49] A. H. Shivola, "Effective permittivity of dielectric mixtures," *IEEE Transactions on Geoscience and Remote Sensing*, vol. 26, no. 4, p. 420, 1988. 28

[50] L. Jylha and A. Sihvola, "Equation for the effective permittivity of particle-filled composites for material design applications," *Journal of Physics D: Applied Physics*, vol. 40, p. 4966, 2007. 28, 29, 30

[51] G. Kofod, S. Risse, H. Stoyanov, D. N. McCarthy, S. Sokolov, and R. Kraehnert, "Broad-spectrum enhancement of polymer composite dielectric constant at ultralow volume fractions of silica-supported copper nanoparticles," *American Chemical Society Nano*, vol. 5, no. 3, p. 1623, 2011. 28

[52] G. Gallone, F. Carpi, D. D. Rossi, G. Levita, and A. Marchetti, "Dielectric constant enhancement in a silicone elastomer filled with lead magnesium niobate-lead titanate," *Materials Science and Engineering*, vol. 27, no. C, p. 110, 2007. 30

[53] J. P. Calame, "Dielectric permittivity simulation of random irregularly shaped particle composites and approximation using modified dielectric mixing laws," *Journal of Applied Physics*, vol. 104, p. 114108, 2008. 31

[54] D. W. Greve, I. J. Oppenheim, A. P. Wright, and W. Wu, "Design and testing of a MEMS Acoustic Emission sensor system," in *Sensors and Smart Structures Technologies for Civil, Mechanical, and Aerospace Systems 2008*, 10th March 2008 2008. 33

[55] B. E. Jones and T. Yan, "Acoustic Emission traceable sensing," *Journal of Strain Analysis - Special Edition*, vol. 40, no. 1, p. 17, 2005. 34, 35

[56] American Society for Testing and Materials, "ASTM E 976, standard guide for determining the reproducibility of Acoustic Emission sensor response.." 34, 94

[57] J. J. Scholey, P. D. Wilcox, M. R. Wisnom, and M. I. Friswell, "A practical technique for quantifying the performance of Acoustic Emission systems on plate-like structures.," *Ultrasonics*, vol. 49, p. 538, 2009. 34

[58] K. Ono, "Current understanding of mechanisms of Acoustic Emission," *Journal of Strain Analysis*, vol. 40, no. 1, 2004. 35

[59] European Physical Acoustics Corporation, "Acoustic Emission amplifiers." http://www.pacndt.com/index.aspx?go=products&focus=Amplifiers.htm, 11/02 2010. 36

[60] M. M. Shea, "Amplitude distribution of Acoustic Emission produced during martensitic transformation," *Materials Science and Engineering*, vol. 64, pp. L1–L6, 5 1984. 40

[61] Y. Berlinsky, M. Rosen, J. A. Simmons, and H. N. G. Wadley, "Acoustic Emission: An NDE technique for characterizing the martensitic transformation.," in *Review of Progress in Quantitative Nondestructive Evaluation*, vol. 5 B, pp. 1345–1354, 1986. Cited By (since 1996): 6. 40

[62] R. K. Miller, E. v. K. Hill, and P. O. Moore, *Acoustic Emission testing*, vol. 6. American Society for Nondestructive Testing, 3 ed., 2005. 41

[63] Q. Q. Ni and M. Iwamoto, "Wavelet transform of Acoustic Emission signals in failure of model composites," *Engineering Fracture Mechanics*, vol. 69, pp. 717–728, 4 2002. 42, 44

[64] E. P. Serrano and M. A. Fabio, "Application of the wavelet transform to Acoustic Emission signals processing," *IEEE Transactions on Signal Processing*, vol. 44, p. 1270, 5/96 1996. 43

[65] I. Daubechies, "Orthonormal bases of compactly supported wavelets," *Communication on Pure and Applied Mathematics*, vol. 41, no. 7, p. 909, 1988. 44

[66] L. Debnath, *Wavelet transforms and their applications*. Boston, USA: Birkhauser, 2002. 46

[67] W. Heywang, K. Lubitz, and W. Wersing, *Piezoelectricity: Evolution and Future of a Technology*. Berlin: Springer, 2008. 46

[68] B. Ando, P. Giannone, S. Graziani, and N. Pitrone, "Characterization of the dielectric and pyroelectric properties of ferroelectric material," *Instrumentation and Measurement, IEEE Transactions on*, vol. 57, no. 9, pp. 1939–1948, 2008. ID: 1. 47

[69] J. Valasek, "Piezoelectric and allied phenomena in rochelle salt," *Physical Review*, vol. 15, p. 537, 1920. 47

[70] G. H. Haertling, "Ferroelectric ceramics: History and technology," *Journal of the American Ceramic Society*, vol. 82, no. 4, p. 797, 1999. 47, 48, 51, 54, 59

[71] W. D. Callister, *Materials science and engineering: an introduction*. New York: John Wiley and Sons, Inc, seventh edition ed., 2007. 47

[72] M. E. Lines and A. M. Glass, *Principles and Applications of Ferroelectrics and Related Materials*. Oxford: Oxford University Press, 2004. 47

[73] A. J. Moulson and J. M. Herbert, *Electroceramics: Materials, Properties, Applications*. New York: John Wiley and Sons, Ltd, second edition ed., 2003. 47, 52, 56

[74] S. Tsurekawa, K. Ibaraki, K. Kawahara, and T. Watanabe, "The continuity of ferroelectric domains at grain boundaries in lead zirconate titanate," *Scripta Materialia*, vol. 56, pp. 577–580, 4 2007. 47, 52

[75] G. Gautschi, *Piezoelectric sensorics: Force, Strain, Pressure, Acceleration and Acoustic Emission sensors, Materials and Amplifiers*. Berlin, Heidelburg, New York: Springer-Verlag, 2002. 48, 49, 52, 190

[76] N. Setter, D. Damjanovic, L. Eng, G. Fox, S. Gevorgian, S. Hong, A. Kingon, H. Kohlstedt, N. Y. Park, G. B. Stephenson, I. Stolitchnov, A. K. Taganstev, D. V. Taylor, T. Yamada, and S. Streiffer, "Ferroelec-

tric thin films review of materials, properties, and applications," *Journal of Applied Physics*, vol. 100, p. 051606, 2006. 49, 50, 55, 196

[77] M. A. Dubois and P. Muralt, "Measurement of the effective transverse piezoelectric coefficient $e_{31,f}$ of AlN and $Pb(Zr_x,Ti_{1-x})O_3$ thin films," *Sensors and Actuators A: Physical,*, vol. 77, pp. 106–112, 10/12 1999. 49, 55

[78] S. A. Wilson, R. P. J. Jourdain, Q. Zhang, R. A. Dorey, C. R. Bowen, M. Willander, Q. U. Wahab, M. Willander, S. M. Al-hilli, O. Nur, E. Quandt, C. Johansson, E. Pagounis, M. Kohl, J. Matovic, B. Samel, W. van der Wijngaart, E. W. H. Jager, D. Carlsson, Z. Djinovic, M. Wegener, C. Moldovan, R. Iosub, E. Abad, M. Wendlandt, C. Rusu, and K. Persson, "New materials for micro-scale sensors and actuators: An engineering review," *Materials Science and Engineering: R: Reports*, vol. 56, pp. 1–129, 6/21 2007. 49, 50

[79] S. Imai, M. Tokuyama, S. Hirose, G. J. Burger, T. S. J. Lammerink, and J. H. J. Fluitman, "A thin-film piezoelectric impact sensor array fabricated on a Si slider for measuring head-disk interaction," *IEEE Transactions on Magnetics*, vol. 31, no. 6, pp. 3009–3011, 1995. ID: 1. 50

[80] Y. S. Lim, J. S. Jeong, J. Bang, and J. Kim, "CaO buffer layer for the growth of ZnO thin film," *Solid State Communications*, vol. 150, p. 428, 2010. 50

[81] Y. Qi, N. T. Jafferis, K. L. Jr., C. M. Lee, H. Ahmad, and M. C. McAlpine, "Piezoelectric ribbons printed onto rubber for flexible energy conversion," *Nano Letters*, vol. 10, no. 2, p. 524, 2010. 50

[82] H. B. Sharma and A. Mansingh, "Sol-gel processed barium titanate ceramics and thin films," *Journal of Materials Science*, vol. 33, p. 4455, 1998. 51

[83] T. Hayashi, N. Ohji, K. Hirohara, T. Fukunaga, and H. Maiwa, "Preparation and properties of ferroelectric $BaTiO_3$ thin films by sol-gel process," *Japanese Journal of Applied Physics Part 1*, vol. 32, no. Pt. 1 9B, p. 4092, 1993. 51

[84] C. E. Zybill, E. Hechtl, D. Kovalev, and W. Eckstein, "Improvement of loss factor tan of PZT $PbTi_{0.75}Zr_{0.25}O_3$ films by O-ion-implantation," *Integrated Ferroelectrics*, vol. 29, no. 3, pp. 283–290, 2000. 52

[85] D. Czekaj, A. Lisinska-Czekaj, M. F. Kuprianov, and Y. N. Zakharov, "Pyroelectric properties of the multi-component ferroelectric ceramic materials," *Journal of the European Ceramic Society*, vol. 19, pp. 1149–1152, 6 1999. 52

[86] R. A. Dorey, S. B. Stringfellow, and R. W. Whatmore, "Effect of sintering aid and repeated sol infiltrations on the dielectric and piezoelectric properties of a PZT composite thick film," *Journal of the European Ceramic Society,*, vol. 22, pp. 2921–2926, 12 2002. 53, 56, 59, 62

[87] V. Kalem, I. Cam, and M. Timucin, "Dielectric and piezoelectric properties of PZT ceramics doped with strontium and lanthanum," *Ceramics International*, vol. 37, p. 1265, 2011. 53, 54

[88] W. Chen, Z. H. Wang, W. Zhu, and O. K. Tan, "Ferromagnetic, ferroelectric and dielectric properties of $Pb(Zr_{0.53}Ti_{0.47})O_3.CoFe_2O_4$ multiferroic composite thick films," *Journal of Physics D: Applied Physics*, vol. 42, p. 075421, 2009. 53

[89] S. Y. Cheng, S. L. Fu, and C. C. Wei, "Low-temperature sintering of PZT ceramics," *Ceramics International*, vol. 13, p. 223, 1987. 53, 54

[90] D. L. Corker, Q. Zhang, R. W. Whatmore, and C. Perrin, "PZT composite ferroelectric thick films," *Journal of the European Ceramic Society,*, vol. 22, pp. 383–390, 3 2002. 53, 54, 62, 81

[91] R. A. Dorey and R. W. Whatmore, "Electroceramic thick film fabrication for MEMS," *Journal of Electroceramics*, vol. 12, no. 1/2, pp. 19–32, 2004. NR: 89. 53, 54, 57, 60, 61, 64, 65, 66, 67, 68, 69, 70, 164

[92] D. Wang, M. J. Edirisinghe, and R. A. Dorey, "Formation of PZT crack-free thick films by electrohydrodynamic atomization deposition," *Journal of the European Ceramic Society*, vol. 28, p. 2739, 2008. 54, 61, 64, 65, 66, 164

[93] D. Wang, S. A. Rocks, and R. A. Dorey, "Formation of PZT microscale structures using electrohydrodynamic atomization filling of metallic moulds," *Journal of the European Ceramic Society*, vol. 30, p. 1821, 2010. 54, 68

[94] S. Takahashi, "Sintering of $Pb(Zr,Ti)O_3$ ceramics at low temperatures," *Japanese Journal of Applied Physics*, vol. 19, no. 4, p. 771, 1980. 54

[95] T. Ohno, M. Kunieda, H. Suzuki, and T. Hayashi, "Low-temperature processing of $Pb(Zr_{0.53}Ti_{0.47})O_3$ thin films by sol-gel casting," *Japanese Journal of Applied Physics*, vol. 39, p. 5429, 2000. 54

[96] A. Wu, P. M. Vilarinho, and A. I. Kingon, "Ceramic processing strategies for thick films on copper foils," *Acta Materialia*, vol. 58, p. 2282, 2010. 54, 72, 75, 76, 77

[97] M. D. Losego, J. F. Ihlefeld, and J. P. Maria, "Importance of solution chemistry in preparing sol-gel PZT thin films directly on copper surfaces," *Chemistry of Materials*, vol. 20, p. 303, 2008. 54, 72, 75, 123

[98] B. Jaffe, W. R. Cook, and H. Jaffe, *Piezoelectric Ceramics*, vol. 3. New York, USA: Academic Press, 1971. 54

[99] K. P. Rema, A. S. Divya, and V. Kumar, "Influence of low lanthanum doping on the electrical characteristics of PZT," *Journal of Physics D: Applied Physics*, vol. 42, p. 6, 2009. 54

[100] H. K. Seo and J. Y. Park, "Fully integrated piezoelectric RF MEMS in-line DC contact switches with ultra-low voltage operation," *Integrated Ferroelectrics*, vol. 76, p. 69, 2005. 54

[101] C. Kugeler, S. Tappe, U. Bottger, and R. Waser, "A novel design for integrated RF-MEM switches using ferroelectric thin films," *Integrated Ferroelectrics*, vol. 76, p. 59, 2005. 54, 70

[102] R. W. Whatmore, "Ferroelectrics, microsystems and nanotechnology," *Ferroelectrics*, vol. 225, no. 1, pp. 179–192, 1999. 55

[103] W. W. Wolny, "Application driven industrial development of piezoceramics," *Journal of the European Ceramic Society*, vol. 25, p. 1971, 2005. 55

[104] M. D. Maeder, D. Damjanovic, and N. Setter, "Lead free piezoelectric materials," *Journal of Electroceramics*, vol. 13, p. 385, 2004. 55

[105] F. Dauchy and R. A. Dorey, "Patterned crack-free PZT thick films for micro-electromechanical system applications," *International Journal of Advanced Manufacturing Technology*, vol. 33, no. 1-2, pp. 86–94, 2007. Cited By (since 1996): 8. 56, 62, 63, 64, 65, 68, 69

[106] R. A. Dorey, S. A. Rocks, F. Dauchy, D. Wang, F. Bortolani, and E. Hugo, "Integrating functional ceramics into microsystems," *Journal of the Euro-*

pean Ceramic Society, vol. 28, no. 7, pp. 1397–1403, 2008. 57, 61, 62, 65, 68, 70

[107] X. T. Yan and Y. Xu, *Chemical Vapour Deposition: An Integrated Engineering Design for Advanced Materials*. Springer, 2010. 58

[108] A. C. Jones, T. J. Leedham, P. J. Wright, D. J. Williams, M. J. Crosbie, H. O. Davies, K. A. Fleeting, and P. OBrien, "Metalorganic chemical vapour deposition (MOCVD) of zirconia and lead zirconate titanate using a novel zirconium precursor," *Journal of the European Ceramic Society*, vol. 19, pp. 1431–1434, 6 1999. 58

[109] Z. J. Wang, H. Kokawa, and R. Maeda, "Electrical properties and microstructure of lead zirconate titanate (PZT) thin films deposited by pulsed-laser deposition," *Ceramics International*, vol. 30, no. 7, pp. 1529–1533, 2004. Cited By (since 1996): 4. 58

[110] A. Bardaine, P. Boy, P. Belleville, O. Acher, and F. Levassort, "Influence of powder preparation process on piezoelectric properties of PZT sol-gel composite thick films," *Journal of Sol-Gel Science and Technology*, vol. 48, p. 135, 2008. 59

[111] D. L. Corker, R. W. Whatmore, E. Ringgaard, and W. W. Wolny, "Liquid-phase sintering of PZT ceramics," *Journal of the European Ceramic Society,*, vol. 20, pp. 2039–2045, 11 2000. 59, 72, 74

[112] M. A. Aegerter and M. Mennig, *Sol-gel technologies for glass producers and users*. Springer, 2004. 59, 60

[113] S. P. Beeby, A. Blackburn, and N. M. White, "Processing of PZT piezoelectric thick films on silicon for microelectromechanical systems," *Journal of Micromechanics and Microengineering (UK)*, vol. 9, pp. 218–229, Sept. 1999. 15 ref., Photomicrographs, Numerical Data; 15 refs. Photomicrographs; Numerical Data; IL: Photomicrographs; NR: 15 RX: 1 (on Nov 07, 2008). 64, 70, 71, 86

[114] R. Maas, M. Koch, N. R. Harris, N. M. White, and A. G. R. Evans, "Thick-film printing of PZT onto silicon," *Materials Letters,*, vol. 31, pp. 109–112, 5 1997. 64

[115] L. Simon, S. L. Dren, and P. Gonnard, "PZT and PT screen-printed thick films," *Journal of the European Ceramic Society*, vol. 21, no. 10-11, pp. 1441–1444, 2001. 64

[116] J. Stringer and B. Derby, "Limits to feature size and resolution in ink jet printing," *Journal of the European Ceramic Society*, vol. 29, pp. 913–918, 3 2009. 66

[117] H. Wensink and M. C. Elwenspoek, "Reduction of sidewall inclination and blast lag of powder blasted channels," *Sensors and Actuators A: Physical,*, vol. 102, pp. 157–164, 12/1 2002. 67, 68

[118] D. Wang, S. A. Rocks, and R. A. Dorey, "Micromoulding of PZT film structures using electrohydrodynamic atomization mould filling," *Journal of the European Ceramic Society*, vol. 29, p. 1147, 2009. 68

[119] K. Zheng, J. Lu, and J. Chu, "A novel wet etching process of $Pb(Zr,Ti)O_3$ thin films for applications in microelectromechanical systems," *Japanese Journal of Applied Physics*, vol. 43, no. 6B, p. 3934, 2004. 68

[120] K. R. Williams, "Etch rates for micromachining processing: Part ii," *Journal of Microelectromechanical Systems*, vol. 12, no. 6, p. 761, 2003. 70, 71

[121] I. Zubel and M. Kramkowska, "Etch rates and morphology of silicon (h k l) surfaces etched in KOH and KOH saturated with isopropanol solutions," *Sensors and Actuators A*, vol. 115, p. 549, 2004. 70, 88

[122] J. Ohara, Y. Takeuchi, and K. Sato, "Improvement of high aspect ratio Si etching by optimized oxygen plasma irradiation inserted DRIE," *Journal of Micromechanics and Microengineering*, vol. 19, no. 9, p. 095022, 2009. 71

[123] J. Li, A. Q. Liu, and Q. X. Zhang, "Tolerance analysis for comb-drive actuator using DRIE fabrication," *Sensors and Actuators A: Physical*, vol. 125, pp. 494–503, 1/10 2006. 71, 72

[124] J. J. Choi, J. Ryu, B.-D. Hahn, W.-H. Yoon, and D.-S. Park, "Effects of a conducting $LaNiO_3$ thick film as a buffer layer of a $Pb(Zr,Ti)O_3$ film on titanium substrates," *International Journal of Applied Ceramic Technology*, vol. 6, no. 6, pp. 687–691, 2009. 72, 74

[125] R. Seveno, P. Limousin, D. Averty, J. L. Chartier, R. L. Bihan, and H. W. Gundel, "Preparation of multi-coating PZT thick films by solgel method onto stainless steel substrates," *Journal of the European Ceramic Society*, vol. 20, pp. 2025–2028, 11 2000. 72

[126] K. Kanda, I. Kanno, H. Kotera, and K. Wasa, "Simple fabrication of metal-based piezoelectric MEMS by direct deposition of thin films on titanium substrates," *Microelectromechanical Systems, Journal of*, vol. 18, no. 3, pp. 610–615, 2009. ID: 1. 72, 74

[127] T. Kim, A. I. Kingon, J. P. Maria, and R. T. Croswell, "Lead zirconate titanate thin film capacitors on electroless nickel coated copper foils for embedded passive applications," *Thin Solid Films*, vol. 515, p. 7331, 2007. 72, 75

[128] K. Li, H. L. W. Chan, K. W. Lee, and C. L. Choy, "Preparation of thick PZT films on stainless steel substrates," *Integrated Ferroelectrics*, vol. 30, p. 253, 2000. 73

[129] T. Suzuki, I. Kanno, J. J. Loverich, H. Kotera, and K. Wasa, "Characterization of $Pb(Zr,Ti)O_3$ thin films deposited on stainless steel substrates by RF-magnetron sputtering for MEMS applications," *Sensors and Actuators A: Physical*, vol. 125, no. 2, p. 382, 2006. 73

[130] K. Maruyama, M. Tsukada, O. Matsuura, M. Kurasawa, H. Yamawaki, M. Kondo, K. Kurihara, Y. Horii, and T. Eshita, "Highly-oriented crystallinity of ferroelectric layers for reliable FRAM capacitors," in *Dielectrics for Nanosystems: Materials Science, Processing, Reliability, and Manufacturing : Proceedings of the First International Symposium* (R. Singh, ed.), vol. 2004, The Electrochemical Society, 2004. 73, 103

[131] A. I. Kingon and S. Srinivasan, "Lead zirconate titante thin films directly on copper electrodes for ferroelectric, dielectric and piezoelectric applications," *Nature Materials*, vol. 4, no. 3, 2005. 76, 77, 123

[132] R. A. Dorey and R. W. Whatmore, "Apparent reduction in the value of the d_{33} piezoelectric coefficient in PZT thick films," *Integrated Ferroelectrics*, vol. 50, pp. 111–119, 2002. Cited By (since 1996): 8. 101, 110

[133] F. Cverna, *ASM Ready Reference: Thermal Properties of Metals*. ASM International, illustrated ed., 2002. 103, 158

[134] H. O. Pierson, *Handbook of Chemical Vapor Deposition (CVD): Principles, Technology, and Applications*. William Andrew, 2 ed., 1999. 116

[135] P. Walker and W. H. Tarn, *CRC Handbook of Metal Etchants*. Handbook of Metal Etchants, London: CRC Press, 1st ed., 1991. 123

[136] A. I. Zaitsev, N. E. Shelkova, N. P. Lyakishev, and B. M. Mogutnova, "Thermodynamic properties and phase equilibria in the Na_2O-SiO_2 system," *Physical Chemistry Chemical Physics*, vol. 1, p. 1899, 1999. 130

[137] H. Nafe, "Determining extremely low sodium activities at elevated temperatures," *Journal of the Electrochemical Society*, vol. 151, no. 5, p. J27, 2004. 130

[138] Ferroperm Piezoceramics A/S, "Ferroperm piezoceramics: High quality components and materials for the electronic industry." http://goo.gl/o12l4, 05/2003 2003. 172

[139] N. Lamberti, F. M. de Espinosa, N. Perez, H. Gomez, and C. Negreira, "Optimization of acoustic matching layers for piezocomposite transducers," vol. 2, p. 1105, 22-25 October 2000 2000. 190

[140] V. V. Klimov, I. K. Skirdina, N. I. Selikova, A. N. Bronnikov, S. N. Loboda, and A. S. Shtonda, "Electrical properties of thick PZT-based films," *Inorganic Materials*, vol. 44, no. 5, p. 527, 2008. 194

[141] C. U. Grosse, M. Kruger, and S. D. Glaser, "Wireless Acoustic Emission sensor networksfor structural health monitoring in civil engineering," pp. Tu–1.7.3, 25-29 September 2006 2006. 197